PEOPLE'S DEMOCRATIC REPUBLIC OF ALGERIA
MINISTRY OF HIGHER EDUCATION AND SCIENTIFIC RESEARCH

University of Mohamed Boudiaf - M'sila
Faculty of Technology
Department of Electronic

THESIS

A dissertation submitted in fulfillment of the requirements for the degree of

DOCTORATE OF SCIENCE IN ELECTRONICS

Field: Electronic

Option: Instrumentation

By: Samah BOUDOUR

THEME

Optimization of doped and co-doped zinc oxide quality: application for silicon-based solar cells

Presented and publicly defended the 21/02/2021

JURY MEMBERS:

Amar MEZACHE	**Professor**	**Univ. of M'sila**	**Chairman**
Idris BOUCHAMA	**Professor**	**Univ. of M'sila**	**Supervisor**
Ammar MESSOUS	**Professor**	**Univ. of Setif**	**Examiner**
Abdelouahab HASSEM	**Professor**	**Univ. of Setif**	**Examiner**
Fayçal DJEFFAL	**Professor**	**Univ. of Batna**	**Examiner**
Hamza BENNACER	**Senior Lecturer**	**Univ. of M'sila**	**Examiner**

2020/2021

الحمد لله الذي به تتم النعم

إلى أمي حفظها الله

إلى أبي رحمه الله

My beloved sisters and brothers

My darling kids

مريم رقية ، هارون ، موسى بودور

رونق ، ضياء الدين ، زكرياء ، زيد ، محمد ريان زيغم

أروى ، خديجة ، عبد الواحد عياش

صفية ، خولة ، هاجر قادري

جواد تقي الدين بودور

Thank you for your love and support

سماح بودور

ACKNOWLEDGEMENTS

Foremost I would like to express my sincerest gratitude to my supervisor **Prof. Idris BOUCHAMA** for his continuous support and critical guidance during my PhD study. His patience, endless motivation and priceless advice had helped me to make progress in my research career. His encouragement and kind support throughout my PhD period was enormous.

Thanks to Dr. M. HADJAB, Mr. H. KHEMLICHE, Mr. W. BEDJAOUI, and the other colleagues in the Thin Films Development and Applications Unit – UDCMA-CRTI for their encouragements, supports, and invaluable assistance.

I express my deep gratitude to Amar MEZACHE professor at the University of M'sila, for his interest in my work by doing the honor of chairing the jury of my defense.

I would like to extend my sincere thanks to all members of the jury:

I would like to thank Fayçal DJEFFAL, professor at the University of Batna for his interest in this work and for having agreed to examine my work by taking part in the thesis jury.

I would like to thank Abdelouahab HASSEM, professor at the University of Setif for his interest in this work and for having agreed to examine my work by taking part in the thesis jury.

I would like to thank Ammar MESSOUS, professor at the University of Setif for his interest in this work and for having agreed to examine my work by taking part in the thesis jury.

I would like to thank Hamza BENNACER, Senior Lecturer at the University of M'sila for his interest in this work and for having agreed to examine my work by taking part in the thesis jury.

CHAPTER I THIN FILMS SOLAR CELLS OVERVIEW

GENERAL INTRODUCTION

Since primitive era to modern life, human have been devoted their inspiration for developing various types of energy production, consumption and saving equipment, which can be subject to touch and improve their lives worldwide. At early ages, humans exploited their muscular powers in addition to primitive physical powers for hunting animals. Later, they domesticated animals for agriculture. When human began to populate more and more, they burnt the classical elements of earth, specifically wood, coal and water to provide their energy needs. With dawning industrial age, humans head to exploring the earth core and extracting the fossil fuels, coal, natural gas and oil to produce energy. By coming the actual modern age, human have mastered the harnessing of nature and earth elements like wind, solar, water, tidal, geothermal and biomass elements to produce renewable and sustainable energies like solar photovoltaic electricity, solar thermal electricity, ocean energy, wind electricity, geothermal energy, hydroelectricity, biomass energy [1]. By considering that the electricity is the most common type of energy what if humans forget about electricity, this is mean that the public humans forget about the lighting, alarms, detector sensors, computers, HD TVs, mobiles, washing machines, tramway, metro, medical healthcare devices, etc. In overall terms, every used devices in human's daily life is running by electric-type energy, the devices in transport and traffic field, internet and computers field, safety and healthcare field, communication field and space hardware, etc. [2].

Through semiconductor materials, a solar cell is a junction, which harvests the electricity through the photovoltaic effect. In which, the photovoltaic is all about efficiency; it is about absorbing and relocating photon energy to electrical energy, decreasing solar cell's cost by using earth-abundant, easy targets, relatively safe and environmentally friendly, inexpensive, efficient, flexible or solid, and bulk or thin semiconductor materials. Zinc oxide (ZnO) semiconductor materials as versatile transparent conducting oxides (TCOs), they are electrically high n-type conductive and optically an excellent transparent (85%) in the visible range with wide energy band gap of around ~3.37 eV at room temperature [3]. They act extensively as most suitable n-type partner in thin-film silicon solar cells [4]. Considering the enormous use of the robust thin film silicon (Si) materials in advanced photonics and electronics, it should be advisable to diversify the materials that are eligible to take part side by side with p-type Si materials to fabricate thin film solar cells [3]. Many eminent experimental researchers have been studied the thin-film ZnO/Si solar cells, and they have been showed low

performances, which were likely due to numerous problems [5-7]. It was found that most of those problems are limited to the large band bending at n-ZnO/p-Si interface, the high carrier charge recombination at the junction and the formation of the Schottky when contacting the p-Si layer with the n-ZnO TCO layer [7].

In order to overcome these problems, also to avoid wasting resources, effort, and time at hope to solve these encountered problems, solar community have resorted to numerical simulation. Eminent researches have been ruled various software tools (AMPS-1D, SCAPS, etc.), to understand, explain and solve the physical and practical problems, which encountered the laboratory research of solar cell devices [3].

Thereby, different characteristics and measurements of used parts or layers in a solar cell device are needed in order to achieve a successful and complete simulation study. These measurements are mostly brought from practical works. Thus, the simulation work and the experimental work are inseparable and complementary two fields. When the experimental or practical work slowing down or falters, the simulation work begins.

Therefore, in this Ph.D. thesis, we focus in two main objectives: optimization of thin film solar cells through numerical modeling by AMPS-1D software; elaboration and characterization of pure (undoped) and Mg-doped ZnO thin films via sol-gel spin coating method. In the context of performing and clarify these two main tasks, the present thesis is divided into an introduction, four chapters and a conclusion:

The introduction: This part reviews status of energy, appreciate photovoltaics, appraises zinc oxide and silicon materials as a potential semiconductors for thin film solar cell, relate the simulation towards experimental, and finally presents the structure of this thesis.

The first chapter presents the types of renewable and sustainable energies, elicits the impact of electrical energy in Algeria, and deals with the fundamentals of semiconductors and photovoltaics, losses in a solar cell and finally brief state on specific types of thin film solar cells.

The second chapter reviews the physics of transparent conducting oxides (TCO), specifically zinc oxide (ZnO) materials, emphasis on elaboration of pure (undoped) and doped ZnO materials by using sol-gel spin coating technique, and finally, presents the characterization techniques which will employ in our work to analysis the fabricated samples.

The third chapter starts by a brief about the simulation approach and AMPS-1D simulator tool. After, it concenters on the optimization of J-V characteristics to predict the performances of three thin film solar cells through AMPS-1D by changing the structural, electrical and external parameters of: defected n-ZnO/p-Si/p-Cu_2O, ideal n^+-HGMZO/n-LGMZO/p-CdTe/$MoTe_2$ and superstrate SLG/TCO/p-CIGS/n-ODC/n-In_2Se_3/Metal structures.

The fourth chapter is a record of characterization results of deposited pure ZnO and Mg doped ZnO samples by using X-ray diffraction (XRD), atomic force microscopy (AFM), scanning electron microscopy (SEM) and UV-Visible spectrophotometry. On the spot of the recorded characterizations: the structural, morphological and optical properties will be discussed. Finally, the feasibility of the obtained properties and their interest and utility in thin film solar cells will be exposed.

In the general conclusion part of this thesis, the important comprehension of pure and doped zinc oxide films in the silicon, CdTe, CIGS-based solar cells will be summarized. Therefore, the orientation for potential ZnO and Mg doped-ZnO thin films be concluded. Future work based on this mixed work between simulation and experimental will proposed.

CHAPTER I

THIN FILMS SOLAR CELLS OVERVIEW

I.1 Introduction

The first chapter is mainly devoted to present thin films solar cells devices. This is associated with the relationship between the p-n junction and the photovoltaic effect, considering the transport behavior through the semiconductor materials. Particular types, silicon-based, CdTe-based and CIGS-based thin films solar cells that accord with the optimization work in this thesis will be reviewed. At the end, the transparent conducting oxides (TCOs) and their advantages and utilization in thin films solar cells will be presented.

I.2 Background: Solar Energy

I.2.1 Renewable energy

When human began to populate more and more, they burnt the classical elements of earth and nature, specifically wood, coal and water to provide their energy needs. By coming the current era, human harness more elements of nature and earth like wind, sun, water, tidal, geothermal and biomass, producing sustainable and renewable energy in many forms in order to replace the depleted biological materials, the fossil fuels, like coal, natural gas and oil [1,8].

Figure 1.1 From up to down and from left to right: Ocean Energy, Solar Photovoltaic Electricity, Wind Energy, Solar Thermal Electricity, Geothermal Energy, Hydroelectricity, and Biomass Energy.

The modern energies include the ocean energy, solar photovoltaic electricity, solar thermal electricity, wind electricity, geothermal energy, hydroelectricity, biomass energy, as shown in Figure 1.1 [9]. In addition, the produced energy is described in different units, and the most important are expressed by the following units:

$$1\ kWh = 1000\ Wh = 1000W \times\ 3600\ s = 3.6\ \times 10^{6}\ Ws = 3.6\ MWs = 3.6\ MJ$$

Moreover, to express the produced electrical power, which converted from the photons energy through the solar panels, the kilowatt-hour (KWh) [10] is the most useful between the previous expressed terms.

I.2.2 Early solar photovoltaic energy

The first-time discovery of the photovoltaic effect was in the 19^{th} century. As 1954, Bell Labs demonstrated this discovery by a modern silicon solar cell device with 6% of efficiency made of a p-type silicon layer with $0.0001\ inch$ thick on an n-type silicon substrate [11]. At same time, thin films solar cells were already conducted by Reynolds et al [12] on a 3 mm thick CdS sample, which yielded an open circuit voltage of $0.45\ V$ and a short circuit density current of $15\ mA/cm^2$ in direct sun light. Those early devices were responsible to open the way for success satellite manufacturing, which mainly supplied by silicon solar cells [11].

With the advent of the first fuel crises in the early 1970s [8], the researchers deliberately harnessed solar cells in terrestrial applications. From that date until the end of 20^{th} century, solar cell devices have been developed with accelerated steps by using abundant, non-toxic and low price materials in order to obtain performant devices applicable in large area of applications with highly cost-efficiency ratio.

I.2.3 Statistical publication in the photovoltaic field

Receiving the torch from the 20^{th} century, engineers and scientists have been working to develop several types of solar photovoltaic devices, in which they revealed huge and strong amount of laboratory researches, theoretical analyses and simulation tasks.

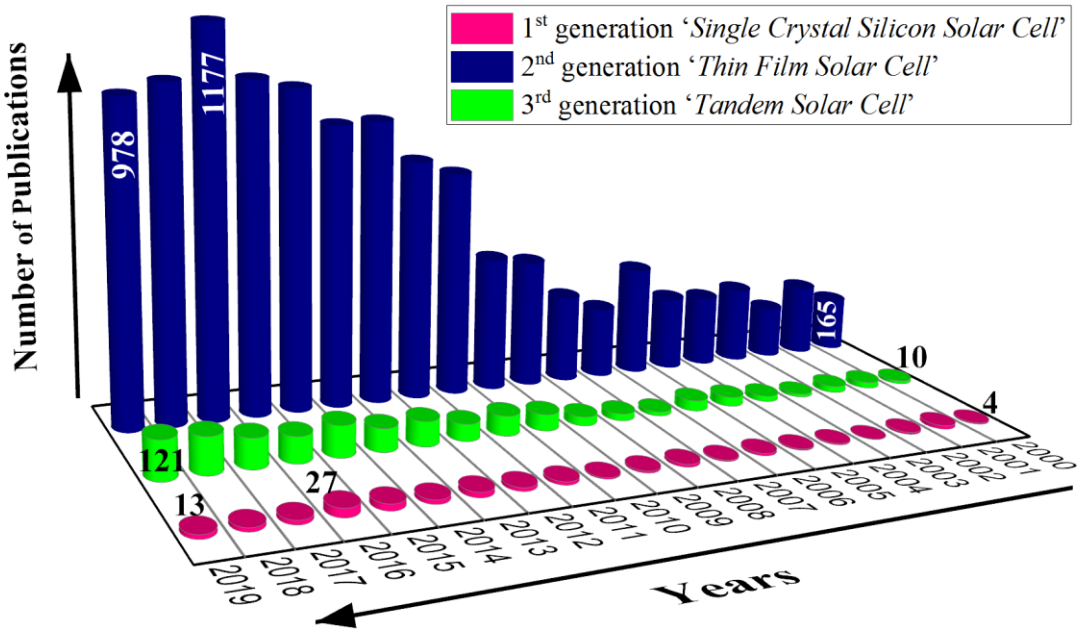

Figure 1.2 Statistical of three generations of solar cell devices: Number of articles over last 20 years, according to the ScienceDirect Elsevier database [13].

Figure 1.2 presents a statistical comparison among three generations of solar cell devices by outlining the number of the published review and research articles over the last 20 years, according to the ScienceDirect Elsevier database [13] by an advanced search involves two words '*photovoltaic*' and '*solar cell*'. It was noticed that the 2nd generation '*Thin Film Solar Cell*' took the lion's share of research compared to the 1st generation '*Single Crystal Silicon Solar Cell*' and the 3rd generation '*Tandem Solar Cell*'.

Involving the words '*photovoltaic*', '*solar cell*', '*Modeling*', '*Simulation*' and '*AMPS-1D*' by means of the same advanced search [13], Figure 1.3 summarizes the growth of publications on the topic of solar cell simulation compared with the total number of publications that addressed the entire solar cell activities over the last 20 years. It was found that, in every year, the total number of articles dealing with solar cell simulation was nearly half of the grown total number of solar cell activities.

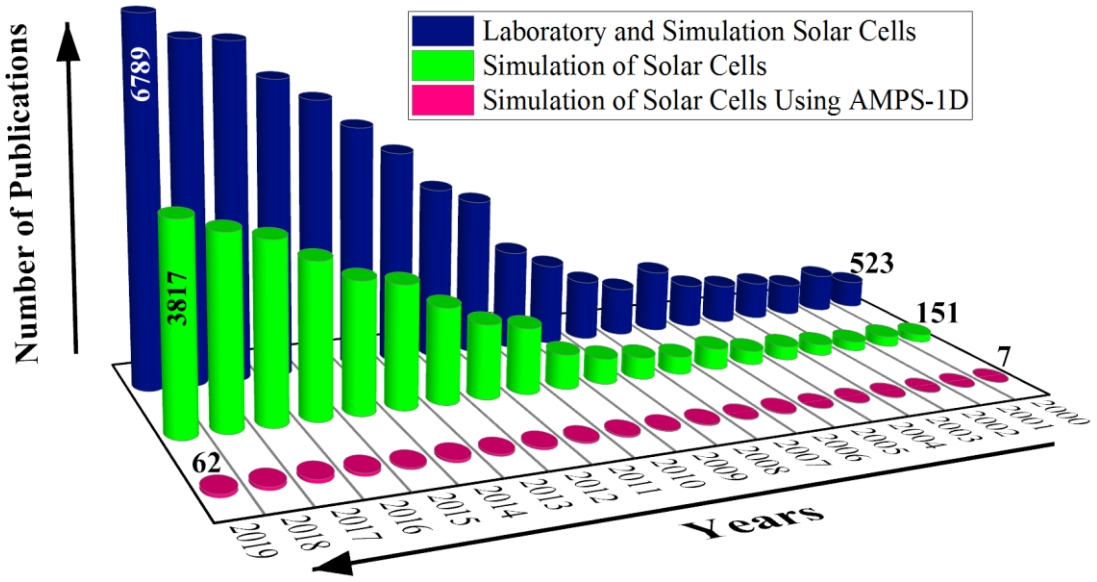

Figure 1.3 Statistical of laboratory and simulation solar cell activities: Number of published articles over last 20 years, according to the ScienceDirect Elsevier database [13].

Furthermore, the simulation activities through AMPS-1D software [14] achieved a record number of 62 articles (Figure 1.3) last year (2019), and two of those articles were accomplished during the preparation for this PhD thesis.

I.2.4 Statistical energy in Algeria versus world, during 2008-2018

Figure 1.4 and 1.5 present the energy statistics in Algeria versus the world, during 2008-2018, according to BP Company [15]. In view of those findings, it is found that the primary energy consumption in Algeria increased to 56.7 TWh, during 2018, at a rate equivalent to 0.4 % of the world primary energy consumption (13864 TWh), as shown in Figure 1.4 (a). As a result, during 2018-2008, Algeria has had a growth rate of 22.92 % of energy consumption per capita compared to world growth rate, which was 5%, at same time, as shown in Figure 1.4 (b). This increasing trend is explained by the increase of generated electricity from the primary fossil fuels that reached a total world of 26614.8 TWh, during 2018, in which a share of 0.3 % of them was in Algeria, which is equivalent to 76.4 TWh, as illustrated in Figure 1.4 (c).

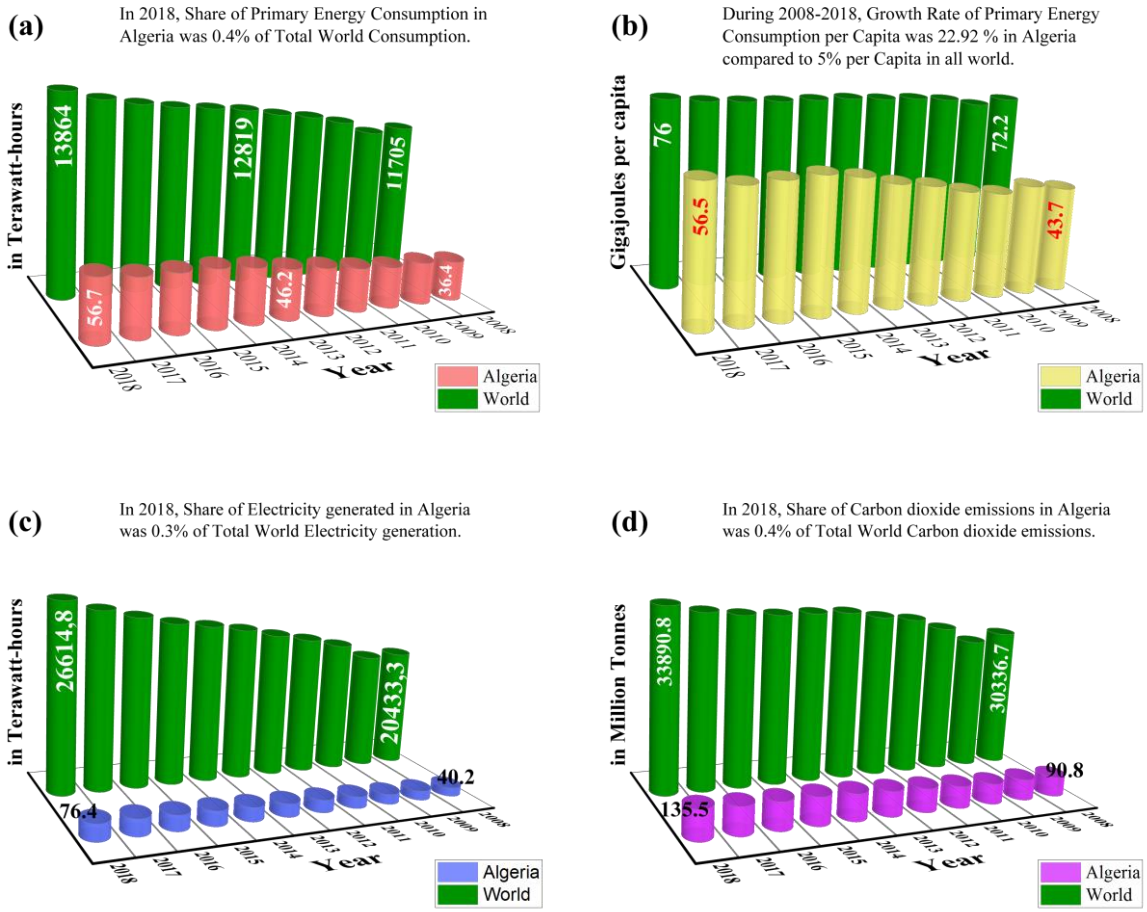

Figure 1.4 Algeria Energy Statistics vs. World Energy Statistics, during 2008-2018, according to [15]: (a) Primary Energy Consumption, (b) Primary Energy Consumption per Capita, (c) Electricity generation, (d) Carbon dioxide emissions. 1 TW*h* (Terawatt-hour) = 10^9 KW*h* / 3.6 Giga joule = 10^3 KW*h* / 1 Tonne ~ 4300 KW*h* of electricity or 1800 Kg of paper.

However, the growing use of fossil fuels to generate the required demanded of electricity has led to increase the carbon dioxide emissions in the entire world by around 10.5 % during 2008-2018. By 2018, compared with 2008, Algeria has also seen an increase in carbon dioxide emissions from $90.8\,million-tonnes$ to $135.5\,million-tonnes$, or roughly, 32.99 %, equivalent to three times to the world increase-percentage (Figure 1.4 (d)). Thereby, the switching from the fossil fuels-based electricity to renewable energies has become a necessity.

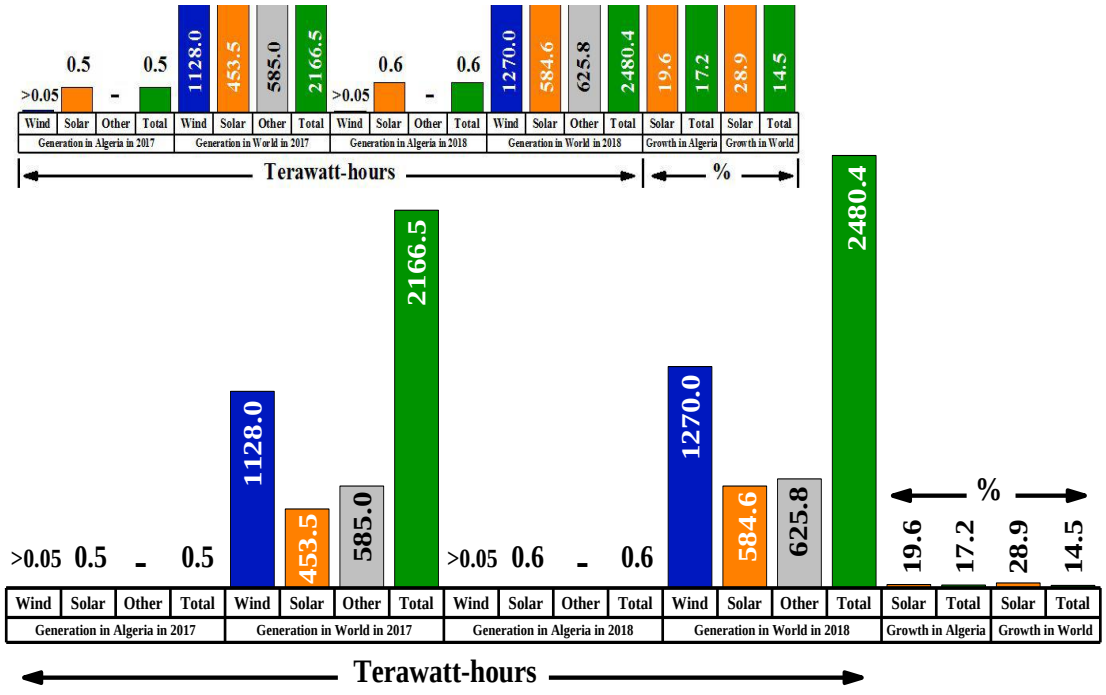

Figure 1.5 Statistics of Generated Electricity from renewable Energy in Algeria vs. World during 2017 and 2018, according to [15] (Others: geothermal, biomass and other renewables).

However from Figure 1.5, it is noticed that the renewable energy supplies, in Algeria, are not doing well, where, the amount of all types of them lies below 1 % of percentage, if not non-existent. As shown in this figure, in 2017 and 2018, the generated world-electricity based on solar energy technologies was 453.5 and 584.6 TWh, at an increase equivalent to 12.65 %. While, at same years, the generated electricity amount based on solar energy in Algeria was 0.5 and 0.6 TWh, respectively, far from the world production.

I.2.5 Solar radiation

Being of our world within the habitable zone of the sun, it was inevitable to focus on harnessing the emitted radiations from the sun to the earth in order to produce a sustainable and renewable energy. This reached amount of radiations, which for millions of years supported multiple uses by all life forms on the earth, comes every day shiny and strong as tiny packages of energy called photons. Those photons are the basic element of the sun's electromagnetic

spectrum that may classified the electromagnetic quantum versus a wide range of wavelength (λ) into: cosmic, gamma-, and X- rays, ultraviolet, visible, infrared, microwaves, radar, radio waves and broadcast band [16], as illustrated by the diagram (a) in Figure 1.6.

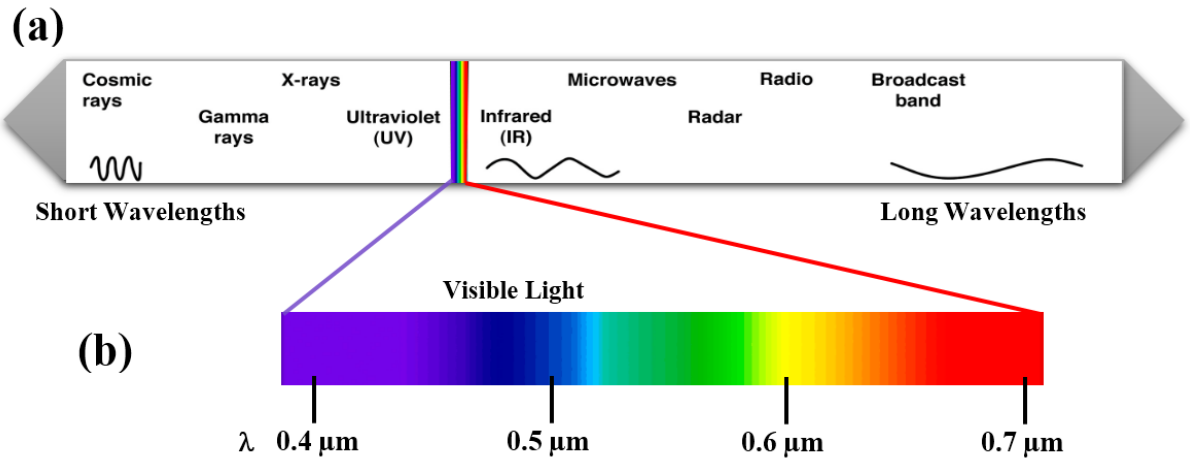

Figure 1.6 (a) Electromagnetic radiation spectrum and (b) Visible light energy wavelength.

As well known the visible light part, which consist of 44 % of the fallen sun's radiation on the earth, is may detected by the human eye and is classified in the relatively short wavelengths in range from 0.4 µm (violet) to 0.7 µm (red) [17] as shown by the diagram (b) in Figure 1.6.

I.2.6 Air mass

The Electromagnetic radiations emitted from the sun outside the earth's atmosphere is so called AM 0 acronym of Air Mass 0, whereas the term AM 1 means that the emitted light has passed through the atmosphere, as shown in Figure 1.7. Furthermore, Planck's Law of Radiation draws AM 0 as a radiation released from a black body (sun surface at temperature of 5778 K, Figure 1.7). In which, the path $(1/\cos\theta)$ of radiation inside the atmosphere (Figure 1.8) plus the intervention of nature factors (Figure 1.7) affects the light in which the $AM\ x$ spectrum will be, as shown in Figure 1.8, where $(x = 1, \dots, 4)$. The integrated surface under AM1.5 curve, $(1/\cos 48°)$, result an irradiance of 1000 W/m^2. As a result, the photovoltaic community has devoted the AM 1.5 spectrum as standard light optimizer during solar cell laboratory activities and in software tools which are made specially for optimizing the performance of solar cell devices [18].

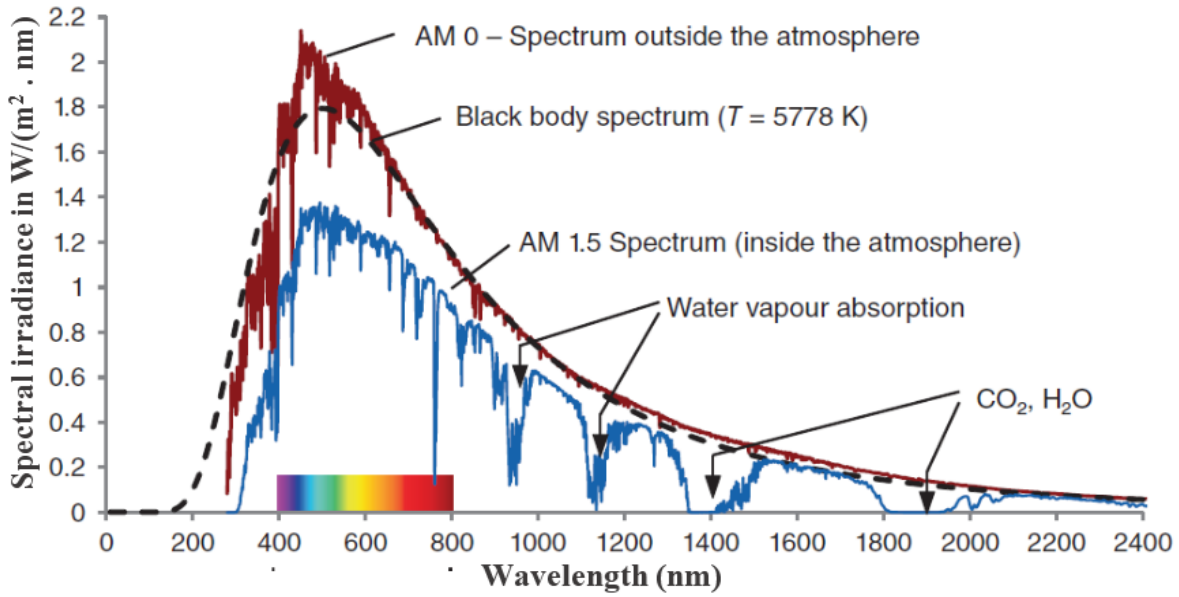

Figure 1.7 Spectrum outside and inside the atmosphere [18].

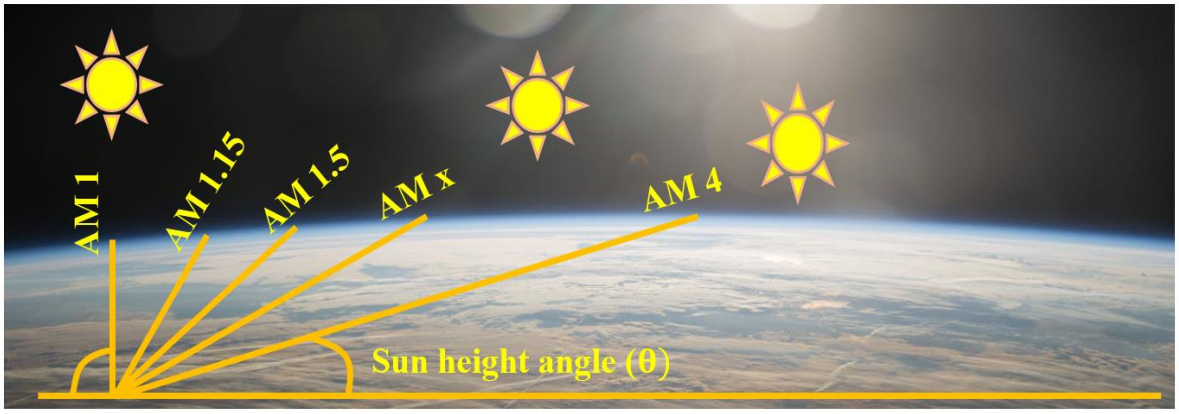

Figure 1.8 Path of light in terms of Air Mass compared to the vertical distance to earth through the atmosphere [18].

I.3 Physics of Semiconductors

Materials can be categorized in terms of their electrical properties into three types including: Conductor, Insulator, and Semiconductor. As shown in Figure 1.9, these three types

of materials can be represented by the electronic band structure, which depicts the potential energy levels an electron could occupy in the lattice of these materials.

I.3.1 Conductor, insulator, semiconductor and their electronic band structure

Metals are extremely good conductors of electricity, because the outer electrons of atoms are weakly bond. This results a large number of free negative electrons that can be excited in an empty and available energy state (Figure 1.9 (a)). Insulators do not conduct electricity. Which means that all electrons are bond to the background of atoms (Figure 1.9 (c)). Semiconductors are materials distinct by intermediate conductivity ranged between of the metals and of insulators. Under certain conditions, this amount of conductivity provides more tendency to a number of electrons to leave the background of atoms, leaving behind positive holes (Figure 1.9 (b)) [18].

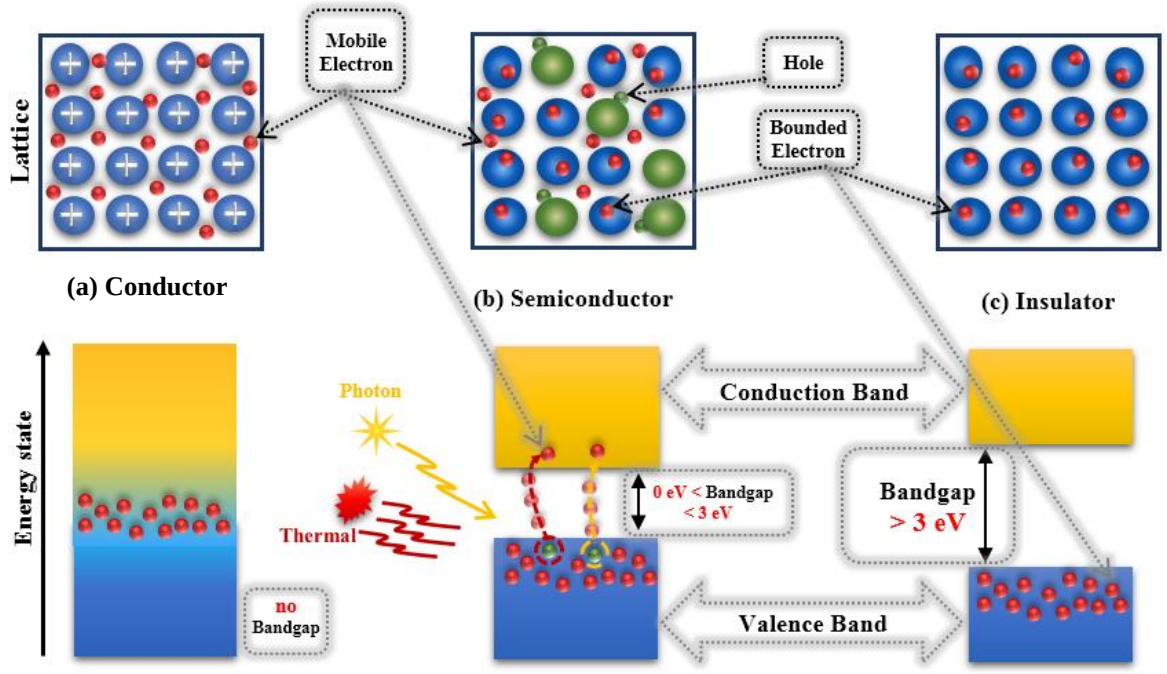

Figure 1.9 Conductor, semiconductor and insulator lattices and their electronic band structures.

Conductors, especially metals have a wide electronic band, which is not completely filled with electrons. This electronic band corresponds to the energy levels in which electrons can freely move around in the lattice of metal. A semiconductor and an insulator have two separated bands with considered forbidden gap between them. Most electrons occupy the lower band known by the valence band. If electrons occupy the valence band, they are not moving. Those electrons have strong bound to their atoms in the lattice of semiconductor. Electrons in upper band, known by the conduction band, are free and mobile and take part in the conduction, just like the free and mobile electrons in a lattice of metal. The forbidden gap energy between the valence band and the conduction band is called the bandgap energy. In this gap, no energy states exits, which can be occupied by electrons.

The difference between insulators and semiconductors is that the band gap of an insulator is much larger than the band gap of a semiconductor. The band gap of an insulator is typically broader than 3 eV. For a semiconductor, the band gap is typically smaller than 3 eV. In semiconductor, some electrons can have enough thermal energy or photon energy, leading them to jump from the valence band to the conduction band, making the semiconductor more conductive. Those conditioned energies must be equal or larger than the band gap energy of a semiconductor [19].

I.3.2 Semiconductors doping

To increase the conductivity of semiconductors, we need more electrons to jump from the valence band to conduction band by using thermal energy or by incorporating impurities in their lattice. This incorporating process is so-called the doping.

Typically, semiconductor are doped to be more conductive or to alter in conductivity between n-type or p-type. The majority charge carriers in an n-type semiconductor are the electrons, which are moving around in the lattice of the fixed positive dopants that donated them (Figure 1.10 (a)). While, the majority charge carriers in p-type semiconductor are holes, which are diffusing and compensating the accepted electrons by fixed negative dopants (Figure 1.10 (b)) [18].

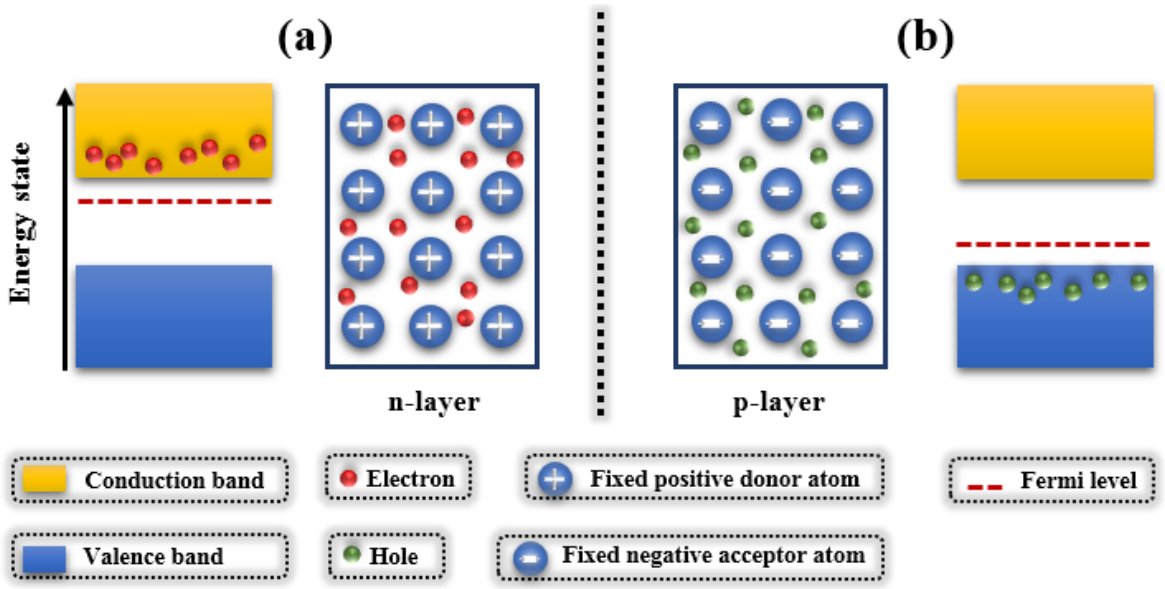

Figure 1.10 n-type and p-type layers and their electronic band structures.

I.3.3 Charge carrier transport in semiconductor

In the lattice of an n- or p-type semiconductor, there are surplus mobile carriers: holes and/or electrons, moving under the stimulation of two forces: diffusion and/or the drift.

The diffusion, as shown in Figure 1.11, is produced by the concentration gradient (dx/dn) along the direction x, going from the right to the left according to the flux low of diffusion ($J_{n/p}^{diff}$ in Figure 1.11) until the density of carriers is uniformly distributed in all area of a semiconductor. While the drift current is produced by an electric field (ζ), where the holes in this field will move in the same direction of this field in contrary to the electrons, which will move in the opposite direction of the electric field, according to the equations ($J_{n/p}^{drif}$ in Figure 1.10) [19] as summarized in Figure 1.11.

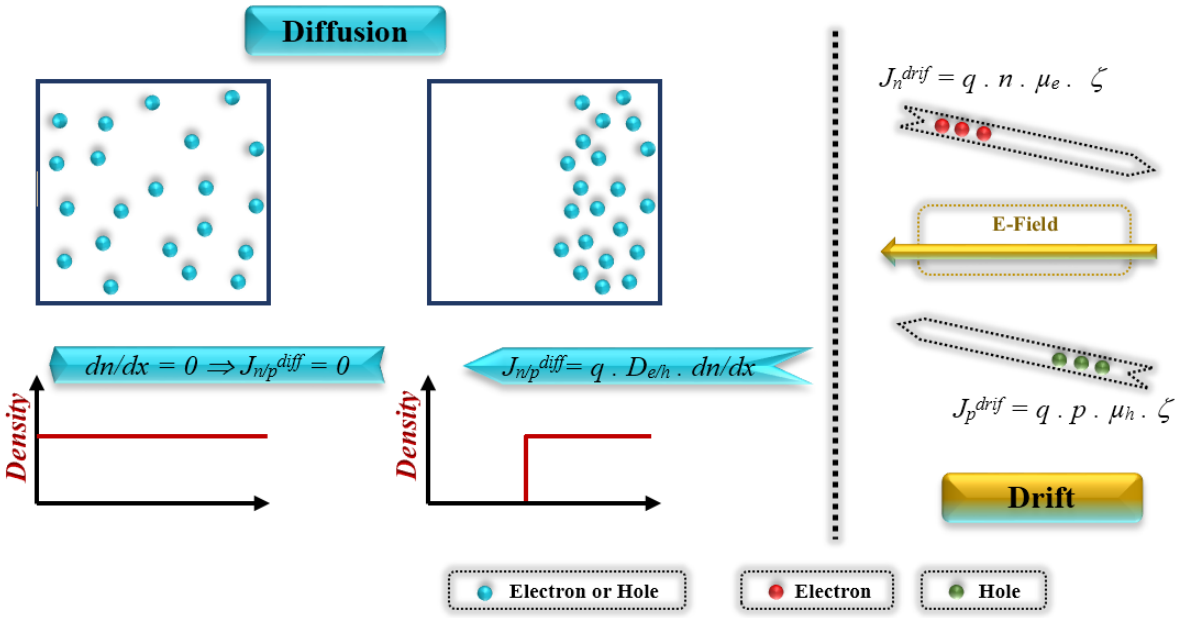

Figure 1.11 Carrier transport in semiconductor through Diffusion and Drift, where J: diffusion/drift electron/hole current density, q: elementary charge, D: diffusion coefficient, dn/dx: density gradient along x, n/p: density of electrons/holes, μ: mobility constant of electron/hole and ζ: electric field.

I.3.4 p-n junction formation

The basic structure of most solar cells is the p-n junction, which is a joining of p-type semiconductors and n-type semiconductors or metals. Figure 1.10 shows the two sides n-type layer and p-type layer with their energy bands before making the n-p junction. It is clear that there is a level energy in the forbidden gap, which named 'Fermi level: E_F' after the physicist Enrico Fermi. This Fermi level tells us the average of electrons in the lattice of layer, and it lies close to the most-down edge of the conduction band in n-type layer, while in the p-type layer it lies close to the most-upper edge of the valence band [18].

After joining the two sides, in Figure 1.12, it is obviously that the surplus free electrons and holes will diffuse through the formed junction from both sides, leaving behind their fixed positive donor atoms and fixed negative acceptor atoms. However, they will drift again under the influence of a resulted electric field at the neighborhood of the formed junction, creating a

new balance that makes diffusion and drift cancel each other. At that time, a space charge (or depletion) region exists at the p-n junction, and a situation of equilibrium will be, making the Fermi level at same level in both joined layers with a built up potential step of qV_D, as illustrated in Figure 1.12. In this situation, the total electrons and holes currents at any time are expressed by using the mentioned equations (1.1) [19], then:

$$\begin{cases} J_n = J_e^{drif} + J_e^{diff} \\ J_p = J_h^{drif} + J_h^{diff} \end{cases} \quad (1.1)$$

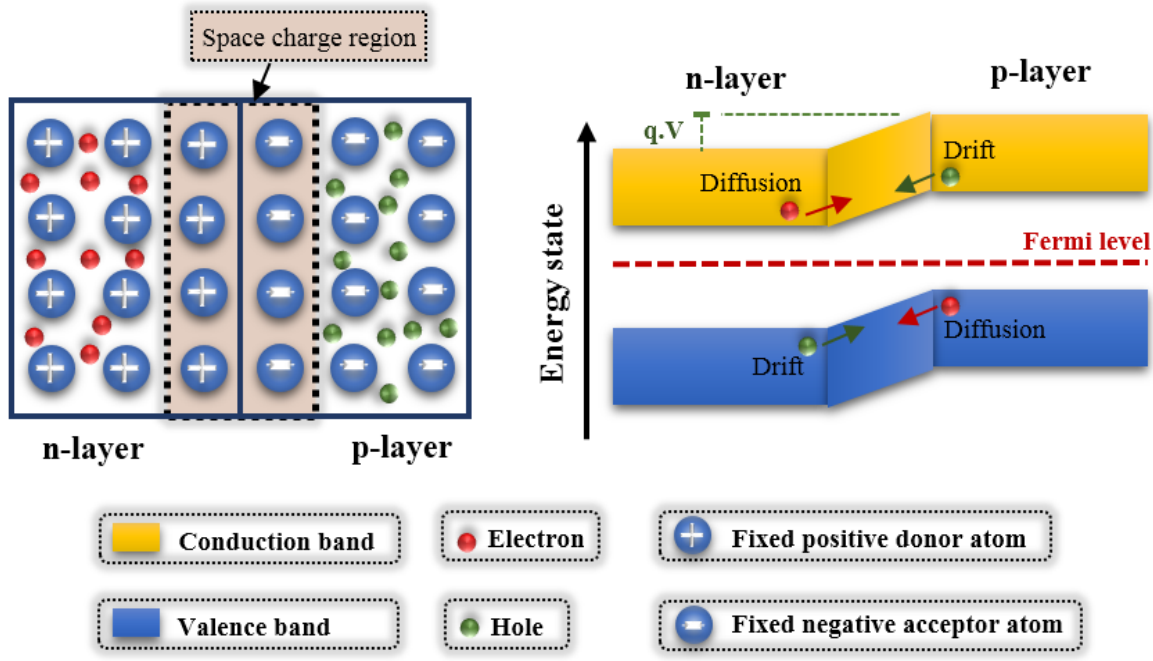

Figure 1.12 p-n junction and its band energy diagram under thermal equilibrium.

I.4 Photovoltaic Effect

I.4.1 Description of photovoltaic effect

The photovoltaic is about absorbing photons, after that converting their energies to electrical energy through a p-n junction device of few tens nanometers to hundreds micrometers of thickness. The photons are therefore absorbed, then transfer their quantum energies to the

atoms of materials, finally exit the device and both current and voltage can be generated inside [14]. It can describe this phenomenon by three steps (Figure 1.13):

- At first step, the incident photons, which have energies smaller or equal to the band gap of n-type semiconductor, will be absorbed near the depletion region of p-n junction, and generate electron-hole pairs.
- At second step, the generated electron-hole pairs will subject to drift and diffusion forces, which will separate them. For example, in the case of generation inside p-region, electron will move through the junction from the p-region to the n-region, and holes move in the opposite direction.
- At third step, as the free electrons competently travel through the n-type region thus they will be collected at the terminal, the free holes travels oppositely through the p-type region thus they will be collected at the opposite terminal.

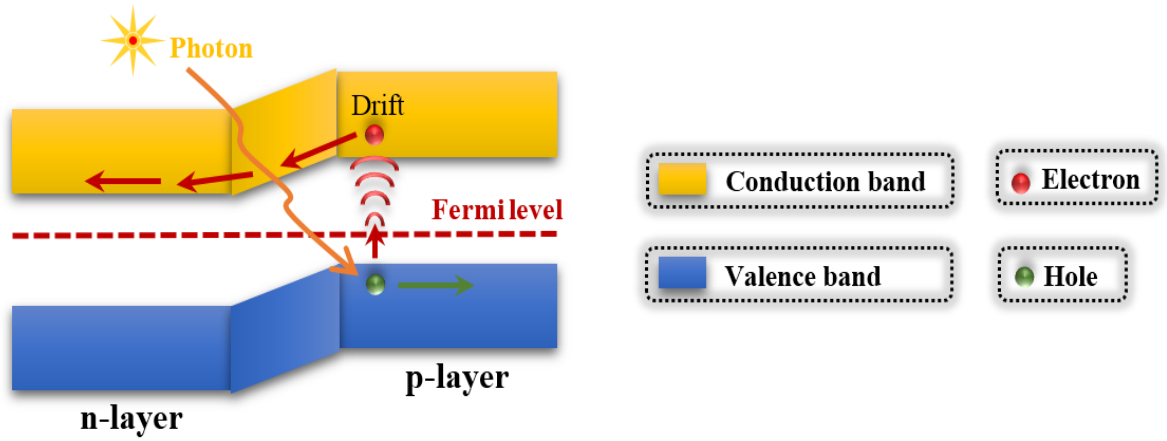

Figure 1.13 Photovoltaic effect.

I.4.2 Equivalent circuit of real solar cell

The left diagram in Figure 1.14 illustrates the equivalent electrical circuit of real solar cell that consist of a single diode, a current source, which represents the photo-generated current (I_L), in parallel with the diode along with series (R_s) and shunt (R_{sh}) resistance.

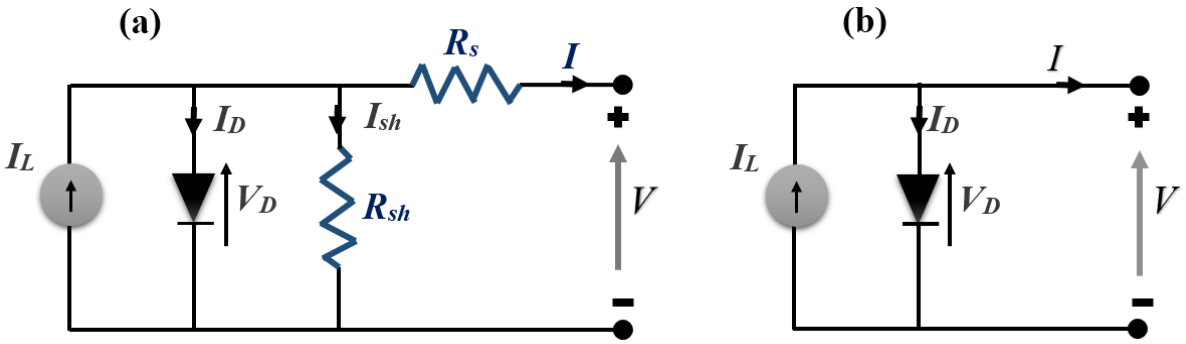

Figure 1.14 (a) Equivalent circuit of real solar cell and its (b) simplified equivalence.

The extracted current (I) through an external load from the circuit shown in Figure 1.145a) or the real solar cell can be given by the equation (1.2) [19].

$$I = I_L - I_0 \left[exp\left(\frac{q(V+IR_s)}{nkT}\right) - 1 \right] - \frac{V+IR_s}{R_{sh}} \tag{1.2}$$

In which	I_L	– Photo-generated current generated due to photovoltaic effect,
	I_0	– Reverse saturation current of the diode or solar cell,
	n	– Ideality factor of the diode,
	R_s and R_{sh}	– Series and shunt resistances, respectively,
	V	– Applied voltage across the solar cell.

Moreover, an illuminated ideal p-n junction has similar electrical characteristics as of a diode. It can be simplified to the diagram at Figure 1.14 (b) and described by the following equation (1.3) [19]:

$$I = I_L - I_0 \left[exp\left(\frac{qV}{nkT}\right) - 1 \right] \tag{1.3}$$

I.4.3 I-V characteristics of solar cells

The basic measurement to evaluate and rating a solar cell is I-V measurement, in which by applying a voltage across a real solar cell (Figure 1.14(a)), it can be measured the current through it. This measurement can be done either in dark (dark I-V) or under illumination (light I-V), as shown in Figure 1.15.

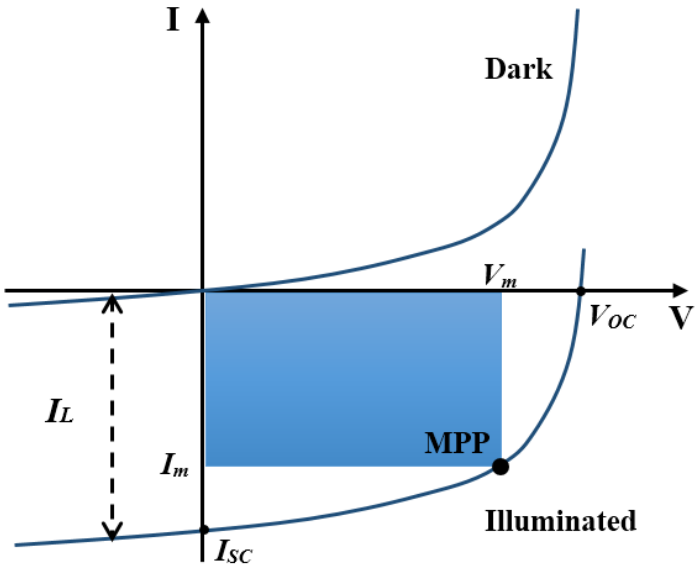

Figure 1.15 I-V characteristics of solar cell under illumination and dark.

In dark conditions, solar cell or a p-n junction has similar electrical characteristics as a simple diode, as we mentioned above. When light falls on the solar cell, electrical power can be extracted and I-V curve shift down along with the current-axe to the bottom quadrant. The amount of the curve shifting is directly proportional to the incident light intensity on a solar cell. Adding this current amount to diode dark current, the equation (1.3) will be. In that case, a maximum power indicated by the bleu area, in Figure 1.15 will be. Using illuminated I-V curve, we can derive various characteristics of a real solar cell like short circuit current (I_{SC}), open circuit voltage (V_{OC}), maximum power point MPP, fill factor (FF) and conversion efficiency (η). Those characteristics are illustrated in more details [19] in Figure 1.16.

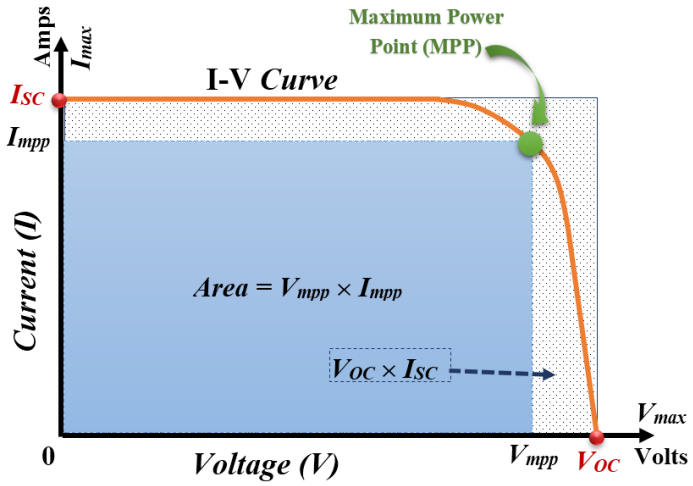

Figure 1.16 I-V characteristics of solar cell under illumination.

I.4.3.1 Short circuit current I_{SC}

The short circuit current (I_{SC}) is delivered by a solar cell at zero load condition ($R_L = 0$) or by short-circuiting its connections. This amount of current mainly depends on the number of incident photons as well as the collection probability of light generated carriers, the spectrum, the optical properties and the area of solar cell. The graphical depiction of I_{SC} is given in Figure 1.16, and by resolving the equation (1.3), we can describe I_{SC} by equation (1.4) [19].

$$I_{SC} = I(V = 0) = I_L - I_0[exp(0) - 1] = I_L \quad (1.4)$$

I.4.3.2 Open circuit voltage V_{OC}

When the current becomes zero ($R_L = \infty$), the resulting voltage (Figure 1.16) is so-called open circuit voltage (V_{OC}). By resolving the equation (1.3) at net current equal to zero, V_{OC} will be given by the equation (1.5):

$$V_{OC} = V(I = 0) = \frac{nkT}{q} ln\left(\frac{I_L}{I_0} + 1\right) \quad (1.5)$$

From equation (1.5), it is noticed that V_{OC} depends on I_L (light generated current) and I_0 (saturation current), in which this last depends on recombination process in the solar cell [19].

I.4.3.3 Maximum power point MPP

The ideal capacitance for a solar cell to operate at is the Maximum Power Point (MPP). For example, the green point on the Figure 1.16 corresponds to MPP, in which the product of its associated current I_{mpp} and voltage V_{mpp} must be the maximum area (P_{mpp}) under I-V curve [19].

I.4.3.4 Fill factor FF

The fill factor (FF) measures the percentage of quality of a solar cell through the ratio of MPP power towards the product ($V_{OC} \times I_{SC}$), as described by the equation (1.6). Graphically, FF shows the size of the MPP-surface (bleu area) compared to the ($V_{OC} \times I_{SC}$)-surface (pointed area) [19], as shown in Figure 1.16.

$$\text{FF} = \frac{V_{mpp} \times I_{mpp}}{V_{OC} \times I_{SC}} = \frac{P_{mpp}}{V_{OC} \times I_{SC}} \quad (1.6)$$

I.4.3.5 Efficiency η

Efficiency (η) or also power conversion efficiency (PCE) is the most used characteristic to evaluate the performance of a solar cell. It describes the portion of the incident power (P_{in}) from the sun on the solar cell that converted to electrical energy (P_{mpp}). Therefore, it can express the efficiency by the following equation (1.7) [19]:

$$\eta = \frac{P_{mpp}}{P_{in}} = \frac{\text{FF} \times V_{OC} \times I_{SC}}{P_{in}} \quad (1.7)$$

I.4.3.6 Quantum efficiency QE

The external quantum efficiency (QE) is the ratio of the electron-hole pairs generated and collected by the solar cell to the number of impinging photons. In other words, QE relates to the response of a solar cell to different wavelengths (λ). In this case, it can express the external quantum efficiency (QE) by the following equation (1.8) [19]:

$$\mathrm{QE} = \frac{Number\ of\ collected\ carriers(\lambda)}{Number\ of\ impinging\ photons\ (\lambda)} \tag{1.8}$$

I.5 Losses in Real Solar Cells

There are different loss factors that occur by which a real solar cell suffer from a reduction in its conversion efficiency lower than that of its ideal. Some of them are avoidable but others are intrinsic to the system. Figure 1.17 schemas the important factors, which cause loss mechanisms in a practical solar cell [21].

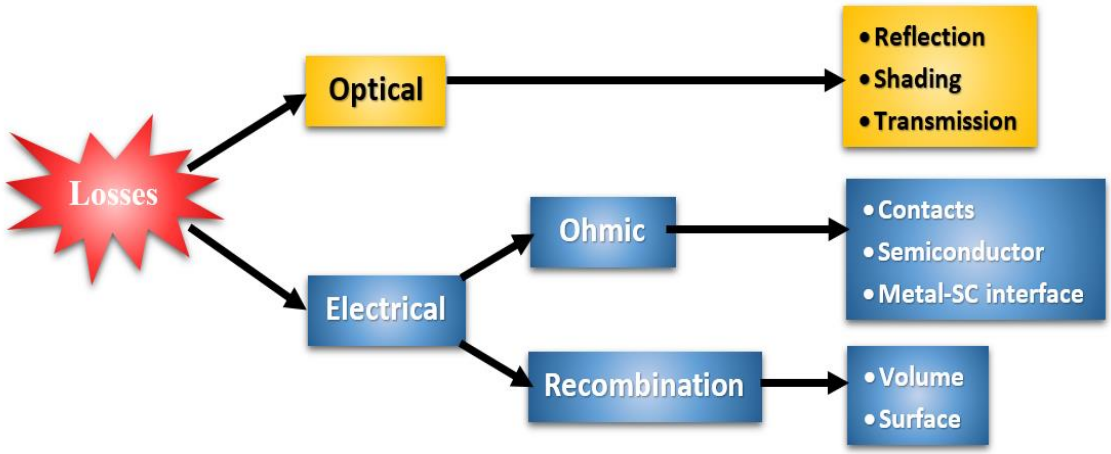

Figure 1.17 Factors of losses in solar cells devices.

I.5.1 Reflection on the Surface

The reflection loss is caused by the top surface of a solar cell. A part of incident spectrum is not absorbed thus reflected by the cell surface. An anti-reflective coating helps to lower the

average reflection. As a result the short circuit current is increased and thus the efficiency of the cell.

I.5.2 Shading by means of contact finger

The front metal contact of a solar cell is made like finger in its form to lead the generated current to the connection wires. This finger shadows some light, and the loss is greater when making the finger greater. Making the contact finger narrow and high may lead to reduce the shading losses.

I.5.3 Loss through transmission

There are photons with long wavelength, which have enough energy to be absorbed, but suffer from incomplete absorption due to the limited thickness of an absorber layer in a solar cell. Therefore, a limited thickness of a solar cell leads to an additional loss in its total efficiency. For example, in thin film solar cells, reducing the active-layers thickness is a basic and standard in which light trapping methods (texturization, etc.) are in need to reduce this type of transmission loss.

I.5.4 Electrical losses and ohmic losses

As mentioned above, making fingers on the top side of the cell narrow and high reduces electrical losses at the contact. As the conductivity of the doping semiconductor is limited, ohmic losses will occur in solar cell, reducing its efficiency. Thus, an increase in the n-doping of semiconductor lead to improvement, however, it leads to a strong recombination. In addition, bringing semiconductor and metal together to make a junction (so-called Schottky contact) build a potential step, which reduces the open circuit voltage of solar cell.

I.5.5 Recombination losses

There are several reasons that not all generated electron-hole pairs contribute to current and voltage in solar cell device. Those reasons are summarized in the occurrence of recombination at different scales of a solar cell like at the bulk of layers (volume), at the interfaces between two layers (surface), where there will be open bonds at the border of the crystal lattice, and/or at the surfaces of the junction. Many techniques are used for reducing the recombination. For example at the bottom side of a solar cell, a back surface field is used to

minimize the several recombination problems. At the top side, the using of an oxide helps to saturate the open bonds, and this process is so-called passivation.

I.6 Thin Films Solar Cells

As mentioned in the section I.2.3, the 2nd generation '*Thin Film Solar Cell*' (Figure 1.18) takes the lion's share of research compared to other generations of solar cells.

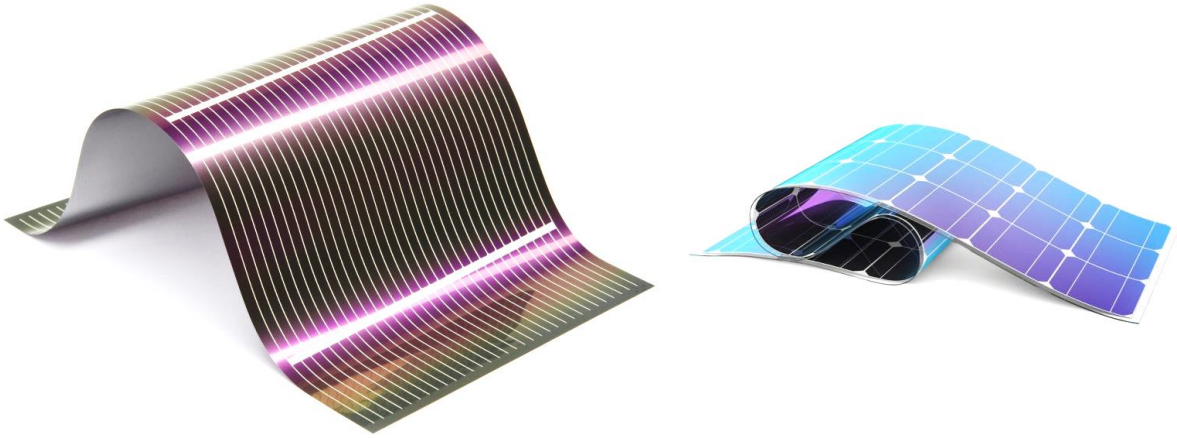

Figure 1.18 Thin films based solar cells.

Typically, this generation contains four types depending on the used material, the amorphous silicon (a-Si) and thin film silicon; the cadmium telluride (CdTe) and copper indium gallium deselenide (CIGS); and the dye-sensitized solar cell plus other organic materials. In this section, we will look in more details at how transparent conductive oxides (TCOs) are doing in thin film solar cells. Then we will make the acquaintance of thin film silicon solar cells, thin film CdTe solar cells and thin film CIGS solar cells.

I.6.1 TCO and thin film solar cells

During the last decades, transparent conducting oxide (TCO) technologies have been materialized in a fastest ways to achieve better electronic and optoelectronic devices. Such pulse laser deposition [22], sol gel [23], electrodeposition [24], spray [25], sputtering [26] and other

methods are potential technologies offers a range of versatile new features and enhancements that meet the needs of TCO based photovoltaic (PV) devices.

So far, a large number of studies have been widely conducted to apply mostly the common TCO, especially, indium tin oxide (ITO) [27], zinc oxide (ZnO) [28], fluorine doped tin oxide (FTO) [29] in thin film solar cells. The properties of TCO films, such as resistivity, band-gap energy and work function, affect obviously the performance of solar device because they affect both the energy barrier height at the heterojunction interfaces and the electron field emission [30]. The majority of TCO films are n-type degenerated semiconductors (metallic oxides), they are, also, formed from binary oxides, such as In2O3, SnO2 and ZnO; ternary oxides, such as $Zn_2In_2O_5$, Zn_2SnO_4, $CdSb2O_6$, $MgIn_2O_4$, $ZnSnO_3$, $GaInO_3$, and $In_4Sn_3O_{12}$ and multi-component oxides composed of combinations of these binary or ternary oxides [31].

Ritzau et al. [32] have reported the role of the work function and back contact barrier height on the performance of a-Si:H solar cells. Besides, Belfar et al. [33] investigated the effect of work function of the TCO films for the performance of n-i-p^+ and n-i-p-p^+ solar cells based on hydrogenated amorphous silicon (a-Si:H) and hydrogenated nanocrystalline silicon (nc-Si:H) absorber layers using AMPS-1D simulation tools.

ZnO-based TCO as an excellent transparent (85%) in the visible range, with wide energy band gap of around ~ 3.37 eV at room temperature and high carrier concentration, they act extensively as most suitable n-type partner with common p-type thin films such as Cu_2O [34], CIGS [35], CdTe [36] and silicon [37]. In addition, Cu_2O-based TCO are non-stoichiometric, electrically natural p-type conductive and optically absorbing in the short-wavelength considered amount (~10^4/cm) of the luminous spectrum as they have direct energy band gap of 1.9–2.1 eV [38] with low carrier concentrations of ~10^{-16} cm^{-3} at room temperature [39]. To enhance the open-circuit voltage (V_{OC}) by adding Cu_2O back-layer in CuO based solar cells, the one dimensional simulation of Zhu et al. [40] has shown that the conversion efficiency increased from 19 % for a non-defected TiO_2/CuO two-layer structure to 28.5 % for a non-defected TiO_2/CuO/Cu_2O three-layers structure.

Wei et al. [41-42] suggested that Ga-doped $Mg_xZn_{1-x}O$ (GMZO) thin films grown using pulsed laser deposition (PLD) have a good and distinctive electro-optical properties by controlling the concentration of the Ga and Mg dopant materials. They demonstrated that the band gap of GMZO can be tailored by noticeable decimal places from 3.35 to 3.94 eV by using

a few or almost nonexistent percent of Ga (0.05 at.% to 3 at.%) and Mg (5 at.% to 15 at.%). Furthermore, the absorption edge of these degenerate semiconductors were shifted to shorter wavelengths (200-300 nm) with increasing charge carrier concentrations in which the overall transmittance was above 85 % in the wavelength range from 370 to 800 nm. In addition, the conductivity was increased or decreased by varying the concentration of the Ga dopant in GMZO thin films. The low-Ga-content showed increased resistivity in low-Ga-doped $Mg_xZn_{1-x}O$ (LGMZO) films, which could reach 0.9 Ω.cm. However, the high-Ga-content, the high-Ga-doped $Mg_xZn_{1-x}O$ (HGMZO) films displayed low resistivity, which is in the order of 10^{-3} Ω.cm.

I.6.2 Silicon-based thin film solar cells

Silicon (Si) based solar cells are currently the most commercialized among the thin film solar cells. Furthermore, thin film Si solar cells have several advantages like high stability, high reliability and ease of fabrication [4]. In which, a thin film Si minimodule confirmed a lab-scale efficiency of 10 % by CSG Solar (<2 μm on glass) [43]. Considering the enormous use of the robust and expensive crystalline silicon materials in advanced photonics and electronics, it should be advisable to motivate the present-day extensively studied materials such as the TCOs and chalcopyrite thin films by using them as partners or supporters, side by side with thin films of crystalline silicon. Thin film Si technology is still pretty much in its beginnings but has the potential to be significantly less expensive [4]. Based on one-dimensional simulator (SCAPS) and using an absorber of 1μm of CIGS backed by 1μm of crystalline silicon (c-Si) thin film in order to minimize the indium and gallium constituents, Heriche et al [35] have reported conversion efficiency of 21.3 %. In addition, because of its transparency and excellent electrical properties, ZnO has been integrated as n-type partner with p-type silicon to fabricate thin film solar cells at low costs. Currently, the achieved practical power conversion efficiencies of the ZnO/Si heterojunction solar cells are also remained at modest percentages, under 8.5 % [44-45]. This modesty is likely due to the strong dependence of the common ZnO/Si heterojunction performance on the properties of deposited ZnO films.

I.6.2 CdTe-based thin film solar cells

Among all thin film solar cells, CdTe heterojunctions [46-48] are the most capable applicant for high photovoltaic energy conversion. Since its inception in 1970's, there are potentials to realize high efficiency, low cost, reliable, and stable cells. CdTe, which is an II^{nd} and VI^{th} group compound semiconductor with a near optimum band gap of 1.45 eV, solar cells

draw a theoretical efficiency of 29.7% within 2 µm of thickness [47] and a confirmed lab-scale efficiencies of 21% by First Solar [43]. However till date, the absorber layer in the CdTe solar cells requests an alternative transparent conducting oxide (TCO) window and buffer dual-layers with dissimilar electronic properties (opposite polarities) to provide a thin electronic barrier in between to separate the carriers.

I.6.3 CIGS-based thin film solar cells

$CuIn_{1-x}Ga_xSe_2$ (CIGS) has a major potential as a semiconductor material for thin film photovoltaic devices. This is due to its high optical absorption coefficient, appropriate band gap and outstanding electro-optical properties [49-54]. CIGS-based solar cells with $x = 0.3$ corresponds to a bandgap energy range of $1.1 - 1.2\ eV$ and yields the best efficiency both in laboratory and commercial solar cells [51]. Recently CIGS thin film solar cells approached efficiencies of 22.8% for substrate configuration [52]. The superstrate configuration is an alternate design, where the deposition sequence is reversed, the absorber is grown on glass coated with the transparent front contact (TFC), followed by an evaporated CdS or In_2Se_3 buffer layers and finished by a sputtered metallic back contact layer [53]. Further improvements of the superstrate CIGS solar cells performance require an accurate knowledge of the electronic loss mechanisms. Recently, Bouchama et al. [54] have reported that the CIGS solar cell with superstrate configuration has a better photovoltaic performances when lighting through SnO2:F front contact layer. Moreover, an efficiency higher than 16%, could be obtained for superstrate SLG/SnO_2:F/CIGS/ODC/In_2Se_3/Zn solar cell structure for $300\ nm$ p-CIGS absorber thick.

I.7 Summary

In this chapter, the physics of thin film semiconductors and the background of solar cell devices have been reviewed. The working principle of the p-n junction and the I-V characteristics of an illuminated solar cell were well explained. Various types of losses in real solar cell devices were ticked off. The acquaintance of thin films silicon, CdTe and CIGS solar cells were highlighted.

CHAPTER I

ZINC OXIDE MATERIALS PROPERTIES: SYNTHESIS AND CHARACTERIZATION OF PURE AND DOPED THIN FILMS

II.1 Introduction

The second chapter highlights the transparent conductive oxides especially the zinc oxide thin films and their well-known physical properties and also the doping and co-doping effects on zinc oxide films. Then, the sol-gel technology will be reviewed, emphasizing the spin-coating method. Finally, the characterization instruments, which will used for analyzing the films properties will be presented.

II.2 Transparent Conductive Oxides

During the last decades, Transparent Conductive Oxides (TCOs) have been studied in a fastest ways to achieve better technological applications, especially optoelectronic devices [28]. Apart from being semiconductors, the majority of TCOs are optically high transparent in the visible light range and electrically conducting (low resistivity), containing one metallic or two metallic or three metallic elements in binary (ITO, ZnO, NiO, CuO, In_2O_3, SnO_2), ternary (Cd_2SnO_4, $CdSnO_3$, and $CdIn_2O_4$) [55] and quaternary (Mg-Al-Zn-O, Mg-In-Zn-O, and Mg-Ga-Zn-O) systems [28], respectively. Furthermore, a heavy doping makes those TCO systems have tunable band gad could be greater than $3\ eV$ and behave like conductors in the range conductivity from 1 to $10^4\ \Omega cm^{-1}$ [56]. Many researchers suggest that interesting optical and electrical properties like transparency and conductivity behaviors in the transparent conductive oxide material make it possible to use it for the transparent electrodes in solar cell devices. p-type conductivity in transparent conductive oxides such as p-ZnO, p-NiO [57] and Cu-based p-type [58] films is a highly desirable goal given its larger work function, good optical absorption and ease of inducing complementary n-conductivity for metal oxide-based homojunction solar cell devices [59-60].

Hereafter and based on this reasons, we decided in this thesis to limit the investigation only on preparation and characterization of undoped (pure) and doped zinc oxide thin films using sol-gel spin-coating deposition procedure.

II.2.1 Zinc oxide films

As a simple binary, Zinc oxide (ZnO) is a II-VI compound Material. Recently, it has received increasing concern because of their strong points of earth-abundance, non-toxicity, high transparency in the visible range, high photoconductivity in the ultraviolet region, tunable

optical band gap, good chemical and thermal stability, low-cost in resources and ease of processing by versatile nanotechnology routes. Such potential nanotechnologies offers a range of versatile new features and enhancements that meet the needs of ZnO of particle sizes in nanometer range based applications. So far a large number of studies have been widely conducted to apply pure and doped ZnO films in broad optoelectronic and electronic applications such as gas sensor [61], glucose sensor [62], photocatalytic sensor [63], photodegradation sensors [64], photoluminescence sensors [65], conductive switching [66], sunscreens [67], antibacterial agents [68], surface acoustic wave [69] and solar energy conversion [70].

II.2.2 Zinc oxide properties

The different type of ZnO crystal structures are rock salt, zinc blende and wurtzite [71]. Among of those structures, the wurtzite hexagonal (space groupe $P6_3mc$) is considered as the most stable and ground state structure of ZnO having energy favorable than of two other structures with lattice parameters $a = b = 3.2495$ Å and $c = 5.2069$ Å and hence a c/a ratio of 1.602, which is close to an ideal hexagonal structure (1.633) [72]. As schemed in Figure 2.1, hexagonal wurtzite structure ZnO consists of number of alternating planes composed tetrahedrally coordinated zinc atoms to four oxygen atoms, stacked alternately along the hexagonal (c-) axis.

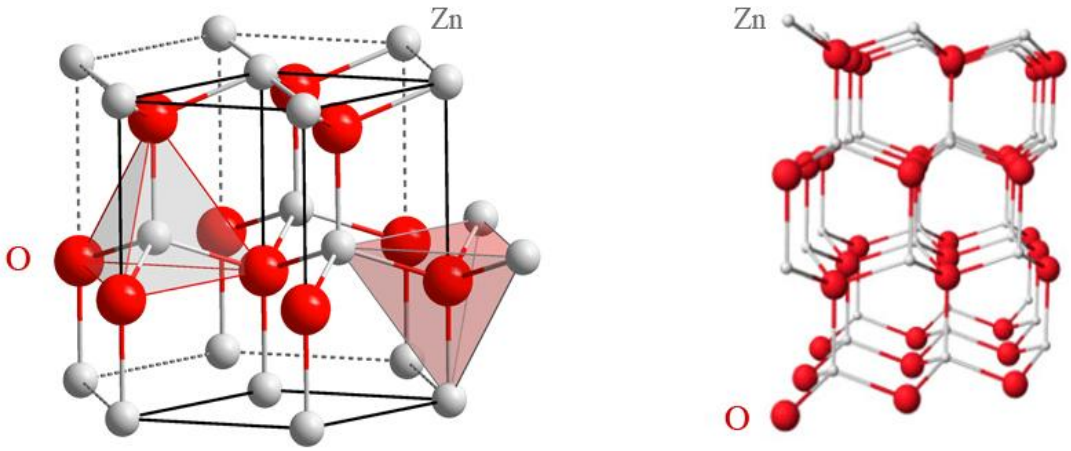

Figure 2.1 Wurtzite crystal structure of ZnO. Gray and red spheres are zinc and oxygen atoms, respectively [73].

Thus, the features of ZnO are responsible for the crystal growth orientation and defect generation [73]. In addition, the obtained physical, electrical and optical properties are a key factor in photovoltaic applications. The different physical properties of wurtzite structure of ZnO are listed in Table 2.1 and are taken from [72].

Intrinsic or doped, either by oxygen vacancies or by substitution of some of the atoms, ZnO films are direct II-VI semiconductors and electrically degenerated n-type conductivity, having wide optical band gap greater than 3 eV and high exciton binding energy of 60 meV at room temperature.

Table 2.1 Properties of wurtzite ZnO [72].

Property	**Value**
Lattice parameters at 300 K	$a = 3.2495$ Å, $c = 5.2069$ Å, $c/a = 1.633$
Density	5.606 g/cm^3
Stable phase at 300 K	Writzite
Melting point	1975 $C°$
Thermal Conductivity	$0.6, 1 - 1.2$
Static dielectric constant	8.656
Bandgap energy at room temperature	3.4 eV (direct)
Intrinsic carrier concentration	$< 10^6/cm^3$
Exciton binding energy	60 meV
Electron effective mass	0.24
Electron Hall mobility at 300K for low n-type conductivity	200 $cm^2/V.s$
Hole effective mass	0.59
Hole Hall mobility at 300K for low p-type conductivity	$5 - 50$ $cm^2/V.s$

Furthermore, the carrier effective mass in ZnO materials is equal to 0.24 and 0.59 for electrons and holes, respectively. The electron and hole motilities in ZnO films are close to $200\ cm^2/V.s$ and between $5-50\ cm^2/V.s$ at room temperature, respectively, low than of the bulk materials. The resistivity of doped zinc oxide is in the range of $10^{-5}-10^{-4}\ \Omega cm$. The static dielectric constant is 8.656 along the c axis. ZnO films with high conductivity have high reflectivity in the infrared part of the spectrum and an excellent optical transparency (85%) in the visible range better than indium doped tin oxide. Surface and bulk defects play an important role in solar energy conversion activities of metal oxides as they increase the number of induced intrinsic lattice defects either acceptor level or donor level in the band gap. Thus, the optical and electrical properties of ZnO would be greatly affected.

II.2.3 Doping effect on the ZnO thin film properties

A selective doping, alloying or introducing elements into thin films offers to enhance and control many properties and functions of films nanoparticles.

For example, the resistivity of intrinsic stoichiometric ZnO films can be decreased either by introducing oxygen vacancies or non-stoichiometric composition or by introducing appropriate dopants. When introducing some of those dopants in ZnO lattice, the electrical conductivity is enhanced by releasing free electrons when zinc is replaced by impurities, so the increase of carrier concentration can improve the conductivity [74], which makes doped ZnO films suitable candidate for photovoltaic applications, as a window layer in solar cell devices.

Therefore, a proper choice of dopants makes the ZnO films having remarkable conductivity, transparency and structural features [75]. Numerous metal dopants have recently been studied to implement doped ZnO films in many ways: V [76], Fe [77], Cu [78], Ni [79], Co [80], Mn [81], Ga [82], Sn [83], Al [84], Tm [85],Gd [86],Eu [87], In [88], N and B [89] because of their cheapness or abundance or stability.

Thus, many sol-gel based experimental investigations have been performed to prepare undoped and doped ZnO thin films on various types of substrates like glass [90], Si [91], quartz [92], ITO [93], FTO [94] coated glasses and polymers sheets [95] with different doping concentrations.

A porous zinc oxide film prepared by the sol-gel type dipping method showed a low transmittance in the visible range, in comparison with a compact ZnO film [96]. A highly crystalline zinc oxide sample prepared by simple sol-gel using zinc acetate as a precursor showed that the nanoparticles is spherical in shape. The average particle size was found to be 58.3 nm using Scherrer's equation and 100-200 nm obtained from SEM measurement for ZnO nanoparticles dried at 80℃. The absorption spectrum was a typical spectrum for ZnO nanoparticles [97]. Moreover, Amari et al. [94] prepared zinc oxide thin films onto glass substrates using sol-gel spin-coating method, they found that all samples had a polycrystalline hexagonal wurtzite structure. The texture of samples was influenced by the precursor concentrations. When the sol concentration was increased from 0.3 to 0.7 M, the optical band gap varied slightly, after that it decreased for precursor concentration over 0.7 M. In addition, the transmission spectra exhibited a high transparency in the visible region at sol concentrations below 0.7 M.

Furthermore, zinc oxide multilayer thin films performed on glass substrate using sol-gel spin-coating technique. It was found that these multilayer structure have great impact on the properties of ZnO. The obtained multilayer thin films had uniformly distributed grains structures without cracks. Both micro and nano particles of ZnO were present on thin films. The electrical properties showed the decreasing trend between the average resistivity and the number of layers. The average transmittance in the visible region of all films was 80%. It was concluded that the performance of the multilayer as transparent conducting material is better than the single layer of ZnO [98].

By doping zinc oxide with gallium, the optical transmittance of prepared films was enhanced over 85% in the visible range of the solar spectrum, and the strain lattice and dislocation defects were minimal because the Ga atoms has a radius similar to zinc atoms, which makes easily gallium atom substitutes zinc atom in the lattice film [99]. Wei et al. [41-42] have been investigated the electrical conductivity in zinc oxide films by controlling the concentration of gallium (Ga) and magnesium (Mg) co-dopant during pulsed laser deposition. A high Ga dopants in $Mg_xZn_{1-x}O$ films showed a low resistivity in the order of $10^{-3}\Omega.cm$, compared to a low Ga dopants in $Mg_xZn_{1-x}O$ films, which showed degraded resistivity closed to $0.9\ \Omega.cm$. They demonstrated that the band gap of Ga-doped $Mg_xZn_{1-x}O$ (GMZO) can be tailored by noticeable decimal places from 3.35 up to 3.94 eV by using a few or almost nonexistent percent of Ga (0.05 at.% to 3 at.%) and Mg (5 at.% to 15 at.%). Furthermore, the absorption edge of

these degenerate oxide semiconductors were shifted to shorter wavelengths between 200-300 nm with increasing the charge carrier concentrations in which the overall transmittance was above 85% in the visible range of the solar spectrum (370 to 800 nm).

From the literature reviews, the incorporation of magnesium element of group II into zinc oxide lattice to substitute zinc atom is expected to lighten the weight and to increases flexibility in spinning process into ZnO lattice because the ion radius of the Mg^{+2} ion which is 0.57 Å is slightly smaller than that of the Zn^{+2} ion which is 0.60 Å [100]. Also, the diffusion of Mg atoms into ZnO can lead to broad its band gap from 3.3 to 7.8 eV[101-102]. It was found that with the rise of Mg concentration in spin-coated ZnO films from 0.5 to 2.5%, the optical band gap increased from 3.155 to $3.217\ eV$ because Mg doping increases the defect concentration, and the biggest optical transmission values were in the range of $310 - 420\ nm$. It was also noted that the Mg-doped ZnO showed wurtize hexagonal structure with the smallest size of $24\ nm$ for Mg concentration of 0.5% and the biggest size of $28\ nm$ for Mg concentration of 2.5% [103]. Huang et al. [104] prepared undoped and Mg-doped ZnO thin films on Si and quartz substrates by the sol-gel method. The thin films were annealed. They found that the films with low Mg concentration < 4% were polycrystalline with hexagonal wurtzite structure, while the film with high Mg concentration = 8% had a secondary phase of MgO evolved in. The roughness of the thin films changed from 7.89 nm to 16.9 nm with increasing Mg concentrations. The obtained films showed a transmittance over 85% along the visible region. The optical band gap increased from 3.26 eV to 3.34 eV with increasing Mg concentration. On the other hand, the resistivity of the ZnO films were enhanced by Mg introduction and increase with increasing doping concentrations.

Some properties of zinc oxide thin films can be improved by single metal dopant. However, this simple doping is insufficient to improve all properties of ZnO thin films in same time, thus, the use of more than one metal dopant in ZnO lattice is required. Therefore, Sarkar et al. [92] performed (Mg,Al) co-doped ZnO films onto quartz glass substrate via sol-gel method for sensing layer use. This processed technique was chosen because of doping homogeneity on molecular level and crystallization temperature. An increase trend between the annealing temperature and the grain size which was uniform within larger size. Aksoy et al. [105] prepared (Li,Mg) co-doped ZnO thin films by sol-gel spin-coating method. They found that the crystallite size of deposited films decreased from 41.2 to 30.4 nm with increasing Mg

concentration. The average transmittance of the films was found to be almost 80% in the visible range of solar spectrum. The absorption band edge values of the films increased from 3.29 to 3.39 eV with increasing Mg concentration. The blue shift in the optical band gap of the films was attributed to the band Burstein–Moss effect. Also, Khanizadeh et al. [106] deposited La and Mg doped, and (La,Mg) co-doped ZnO nanoparticles using the sol-gel method for photocatalytic activity. They found that the samples have uniform spherical-like morphology with a homogenous distribution. The incorporation of La and Mg into the ZnO lattice had no effect on the morphology of the nanoparticles, but a reduction in the grain sizes from 14 to 7 nm. The band gap energy and a blue shift at the absorption edge for doped and co-doped samples showed an increase behavior.

II.3 Sol-gel Type Spin-Coating Synthesis

II.3.1 Thin films fabrications

Thin films are materials that have been widely used in our daily life especially in the field of nanotechnology. They range from fraction nanometers to micrometers of thickness which shows many features including low total cost and enhanced efficiency of thin film-based applications. In modern thin film deposition techniques, it is possible to have control over the extern environmental and intern condition parameters during all the processing fabrication. So far a grown number of chemical and physical surface coating techniques are under way. Among this diversity, the solution state-based chemical methods have been allowed to synthesis thin films with desired characteristics of compositions, structures and sizes, by growing of atoms or molecules of precursors onto different types of substrates [107]. Thus, the focal view will be on sol-gel spin-coating technique used for thin films as a low-cost/temperature technique for thin film synthesis onto glass substrate.

II.3.2 Sol-gel technology

The sol-gel (Solution-Gelation) deposition method is a well-known chemical route for making glass and ceramic materials. From the beginning, the researchers have been mastered the sol-gel route for synthesis metal oxide thin films. The different routes involved in the sol-gel technique and their resulting materials are presented in Figure 2.2.

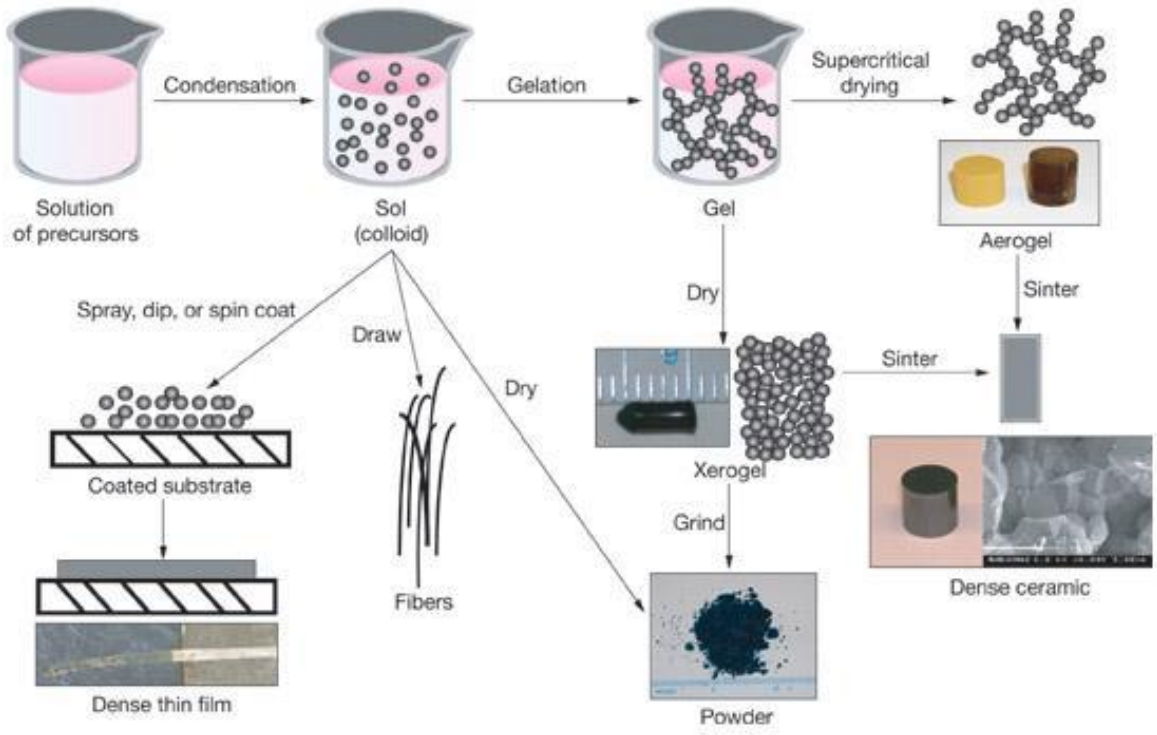

Figure 2.2 Representation of different routes in the sol-gel process.

Sol-gel process is a wet chemical method involves the transformation of molecular precursors into a nano-structured solid network by hydrolysis and condensation reactions. The evolution of oxide networks demands a formation of a colloidal liquid called sol and gelation of the sol to form a three dimensions network in a continuous liquid phase called gel, enabling the fabrication of fibers, powders, ceramics, and especially thin films [108]. By simple drying, the liquid gel is transformed to dried gel called xerogels, and then a grind treatment is necessary to achieve the target powder. While by supercritical drying, the liquid gel is transformed to aerogels, and then a sinter treatment is necessary to achieve the targeted dense ceramic. While coating by way of spraying, dipping or spinning of the precursor solution over a chosen substrate, the targeted product it is necessary a film. During the deposition, an extraction of solvent and a subsequent drying process result in densification of the produced film. A thermal treatment is necessary to achieve a film oxide with desired composition and structural features [109].

II.3.3 Chemistry of sol-gel

In case that the starting reagents are alkoxides $M(OR)_n$, in which M is the element with valence n and OR the alkoxide group, the chemical synthesis of oxides requires two key mechanisms to transit from sol phase to gel phase, namely hydrolysis of the metal precursor and condensation to form the oxide network.

Hydrolysis consist of the degradation of a substance, tacking place by the addition of small quantities of water. In order to increase the homogeneity of solution, alcohol solvent (non-aqueous) are usually used. During this reaction, the M-OH bonds are formed, replacing the alkoxide groups ($-OR$) by hydroxyl groups ($-OH$) and following by the formation of an alcohol ($R-OH$):

$$M(OR)_n + xH_2O \rightarrow M(OH)_x(OR)_{n-x} + xR(OH) \qquad (2.1)$$

This process of hydrolysis repeats until all the alkoxide groups are replaced by hydroxyl groups.

Subsequently, the condensation of the resulting hydroxyl groups take place, in which the hydrolyzed species lead to the formation of a 3-D network. The condensation reactions lead either to the disappearance of a water molecule (water condensation) viaolation or oxolation:

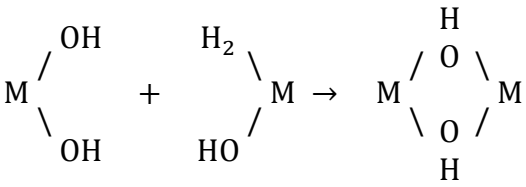

olation (2.2)

$$M-OH + M-OH \rightarrow M-O-M + H_2O \qquad \text{oxolation} \qquad (2.3)$$

or to the disappearance of an alcohol molecule (alcohol condensation) via alcoxolation:

$$M-OH + M-OR \rightarrow M-OM + H_2 \qquad \text{alcoxolation} \qquad (2.4)$$

In any case hydroxyl or oxygen bridges are formed leading to condensed species. At the end of the process all oxygen atoms are bridging oxygen atoms and a shrink hydrated oxide network is obtained [110].

II.3.4 Spin-coating method

During sol-gel process and before the gelation, it is possible to employ the obtained colloidal solution in applying thin films by dip- or spin-coating. There continue to be a large number of ZnO produce for which the spin-coating is at most a quick and easy method to reproduce deposition of ZnO thin film coatings over large areas with high structural uniformity from a few nanometers. Basically, the spin-coating techniques can be described as a process where a sol of the desired materials are coated evenly across the surface of a rotating substrate with a well-defined speed [108].

The typical spin-coating process can be divided into four stages, which are illustrated in Figure 2.3, and wrote as following:

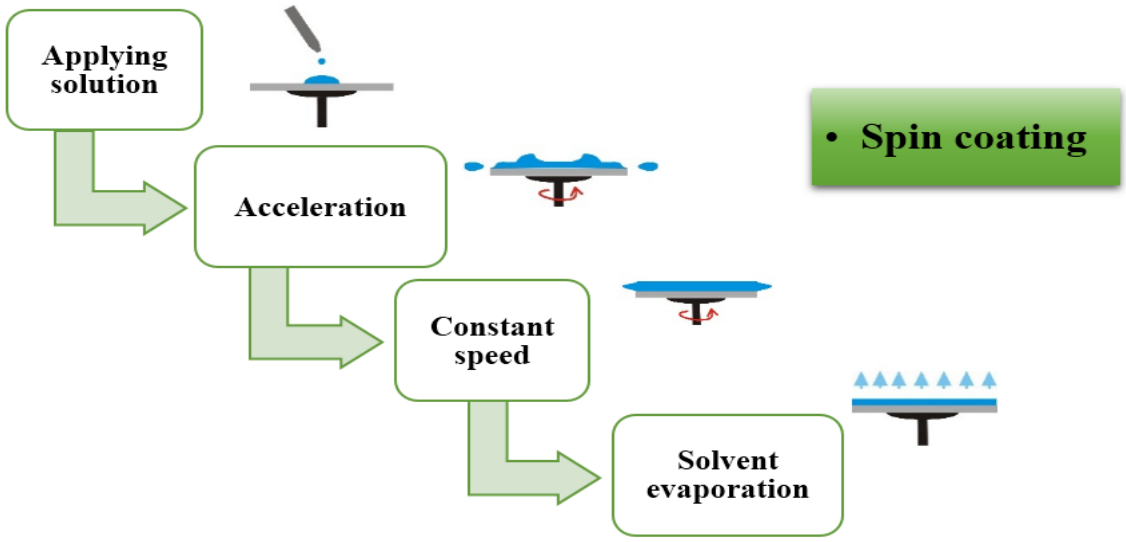

Figure 2.3 Spin-coating Process.

- At first a static dispense stage in which the resin fluid is deposited near the center of the substrate surface;
- At the acceleration stage, a rotational motion is applied on the substrate which it usually makes an aggressive fluid expulsion from the substrate surface;
- At stage of substrate spinning at a constant rate, an excess liquid is flowed to the perimeter of substrate, and then leaving as a droplet, so gradual doing the thinning of uniform coating thickness;
- During evaporation stage, the solvent evaporates leaving the desired film on the flat substrate.

The coating thickness is mainly depends on many different parameters. Therefore, the following formula (2.5) shows how these parameters will affect the thickness of prepared film [111]:

$$h = \left(1 - {}^{\rho_A}/_{\rho_{A0}}\right)\left(\frac{3\eta m}{2\rho_{A0}\omega^2}\right)^{\frac{1}{3}} \quad (2.5)$$

With	h	– Thickness,
	ρ_A	– Density of volatile liquid,
	η	– Viscosity of solution,
	m	– Rate of evaporation,
	ω	– Angular speed.

II.4 ZnO Film Spin Coating Elaboration

As here-above discussed the sol-gel spin-coating has progressively been proposed as a ambient temperature wet chemical process featured by the ability of controlling chemical composition, structure and morphological properties of final materials by adjusting processing parameters including the starting precursors and their concentrations, solvent and environment acidity, additives nature and their concentrations, curing time of solution, substrate nature,

coating method of substrate and its motion, drying and annealing of thin film. Thus, the common step of the sol-gel synthesis of ZnO thin films include:

- Preparation of the starting solution by dissolving zinc molecular precursor in alcoholic solvent in addition to use of complexing agents of Zn^{+2} in order to achieve a stable colloidal solution of ZnO;
- Deposition of the prepared sol on a flat substrate by the spinning technique;
- Heating treatments in two steps, firstly by drying in order to remove the solvent from the coated film followed by annealing treatment in order to obtain a dense thin film.

On overall, the nature and concentration of the precursor act as a major factor during the thin film preparation. Furthermore, the choice of solvent and additives, the coating and deposition parameters, the nature of the substrate, and the selection of the heat treatment affect the feature of the targeted thin film [108].

Sol-gel method has been preferred for ZnO thin films preparation because of its many advantages like compositional control ability, doping and homogeneity of high quality and pure final product on molecular level as well as the comparatively lower temperature of crystallization and low costs of employed materials and technologies over complex geometries on a small as well as large-area coating [92].

The starting employed materials used during the preparation of the ZnO sol are usually aqueous solutions of inorganic salts or organic salts or alkoxides, dissolved in alcoholic media. It was found that many zinc precursors have been used in sol preparations like nitrate $Zn(NO_3)_2$, chloride $ZnCl_2$, perchlorate $Zn(ClO_4)_2$, acetylacetonate $Zn(CH_3COCHCOCH_3)_2$, and alkoxides $Zn(OR)_n$. On the other hand, different alcohols of high molecular weight have been used as a solvent like methanol CH_3OH, ethanol CH_3CH_2OH, 1-Propanol $CH_3CH_2CH_2OH$, 2-Propanol $CH_3CH(OH)CH_3$, 2-Methoxyethanol $CH_33OCH_2CH_2OH$, in addition to the use of complexing agents of Zn^{2+} like monoethanolamine (MEA) $(HOCH_2CH_2)NH_2$, diethanolamine (DEA) $(HOCH_2CH_2)_2NH$ and triethanolamine (TEA) $(HOCH_2CH_2)_3N$ which provides a complete dissolution and high stability to the ZnO sol [108,109].

II.5 Characterization Techniques and Instruments

II.5.1 X-ray diffraction (XRD)

An X-ray diffraction (XRD) is a non-destructive tool, which is used to analyze the crystallographic structure (crystals, amorphous, fluids and prouder) of materials. By using software to control the instrument, X-ray diffraction peaks are recorded by constructive interface of monochromatic beam scattered from each set of lattice planes at specific angles during displacement of simple material. Once the analysis is performed, the X-ray crystallographic may be used to determine the structure and measurements such as the shape and the size of unit cell for the analyzed material [73].

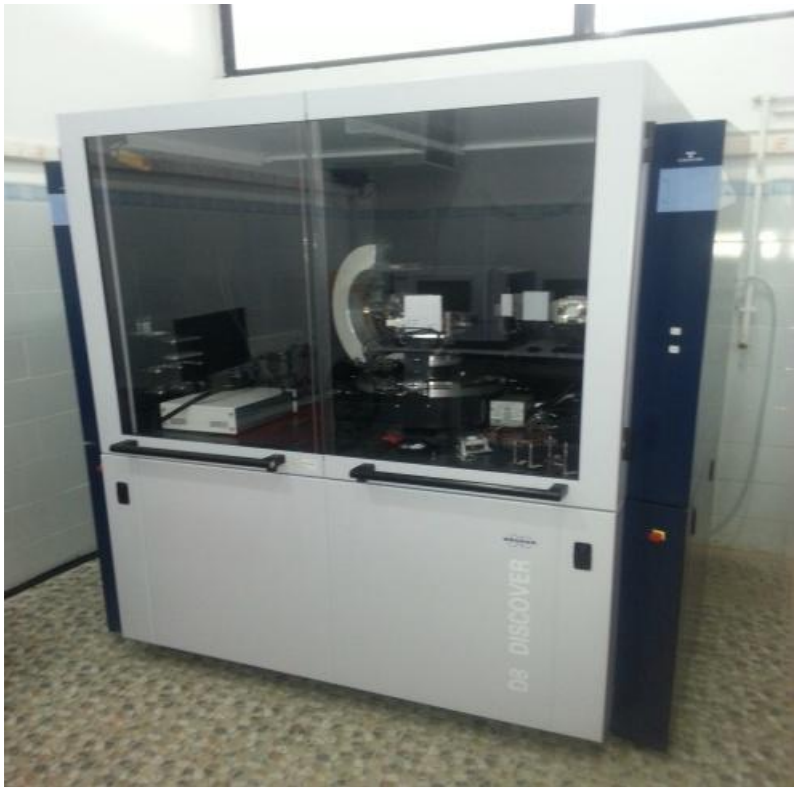

Figure 2.4 X-ray diffraction instrument used in our work.

Here to analyze the structural proerties of undoped and Mg-doped ZnO samples deposited on glass substrates, we were used the instrument showed in Figure 2.7 which is working under X-rays source of Cu-Kα (wavelength= 1.5405 Å).

II.5.2 Surface atomic force microscopy (AFM)

Atomic force microscopy (AFM) is an imaging technique applied to sample surfaces down to atomic scale. It uses a fine tip to measure surface properties through an interaction between the tip and surface. It provides information on surface topography with atomic resolution. AFM is used to study the microstructure grain size and roughness of the films [73].

The surface analysis and roughness of undoped and Mg-doped ZnO samples were perfermed using BRUKER ICON DIMENSION device (Figure 2.8).

Figure 2.5 Atomic Force Microscopy used in our work.

II.5.3 Surface scanning electron microscopy (SEM)

Scanning electron microscopy (SEM) falls under the electron microscopy family of techniques. It has been used to provide the information on the surface morphological features of samples. SEM analysis has been mainly applied to analyze the quality, and uniformity of the layers. Furthermore, energy dispersive X-Ray analyzer (EDX or EDA) was used to get comprehensive information of elemental identification of the samples surface [73].

The surface analysis of undoped and Mg-doped ZnO samples were performed using ZEISS Gemini SEM 300 (Figure 2.9).

Figure 2.6 Surface Scanning Electron Microscopy used in our work.

II.5.4 Optical transmittance measurements

UV-Visible spectroscopy is very useful technique to analysis the optical properties like as transmittance, absorption, band gap, etc. of semiconductor nanostructures. Light absorb by nanoparticles is depend on several factors such as size of nanoparticles, surface morphology, energy band gap, and impurity centers. The UV-vis absorption and transmittance spectra for deposited samples are taken as a function of wavelength at room temperature [73].

II.6 Summary

At the beginning of this chapter, the interest of transparent conductive oxide materials and their applications were highlighted. We have shown that the transparent and conductive undoped and doped zinc oxides have a multitude of applications epically in solar cell devices. The sol-gel technique is the most used method that we have detailed in this chapter, as well as the different production conditions. The sol-gel spin-coating technique process to deposit undoped and magnesium-doped zinc oxide thin films onto glass substrates was presented. In order to analysis the structural, morphological and optical properties of prepared films, different analysis instruments were presented such as DRX, MEB, AFM and UV-Visible.

CHAPTER III

SIMULATION AND PERFORMANCE ANALYSIS OF THIN FILMS SOLAR CELLS

III.1 Introduction

This chapter is devoted to the numerical simulation of ZnO/Si/Cu2O [3], TCO/Ga-doped MgxZn1-xO/CdTe [36] and TCO/p-CIGS/n-ODC/n-In2Se3 [112] solar cell structures, in order to optimize their performances. Therefore, we will first have a clear picture about the one-dimensional Analysis of Microelectronic and Photonic Structures (AMPS-1D) software simulator. After, we will take an overview on the design parameters (e.g., layer thickness, structure) and the input parameters of used materials (e.g., band gap, acceptor and donor densities, hole/electron motilities, affinities, metal work functions …). Finally, we will master and optimize these input parameters to study the behavior of the J-V characteristics and all other related photovoltaic parameters of studied solar cells by using AMPS-1D software.

III.2 AMPS-1D Simulator

To avoid wasting resources, effort and time, solar cell community need to understand, explain and solve the physic and technology interferences of solar cell devices by using numerical simulators [7,35,113]. These requirements have been reflected on the development of solar cells in which diverse abundant/non-abundant and low/high-cost materials, as well as their large influencing parameters, have been explored to renovate solar cell devices.

The freely available one dimensional Analysis of Microelectronic and Photonic Structures (AMPS-1D) program was developed in 1990's by professor Fonash's team at the Pennsylvania State University [14] in order to analyze the physics of charge carrier transport in solar cell devices. AMPS-1D solves the dipolar problems of device based semiconductors according to the Poisson equation and the continuity equations for electrons and holes. Thus, AMPS-1D simulator is a software environment, which is used to emulate a real solar cell behavior. Typically, the process of simulation would have to go through the steps, which are described by the screenshots of Figure 3.1.

The screenshot (a), in Figure 3.1 shows the typical information input panel of the AMPS-1D graphical user interface for simulation process of solar cell. The input buttons in this panel allow to specify the model of simulation and to access to the device operating conditions and the device structure and material parameters panels. The DOS mode is chosen for the device simulation. The screenshot (b) demonstrates the structure and the set of the material parameters of one particular layer as well as the input buttons of optical properties and defects. The screenshot (c) shows the results of light J-V characteristics visualized in the form of curve and

numerals. During simulation handling, the $AM1.5$ illumination spectrum with incident power of $100mW/cm^2$ is considered.

Unlike what is used in the first chapter to calculate the total current (I), which is generated in Amps (A) from all area of a solar cell device, in this chapter, we will use the current density (J) to measure the generated current in milliamps (mA) per unit area in square centimeter (cm^2) of a solar cell device. Thus, the J-V measurement enables standard analysis to optimize the solar cell devices through simulation and laboratory work.

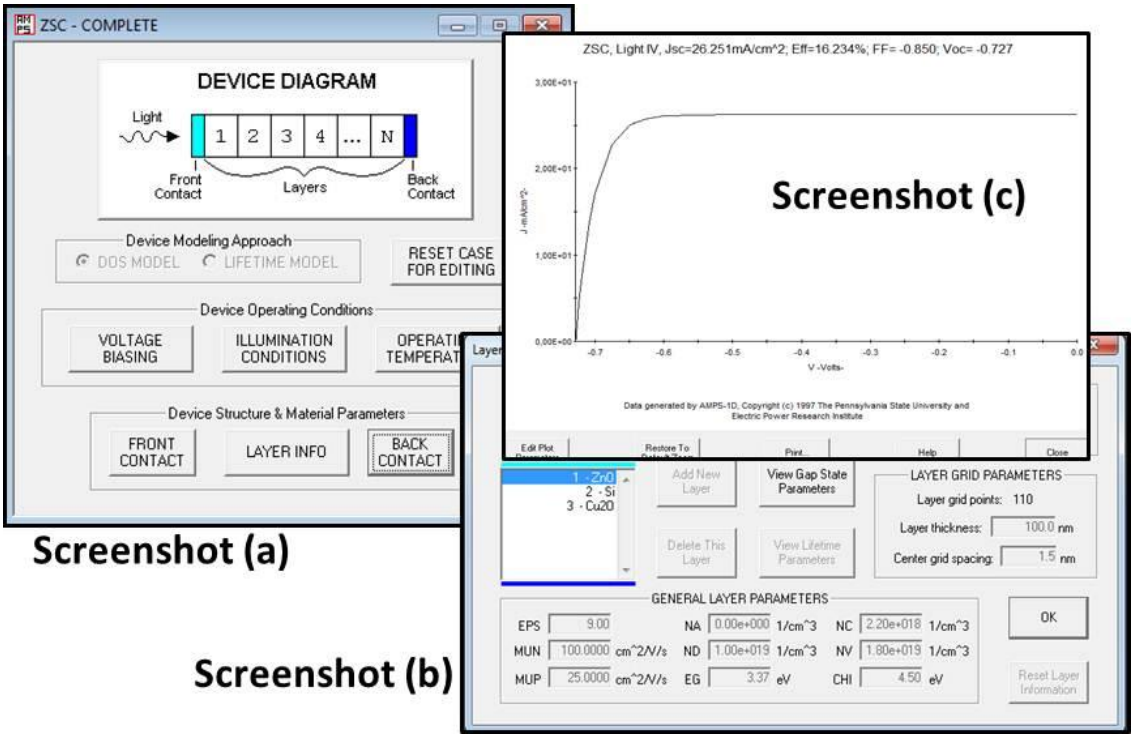

Figure 3.1 Typical data input panels of the AMPS-1D graphical user interface, allowing solar cell device and its settings.

The input *parameters* of each layer of each proposed structure have been summarized in Table 3.1 (sec. III.3.1), for defected ZnO/Si/Cu_2O thin film solar cell, Table 3.3 (sec. III.4.1) for ideal Ga-doped $Mg_xZn_{1-x}O$/Ga-doped $Mg_xZn_{1-x}O$/CdTe thin film solar cell, and Table 3.4 (sec. III.5.1) for TCO/p-CIGS/n-ODC/n-In2Se3 thin film solar cell. These parameters were the thickness, t, permittivity constant $\varepsilon/\varepsilon_0$, band gap E_g, electron affinity χ_e, electron/hole mobility μ_n/μ_p, effective density of states in conduction/valence band N_c/N_v, donor/acceptor

concentration N_d/N_a, defect concentration N_{def} and the absorption coefficient in the visible range.

At the front and back contacts, the reflection was neglected. The thermal velocity recombination for holes/electrons S_n/S_p at front and back contacts were $1 \times 10^7 cm/s$. The barrier height potentials $PHIBO$ and $PHIBL$ were considered Ohmic or slight Schottky barrier.

III.3 Optimization of Defected ZnO/Si/Cu2O Solar Cell

In this section, AMPS-1D simulator is considered to optimize a newly proposed defected ZnO/Si/Cu_2O thin film solar cell by changing different input parameters such as thickness (w), doping (N_a) and defect (N_{def}) densities, and temperature (T). This newly device consists of a p-type silicon absorber (p-Si) layer fronted by a n-type zinc oxide (n-ZnO) layer and backed by a p-type cuprous oxide (n-Cu_2O) layer.

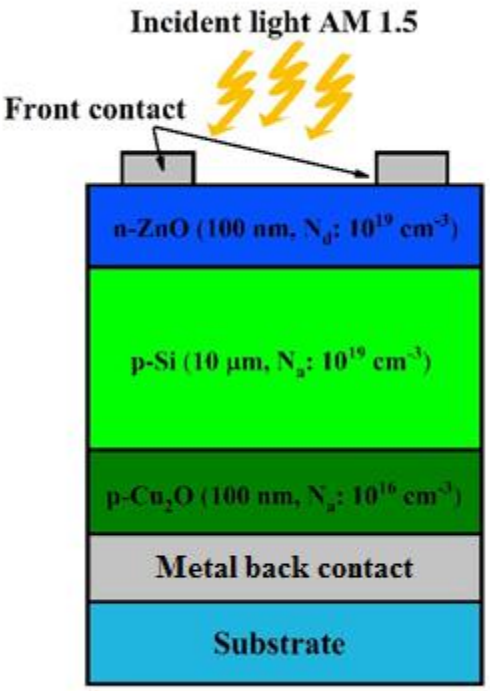

Figure 3.2 Schematic of the newly ZnO/Si/Cu_2O thin film solar cell.

III.3.1 Device settings and band diagram

Figure 3.2 shows the schematic view of this n-ZnO/p-Si/p-Cu_2O device which will be analyzed numerically. Based on the settings summarized in Table 3.1, we will examine the performance efficiency of this device.

Table 3.1 Settings for ZnO, Si and Cu_2O layers used in simulation [3].

Parameters	**n-ZnO**	**p-Si**	**p-Cu_2O**
$w(\mu m)$	0.1	10	0.1
$\varepsilon/\varepsilon_0$	9.0	11.9	9.0
$E_g(eV)$	3.37	1.12	1.9
$N_{d,a}(cm^{-3})$	N_d: 1×10^{19}	N_a: 1×10^{19}	N_a: 1×10^{16}
$\chi_e(eV)$	4.5	4.05	3.2
$\mu_n(cm^2V^{-1}s^{-1})$	100.0	1450	20.0
$\mu_p(cm^2V^{-1}s^{-1})$	25.0	500	40.0
$N_C(cm^{-3})$	2.22×10^{18}	2.80×10^{19}	2.20×10^{18}
$N_v(cm^{-3})$	1.8×10^{19}	2.65×10^{19}	1.11×10^{19}
$N_{def}(cm^{-3})$	1×10^{14}	1×10^{14}	1×10^{14}

Figure 3.3 shows the separated energy levels diagram for the ZnO, Si, Cu_2O layers. As shown in this figure, $PHIBO$ ($PHIBL$) is the difference between the work function of the metal front-contact (back-contact) and the electron affinity of the semiconductor in contact $[E_C - E_F]$ in the unit of eV at front (back) contact of the solar cell device. Also, the conduction band offset (ΔE_C) at the ZnO/Si junction is the difference between the electron affinities of the ZnO and the Si: $\Delta\chi = \chi_{Si} - \chi_{ZnO} = -0.45eV$. The obtained cliff will allow the photo-generated electrons transport to get form p-Si absorber layer to emitter ZnO layer before they recombine. On the other hand, the small valence band offset (ΔE_V) for Si/Cu_2O is found to be about $-0.07eV$, where $\left[\chi_e(Cu2O) + E_g(Cu2O)\right] - \left[\chi_e(Si) + E_g(Si)\right] = -0.07eV$. Therefore, this

established semi-alignment (Figure 3.3) will allow the holes flowing through the rear contact. Thus, there is a good alignment between ZnO and Si and between Si and Cu_2O.

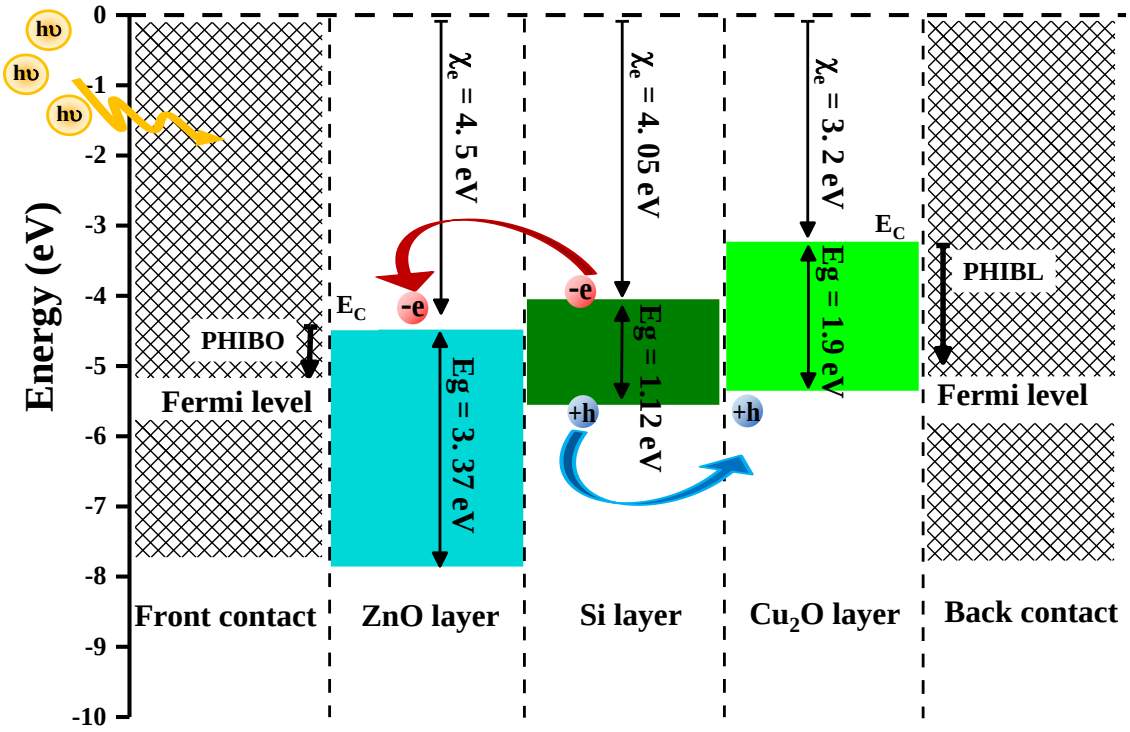

Figure 3.3 Separated layers-energy level diagram of ZnO/Si/Cu_2O thin film solar cell.

III.3.2 J-V light curve generated by AMPS-1D software

The light current density-voltage (J-V) characteristics are the fitting of current density versus the voltage. Based on the settings mentioned in Table 3.1, the light J-V curve and its characteristics, are shown in Figure 3.4. The defect concentration of p-Si absorber layer was fixed at $N_{def} = 10^{14}/cm^3$. It has been demonstrated a good performance with J_{SC}~$26.251 mA/cm^2$, V_{OC}~$0.727 Volt$, FF~0.85 and η~16.234%.

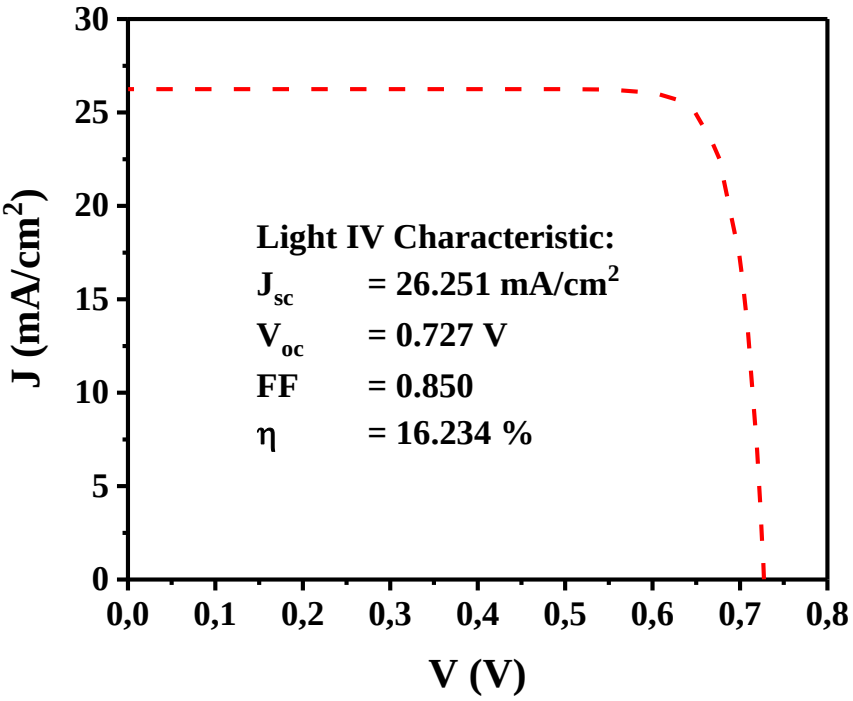

Figure 3.4 Light J-V curve of the 0.1µm-ZnO/10µm-Si/0.1µm-Cu_2O thin film solar cell.

III.3.3 Thickness optimization of ZnO window layer

Figure 3.5 summarizes the effect of the ZnO window layer thickness from 100 nm to 500 nm on the overall performance of the ZnO/Si/Cu_2O solar cell. As shown in Figure 3.5, all J-V characteristics remain unchanged at an efficiency η~16.2%, with J_{SC}~26.2 mA/cm^2, V_{OC}~0.72 $Volt$ and FF~0.85, respectively. This behavior is a result of the deficient of the light-induced carrier generation in the ZnO layer because of its wide band gap.

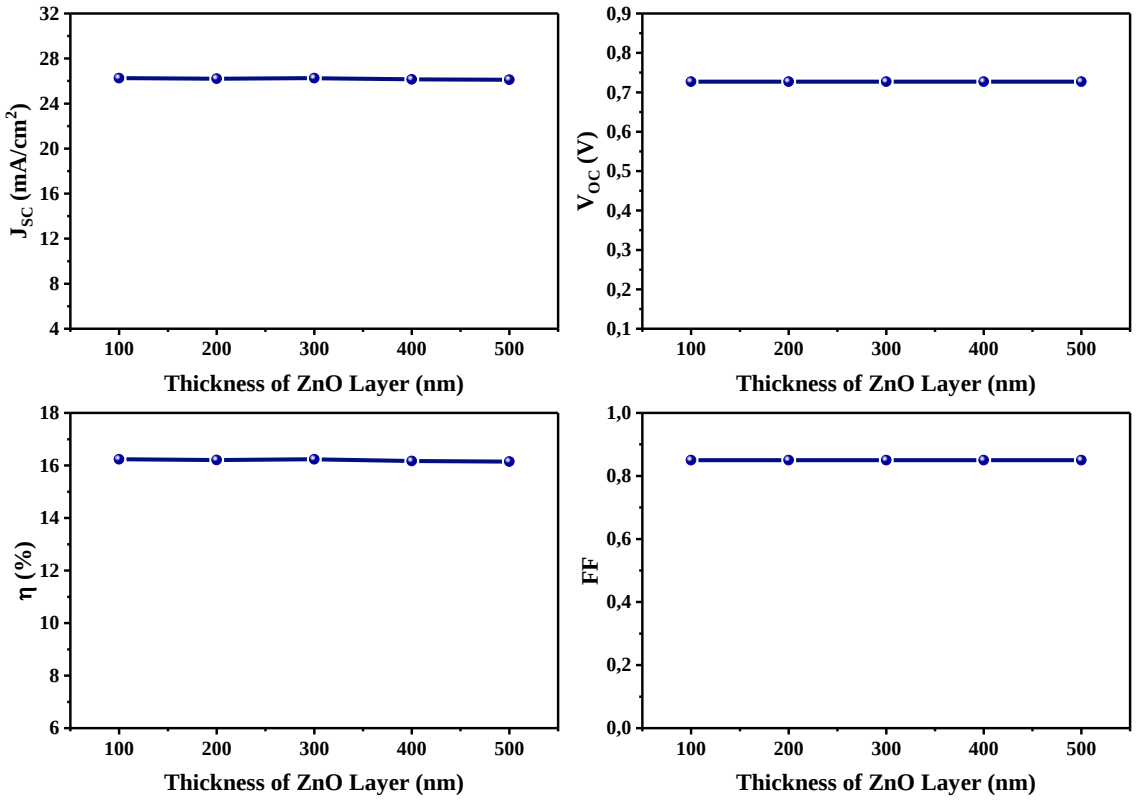

Figure 3.5 Light J-V characteristics vs. thickness of ZnO-window of ZnO/Si/Cu_2O solar cell.

III.3.4 Thickness optimization of Si absorber layer

Figure 3.6 shows the evolution patterns of V_{OC}, J_{SC}, FF and η of ZnO/Si/Cu_2O solar cell as a function of p-Si absorber layer thickness from 0.5 µm to 50 µm. Particularly, J_{SC} and η increase rapidly from 14,377 to about 26,251 mA/cm^2 (by ~45.23%) and from 9,712 to about 16,234% (by ~40.17%), respectively, when the Si layer thickness increases from 0.5 to 10 µm. While, V_{OC} (~ 0.7 V) and FF (~0.85) are almost unchanged. For a thick p-Si absorber layer (more than 10 µm), all photovoltaic parameters have almost unchanged values. This overall behavior is resulted from the increase of the photons absorption and even the increase of the electron-hole generation in the p-Si absorber layer. Therefore, the thickness of 10 µm is chosen as an optimum thickness for p-Si absorber layer for efficient ZnO/Si/Cu2O solar cell.

The obtained optimum thickness (10 µm) is consistent with what has been found in previous research. It was reported that 10~50 µm thick c-Si based solar cells can have conversion efficiencies up to ~17%. Reuter et al. [114] reported that an efficiency of 17.0% is

achieved on mono-crystalline silicon solar with thickness of approximately 47 µm, which is fabricated by using transfer layer process. Yoon et al. [115] reported an efficiency of about 17.5% within 15 µm thick crystalline Si solar cells. Cruz-Campa et al. [116] obtained an efficiency of 14.9% within 14 µm thick crystalline silicon solar cells. Li et al. [117] attempted to demonstrate that tandem ultra-thin a-Si/c-Si solar cells with a nano-pyramid structure could obtain efficiencies as high as 13.3% within only 8 µm thick silicon solar cells.

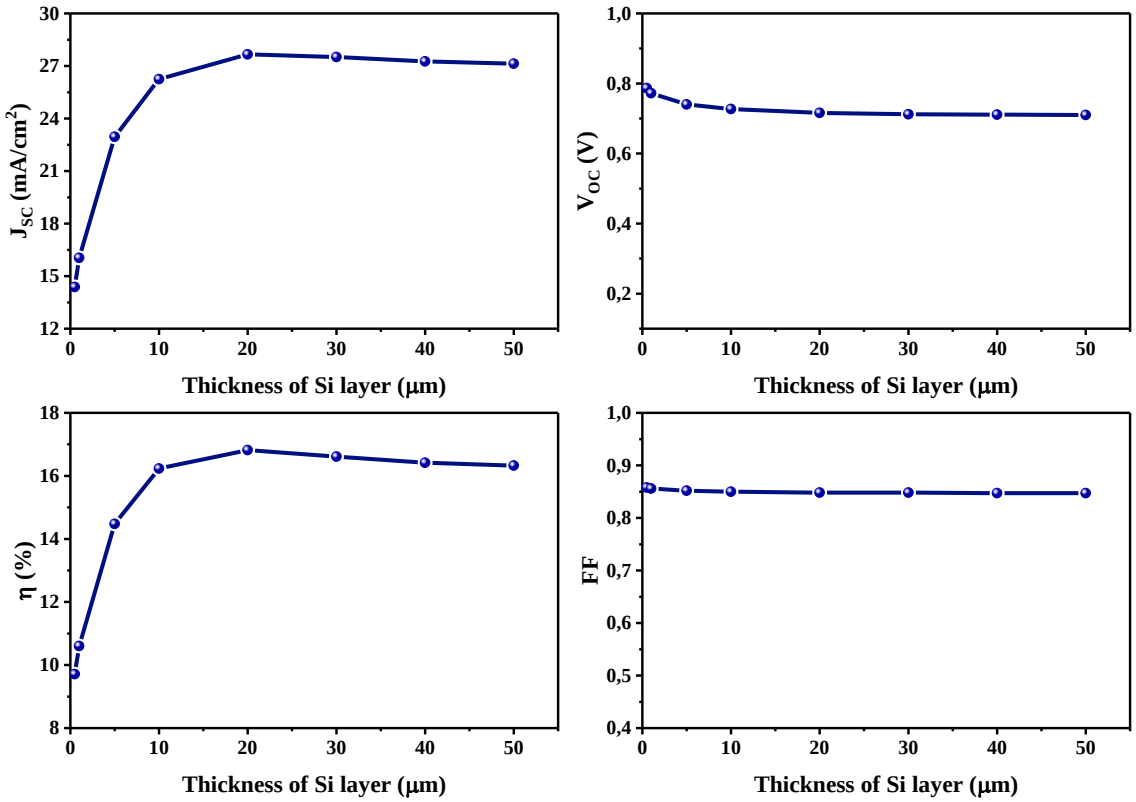

Figure 3.6 Light J-V characteristics vs. thickness of Si-absorber of ZnO/Si/Cu_2O solar cell.

III.3.5 Thickness optimization of Cu_2O back layer

To clarify the effect of the Cu_2O back layer thickness (from 0 nm to 500 nm) on the cell performance, the ZnO/Si/Cu_2O heterostructure was simulated and the results are summarized in Figure 3.7.

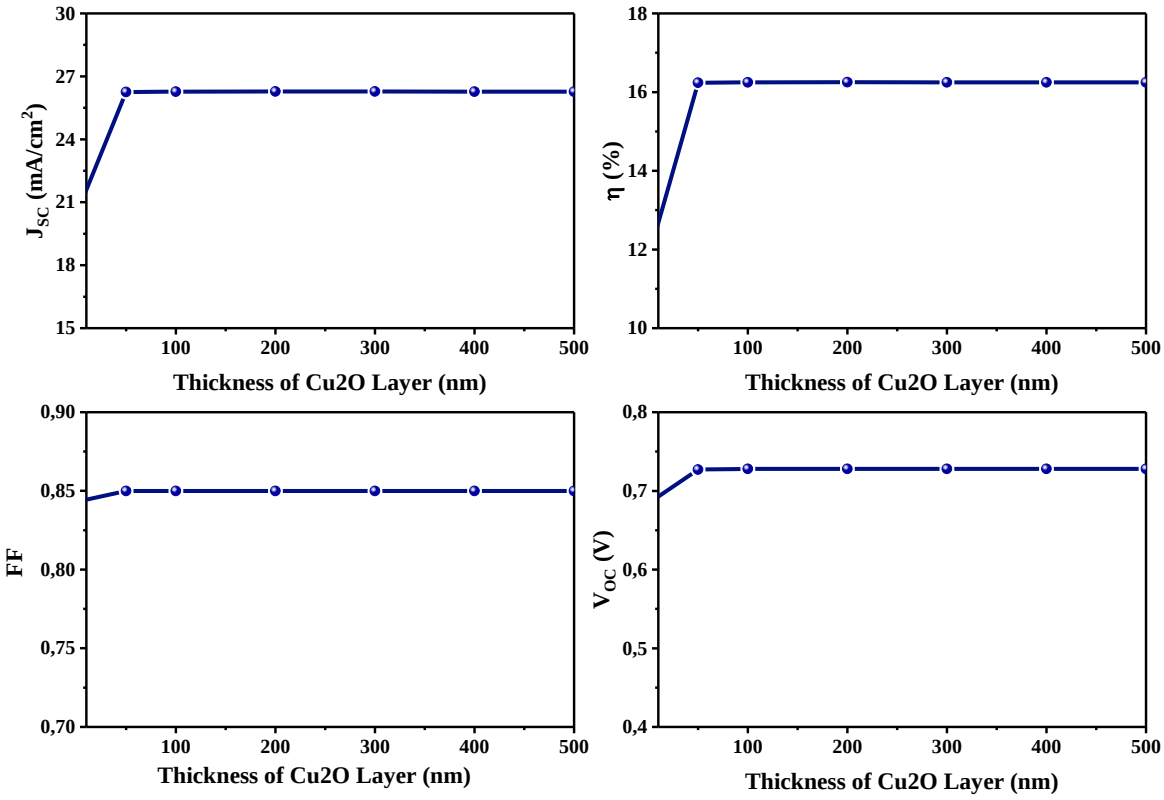

Figure 3.7 Light J-V characteristics vs. thickness of Cu_2O-back of ZnO/Si/Cu_2O solar cell.

Thus, at $0\,nm$ thick Cu_2O layer, the photovoltaic parameters are initially low with J_{SC}~20.42 mA/cm^2, V_{OC}~ 0.68 Volt, FF~0.84 and efficiency η of about 11.77%. In the presence of Cu_2O layer with an increased thickness, all photovoltaic parameters remain almost unchanged at an efficiency η of about 16.2%, with $J_{SC}\sim 26.2 mA/cm^2$, $V_{OC}\sim 0.72V$ and $FF\sim 0.85$. Therefore, a few μm of Si layer give more chances to a few nm of Cu_2O back layer (several hundred nm to a few μm for most experimental Cu_2O based solar cells [118-119]) to absorb the photons who have absorption length longer than the Si absorber interlayer thickness. Thus, a higher efficiency of 16.2% is expected. The optimized thicknesses of ZnO, Si and Cu_2O are 0.1, 10 and $0.1\mu m$, respectively. These small thicknesses mean although the device is three hetero-layers, the carriers would travel in few crystals in the vertical direction, facing limited barriers caused by grain boundaries. Thus, the crystallite size and hence the thickness are typically required to fabricate high-performance thin film solar cell.

III.3.6 Optimization of acceptor density of p-Si absorber layer

Figure 3.8 shows the evolution patterns of V_{OC}, J_{SC}, FF and η of ZnO/Si/Cu_2O solar cell versus different acceptor concentrations of p-Si absorber layer, N_a(p-Si).

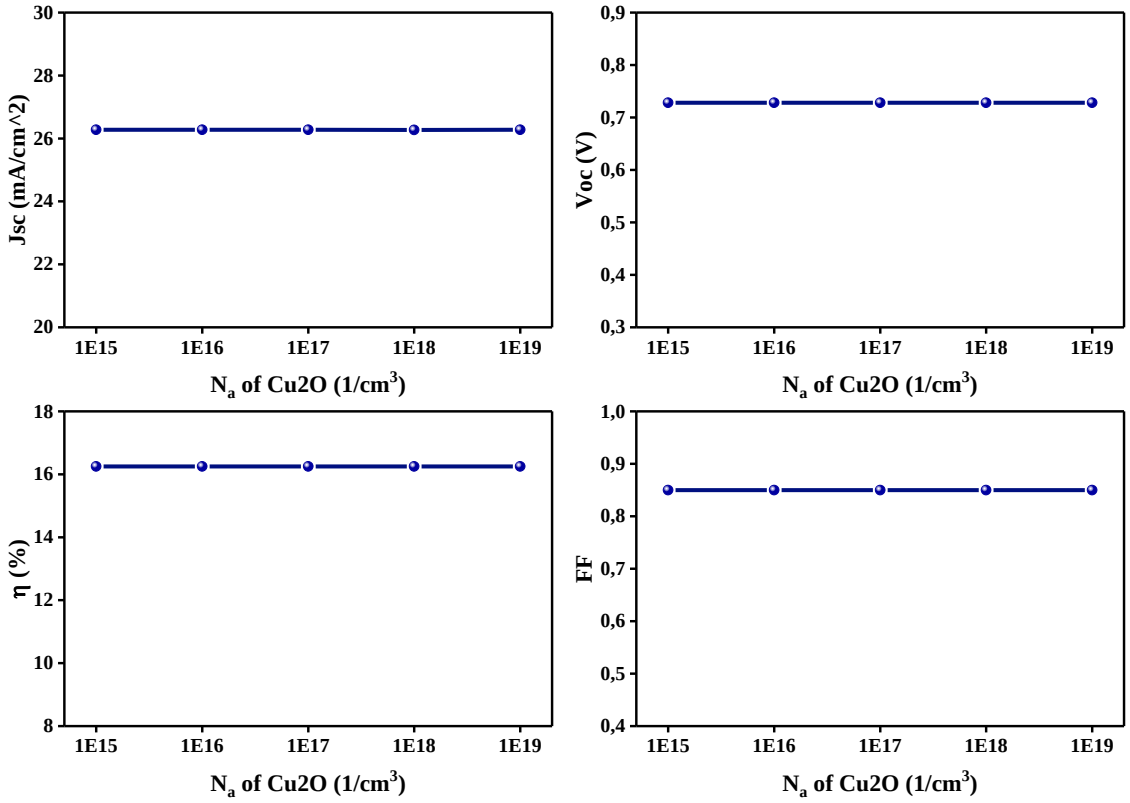

Figure 3.8 Light J-V characteristics vs. doping concentration of Si-absorber of ZnO/Si/Cu_2O solar cell.

Consequently, since lowest or highest ($< 10^{14} cm^{-3}$or $> 10^{19} cm^{-3}$) doping concentrations have large impact on the electronic properties (mobility, conductivity/resistivity and related parameters) of crystalline silicon, the acceptor concentration, N_a, is varied in a moderate range from $1 \times 10^{14}\ cm^{-3}$ to $1 \times 10^{19}\ cm^{-3}$ [120]. In other words, when N_a exceed the effective density of states N_v(p-Si) ($\sim 10^{19} cm^{-3}$), the crystalline silicon becomes degenerate semiconductor, thus the energy band gag narrowing will be [121]. At the beginning, for p-Si of $N_a = 1 \times 10^{14} cm^{-3}$ the efficiency η and FF were achieved small values of about 8.67% and 0.67, respectively. For p-Si of $N_a > 1 \times 10^{14} cm^{-3}$, we observe that J_{SC} shows

slight decrease from 27.41 mA/cm^2 at the concentration $1 \times 10^{14}\ cm^{-3}$ to 26.251 mA/cm^2 at the concentration $1 \times 10^{19}\ cm^{-3}$.

In contrast, the open circuit voltage, V_{OC}, shows a considered increase from 0.47 V at the concentration $1 \times 10^{14}\ cm^{-3}$ to 0.727 V at the concentration $1 \times 10^{19}\ cm^{-3}$. At $N_a = 1 \times 10^{19}\ cm^{-3}$, the efficiency η and FF were increased to about 16.23% and 0.85, respectively. The commended acceptor density of p-Si absorber layer should be higher than that of its defect density (in this case $1 \times 10^{14}\ cm^{-3}$).

III.3.7 Gaussian defect effect on ZnO/Si/Cu$_2$O solar cell

Simulation results for ZnO/Si/Cu_2O heterostructure with different gaussian (both of acceptor-like and donor-like) defects located in the band gap of p-Si absorber layer are shown in Figure 3.9. It this figure, the defect density of p-Si, N_{def}, shows harmful effects on the ovarall performance of the device. The highest possible values of the J-V charactristics were obtained when $N_{def} < 1 \times 10^{14}\ cm^{-3}$. At $1 \times 10^{11}\ cm^{-3}$ of defects the corresponding characterstics were: J_{SC}~27.57 mA/cm^2, V_{OC}~0,78 V, FF~0.90 and η~21.78%.

Increasing the N_{def}(p-Si) more than $1 \times 10^{14}\ cm^{-3}$, the J_{SC} and V_{OC} were significantly affected. Thus, the defect concentration of $1 \times 10^{17} cm^{-3}$ caused a sharp fall in the J-V charactristics with J_{SC}~7.23 mA/cm^2, V_{OC}~0,58 V,FF~0.82 and η~3.46%. This poor behavior of the ZnO/Si/Cu_2O device at high bulk defetcs is resulted from recombination phenomenon. Therefore, the current transport may severely affected by the bulk defect density of the layer. This effect is related to created trapping (recombination) in the bulk layer that limits the efficiency [122].

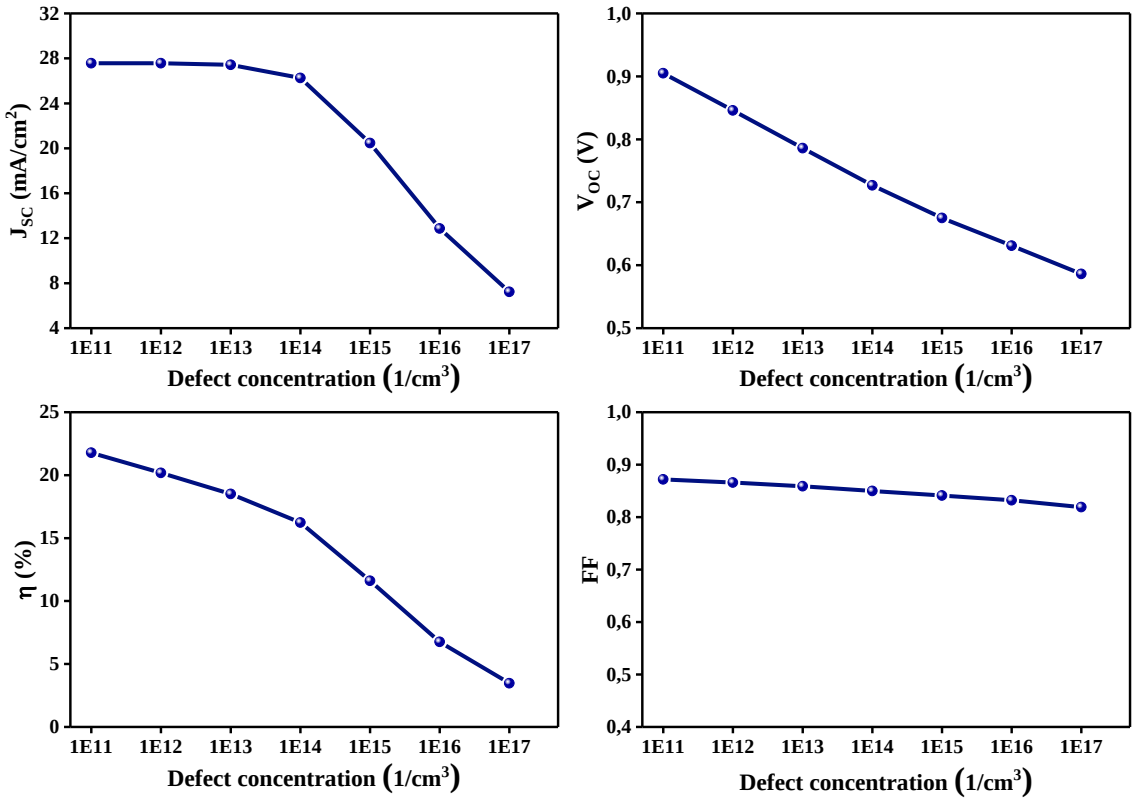

Figure 3.9 Light J-V characteristics vs. defect concentration of Si-absorber of ZnO/Si/Cu_2O solar cell.

III.3.8 Operating temperature effect on ZnO/Si/Cu_2O solar cell

Figure 3.10 shows the evolution of the J-V characteristics as a function of the operating temperature on the overall behavior of ZnO/Si/Cu_2O solar cell.

In the literature, the dependence of the V_{OC} to the operating temperature is used as an indicator on the stability of solar cells [35]. To testify this vital dependence on the defected ZnO/Si/Cu_2O heterostructure solar cell, the operating temperature is stepped from $300K$ to $600K$ by $50K$. Increasing the operating temperature conduct to a decrease of material band gap and eventually an increase to the leakage current and a decrease to the V_{OC}. The current density J_{SC} has almost unchanged pattern ($\sim 26.5\ mA/cm^2$). From Figure 3.10, V_{OC} decreased from $\sim 0{,}73\ V$ (recorded at $300K$) to $\sim 0{,}32V$ (recorded at $600K$). A similar behavior is observed for FF and efficiency which decreased from ~ 0.85 and $\sim 16{,}234\%$ (at $300K$) to $0{,}591$ and $4{,}979\%$ (at $600K$), respectively.

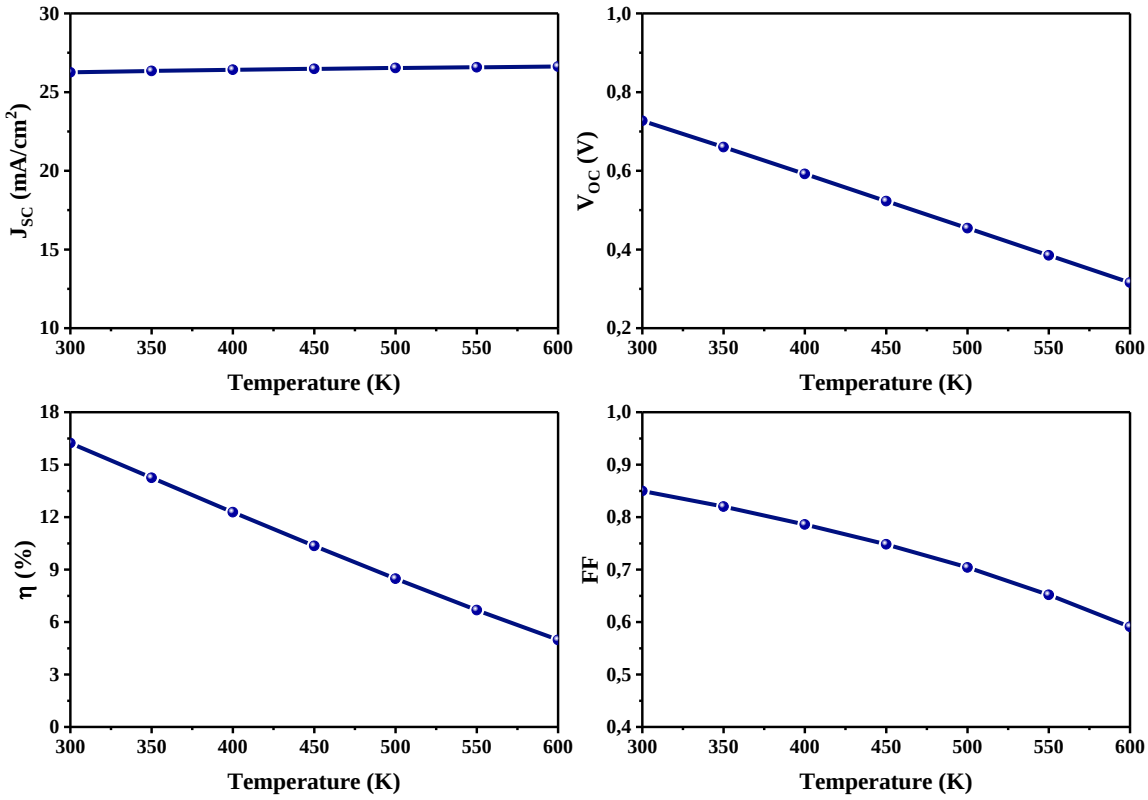

Figure 3.10 Light J-V characteristics vs. temperature of ZnO/Si/Cu_2O solar cell.

III.4 Optimization of Ideal HGMZO/LGMZO/CdTe/$MoTe_2$ Solar Cell

In this section, the AMPS-1D simulator is also considered to deal with the optimization of an ideal high-Ga-doped $Mg_xZn_{1-x}O$/low-Ga-doped $Mg_xZn_{1-x}O$/CdTe/$MoTe_2$ thin film solar cell. This investigated structure consists of p-type CdTe layer fronted by n-type high-Ga-doped $Mg_xZn_{1-x}O$ (or high-gallium and magnesium co-doped zinc oxide or HMGZO) as window layer and n-type low-Ga-doped $Mg_xZn_{1-x}O$ (or low-gallium and magnesium co-doped zinc oxide or LMGZO) as buffer layer, and backed by p-type $MoTe_2$ layer.

III.4.1 Device settings and band diagram

Figure 3.11 shows the schematic view of this HGMZO/LGMZO/CdTe/$MoTe_2$ device which will be analyzed numerically by changing different input parameters of the device such as thickness, doping density and temperature.

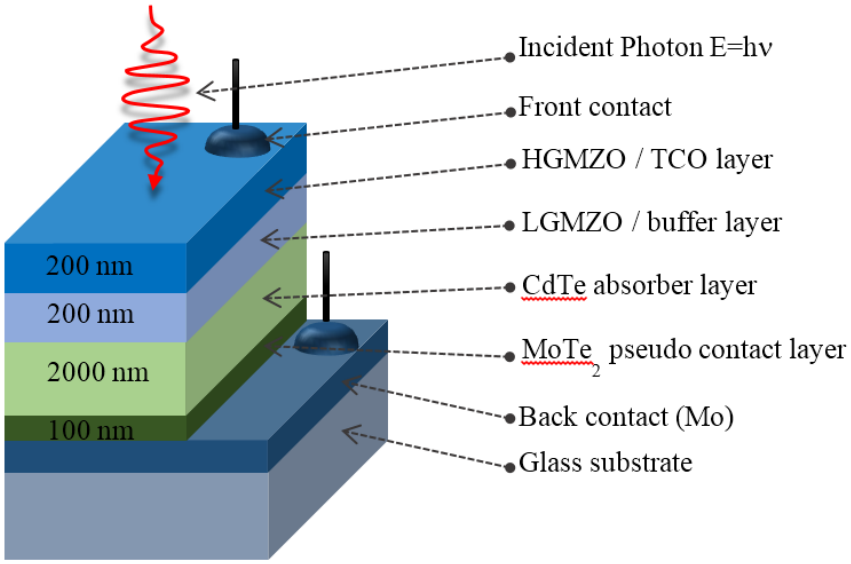

Figure 3.11 Schematic view of HGMZO/LGMZO/CdTe/$MoTe_2$ thin film solar cell.

Table 3.2 Electrical properties of HGMZO-TCO and LGMZO-HRT-BL layers [42,41].

Property	**Unit**	**n^+-HGMZO**	**n-LGMZO**
Ga concentration	%	0.5	0.05
Mg concentration	%	5	15
Doping concentration, N_d	cm^{-3}	9.2×10^{19}	1.59×10^{18}
Mobility	$cm^2V^{-1}s^{-1}$	34	4.0
Resistivity	$\Omega.cm$	19×10^{-4}	0.98×10^{-2}
Band gap energy, E_g	eV	3.47	3.73
n^+-HGMZO : $(0.5at.\%)$ Ga-doped $Mg_{0.05}Zn_{0.95}O$ n-LGMZO : $(0.05at.\%)$ Ga-doped $Mg_{0.15}Zn_{0.85}O$			

We will examine the structural templates HGMZO/LGMZO/CdTe/$MoTe_2$ under light by J-V characteristics: J_{SC}, V_{OC}, FF and η. The electrical properties of selected HGMZO-TCO and LGMZO-HRT-BL partner layers are given in Table 3.2.

Table 3.3 Settings for HGMZO, LGMZO, CdTe and $MoTe_2O$ layers used in simulation [36].

Property	**n^+- HGMZO**	**n-LGMZO**	**p-CdTe**	**$MoTe_2$**
$w(nm)$	200	200	2000	100
$\varepsilon/\varepsilon_0$	9.0	9.0	9.4	13
$E_g(eV)$	3.47	3.73	1.45	0.97
$N_{d,a}(cm^{-3})$	N_d: 9.3×10^{19}	N_d: 1.59×10^{18}	N_a: 1×10^{18}	N_a: 1×10^{15}
$\chi_e(eV)$	4.3	4.3	4.28	4.2
$\mu_n(cm^2V^{-1}s^{-1})$	34	4	320	110
$\mu_p(cm^2V^{-1}s^{-1})$	11	1.5	40	426
$N_C(cm^{-3})$	2.2×10^{18}	2.2×10^{18}	7.5×10^{17}	3×10^{18}
$N_v(cm^{-3})$	1.8×10^{19}	1.8×10^{19}	1.8×10^{19}	4×10^{18}
Property	**Front contact**		**Back contact**	
Φ_{B0}/Φ_{Bl} (eV)	0		0.4	
S_n (cm/s)	1.0×10^7		1.0×10^7	
S_p (cm/s)	1.0×10^7		1.0×10^7	
Reflectance	0.07		0.4	

The $Mg_{0.05}Zn_{0.95}O$ film doped with high-Ga-content of $0.5at.\%$ showed the lowest electrical resistivity of about $19.7 \times 10^{-4}\ \Omega.cm$ with a carrier concentration of $9.3 \times 10^{19}\ cm^{-3}$, while, the $Mg_{0.15}Zn_{0.85}O$ film doped with low-Ga-content of $0.05\ at.\%$ showed a high electrical resistivity of about $0.98\ \Omega.cm$ with a carrier concentration of $1.59 \times 10^{18}\ cm^{-3}$ [41,42]. These interesting experimental data nominate the high electrical resistivity and high optical transparency LGMZO films for buffer layer employment, while the HGMZO films are mentioned for TCO layer employment for CdTe solar cells. To improve the performance of our suggested CdTe cell, one needs to use a material with high work function. As well-known, the CdTe material has a high work function which is more than $5.7\ eV$ [123]. Therefore, it is hard

to form a good ohmic contact on Mo back contact. To tackle this problem, we apply an efficient back ohmic surface that consists of a $MoTe_2$ thin layer with a tuned band gap and high conductivity [124].

From Table 3.3, the electron affinities of HGMZO/LMGZO, CdTe and $MoTe_2$ are 4.3 eV, 4.28 eV and 4.2 eV, respectively, and the band gaps are 3.73 eV, 1.45 eV and 0.97 eV, respectively. These parameters are used to determine the band offsets at layer/layer interfaces. A conduction band offset (ΔE_C) at the n-LGMZO/p-CdTe interface is only 0.02 eV [(E_g(LGMZO)-E_g(CdTe)] and at CdTe/$MoTe_2$ interface is only 0.08 eV [E_g(CdTe)-E_g($MoTe_2$)], while the valence band offset (ΔE_V) at CdTe/$MoTe_2$ interface is large of about 0.56 eV [(χ_e+E_g($MoTe_2$))-(χ_e+E_g(CdTe)].

Figure 3.12 shows the band diagram profiles and the depletion region of n^+-HGMZO/n-LGMZO/p-CdTe/$MoTe_2$ structure calculated by AMPS-1D at equilibrium condition for an acceptor concentration of CdTe: N_a varied from 1×10^{14} to 1×10^{18} cm^{-3} (Figure 3.12 (b)). From Figure 3.12 (b), when N_a of CdTe is 1×10^{14} cm^{-3}, the depletion region fills the most of CdTe and the electric field is weak and deeply constant. The depletion regions become narrow when N_a has a value beyond 1×10^{16} cm^{-3}. The narrow depletion region influences the buildup electric field which reduces the free charge carrier recombination within it.

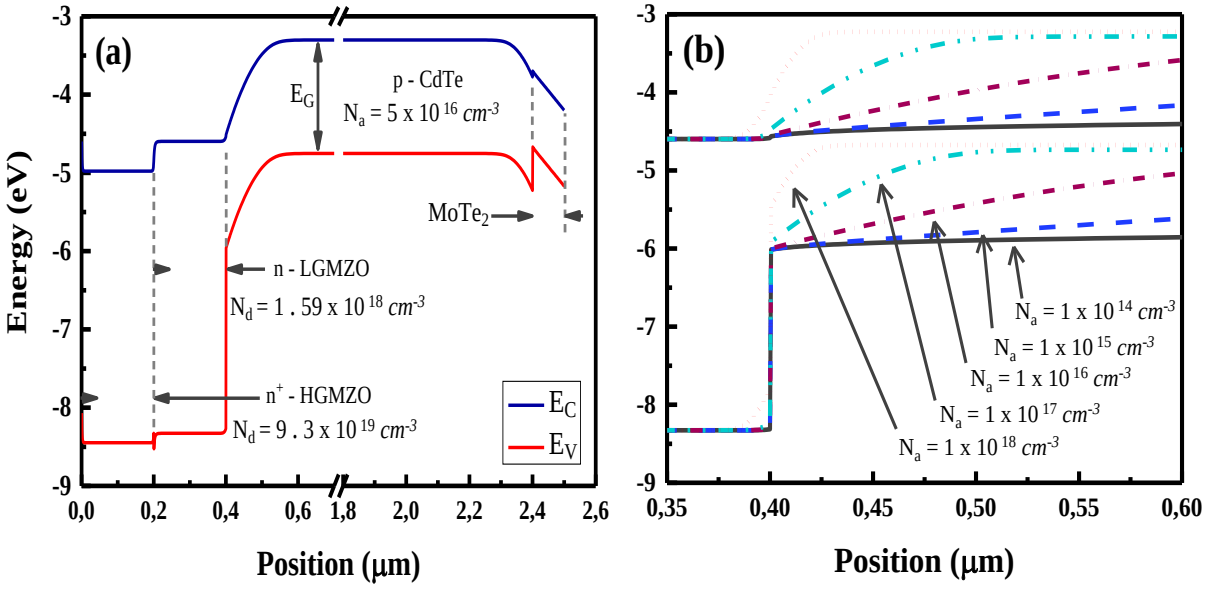

Figure 3.12 (a) Band diagram profile at thermodynamic equilibrium conditions and **(b)** the behavior of the depletion region for various carrier concentrations N_a of CdTe absorber layer.

III.4.2 J-V light curve generated by AMPS-1D software

Figure 3.13 shows that the J-V curves are shifted to higher voltages when N_a of CdTe is varied up from $1 \times 10^{14}$to $1 \times 10^{18} cm^{-3}$. These voltage shifts (from 0.05to $0.969V$) suggest that the open-circuit voltage (when the current density is equal to zero) is strongly dependent on N_a of CdTe. For higher N_a of CdTe, the electric field build-up within the depletion region is influenced. The increase of the electric field leads to the reduction of the free charge carrier recombination, which increases strongly the open-circuit voltage.

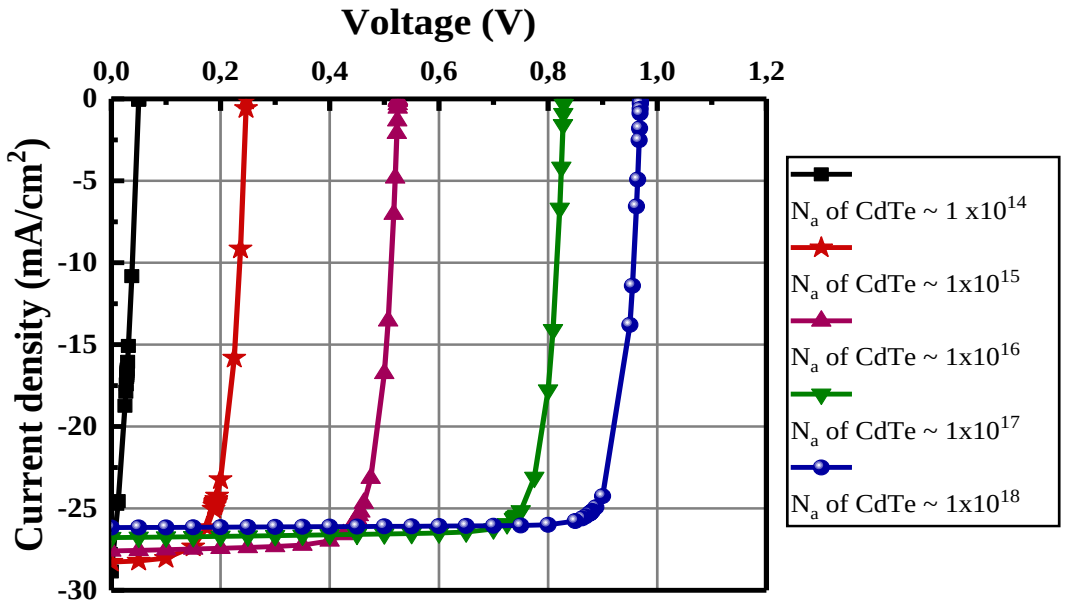

Figure 3.13 Light J-V curves of HGMZO/LGMZO/CdTe/$MoTe_2$ with different acceptor concentrations N_a of CdTe absorber layer.

III.4.3 Optimization of donor density N_d of buffer-LGMZO layer

Figure 3.14 summarizes, the behaviors of the short-circuit current (J_{SC}), the efficiency (η), the open-circuit voltage (V_{OC}) and the fill factor (FF) for a structure shown in Figure 3.11 with the settings shown in Table 3.3 under the effect of the donor concentration N_d of the LGMZO layer.

With varying N_d from 1×10^{17} cm^{-3} to $1 \times 10^{20}\, cm^{-3}$, the cell gives slight improvements of J_{SC}, η and FF, from 25.68 to 26.32 mA/cm^2, 18.63 to 20.28% and 82.3 to

87.4%. This is due to the low absorption coefficient of the GMZO material. Thus, the cell performance does not affect by LGMZO doping concentration.

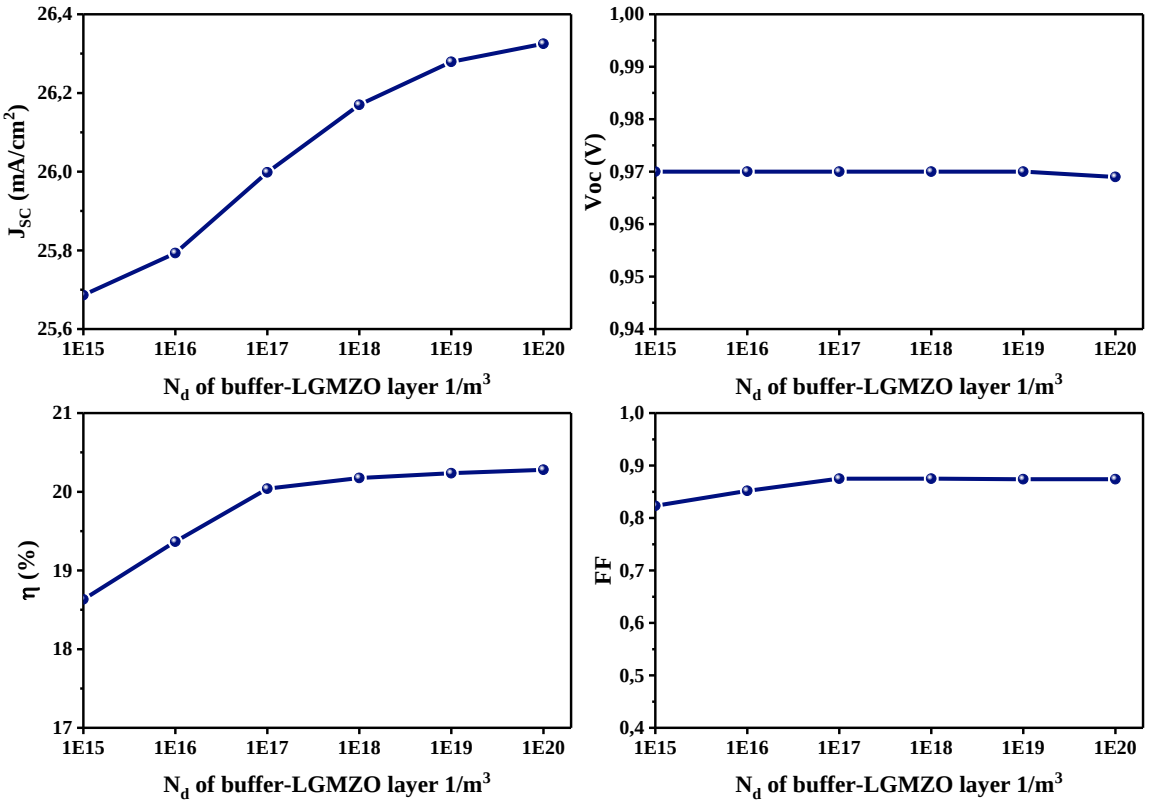

Figure 3.14 Light J-V characteristics of CdTe solar cell vs. donor concentration $N_d$of buffer-LGMZO layer.

III.4.4 Thickness optimization of buffer-LGMZO layer

Figure 3.15 summarizes the effect of the LGMZO buffer thickness (from 10 nm to 700 nm) on the performance of the CdTe solar cell. Because it's wide band gap of 3.73 eV there is no considerable carriers generated in the LGMZO buffer bulk. As expected, from top to bottom, the J_{SC}, the Efficiency, the V_{OC} and the FF are all showed fixed performance of J_{SC}~26.20 mA/cm^2, η~20.91%, V_{OC}~0.97 V and FF~87.4%.

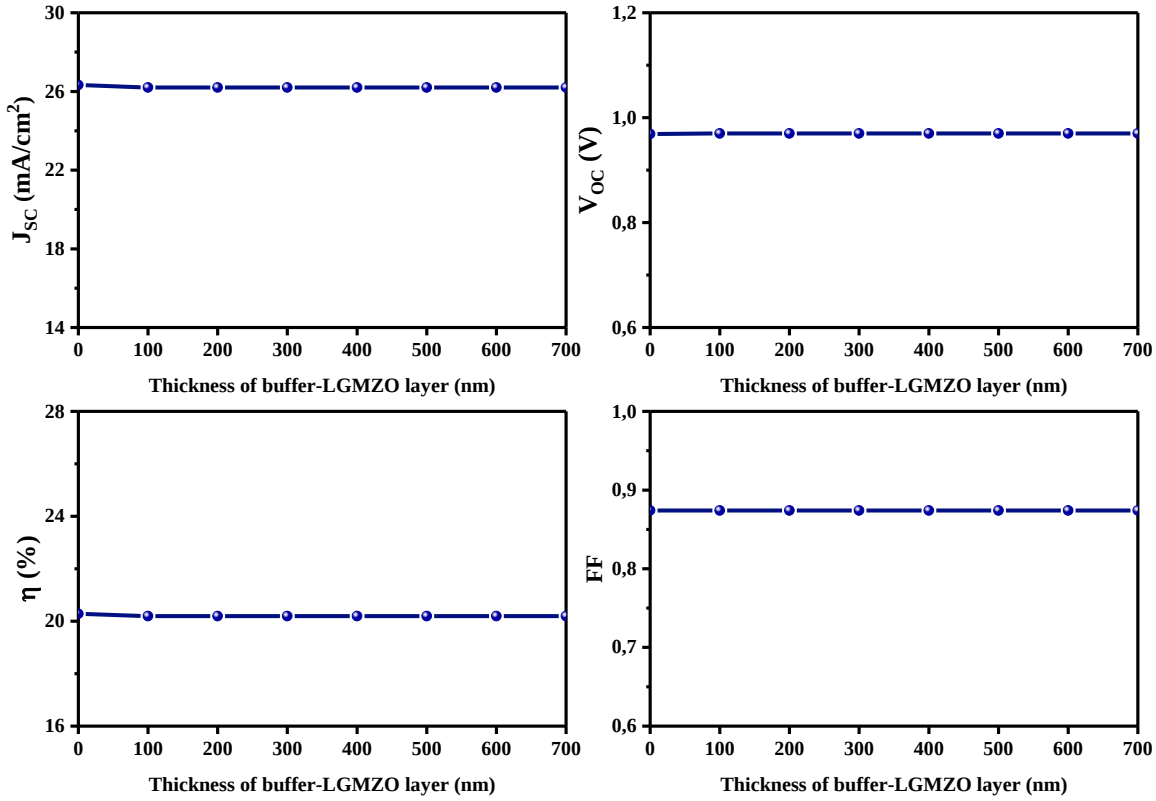

Figure 3.15 Light J-V characteristics of CdTe solar cell vs. thickness of buffer-LGMZO layer.

III.4.5 Optimization of acceptor density N_a of p-CdTe absorber layer

In Figure 3.16, the Efficiency, the V_{OC} and the FF are increased significantly with the increase of the acceptor concentration N_a from 1×10^{14} cm^{-3} to a tolerable limit of 1×10^{18} cm^{-3}. But J_{SC} decrease from 28.85 to 26.87 mA/cm^2 in which this degradation is due to the increase of the free carrier charge recombination which takes place within the bulk. The V_{OC} increases strongly from 0.05 to 0.97 V, and hence the fill factor FF increases sharply from 33% and reaches the maximum value of 87.4%. The efficiency reaches its maximum value of 20.16%. Thus, an optimum performance of CdTe thin film solar cells can be obtained for an acceptor concentration of about 1×10^{18} cm^{-3}.

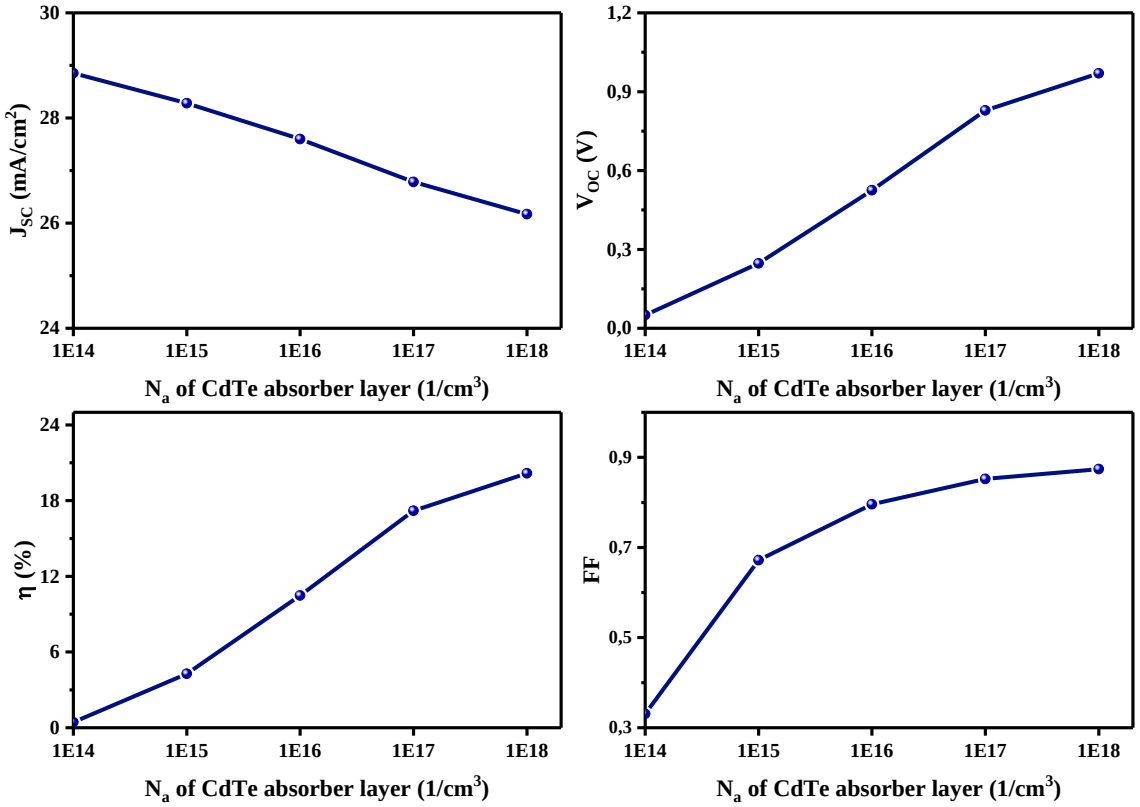

Figure 3.16 Light J-V characteristics of CdTe solar cell vs. acceptor concentration N_a of CdTe absorber layer.

III.4.6 Thickness optimization of p-CdTe absorber layer

The curves shown in Figure 3.17 summarize, top to bottom, the behaviors of J_{SC}, Efficiency, V_{OC} and FF as a function of the thickness of the CdTe absorber layer varied from 50 nm to 8 μm for the CdTe solar cell. The $MoTe_2$ back surface layer of 100 nm is arranged in order to alienate the back contact from the depletion region and avoids the feed-back of electrons to the contact. All characteristics are improved significantly with increasing the CdTe absorber thickness. At thickness 50 nm of CdTe layer, J_{SC}, Efficiency, V_{OC} and FF are 5.18 mA/cm^2, 3.13%, 0.827 V and 71.6%, respectively. When the thickness of the absorber layer is 2 μm, the cell gives the performance of J_{SC}~26.207mA/cm^2, Efficiency~20.16 %, V_{OC}~0.97 V and FF~87.4 %. And at thickness 8 μm, the cell gives the performance of J_{SC}~28.70 mA/cm^2, Efficiency~23.17%, V_{OC}~1.00 V and FF~88.2%.

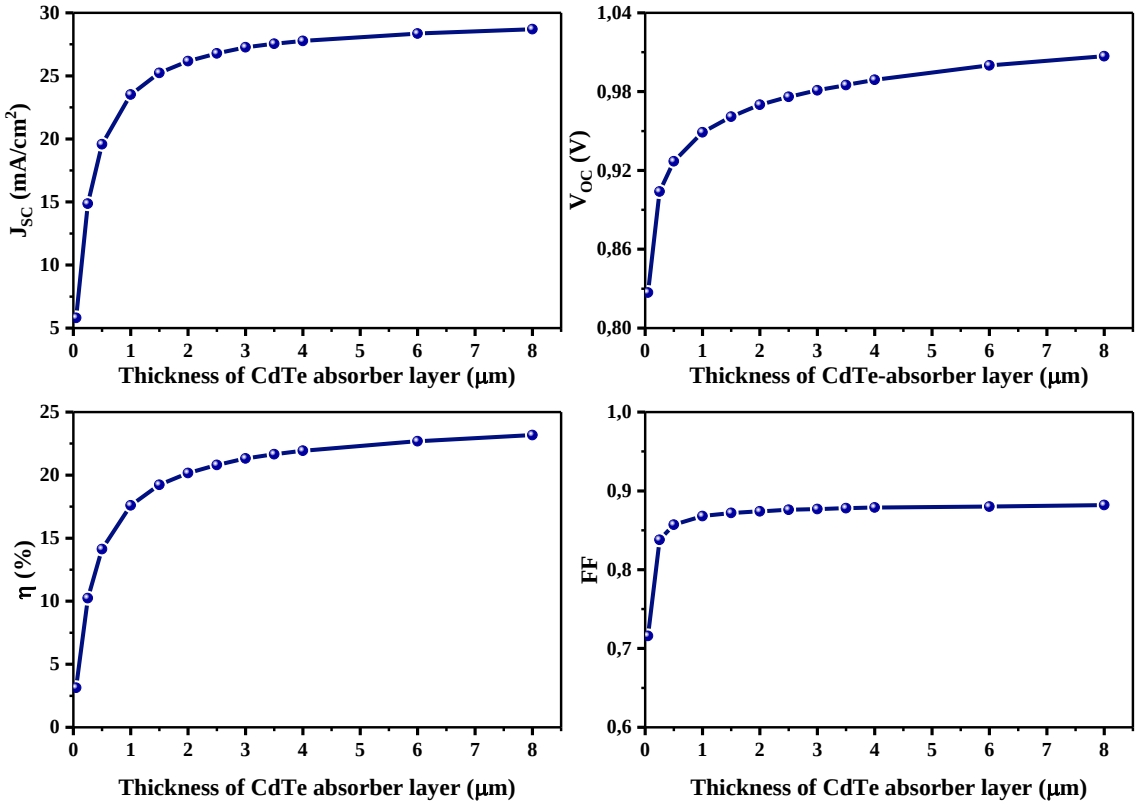

Figure 3.17 Light J-V characteristics of CdTe solar cell vs. thickness of CdTe absorber layer.

The Efficiency improvement is due mostly to the increase of J_{SC} which is due to the increase of the collected carriers which are generated by the absorbed photons in the increased absorber layer. It is noticed that there is an improvement of about ~85% in Efficiency between the beginner tested thickness 50 nm and the thickness of 2 µm. Increasing the thickness by 6 µm (on going from the thickness 2 to 8 µm) causes an improvement of ~16% in Efficiency. Thus, the optimum thickness of CdTe absorber layer is chosen of about 2 µm.

III.5 Optimization of Superstrate TCO/CIGS/ODC/In_2Se_3 Solar Cell

In this section, AMPS-1D simulator was considered to report on systematic studies of TCO and Metal work functions including a discussion of their dependence on the superstrate SLG/TCO/p-CIGS/n-ODC/n-In2Se3/Metal solar cells photovoltaic properties. Our study is focused on reducing the potential barriers so as to increase carrier's collection in the structure.

III.5.1 Device settings

The model used in the simulation is simple as shown in Figure 3.18. Based on the settings summarized in Table 3.4, we will examine the performance efficiency of this device.

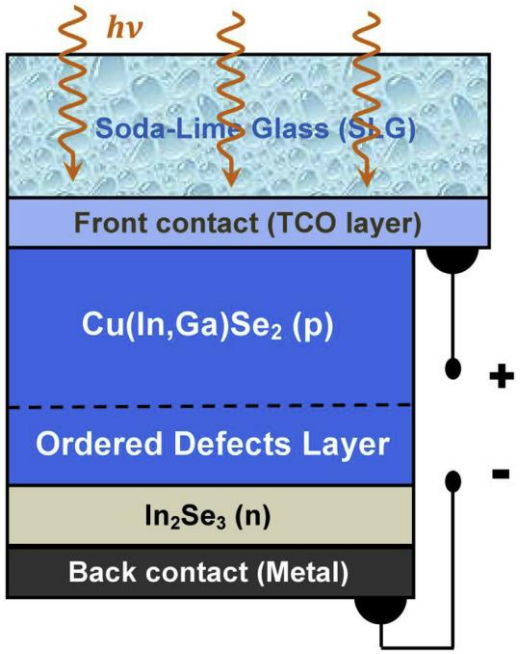

Figure 3.18 Schematic of the SLG/TCO/p-CIGS/n-ODC/n-In_2Se_3/Metal thin film solar cell.

Up to five regions of different material parameters can be used to define the cell structure. The structure consists of SLG/TCO/p-$CuIn_{0.7}$-$Ga_{0.3}Se_2$/n-ODC/n-In_2Se_3/Metal in which the light enters through the TCO layer is considered as the solar cell model in the simulation. We insert in the model a significant Ordered Defect Compounds (ODC) n-type

layer between the In_2Se_3 and CIGS layers. This layer is usually created experimentally in the CIGS absorber part when the In_2Se_3 buffer layer is deposited onto SLG/TCO/CIGS substrate with high substrate temperature [125-126]. The $CuIn_{0.7}Ga_{0.3}Se_2$ absorber and In_2Se_3 buffer parameters were from a previous research work [127]. The radiation $AM1.5G$ with incident power density of $100\ mW/cm^2$ is used as an illuminating source. In superstrate CIGS solar cells, a highly doped TCO front contact and Metal back contact layers serve as the front and back electrodes, respectively.

Table 3.4 Settings of physical parameters used in the simulation model for superstrate CIGS solar cell [112].

Parameters	**p-CIGS**	**n-ODC**	**n-In_2Se_3**
$w(nm)$	500	3500	200
$\varepsilon/\varepsilon_0$	13.6	13.6	10
$E_g(eV)$	1.12	1.3	2.4
$N_{d,a}(cm^{-3})$	N_a: $2\ \times\ 10^{16}$	N_d: $1\ \times\ 10^{15}$	N_d: $1\ \times\ 10^{18}$
$\chi_e(eV)$	4.1	4.1	3.8
$\mu_n(cm^2V^{-1}s^{-1})$	50	50	50
$\mu_p(cm^2V^{-1}s^{-1})$	12	12	12
$N_C(cm^{-3})$	2.2×10^{18}	2.2×10^{18}	2.2×10^{18}
$N_v(cm^{-3})$	1.8×10^{19}	1.8×10^{19}	1.8×10^{19}
$N_{def}(cm^{-3})$	D: 1×10^{14}	A: 1×10^{18}	A: 1×10^{18}

III.5.2 Effect of TCO work function on cell performance

In the superstrate CIGS structure presented in Figure 3.18, an (n^+)-type TCO front contact can be believed to form a barrier with p-CIGS absorber part. The formation of a low resistance, and low barrier TCO/p-CIGS front contact is the most challenging aspects of high performance fabrication of superstrate CIGS solar cells. The wide band gap and highly doped TCO films behave electronically similar to metals elements and the electronic behavior of the

TCO/semiconductor interface was assumed as similar to a metal/semiconductor junction [128]. Moreover, the TCO/p-type CIGS contact does not always form a barrier and has the possibility of forming an ohmic contact, which is determined by the difference in work functions between TCO and p-CIGS [129]. For a p-CIGS type semiconductor with band-gap (E_g) and electron affinity (χ_{CIGS}), and a TCO with work function W_{TCO}, an ohmic TCO/p-CIGS contact is formed when: $W_{TCO} > E_g + \chi_{CIGS}$ and a rectifying (Schottky) barrier contact is formed when $W_{TCO} < E_g + \chi_{CIGS}$ [130]. Most TCO materials, however, do not have sufficiently high work-functions and therefore form a Schottky barrier contact to p-CIGS absorber layer.

The understanding of the effects of TCO work function on TCO/p-CIGS/n-ODC/n-In_2Se_3 solar cells in depth requires the calculation of the energy band diagram at thermodynamic equilibrium and the built-in electric field. Figure 3.19 depicts the schematic band diagram of the TCO/p-CIGS/ODC part for different TCO work functions. The band bending on the p-CIGS part appeared along with the decrease of TCO work function. Two possible carrier transport mechanisms were expected. In the case of high TCO work function, an ohmic contact was formed in (n^+)-TCO/p-CIGS interface and a direct recombination of holes in the valence band of p-CIGS and electrons in the conduction band of (n^+)-TCO was occurred. The second is a trap-assisted tunneling even if the barrier is formed at the (n^+)-TCO/p-CIGS interface [129]. Photogenerated holes in p-CIGS part can passes across the Schottky barrier and reach TCO contact easily thanks to a trap-assisted tunneling.

The performance of superstrate SLG/TCO/p-CIGS/ODC/n-In_2Se_3/Metal solar cells will be investigated numerically by the variation of TCO work function (W_{TCO}). In the model, P-type CIGS and ODC layer parameters were fixed, and only the work function of TCO films was changed from 4 to 5.5 eV. Zn material was used in this section as a back contact. When TCO work function is below 5 eV, the transport of holes is limited because of the occurrence of the band bending in the p-CIGS part. In the case of the TCO work function is higher than 5 eV, the band bending in the p-CIGS absorber part is reduced to form a flat band. The increase in W_{TCO} leads to the decrease of the Schottky barrier height between TCO and p-CIGS layer; therefore more hole carriers can be collected at the front contact.

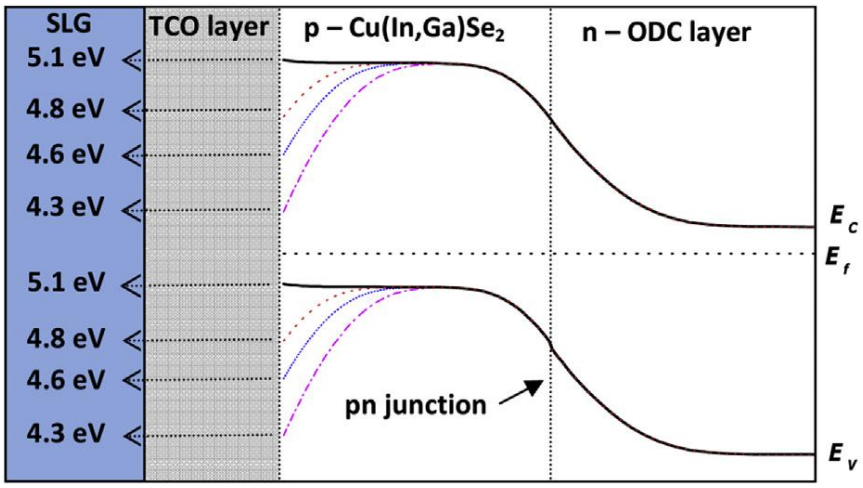

Figure 3.19 Band structure in the TCO/p-CIGS interface with different TCO work functions.

Different TCO work functions at the interface between TCO and p-CIGS layer will lead to different built-in electric field. Figure 3.20 shows the distribution of built-in electric field in the structure as a function of TCO work function. Note that the electric field decreases gradually in the p-CIGS part near the TCO/p-CIGS interface. Nevertheless, in the region of n-ODC layer the built-in electric field keeps unchanged. In the p-CIGS part with $W_{TCO} < 5\ eV$, the built-in electric field is positive near the interface, which hinders holes from reaching the front electrodes. When $W_{TCO} > 5\ eV$, the built-in electric field is negative in the whole of p-CIGS region. This electric field gives the effective force on holes to move to the left region in Figure 3.20, which is very beneficial for holes to transport through the p-CIGS region.

One of the aims of this simulation is to determine the proper work function of TCO front contact for designing high conversion efficiency of superstrate CIGS solar cell. So, it is necessary to calculate the photovoltaic parameters of the solar cell on the wide range of variation of W_{TCO}.

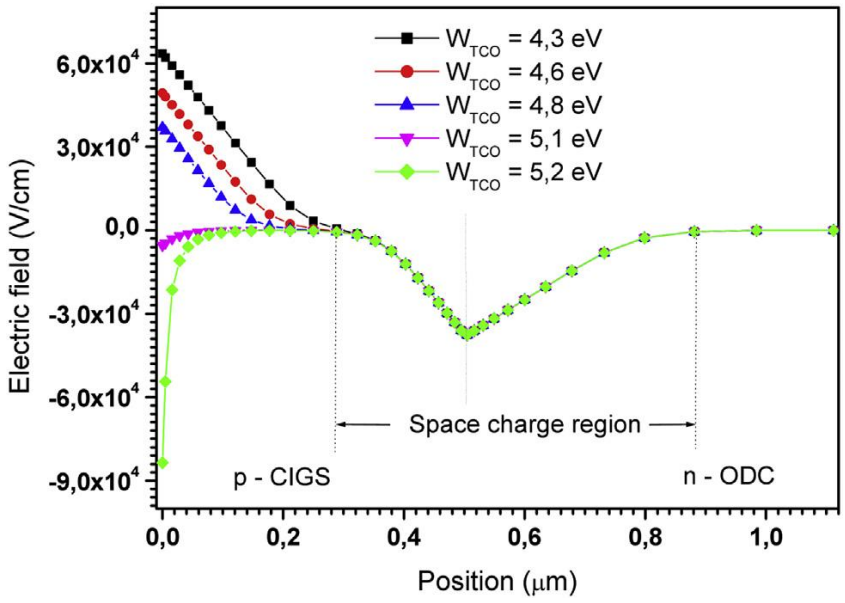

Figure 3.20 Distribution of built-in electric field in the structure with various TCO work functions.

Figure 3.21 shows the simulated performance of SLG/TCO/p-CIGS/n-ODC/n-In_2Se_3/Metal solar cells as a function of TCO work function. It is easy to note that when W_{TCO} is varied between 4.3 and 5.0 eV, the TCO work function has a little impact on J_{SC}. The open-circuit V_{OC} increases rapidly with W_{TCO}, and then become saturated at $W_{TCO} = 4.8\ eV$. As the W_{TCO} increases, FF also increases due to the migration of holes from p-CIGS part to TCO front contact since the hole injection barrier was reduced. Reduction of the band bending was due to the decrease of the electric field at TCO/p-CIGS interface which can provide low leakage current. At $W_{TCO} = 4.8\ eV$, we can achieve an efficiency of about 15.02%, $FF = 80.06\%$, $V_{OC} = 0.63\ V$, $J_{SC} = 29.23\ mA/cm^2$. It is obvious that at $W_{TCO} = 4.3\ eV$, the cell has a poor performance with $\eta = 2.08\ \%$, $FF = 51.4\ \%$, $V_{OC} = 0.13\ V$ and $J_{SC} = 29.21\ mA/cm^2$, while at $W_{TCO} = 5.4\ eV$, the cell has a good performance with $\eta = 20.71\ \%$, $FF = 81.80\ \%$, $VOC = 0.71\ V$ and $JSC = 35.32\ mA/cm^2$. The structure with TCO work function below 4.2 eV does not work at all. This simulation result manifests the critical effect of TCO work function in superstrate CIGS solar cells.

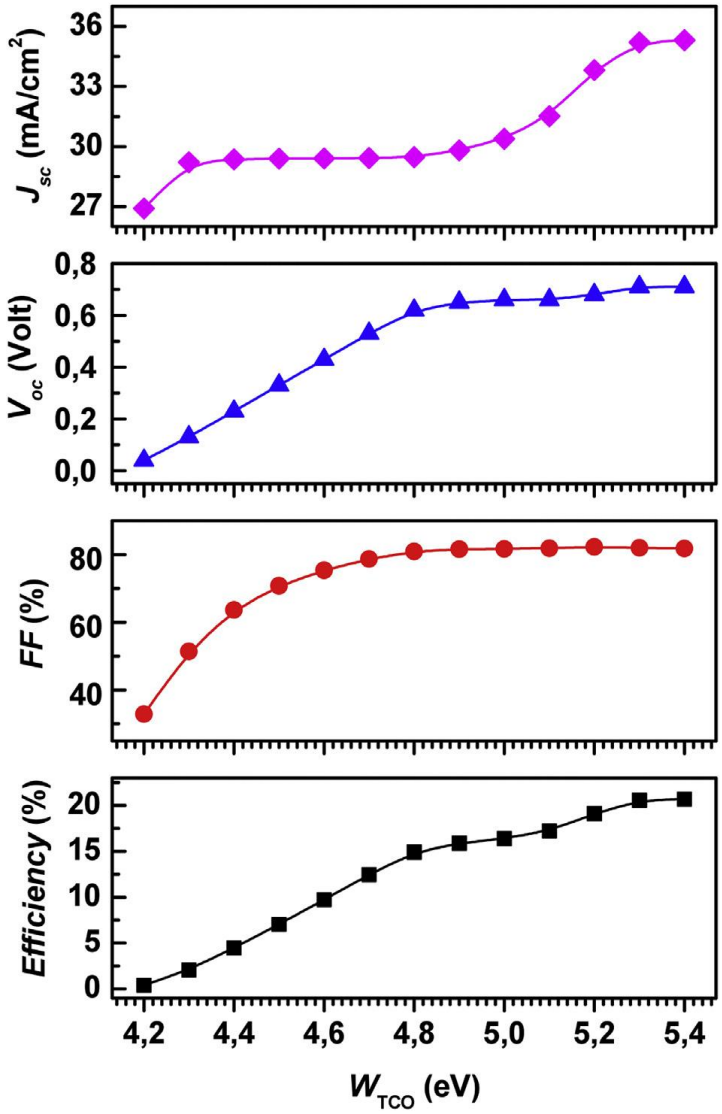

Figure 3.21 Performance of superstrate CIGS solar cells as a function of TCO work function.

The front contact processes are designed to reduce the downward band-bending in the TCO/p-CIGS interface so that the barrier to holes is reduced and current can be collected. Several TCO layers have been tested in the model as a front contact layers for superstrate CIGS solar cells. Figure 3.22 shows the cell-performance results with different TCO front contact layers.

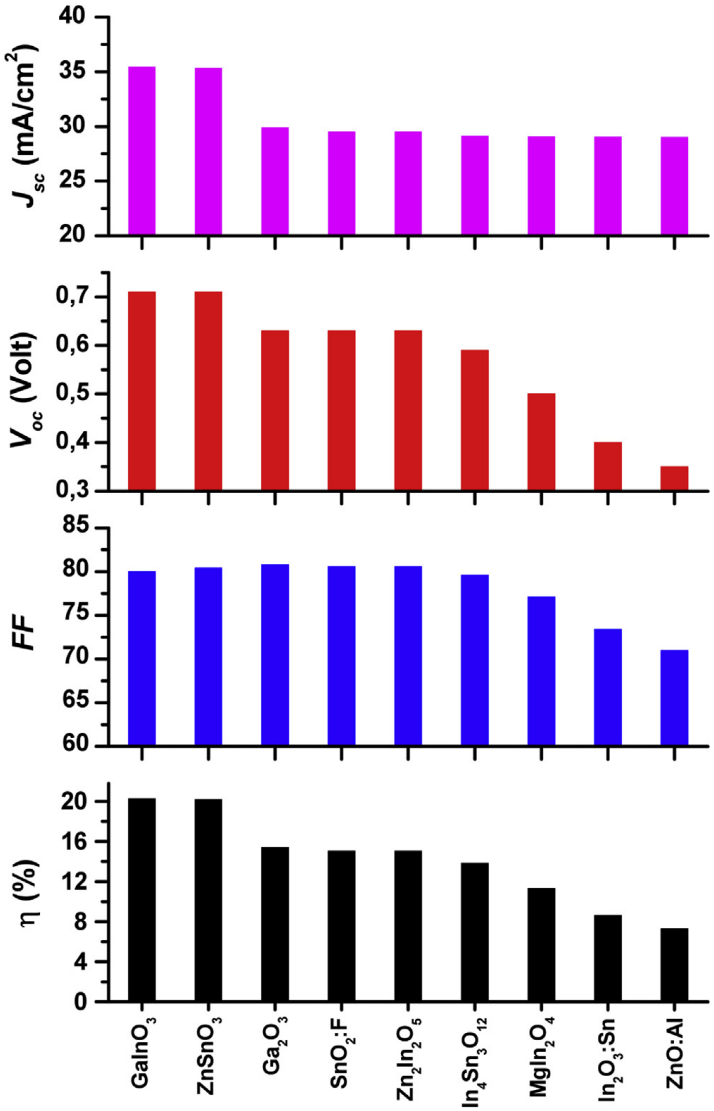

Figure 3.22 A summary results of superstrate CIGS solar cells performances with different TCO films.

$ZnSnO_3$ n-type semiconductor with the wide band gap and high work function of $\sim 5.3\ eV$, considered as a front contact material, is a potential candidate for a good TCO. With $ZnSnO_3$ front contact we can achieve an efficiency of 20.17 %, with $V_{OC} = 0.71\ V$, $J_{SC} = 35.35\ mA/cm^2$ and $FF = 80.4\%$. ITO films have a low work function which is about 4.6 eV. This degrades the conversion efficiency of solar cells to 8.63 %. Solar cell with ZnO:Al front contacts showed also a poor efficiency of 7.31%. The SnO_2:F material with a work function of

$\sim 4.9\ eV$ is another candidate similarly to TCO front contact for superstrate CIGS solar cells presenting an efficiency of 15.06%.

Spectral response of various TCO work functions was studied and presented in Figure 3.23. With increasing W_{TCO}, the spectral response increases in short wavelength region. The quantum efficiency (QE) has a maximum value close to 80% under $100\ mW/cm^2$ when the TCO work function reaches $5.2\ eV$.

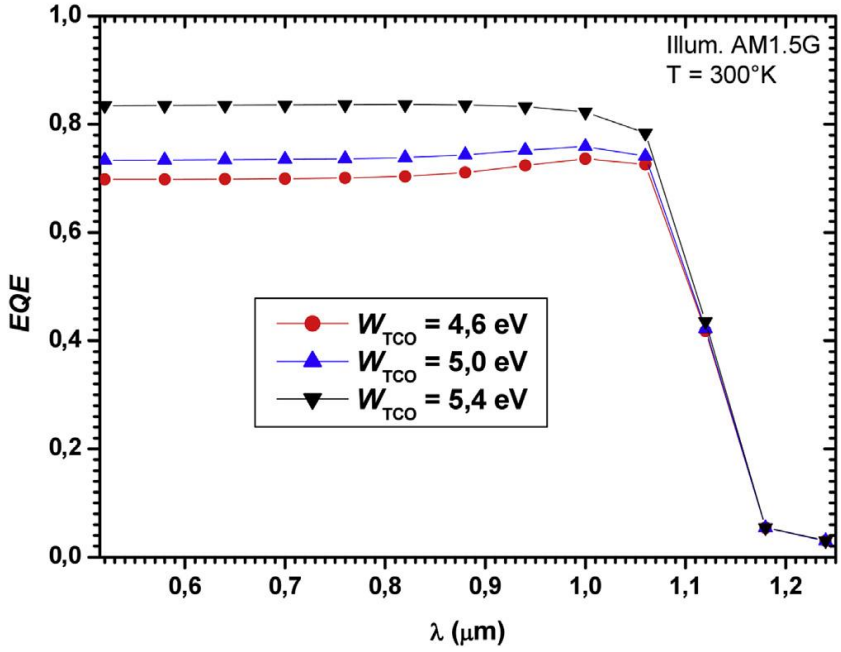

Figure 3.23 Effect of TCO work function on the spectral response.

III.5.3 Effect of back metal work function

The metal back contact forms a barrier to n-type In_2Se_3 semiconductor which depends on the work function of both Metal and n-In_2Se_3 material. If the work function of an n-type In_2Se_3 semiconductor (W_{n-SC}) is greater than that of the Metal (W_{Metal}), $W_{n-SC} > W_{Metal}$, then the n-In_2Se_3/Metal heterojunction forms an ohmic contact. If the relative magnitudes are reversed, i.e. $W_{n-SC} < W_{Metal}$, then the n-In_2Se_3/Metal heterojunction forms a blocking or Schottky barrier [131].

The band bending in the n-In_2Se_3 buffer layer was occurs in the vicinity of the interface. The carrier (electron) transport across n-In_2Se_3/Metal interface is greatly affected by the barrier

height resulting in the n-In_2Se_3/Metal interface. At high Metal work function, the tunneling mechanism through the barrier dominates the current transport with high doping n-type In_2Se_3 semiconductor used in the simulation ($N_D(In_2Se_3) = 1 \times 10^{19} cm^{-3}$), while the thermionic emission acts as a secondary transport mechanism in the n-In_2Se_3/Metal interface. In the case of the thermal emission, the electron has to overcome the whole energy barrier, however, the tunneling takes place through the energy spike resulting in the n-In_2Se_3/Metal interface. The barrier height $\emptyset_b$ is defined as the potential difference between the Fermi energy of the metal and the band edge where the majority carrier reside. For n-type In_2Se_3 semiconductor the barrier height is obtained as [132]: $\emptyset_b = W_{Metal} - \chi_{In_2Se_3}$ where W_{Metal} is the work function of the metal and $\chi_{In_2Se_3}$ is the electron affinity of the n-In_2Se_3 semiconductor.

Figure 3.24 shows the work function of selected metals and their calculated barrier height on n-In_2Se_3 part, where the metal work functions varied between 4.1 and 5.2 eV. We can see that the barrier height in the n-In_2Se_3/Metal interface can be varied from 0.2 to 1.3 eV by using various metals.

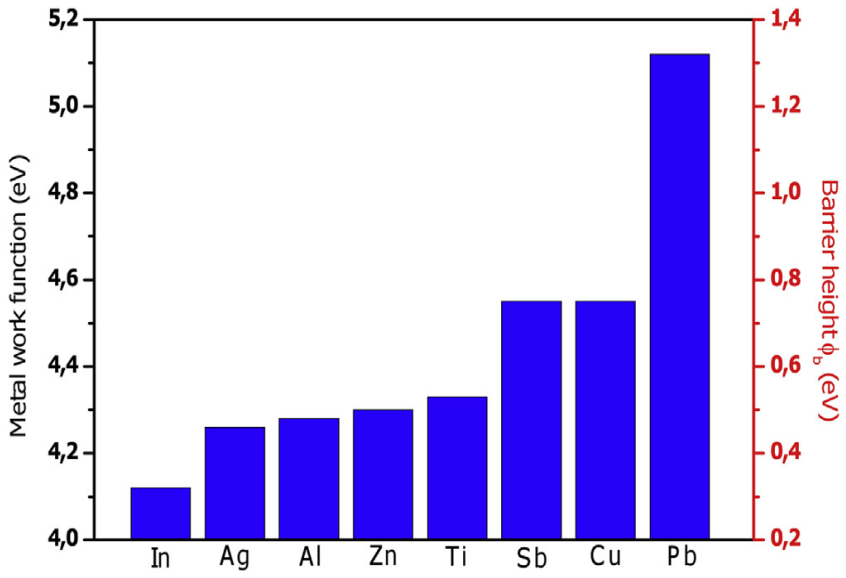

Figure 3.24 Work function of selected metals and their calculated barrier height on n-type In_2Se_3 buffer layer.

To find the influence of the barrier height $\emptyset_b$, on cell performance, we have firstly varied the value of $\emptyset_b$ from 0.46 to 0.6 eV and the simulated current density-voltage (J-V)

characteristics are shown in Figure 3.25. The results of the calculation were obtained by using SnO_2:F as a TCO front contact layer. It is evident from the behavior of the curves that only the fill factor FF was degraded with increasing the barrier height $\emptyset_b$. This may be due to the increase in the resistance and the presence of the rectifying n-In_2Se_3/metal junction which forms a Schottky barrier in the structure (Figure 3.25). The high potential barrier prevents most charge carriers (electrons) from passing to the metal back contact. Only a small number of carriers have enough energy to overcome the whole energy barrier (thermionic emission), however, the tunneling effect takes place in some cases. To clarify this dependence in an interval of variation, the barrier height $\emptyset_b$ was varied from 0 to 0.9 eV.

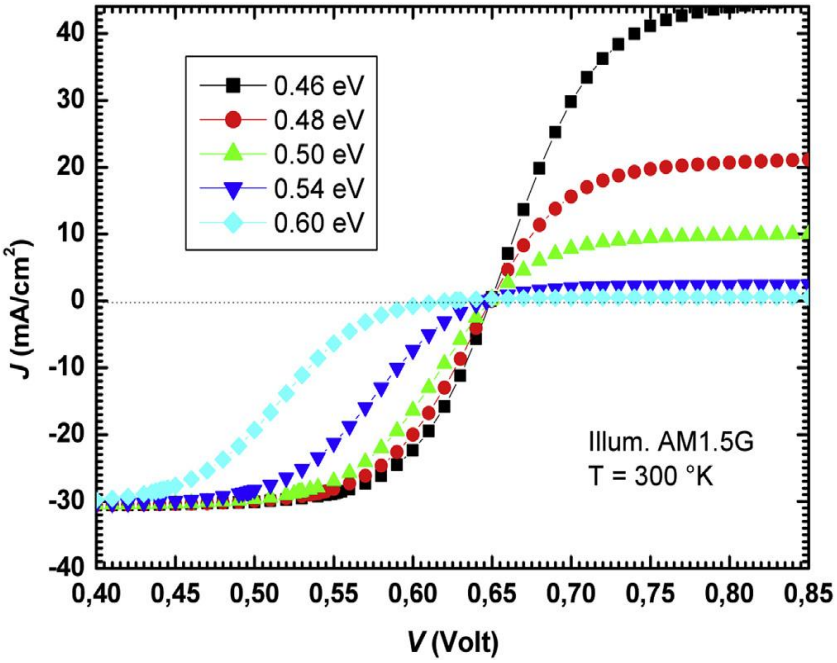

Figure 3.25 J-V characteristics of the selected structure with different barrier heights ϕ_b.

Figure 3.26 summarizes the output performance of J_{SC}, V_{OC}, FF and η as a function barrier height ϕ_b. All photovoltaic parameters remain almost constant for barrier height below 0.4 eV. By an increase in ϕ_b of more than 0.4 eV an incredible decrease in efficiency, $V_{OC}$and FF was found as revealed from Figure 3.26. In this case, the majority carriers have insufficient energy to overcome the potential barrier, and are trapped on back side of the interface and cannot contribute to the diffusion current, reducing thus the solar cell performance. It is evident from Figure 3.26 that the short-circuit current J_{SC} has a slight decrease as the ϕ_b increases from

0.4 to 0.9 eV, which may be due to the tunneling enhancement. The use of SnO_2:F front contact and Zn back contact layers in the structure reported in Ref. [127] led to an efficiency of 15.12%, with $V_{OC} = 0.63\ V$, $J_{SC} = 31.4\ mA/cm^2$ and $FF = 74.6\%$. Using low metal work function as a metal back contact, such as indium (4.12 eV), a best efficiency of 16.31%, with $V_{OC} = 0.64\ V$, $J_{SC} = 31.4\ mA/cm^2$ and $FF = 79.4\ \%$, has been obtained.

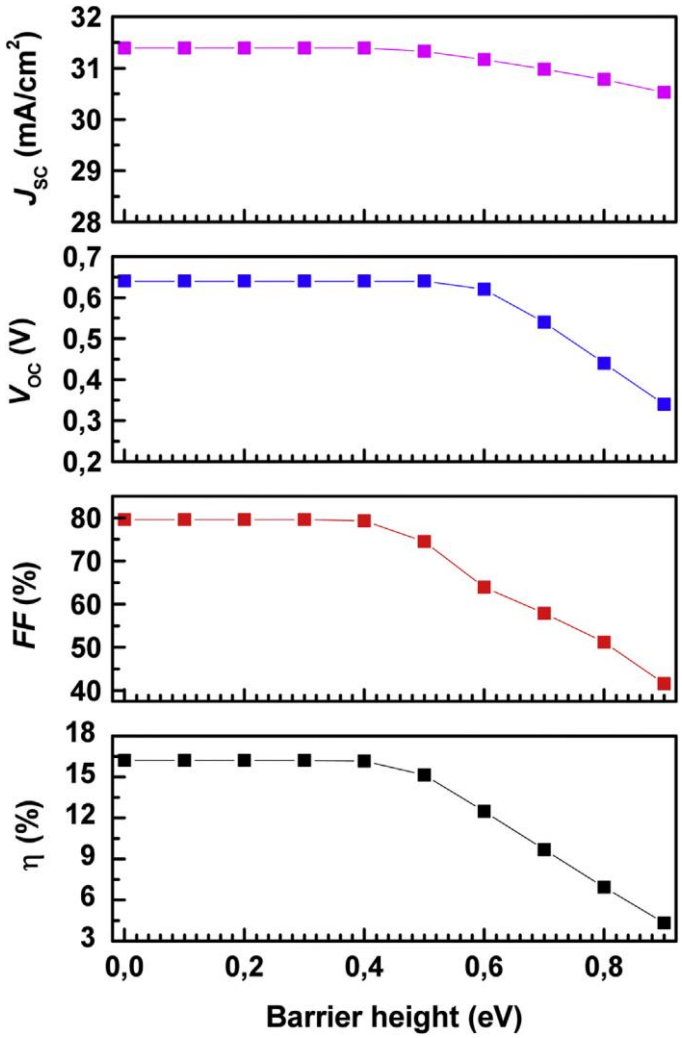

Figure 3.26 Solar cell performances as a function of barrier height at the n-In_2Se_3/Metal interface.

III.6 Summary

In summary, three structures of heterojunction solar cells were numerically optimized using AMPS-1D simulator. The photovoltaic parameters of ZnO/Si/Cu_2O, HGMZO/LGMZO/ CdTe/$MoTe_2$ and TCO/p-CIGS/n-ODC/n-In2Se3 were extracted from the J-V curves under AM1.5G illumination. We studied the effect of thicknesses, the carrier (donor/acceptor) concentration, the defect density, the work function and the operating temperature on the overall performance of studied cells.

CHAPTER IV

ELABORATION AND CHARACTERIZATION OF PURE AND DOPED ZINC OXIDE THIN FILMS VIA SPIN COATING METHOD

IV.1 Introduction

In the fourth chapter we will present the fabrication and characterization of pure and Mg-doped ZnO (or $Mg_xZn_{1-x}O$ with $x = 2\%, 4\%, 5\%$) thin-films using Sol-Gel spin coating method. The starting materials, the experimental conditions, the processing steps using sol-gel spin-coating technique to deposit the thin films on glass substrates will be displayed in details. After, the structural, morphological and optical properties of the obtained samples will determined using X-ray diffraction (XRD), scanning electron microscopy (SEM), atomic force microscopy (AFM), energy dispersive spectroscopy (EDS) and UV-Visible spectroscopy methods, respectively. Optical transmission spectra will used to determine absorption coefficient and gap energy of the samples. Finally, we discuss the results obtained. During the exposition, we will shed light on the feasibility of the obtained properties for solar cells.

IV.2 Fabrication of Pure and Doped ZnO Thin Films

In this section, the sol-gel synthesis of pure (undoped) and Mg-doped ZnO thin films will be presented. The starting materials and conditions for the ZnO sol preparation, the spin-coating of pure and Mg-doped ZnO layers on glass substrates, and the film curing and annealing have been set forth broadly.

Therefore, the spin coating of films is performed through three main steps:

- Preparation of starting solution (precursor sol);
- Film deposition on rotating glass substrate;
- Heating treatment (drying and annealing) for obtaining the desired film.

IV.2.1 Starting materials

The starting materials and their physical and chemical proprieties, which were used in ZnO sol preparation are:

***Zinc acetate dihydrate (ZAD) used as zinc precursor*:**

Chemical formula: $Zn(CH_3COO)_2 \cdot 2H_2O$.
Appearance: White crystalline solid.
Melting point: 237°C.
Molar mass: 219.49 g/mol.
Density at 20°C: 1.74 g/cm³.
Solubility in water at 20°C: 430 g/l.

Magnesium chloride hexahydrate used as Mg dopant precursor:

Chemical formula: $MgCl_2.6H_2O$.
Appearance: White crystalline solid.
Melting point: 237°C.
Molar mass: 203.307 g/mol.
Density at 20°C: 1.57 g/cm³.
Solubility in water at 20°C: 2350 g/l.

Isopropanol (2-propanol) alcohol used as solvent:

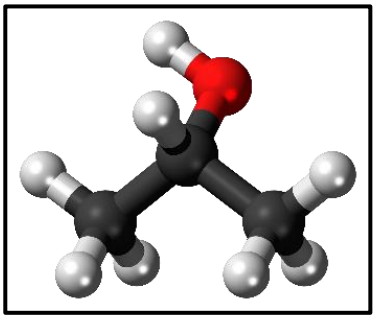

Chemical formula: $CH_3CH(OH)CH_3$.
Appearance: Colorless liquid.
Molar mass: 60.1 g/mol.
Density: 0.786 g/cm³.
Boiling point: 82.2°C.

Monoethanolamine (MEA) used as a stabilizer or additive:

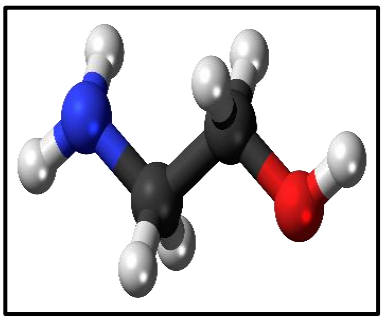

Chemical formula: $NH_2CH_2CH_2OH$.
Appearance: Colorless, clear liquid.
Molar mass: 61.08 g/mol.
Density: 1.01 g/cm³.
Boiling point: 170°C.

IV.2.2 Preparation of ZnO sol

Figure 4.1 and Table 4.1 summarize the flow diagram and starting materials for synthetizing zinc oxide sol for synthetizing pure and Mg-doped thin films.

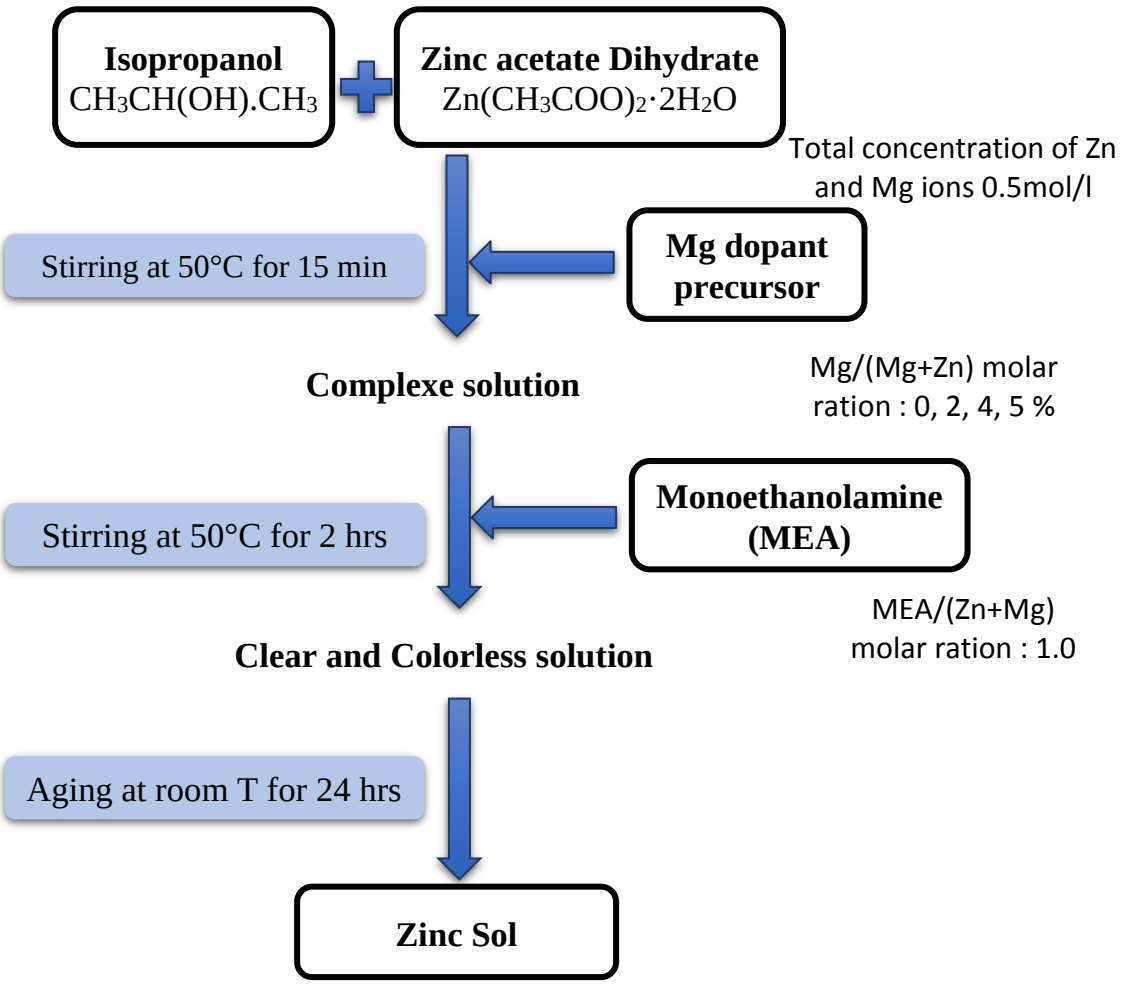

Figure 4.1 Flowchart for preparing zinc sol.

Table 4.1 Summary table of different materials used in preparation of ZnO sol for both pure and Mg-doped ZnO thin films

Molarity (M) of final ZnO solution	**(mol/l)**	0.5	0.5	0.5	0.5
Percentage of $MgCl_2.6H_2O$	**(%)**	0	2	4	5
Mass of Zinc acetate	**(g)**	1.0974	1.0755	1.0535	1.0425
Mass of $MgCl_2.6H_2O$	**(g)**	0	0.0203	0.0406	0.0508
Volume of Isopropanol solvent	**(ml)**	9.0669	9.0665	9.0662	9.0660
Volume of stabilizer solvent (MEA: $H_2NCH_2CH_2OH$)	**(ml)**	0.3023	0.3023	0.3023	0.3023
Volume of final ZnO solution	**(ml)**	10	10	10	10

Therefore, zinc oxide sol was prepared from zinc acetate dihydrate [ZAD: ($Zn(CH_3COO)_2.2H_2O$)] precursor. Monoethanolamine [MEA: $H_2NCH_2CH_2OH$], Isopropanol [2-Propanol: $CH_3CH(OH)CH_3$] and Magnesium chloride hexahydrate [$MgCl_2.6H_2O$] were used as a stabilizer, solvent and source or precursor of Mg dopants, respectively. Magnesium chloride hexahydrate as a source of Mg dopant, which defined by Mg/(Mg+Zn) ratio and took the percentages 0, 2, 4 and 5 mol%, and Zinc acetate dehydrate with 0.5 mol/L for pure ZnO film were dissolved in isopropanol and continuously heated with magnetic stirrer for 15 minutes at 50°C fixed temperature. The doped mixture solutions had a concentration of Zn and Mg metal ions of 0.5 mol/L. After that MEA was added drop-by-drop to the alcoholic solution and was continuously heated with magnetic stirrer for 2 hours at same temperature while maintaining the molar ratio of MEA to metal ions at 1.0. The yielded solutions, which were clear and colorless were kept for aging for 24 hours at room temperature.

IV.2.3 Glass substrate cleaning and chemical treatment

The substrates used in our work are glass slides (Figure 4.2). This choice allows us to perform a good optical and electrical characterizations of the obtained films. The cleaning of the substrates is a very important step, because this step determines the qualities of adhesion and homogeneity of the deposited layers, as well as the uniformity of their thicknesses. The glass substrates were cleaned carefully in beaker with dilute HCl and acetone for 10 min each by using an ultrasonic cleaner and then rinsed in distilled water and dried. Substrates are then stored away from dust.

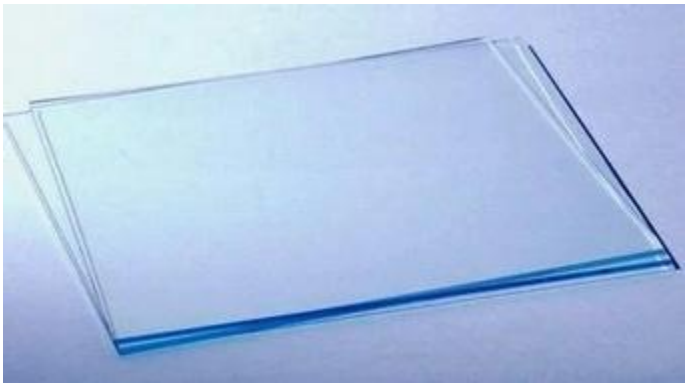

Figure 4.2 Glass substrates.

IV.2.4 ZnO thin films production and spin-coating

The depositions of ZnO samples onto glass substrates are carried out using a spin coater assembly, which is shown in Figure 4.3.

Figure 4.3 Spin coater assembly.

Figure 4.4 shows the flow diagram for preparing pure and Mg-doped ZnO thin films. Following the these diagram, the spin coating of a sample is made by disturbing uniformly few drops of the prepared ZnO sol over the surface of the substrate, which is fixed on a rotary support of a spin coater (see Figure 2.7 in chapter II) of controlled speed with a rate of 3000 rpm for 30s. After the deposition, the sample is drying at 250°C for 4 minutes in a furnace to evaporate the solvent and remove organic residuals.

The spin-coating process together drying (preheating) were repeated a 10 times to acquire a film with considered (multilayers) thickness. Finally, these films were annealed at 500°C for 90 minutes under air ambiance to obtain crystallized ZnO.

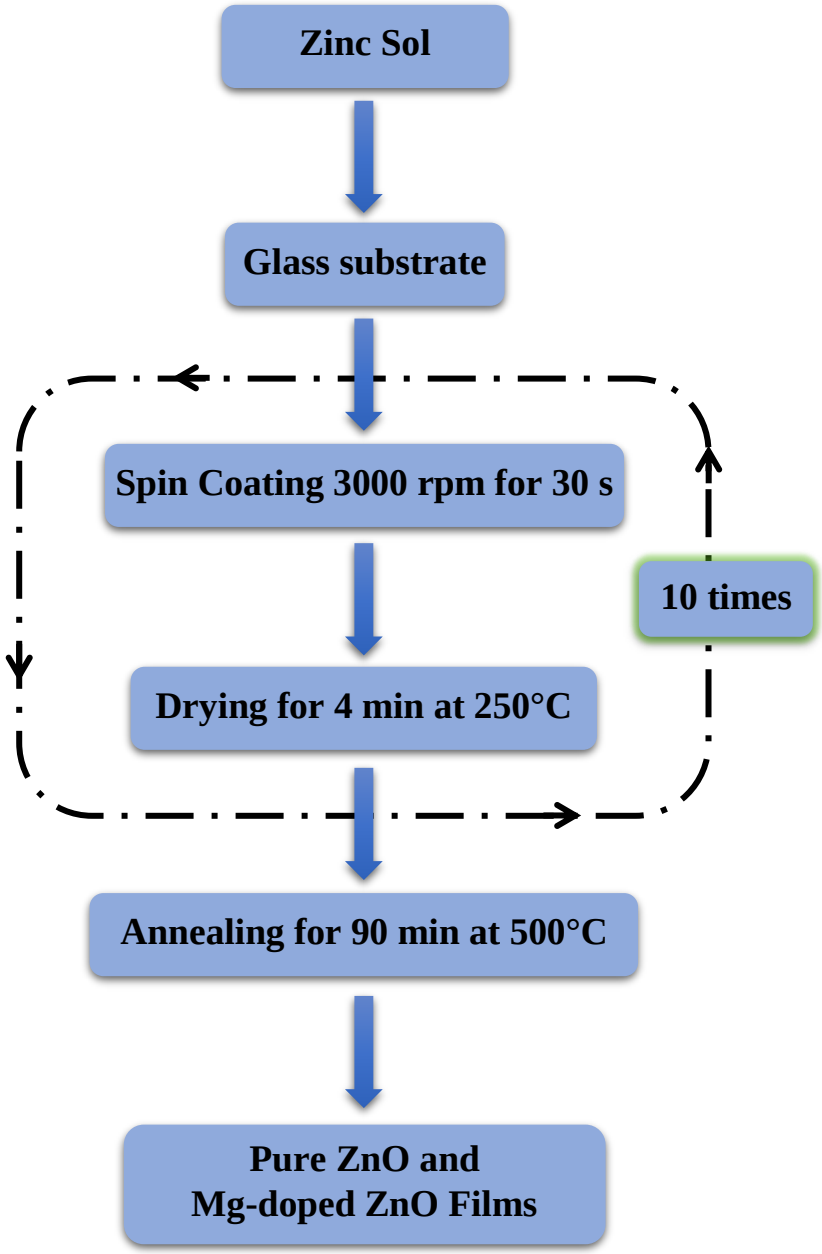

Figure 4.4 Flowchart of synthesis of pure and Mg-doped ZnO films by spin-coating process.

IV.3 Characterization of Coated Thin Films

IV.3.1 Structural characterization using X-ray diffraction technique

An X-ray diffraction (XRD) device is one of the most available tools to examine the crystallographic structures of the deposited materials.

As shown in Figure 4.5 (a), when X-rays of electromagnetic radiation strike a crystal at an angle (θ), a constructive interference and a peak in the reflection intensity are observed in which the Bragg's law is confirmed [133].

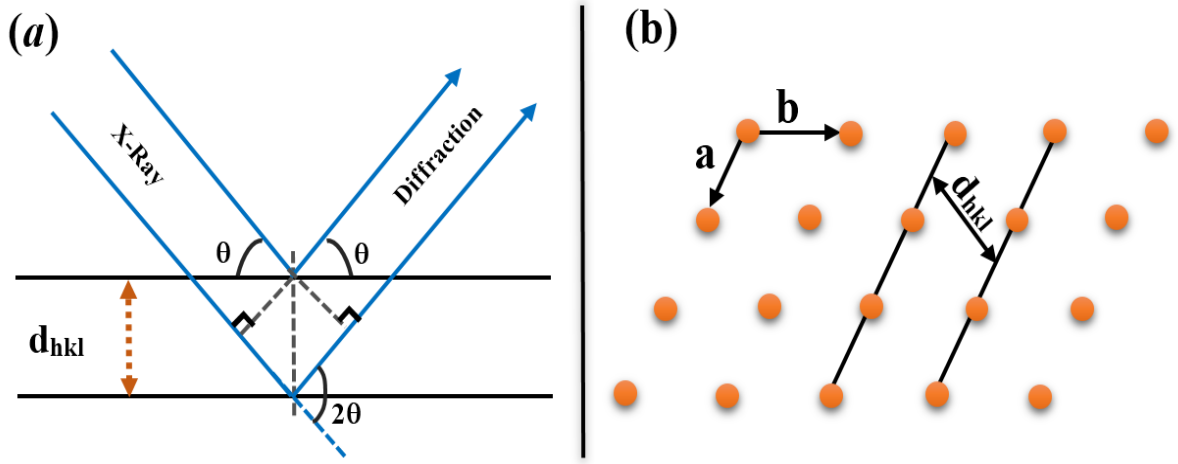

Figure 4.5 Schematic illustration of **a)** the X-ray diffraction principal and **b)** the Distance (d_{hkl}) between two reticular planes.

Therefore, the Bragg's law links the distance (d_{hkl}) between the two parallel reticular planes (Figure 4.5 (b)), the wavelength (λ) of the X-rays and the diffraction angle (θ) (Figure 4.5 (a)) in the following equation (4.1) [133]:

$$2d_{hkl}\, sin(\theta) = n\lambda \qquad (4.1)$$

❖ Lattice constant

In the hexagonal structure, we are looking at the cell parameters: ($a = b$) and (c), which are calculated from the Bragg's law (4.1) and the following equation of the hexagonal system (4.2) [134]:

$$\frac{1}{(d_{hkl})^2} = \frac{4}{3}\left[\frac{h^2+hk+k^2}{a^2}\right] + \frac{l^2}{c^2} \quad (4.2)$$

In which
- d_{hkl} – inter-reticular distance,
- hkl – Miller indices,
- θ – Diffraction angle of Bragg,
- λ – Wavelength of incident radiation CuKα (λ = 1,54056 Å),
- a, c – Lattice parameters (constants) of the hexagonal crystal,
- n – Number of the diffraction peaks.

According to (4.1) and (4.2) formulas, it can be determined (a) and (c) by tacking the (100) and (002) XRD peaks [134],

$$a = \frac{\lambda}{\sqrt{3}sin(\theta_{100})} \text{ (Å)}$$
$$c = \frac{\lambda}{sin(\theta_{002})} \text{ (Å)} \quad (4.3)$$

❖ Average crystallite size

An ideal crystal direction within the meaning of diffraction would be infinite in all three directions in space. No crystal is perfect because of its finite size. The diffraction peaks broaden as the crystallite size decreases. The equation of the Scherrer formula (4.4) links the average crystallite size (D) and the width (β) of a dominant diffraction peak at an angle (2θ) [135]:

$$D = \frac{K\lambda}{\beta\ cos(\theta)}\ (nm) \quad (4.4)$$

In which	D	– Average crystallite size in the perpendicular direction to the planes (hkl),
	K	– Scherrer constant (0.87~1) ,
	θ	– Bragg's diffraction angle (radians),
	λ	– Wavelength of X-ray CuKα (λ = 1,54056 Å),
	β	– Full width at half maximum (FWHM).

❖ **Preferred orientation**

In order to make a quantitative evaluation of preferred orientation of a crystalline material, the texture coefficient (TC_{hkl}) is used. This factor is expressed as following (4.5) [135]:

$$TC_{hkl} = \frac{I(hkl)/I_0(hkl)}{\frac{1}{n}\sum_1^n I(hkl)/I_0(hkl)} \quad (4.5)$$

In which	TC_{hkl}	– Texture coefficient of (hkl) plane,
	$I(hkl)$	– Measured intensity of (hkl) plane obtained from the film,
	$I_0(hkl)$	– Standard intensity (JCPDS data card 36-1451),
	n	– Number of diffraction peaks.

A layer with randomly oriented crystallites presents a TC_{hkl} = 1, while the values of this factor is greater than 1 indicate the abundance of crystallites in a given (hkl) direction.

❖ **Average lattice strain**

The effect of lattice strain (ε) is interpreted on the XRD patterns by the enlargement of the integral width (β) of the diffraction peaks. This lattice strain is calculated from the following trigonometric equation (4.6) [135]:

$$\varepsilon = \frac{\beta}{4}\cos(\theta) \quad (4.6)$$

When the lattice strain is presented, the calculated crystallite size will tend to decrease depending on the (2θ) values. When the crystallite size is enlarged, the calculated lattice strain will tend to decrease depending on the (2θ) values.

❖ **Dislocation density**

The dislocation density ($\delta = (1/D^2)$ $(ligne/m^2)$) is a linear defect which corresponds to a discontinuity in the crystal structure [135].

IV.3.2 Influence of Mg dopant on crystallographic of ZnO samples

The crystallographic structures of the elaborated pure and Mg doped zinc oxide simples were examined by high-resolution X-ray diffraction using CuKα radiation, where λ = 0.15406 nm (D8 Advance Bruker system device).

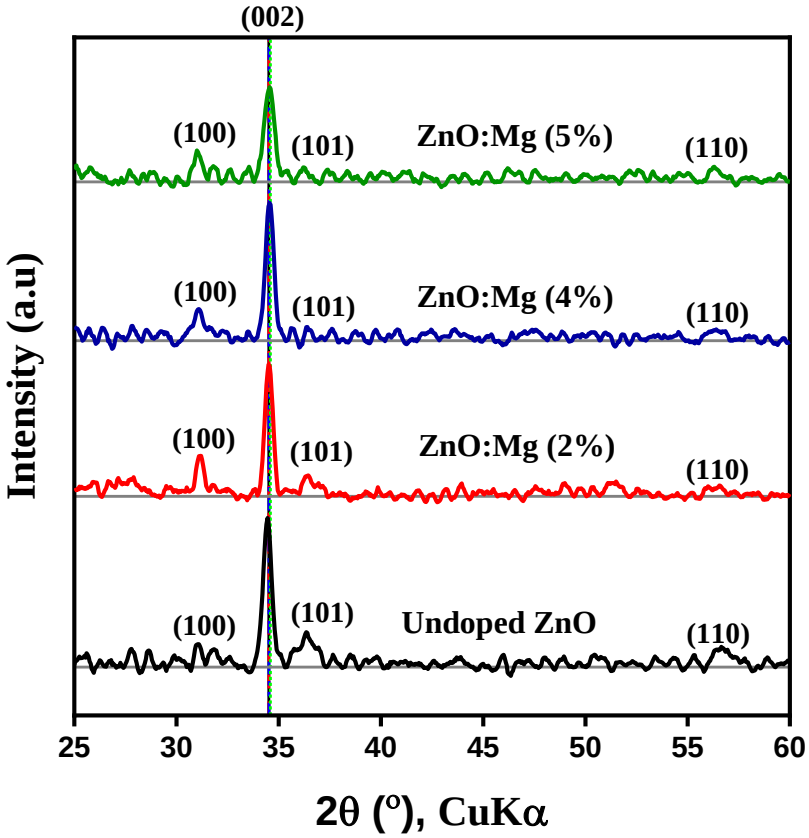

Figure 4.6 Two-dimensions XRD patterns of pure and Mg-doped ZnO (2%, 4%, 5%) films.

Figure 4.6 and Figure 4.7 show the recorded (Two-dimensions) and (Three-dimensions) XRD patterns of pure ZnO and Mg-doped ZnO (2%, 4%, 5%) films deposited on glass substrates by sol-gel spin-coating method indexed in terms of intensity versus angular position (2θ) between [25° − 60°] by using the Xpert-HighScore software. The shown plots revealed the analysis of these recorded patterns, which may be affording the following information: identification of phases, preferred orientation, lattice constants (a) and (c), average crystallit size (D), lattice strain (ε), and dislocation densities (δ), as well the measurable values extracted by these information of the coated simples are listed in Table 4.2.

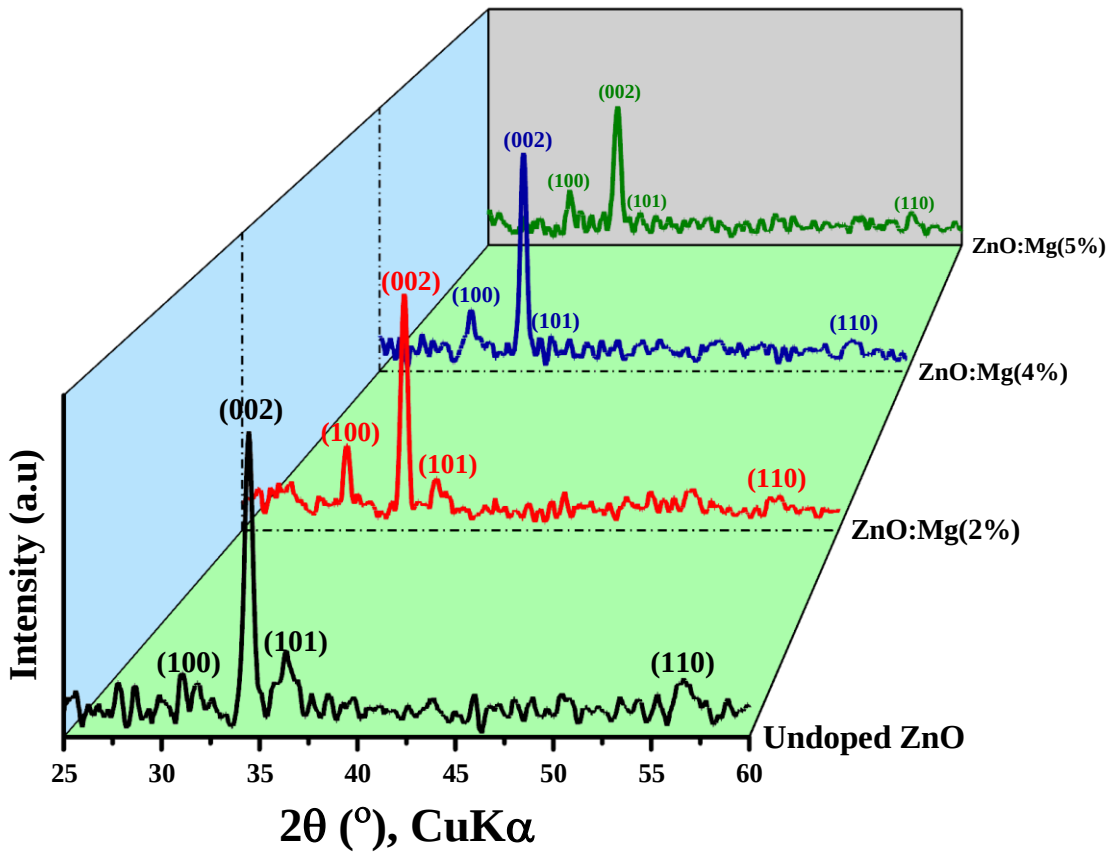

Figure 4.7 Three-dimensions XRD patterns of pure and Mg-doped ZnO (2%, 4%, 5%) films.

It is observed that miscellaneous peaks were recorded for all four simples: (100), (002), (101) and (110) planes around 31.7°, 34.5°, 36.4°, and 56.5°, respectively. These peaks were indexed by JCPDS card. N° 36-1451, which presented in Figure 4.8. They are clearly indicated that all coated samples have a wurtzite hexagonal structure. No extra peaks from impurities (Mg, Zn or MgO) were detected after adding Mg dopant into ZnO matrix. This implies that the films are in the form of a single phase of ZnO and do not change their structure. The (002) peaks were prominent and narrow, showing that the films have polycrystalline nature and that the Mg ions are incorporated into the ZnO lattice [134,135].

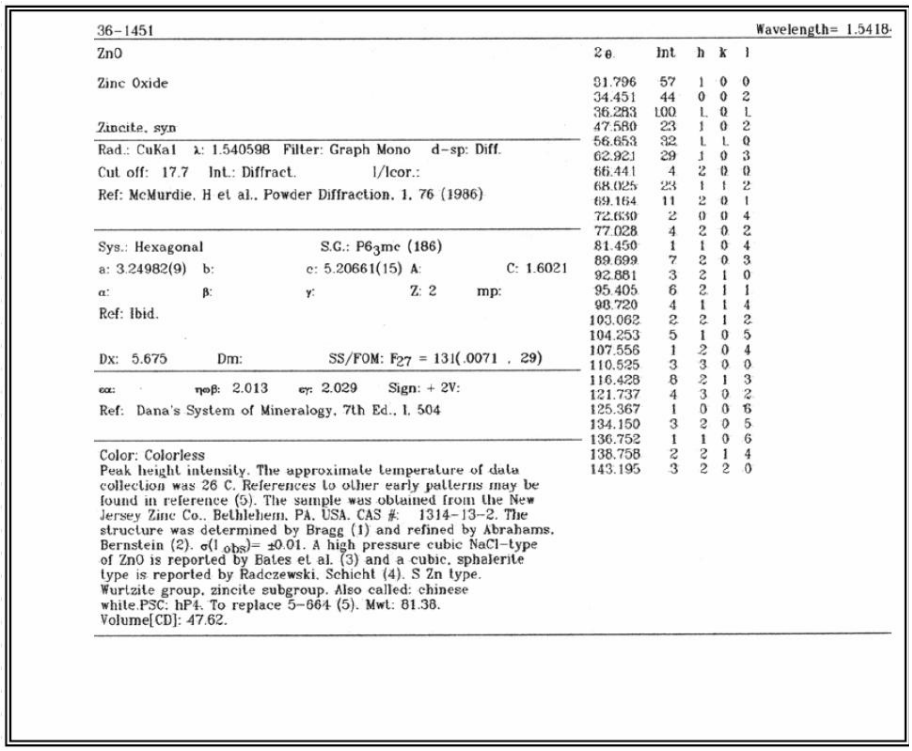

36-1451 Wavelength= 1.5418

ZnO

Zinc Oxide

Zincite, syn

Rad.: CuKa1 λ: 1.540598 Filter: Graph Mono d-sp: Diff.

Cut off: 17.7 Int.: Diffract. I/Icor.:

Ref: McMurdie, H et al., Powder Diffraction, 1, 76 (1986)

Sys.: Hexagonal S.G.: $P6_3mc$ (186)

a: 3.24982(9) b: c: 5.20661(15) A: C: 1.6021

α: β: γ: Z: 2 mp:

Ref: Ibid.

Dx: 5.675 Dm: SS/FOM: F_{27} = 131(.0071 , 29)

ωα: ηωβ: 2.013 εγ: 2.029 Sign: + 2V:

Ref: Dana's System of Mineralogy, 7th Ed., I, 504

Color: Colorless

Peak height intensity. The approximate temperature of data collection was 26 C. References to other early patterns may be found in reference (5). The sample was obtained from the New Jersey Zinc Co., Bethlehem, PA, USA. CAS #: 1314-13-2. The structure was determined by Bragg (1) and refined by Abrahams, Bernstein (2). $\sigma(I_{obs})$= ±0.01. A high pressure cubic NaCl-type of ZnO is reported by Bates et al. (3) and a cubic, sphalerite type is reported by Radczewski, Schicht (4). S Zn type. Wurtzite group, zincite subgroup. Also called: chinese white.PSC: hP4. To replace 5-664 (5). Mwt: 81.38. Volume[CD]: 47.62.

2θ	Int	h	k	l
31.796	57	1	0	0
34.451	44	0	0	2
36.253	100	1	0	1
47.560	23	1	0	2
56.653	32	1	1	0
62.921	29	1	0	3
66.441	4	2	0	0
68.025	23	1	1	2
69.164	11	2	0	1
72.630	2	0	0	4
77.028	4	2	0	2
81.450	1	1	0	4
89.699	7	2	0	3
92.881	3	2	1	0
95.405	6	2	1	1
98.720	4	1	1	4
103.062	2	2	1	2
104.253	5	1	0	5
107.556	1	2	0	4
110.525	3	3	0	0
116.428	8	2	1	3
121.737	4	3	0	2
125.367	1	0	0	6
134.150	3	2	0	5
136.752	1	1	0	6
138.758	2	2	1	4
143.195	3	2	2	0

Figure 4.8 JCPDS card. N° 36-1451.

As recorded in Table 4.2, the narrow (002) peaks located around ($2\theta \sim 34{,}5°$) showed a texture coefficients (TC_{hkl}) higher than that of the other recorded main peaks (100) and (101), this observation indicates that the phase reflection of the preferential growth is following the (002) plane along the c-axis perpendicular to the plane of the substrate surface for all simples. Similar results have been reported in Ref. [135].

Table 4.2 XRD Analyzed data for pure and Mg-doped ZnO (2%, 4%, 5%) films.

Sample		**pure ZnO**	**2% of Mg**	**4% of Mg**	**5% of Mg**
2θ **(degree)**		34.5123	34.5135	34.5251	34.5889
TC_{hkl}	**(100)**	0.34	0.14	0.24	0.34
	(002)	2.92	2.51	3.14	2.54
	(101)	0.49	0.38	0.21	0.28
D **(nm)**		18.22	34.29	35.57	21.11
Cell parameter (Å)	$a = b$	3.2438	3.2478	3.2603	3.2411
	c	5.1933	5.1932	5.1914	5.1821
	c/a	1.6009	1.5989	1.5923	1.5989
ε ***10^{-2}**		0.202	0.222	0.182	0.243
δ ***10^{15}** ($ligne/m^2$)		2.758	3.337	2.233	3.970
Roughness (nm)		26.3	32.3	48.2	82.9

Figure 4.9 reveals that the increase of Mg dopant amount causes gradually decreasing in the peak intensity of (002) plane lower than the intensity of pure ZnO, indicating low structure factor of (002) plane oriented perpendicular to X-ray flux, hence decreasing the (c) lattice parameter from 5.1932 Å for Mg doping (2%) to 5.1821 Å for Mg doping (5%) lower than (5.1933 Å) for pure ZnO sample, as listed in Table 4.2. These reverse trend indicates that Mg^{+2} ions are successfully incorporated into ZnO matrix. The incorporation of Mg to substitute Zn is expected to tighten the lattice parameters of ZnO and to create tensile force on c-axis, because the ion radius of the Mg^{+2} ion (0.57 Å) is slightly smaller than that of the Zn^{+2} ion (0.60 Å). Similar results were reported by Rouchdi et al. [135] for Mg-doped ZnO prepared

using spray pyrolysis route and by Ramin et al. [136] for Mg-doped ZnO prepared using sol-gel route.

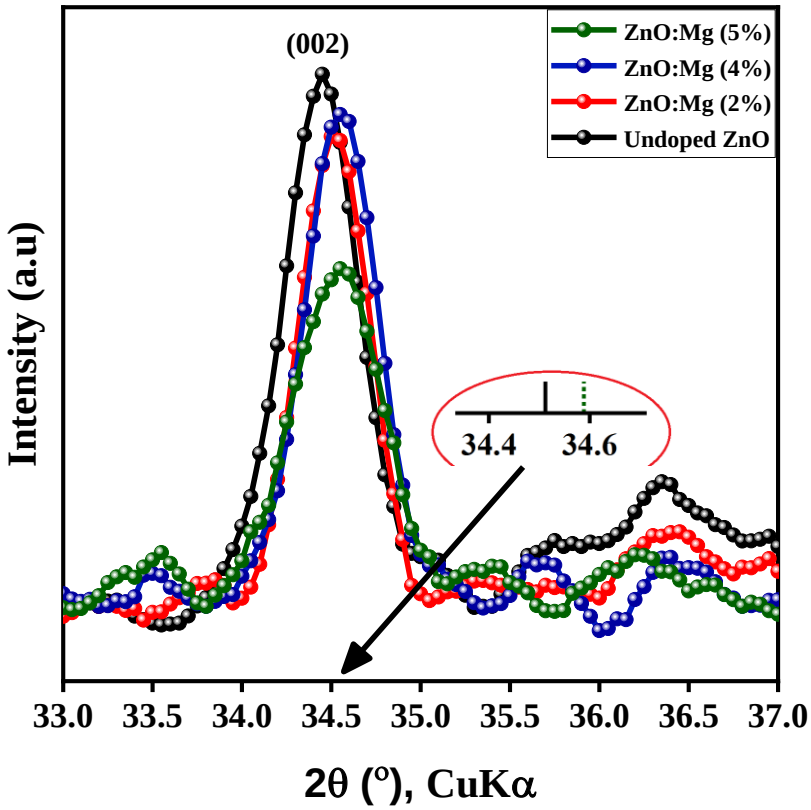

Figure 4.9 Shift of angular position of (002) peak versus 2θ of pure and Mg-doped ZnO (2%, 4%, 5%) films.

Also, it is observed from the plots of pure ZnO simple in Figure 4.3 that the peak intensity of (101) plane is higher than that of (100) plane, on the contrary the peak intensity of (100) plane of Mg doped ZnO simples is higher than that of (101) plane, which is attributed to the good crystal quality of ZnO crystal. Similar results were reported in [136].

Form Figure 4.9, it is noticed that as Mg dopants amount increases, the angular position of (002) peaks shifts toward higher angles with respect to pure ZnO sample, and this shift adheres with diffusion and replacement of Zn^{+2} (0.60 Å) ion in hexagonal lattice by Mg^{+2} (0.57 Å) ion indicating that the lattice parameters of doped samples are smaller than of pure

ZnO sample [137]. The shift in angular position indicated that the Mg^{2+} has successfully been substituted into the host system at Zn^{2+} position.

It is also observed from Table 4.2 that as the Mg dopants amount increases, the value of average crystallite size (D) increases starting from $18.22\ nm$ to $34.29\ nm$ to $35.57\ nm$, which are recorded for pure, Mg-doped (2%) and Mg-doped (4%) ZnO samples, respectively. For Mg-doped ZnO (5%) the average crystallite size (D) decreased to $21.11\ nm$. The ratio (c/a) remains at the same value (~ 1.6) for all samples slightly below than the ideal ZnO (c/a) ratio (1.633), indicating that the hexagonal symmetry is well preserved upon Mg doping.

In addition, it is noticed that the crystal defect parameters are wobbling between the increase and decrease with increase Mg doping. This behavior could explained because of the presence of dislocations and lattice strain in the films due to the Mg doping.

It is also observed from Table 4.2 that as the Mg dopants amount increases, the value of surface roughness increases. This increasing trend may be attributed to the larger crystalline formation and more porosity of the films surface.

IV.4 Morphological Properties of Obtained Films

Figure 4.10 (a), (b), (c) and (d) show the top view SEM images of pure ZnO and Mg (2%, 4%5%) doped ZnO films synthetized by sol gel spin coating process on glass substrates.

Those figures indicate that all films are covered by nanometer crystals, which are extremely dense, homogenous, uniformly distributed and even no pinholes or cracks over all the area. It is shown that the surface morphology of the films is very sensitive to the Mg dopant concentration. In Figure 4.10 (a), the crystallite size is small for pure ZnO sample. While for Mg-doping with 2% and 4% (Figure 4.10 (b and c)), the samples contain large crystallites (as described in Table 4.2). For further Mg-doping (5%), it seems that the crystals break into smaller size (Figure 4.10 (d)). Similar results were observed in Ref. [137].

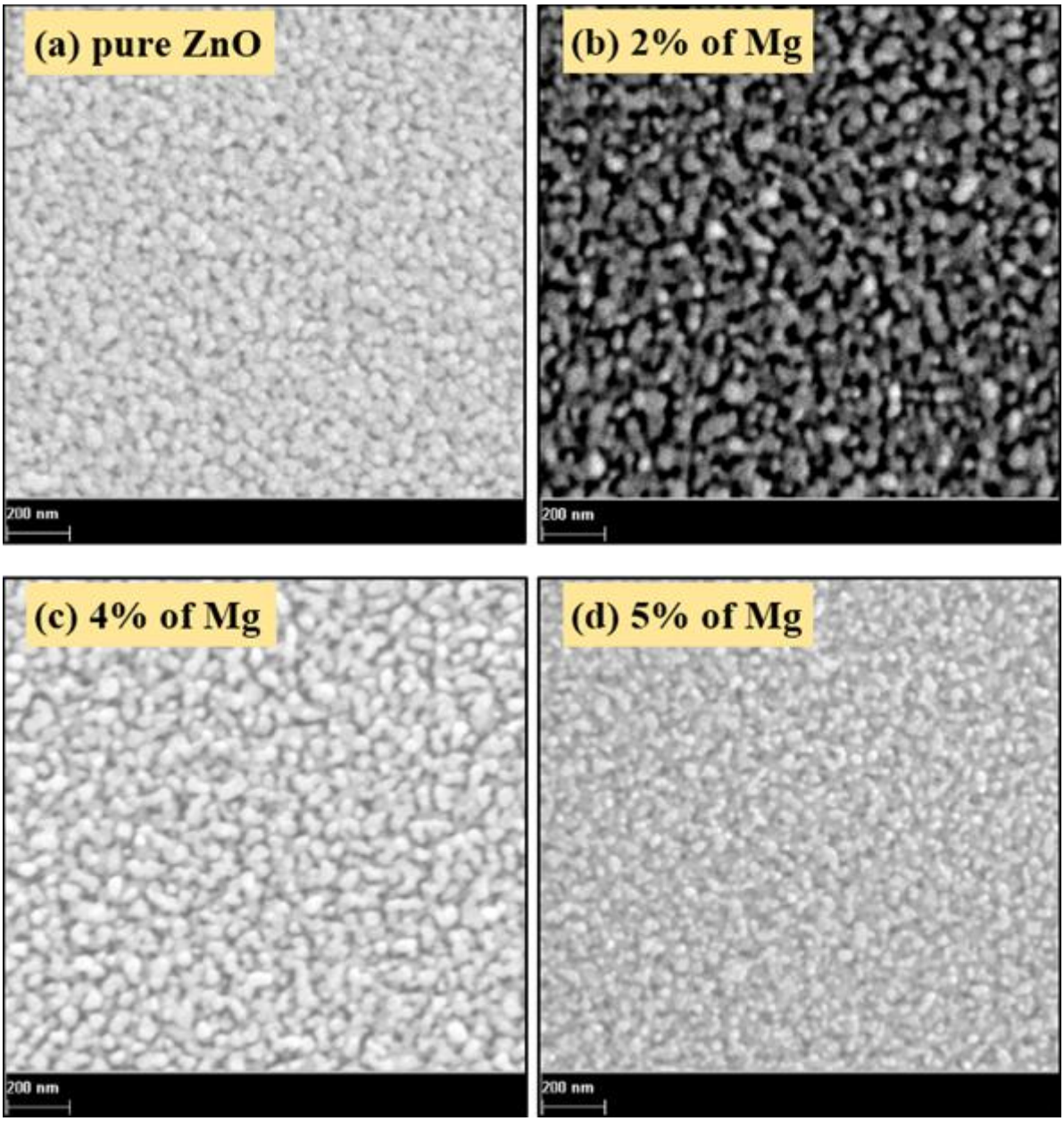

Figure 4.10 SEM images for **a)** pure and **b)** 2%, **c)** 4% and **d)** 5% Mg doped ZnO films.

Figure 4.11 shows a 1 μm^2 SEM images of pure and Mg-doped ZnO films and their segmented images, which are created by 'ImageJ software' (at the top of Figure 4.11). The porosity percentiles taken from segmented images of pure ZnO and Mg-doped ZnO $(2\%, 4\%, 5\%)$ films are 33.67%, 41.72%, 45.02%, 55.99%, respectively. It is clear that the porosity taken from those surfaces is increased by increasing Mg dopant amounts in the ZnO

lattice. However, it is known that an increased porosity degrades many physical properties like the high optical transparency of thin films in the visible wavelength domain [138].

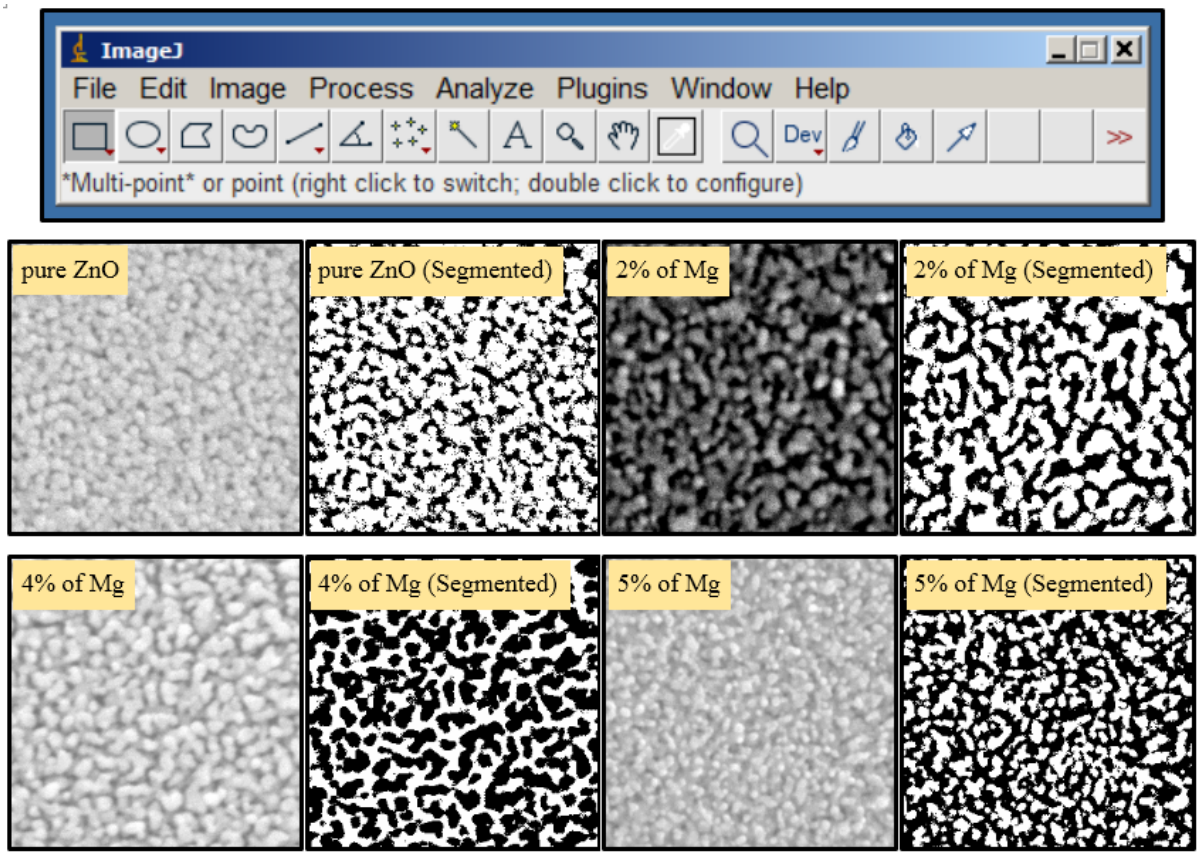

Figure 4.11 SEM images (1 μm^2) for pure and Mg-doped ZnO (2%, 4%, 5%) films and their segmented (threshold by using ImageJ software at the top) images, which display the porosity in black color.

IV.5 Morphological Study by Atomic Force Microscopy

Figure 4.12 shows the Two- and Three-dimensions AFM analysis in a 1 μm^2 scan area of the surface profile for the pure and Mg-doped ZnO (2%, 4%, 5%) films deposited on glass substrates. It is observed that there is a significant change in morphology of the film simples as Mg-dopant amount increased.

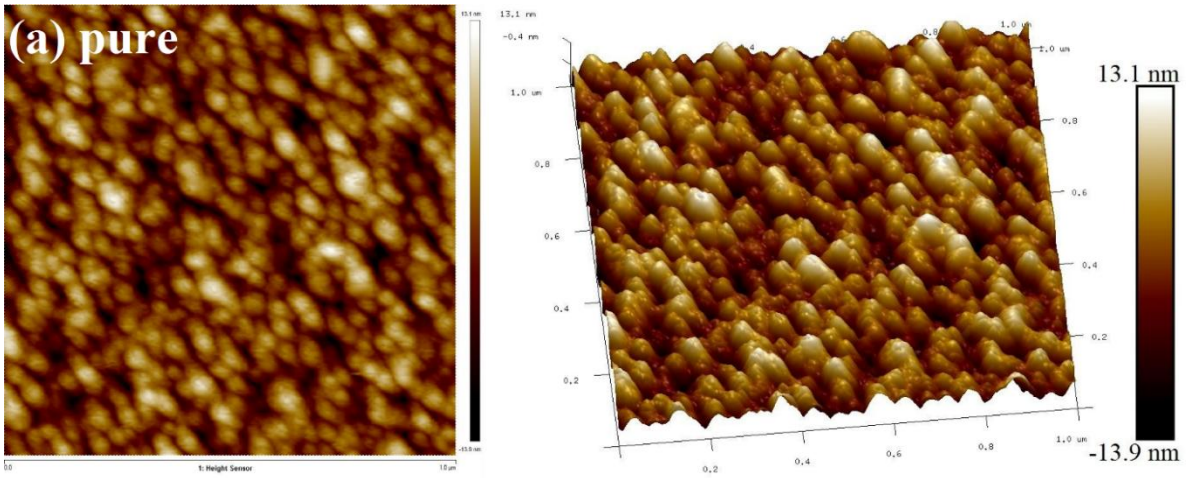
(a) pure
13.1 nm
-13.9 nm

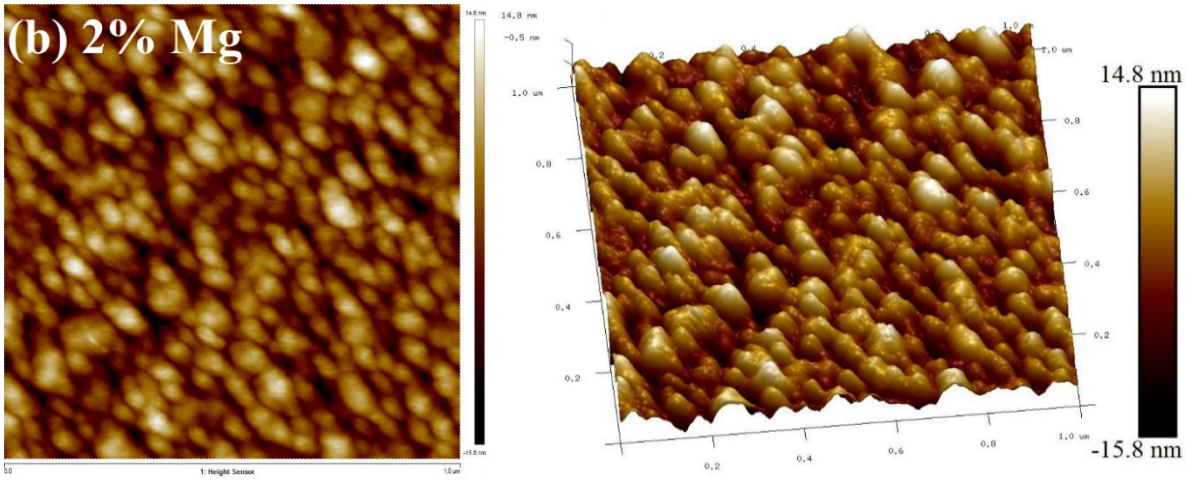
(b) 2% Mg
14.8 nm
-15.8 nm

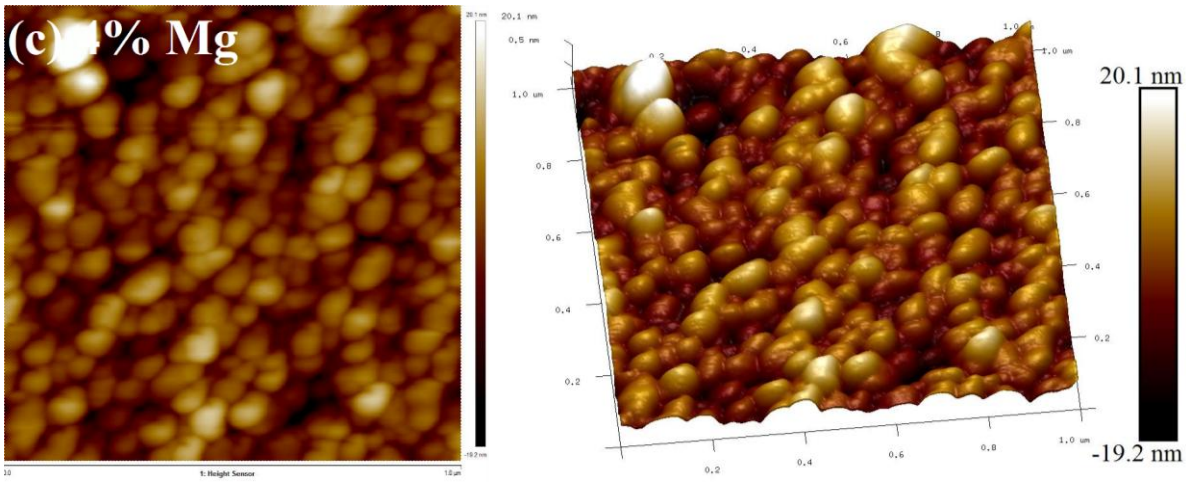
20.1 nm
-19.2 nm

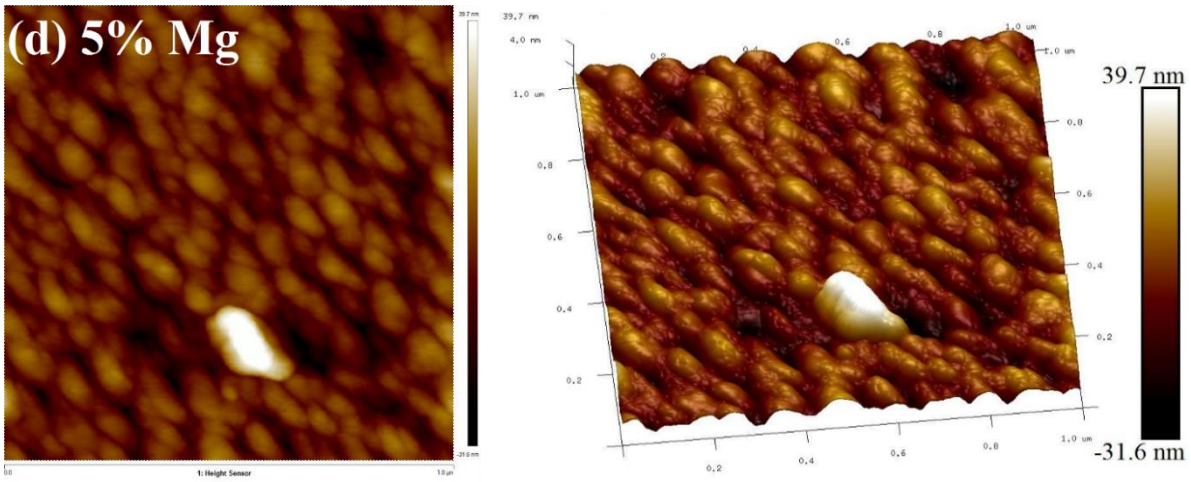

Figure 4.12 2D- and 3D-AFM images for pure and Mg-doped ZnO (2%, 4%, 5%) films.

All the obtained films are highly dense with increased porosity without any cracks. This trend can be caused by incorporating of Mg atoms on the growing surface. It is noticed that with increasing of Mg dopants the grain size becomes larger than with irregular shape. The AFM study of Mg-doped ZnO (5%) sample in Figure 4.12 (c) is not consistent with the results of XRD, and its morphology caused by the coalescence of small size crystallites (~21.11 nm). The surface roughness listed in Table 4.2 was carried out from XRD diffraction analysis to investigate the surface morphologies of the obtained samples. Increasing Mg amount of ZnO from 2% to 5% leads to significantly increased surface roughness from 32.3 nm to 82.9 nm compared with that of pure ZnO (26.3 nm), indicating strong effect of doping on morphology of deposited films. This might be owing to agglomeration of crystallites in films [101]. Opposite results have been reported by Mia et al. [139], where the roughness of the Mg doped ZnO films were seen to be decreased with the incorporation of Mg dopants.

IV.6 Compositional Study by Energy Dispersive X-ray Spectroscopy

Figure 4.13 shows the energy dispersive X-ray (EDX) analysis of the Mg-doped (5%) ZnO sample. This analysis reveals the presence of Mg into the doped sample and its purity. The peak at 1.25 KeV indicates the magnesium (Mg). The two peaks at (~0.5 keV) and (~1.1 keV) validate the presence of oxygen (O) and zinc (Zn), respectively. Another peak at around

(1.7 keV) shows the existence of silicon since the samples were developed on a substrate made with silicon [139]. This proves that Mg are successfully incorporated into ZnO matrix.

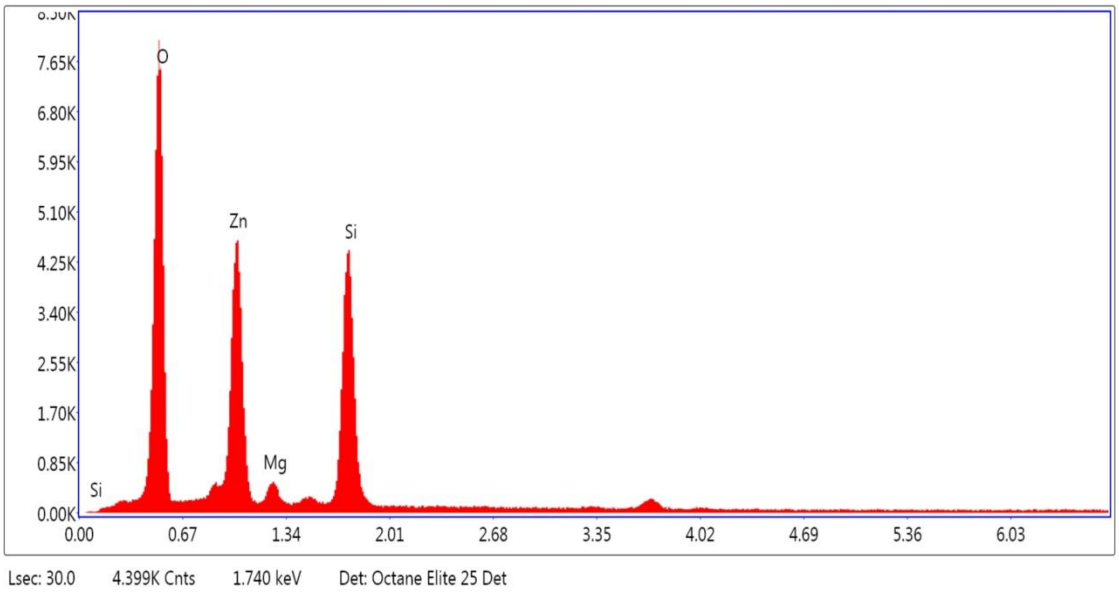

Figure 4.13 EDX spectra of Mg-doped ZnO (5%) film.

IV.7 Optical Properties by UV-Vis Spectroscopy

IV.7.1 Transmittance and absorption coefficient

Figure 4.14 and 4.15 show the recorded absorption and transmittance spectra obtained by UV-Visible spectroscopy in the visible range wavelength from (350nm) to (800 nm) for pure and Mg-doped ZnO (2%, 4%, 5%) films.

The absorption coefficient α can be defined as following [139]:

$$\alpha = (2.303\ A)\ /\ w \qquad (4.8)$$

In which | A – Absorbance and thickness of a film,
w – Thickness of a film.

The Figure 4.14 shows a similar tendency of optical absorption for pure and Mg-doped ZnO films. It was observed a sharp absorption edge located from 375 nm to 400 nm for all films, demonstrating high absorption at UV light that leads to the possible use of Mg-doped ZnO films in UV detection.

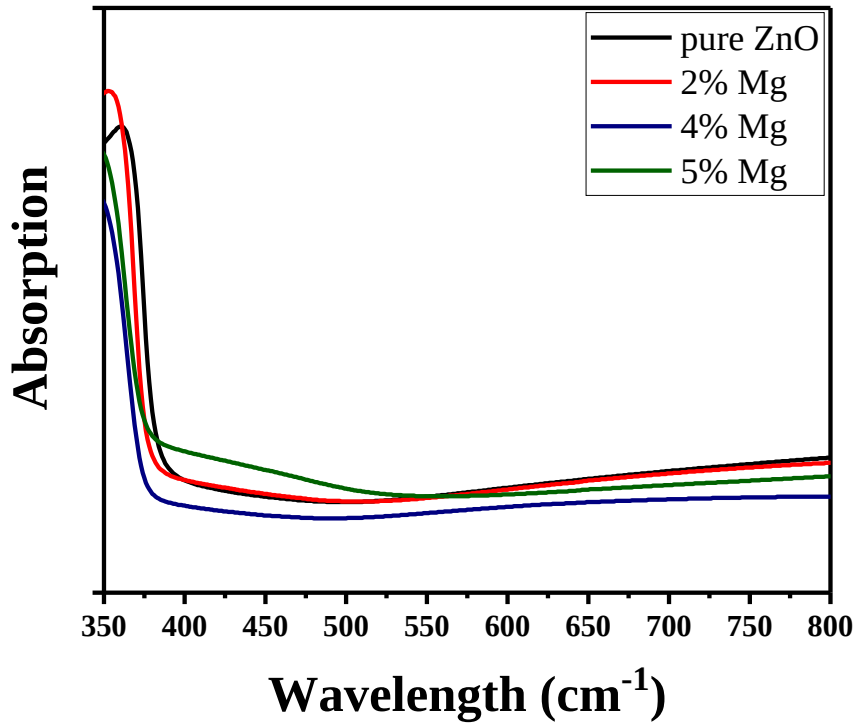

Figure 4.14 Optical absorption spectra for pure and Mg-doped ZnO (2%, 4%, 5%) films.

The Figure 4.15 determines the light transmitting property of the samples. All Samples show a high uniform transparency in visible spectrum. Weakly response was observed for Mg-dopd ZnO (5%) film. This trend is attributed to less defect and more surface porosity (smoothing) due to Mg incorporation into films [139].

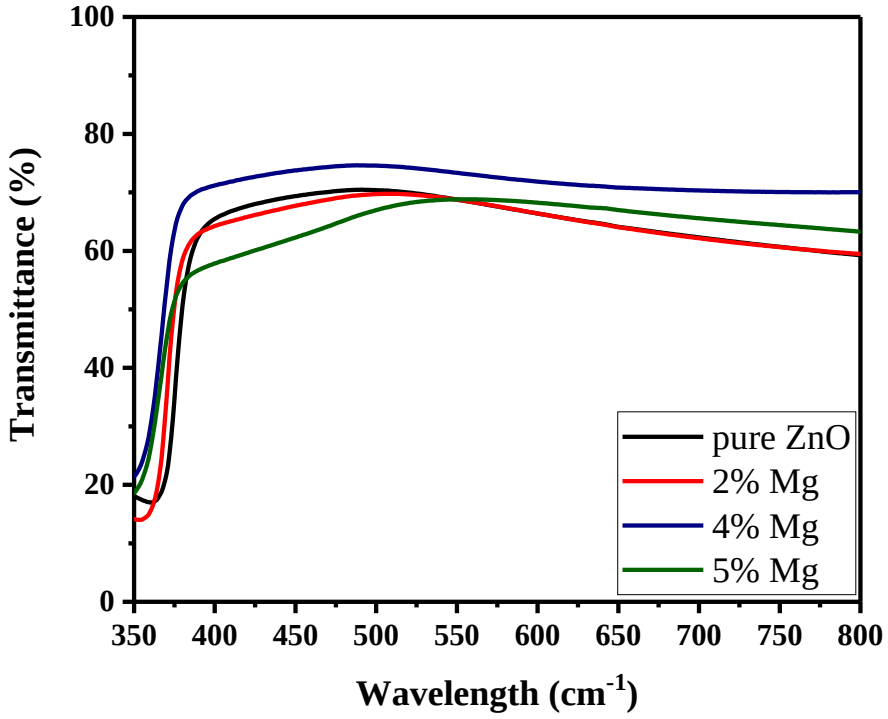

Figure 4.15 Optical transmittance spectra for pure and Mg-doped ZnO (2%, 4%, 5%) films.

IV.7.2 Determination of optical band-gaps

The Tauc's plot which is $(\alpha h\upsilon)^2$ versus $(h\upsilon)$ nonlinear plot, is used to analysis the band gap energy. Considering the type of pure and doped ZnO simples as a direct transition materials, its bandgap energies is the extrapolation of straight line to $(\alpha h\upsilon)^2 = 0$, where (α), (h) and (υ) are absorption coefficient, Plank's constant and frequency of radiation, respectively.

It can be shown in Figure 4.16 (a-d) from the explored band-gaps (E_g) of obtained samples that there is an increasing correlation between the band-gap and Mg doping amount. Therefore, E_g of pure and Mg-doped ZnO samples with concentrations 2%, 4% and 5% are to be $3.268\ eV$, $3.31\ eV$, $3.34\ eV$ and $3.33\ eV$, respectively. It is clear that the band-gap subsequently widens nonlinearly higher than that of pure ZnO film which facilitating the tuning of the band-gap from $3.268\ eV$ to $3.34\ eV$.

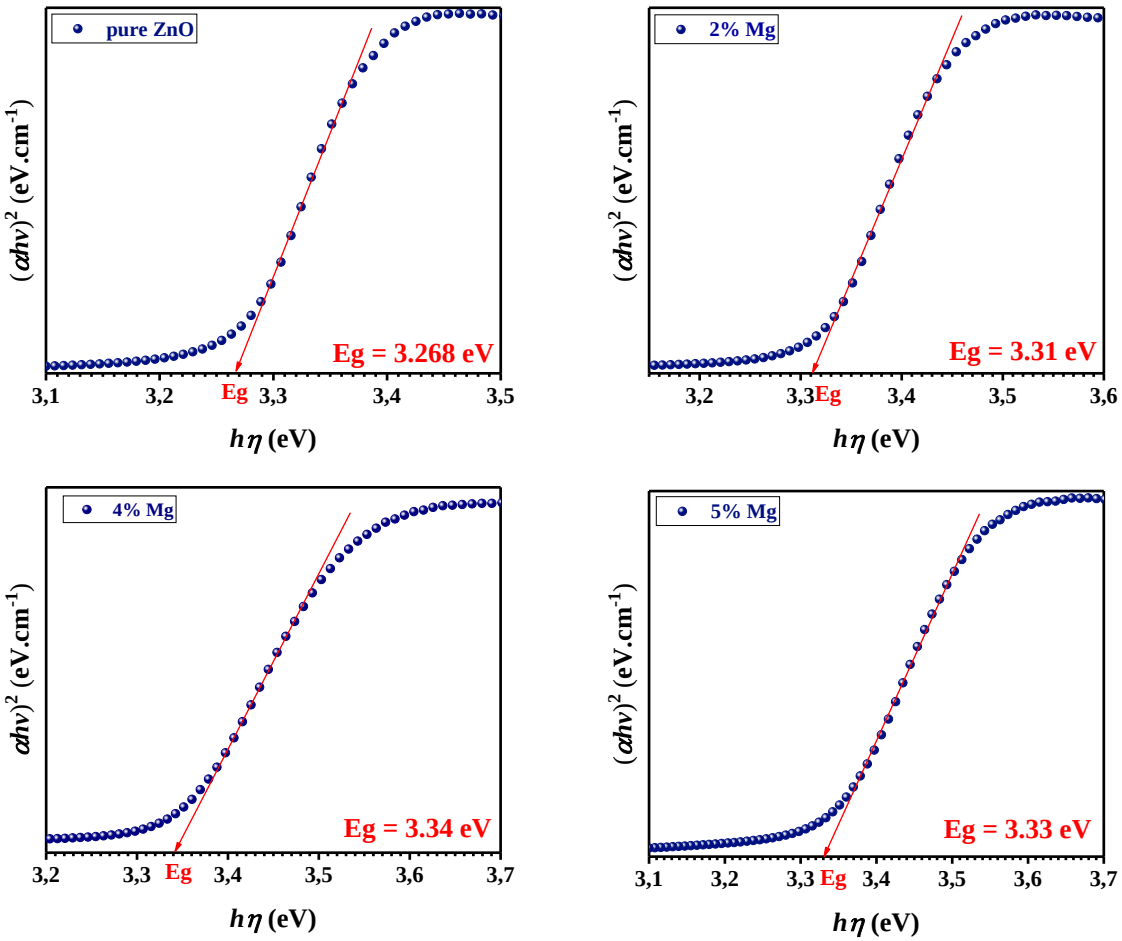

Figure 4.16 plots of $(\alpha h\nu)^2$ versus $(h\nu)$ for pure and Mg-doped ZnO (2%, 4%, 5%) films.

The behavior of band-gap tuning could be justified by the influence of induced stress effects due to creation of intrinsic defects which occurs when Mg^{2+} atom is incorporated in ZnO matrix to extend in the forbidden gap between the conduction-band lower-potential and the valence-band upper-potential. This results are in good agreement with results carried by Mia et al. [139].

IV.8 Summary

In this chapter, we have successfully deposited pure and Mg-doped ZnO ($2\%, 4\%, 5\%$) films using sol-gel spin-coating method on glass substrates. Increasing of Mg dopant amounts affect the crystal structure by changing the lattice parameters (a) and (c). Those structural deformations produce polarization which influences optical band-gap as well. According to the experimental results and their analysis, it is observed that optical band-gap energy becomes larger than pure ZnO film prepared by sol-gel deposition after Mg-doping. The change of band-gap energy takes place in the range of 3.268 to 3.34 eV by increasing Mg content from 2% to 5%. Also, the transmittance is enhanced for Mg-doped ZnO (4%) sample. This enhancement hold promise for window use in photovoltaic applications.

GENERAL CONCLUSION

GENERAL CONCLUSION

The aim of this thesis was the investigation of two main issues: Firstly, the effect of doped and co-doped ZnO thin films properties on the performance of thin films solar cells, the ZnO materials in this case were used as a transparent conducting oxides front-layer (window layer) in the substrate and/or superstrate solar cells structures. The fabrication and characterization of pure and Mg-doped ZnO thin films by sol-gel spin-coating technique were done in the second part of this thesis. A rigorous and concise presentation of transparent conducting oxides (TCO) materials, in particularly zinc oxide materials, and their potentials for thin films solar cells were the fundamental axis of this study. Using AMPS-1D software, we moved from the elaboration framing to the numerical framing that deal with the performance analysis of thin films solar cells through the simulation. Therefore, three thin film solar cells were investigated: ZnO/Si/Cu_2O, TCO/Ga-doped $Mg_xZn_{1-x}O$/CdTe and TCO/p-CIGS/n-ODC/n-In_2Se_3 structures.

In the first structure, the conduction band offset (ΔE_C) at the ZnO/Si junction was 0.45 eV, which enabled the transport of the photo-generated electrons form p-Si absorber layer to ZnO-window layer before they recombine, pointing that there is a good alignment between ZnO-window and Si-absorber layers. In addition, it was clear that a ZnO-window layer of thickness of 100 nm was adequate to the best window working in ZnO/Si/Cu_2O structure, as all J-V characteristics remained unchanged at thicker thickness. This behavior was a result of the deficient of the light-induced carrier generation in the ZnO-window layer because of its wide band gap (3.3 eV). A 0.1 µm-ZnO/10 µm-Si/0.1 µm-Cu_2O structure with an acceptor concentration of $10^{19}\mathrm{cm}^{-3}$ within the Si-absorber layer, showed a good efficiency of 16.23%. This considered value was attributed to the low defect density of $1 \times 10^{14}\mathrm{cm}^{-3}$ in p-Si absorber layer, and when this parameter was smaller than this value, a record efficiency was reached. For example, when this parameter defect was $10^{11}\mathrm{cm}^{-3}$ a best efficiency of about 21.78% was reached.

In the second structure, low-Ga-doped $Mg_xZn_{1-x}O$ (LGMZO) layer showed that having a high band-gap ($3.73\ eV$) and high resistivity ($0.9\ \Omega.\mathrm{cm}$) was found to be important in producing the stable n-partner high-resistivity and transparency buffer layer (HRT-BL) layer for CdTe solar cell. Thus, as expected a thinner LGMZO-buffer layer with a high donor concentration showed a fixed efficiency of 20.91%. In addition, the high Ga-doped $Mg_xZn_{1-x}O$

(HGMZO) layer, which had a low resistivity ($10^{-3}\Omega.\,\mathrm{cm}$) was found to be suitable for a TCO-window layer. Besides, it is found that our results support the previous finding regarding a CdTe absorber layer with an optimal thickness of $2\ \mu m$ and an acceptor concentration of $10^{18} cm^{-3}$. The output of AMPS-1D simulator showed that an optimized HGMZO/LGMZO/CdTe structure achieved a performance of 20.16%.

The presence of the barrier height in the front and back contact layers of the superstrate SLG/TCO/p-CIGS/n-ODC/n-In_2Se_3/Metal solar cells can significantly affect the cell performance by limiting the carrier current flow. The influence of the TCO and Metal work function has been studied using AMPS-1D tool and the corresponding design optimization has been provided. According to the obtained results, the TCO work function should be large enough of over $4.8\ eV$ to prevent the effect of absorber band bending caused by the difference in the work function between p-CIGS absorber and TCO front contact. We notice that all the photovoltaic parameters increase with increasing the TCO work function. This remarkably sharp rise has also been confirmed by the external quantum efficiency. The high W_{TCO} is used to inject holes in the front contact barrier. Thus, the desired values of work functions should be as high as possible. The high work function of $ZnSnO_3$ material is helpful in making low-resistance electrical contact to the p-type CIGS layer. Secondly, a significant performance improvement of the cell efficiency can be expected through the minimization of barrier height ($0.45\ eV$) in the n-In_2Se_3/Metal interface. When the barrier height of the n-In_2Se_3/Metal interface exceeds $0.5\ eV$, the degradation came from the reduction of the fill factor FF and open-circuit voltage V_{OC}. The present simulation results may help in the development of thin films Si, CdTe and superstrate-CIGS solar cells with highly cost-efficiency ratio.

Concerning the elaboration of Mg-doped ZnO thin films by spin-coating Sol-Gel technique, we included explanations from the solution preparation to thin films deposition, starting from alcoholic Isopropanol solutions of Zinc acetate dihydrate (ZAD) with the addition of Monoethanolamine (MEA) and Magnesium chloride hexahydrate. A sol-gel solutions for the fabrication of pure and Mg (2%,4%,5%) doped ZnO thin films on glass substrates were prepared. The curing and annealing conditions were arranged to conduct the deposition of the pure and doped ZnO thin films. The morphological and structural features of the synthetized films were investigated by SEM, EDX, AFM and XRD analysis. Furthermore, UV-Visible spectroscopy analysis was applied to estimate the band gap of the synthetized films from the transmission spectra. SEM analysis demonstrated the effect of the amount of Mg dopant on ZnO

thin film, providing information on the morphology of the synthetized films revealing the formation of nanometer crystals over all the area of synthetized films. Based on Image J-software analysis of SEM images, the porosity of films was found to be higher when increase the Mg dopant. EDX analysis demonstrated the incorporation of Mg dopant on ZnO lattice. The XRD study provided the detailed information on the crystallography of the synthetized films pointing out the dependence of the amount of Mg dopant on crystal size and surface roughness revealing the hexagonal wurtzite structure with preferential growth following the (002) plane along the c-axis perpendicular to the plane of the glass substrate surface. The UV-Visible analysis clearly indicated that Mg-doping was found to modify the optical properties. In particular, 4% Mg-doping resulted a high optical band gap and significant transparency in within the visible spectrum, suggesting 4% Mg doped ZnO as the most suitable among the other synthetized films for photovoltaic device fabrication.

As future perspectives, spin-coated Mg-doped ZnO must be performed under rigorous conditions and endurance tests under different measurement conditions are necessary in order to obtain a suitable product for efficient photovoltaic devices.

BIBLIOGRAPHICAL REFERENCES

[1] L. Elie, C. Granier, S. Rigot, The different types of renewable energy finance: A Bibliometric analysis, Energy Economics, 93 (2021) 104997, https://doi.org/10.1016/j.eneco.2020.104997.

[2] Chapter 1: History of Solar Cell Development, in: L.M. Fraas (2014) Low-Cost Solar Electric Power, Springer.

[3] S. Boudour, I. Bouchama, M. Hadjab, S. Laidoudi, Optimization of defected ZnO/Si/Cu2O heterostructure solar cell, Opt. Mater. 98 (2019) 109433, https://doi.org/10.1016/j.optmat.2019.109433.

[4] A. V. Shah (2010) Thin-Film Silicon Solar Cells, EPFL Press, CRC Press.

[5] S.B. Mitta, P. Murahari, K.R. Nandanapalli, D. Mudusu, R. Karuppannan, D. Whang, Si/ZnO heterostructures for efficient diode and water-splitting applications, Int. J. Hydrogen Energy 43 (2018) 16015-16023, https://doi.org/10.1016/j.ijhydene.2018.07.038.

[6] F.Z. Bedia, A. Bedia, B. Benyoucef, S. Hamzaoui, Electrical characterization of n-ZnO/p-Si heterojunction prepared by spray pyrolysis technique, Physics Procedia 55 (2014) 61-67, https://doi.org/10.1016/j.phpro.2014.07.010.

[7] A.A. El-Amin, High Efficiency Computer Simulation for Au/n-ZnO/p-Si/Al Schottky-Type Thin Film Heterojunctions, Silicon 9 (2017) 385-393, https://doi.org/10.1007/s12633-016-9430-z.

[8] U.L. Muhammad, I.M. Shamsuddin, A. Danjuma, R.S. Musawa, U.H. Dembo, Biofuels as the Starring Substitute to Fossil Fuels, Pet. Sci. Eng. 2 (2018) 44-49, https://doi.org/10.11648/j.pse.20180201.17.

[9] Chapter 11: Energy and Sustainable Development, in: F. Ceschin, C. Vezzoli, R. Moalosi, M. K. M'Rithaa, L. Osanjo, V. Nakazibwe, J.C. Diehl (2018) Designing Sustainable Energy for All, Springer.

[10] Chapter 10: Introduction to Electrical Units and Circuits, in K.M. Smith, P. Holroyd () The Commonwealth and International Library: Electrical Engineering Division, Engineering Principles for Electrical Technicians, Pergamon, 1968, Pages 175-195, https://doi.org/10.1016/B978-0-08-012985-3.50015-7.

[11] Chapter 1: History of Solar Cell Development, in: L.M. Fraas (2014) Low-Cost Solar Electric Power, Springer.

[12] F.A. Shirland, The history, design, fabrication and performance of CdS thin film solar cells, Advanced Energy Conversion 6 (1966) 201-221, https://doi.org/10.1016/0365-1789(66)90016-6.

[13] https://www.sciencedirect.com/search.

[14] S.J. Fonash, A manual for one-dimensional device simulation program (AMPS), Electron. Mater. Process. Res. Lab. (2007) Peensylvania State University.

[15] BP Statistical Review of World Energy, 68th Edition (2019).

[16] P. Sowa, J. Rutkowska-Talipska, U. Sulkowska, R. Rutkowski, Electromagnetic radiation in modern medicine: Physical and biophysical properties, Polish Annals of Medicine 19 (2012) 139-142, https://doi.org/10.1016/j.poamed.2012.07.002.

[17] J.T. Hardy (2003) Climate Change: Causes, Effects, and Solutions, John Wiley & Sons Ltd.

[18] K. Mertens (2014) Photovoltaics fundamentals, technology and practice, John Wiley & Sons Ltd.

[19] Y.H. Khattak, Modeling of High Power Conversion Efficiency Thin Film Solar Cells, PhD Thesis (2019) Universitat Politècnica de València.

[20] L. Zhu, Development of Metal Oxide Solar Cells through Numerical Modelling, PhD Thesis (2012) University of Bolton.

[21] L.C. Hirst, N.J. Ekins-Daukes, Fundamental losses in solar cells. Progress in Photovoltaics: Research and Applications, 19 (2010) 286–293. https://doi.org/10.1002/pip.1024.

[22] C.Q. Luo, F.C.C. Ling, M.A. Rahman, M. Phillips, C. Ton-That, C. Liao, K. Shih, J. Lin, H.W. Tam, A.B. Djurišić, S.P. Wang, Surface polarity control in ZnO films deposited by pulsed laser deposition, Appl. Surf. Sci. 483 (2019) 1129-1135, https://doi.org/10.1016/j.apsusc.2019.03.228.

[23] A.B. Yadav, S. Jit, Particle size effects on the hydrogen sensing properties of Pd/ZnO Schottky contacts fabricated by sol–gel method, Int. J. Hydrogen Energy 42 (2017) 786-794, https://doi.org/10.1016/j.ijhydene.2016.08.201.

[24] Y. Bicer, G. Chehade, I. Dincer, Experimental investigation of various copper oxide electrodeposition conditions on photoelectrochemical hydrogen production, Int. J. Hydrogen Energy 42 (2017) 6490-6501, https://doi.org/10.1016/j.ijhydene.2016.12.067.

[25] H.K. Juwhari, S.J. Ikhmayies, B. Lahlouh, Room temperature photoluminescence of spray-deposited ZnO thin films on glass substrates, Int. J. Hydrogen Energy 42 (2017) 17741-17747, https://doi.org/10.1016/j.ijhydene.2017.03.008.

[26] M.R. Alfaro-Cruz, O. Ceballos-Sanchez, E. Luévano-Hipólito, L.M. Torres-Martínez, ZnO thin films deposited by RF magnetron sputtering: Effects of the annealing and

atmosphere conditions on the photocatalytic hydrogen production, Int. J. Hydrogen Energy 43 (2018) 10301-10310, https://doi.org/10.1016/j.ijhydene.2018.04.054.

[27] A.M. Gheidari, E.A. Soleimani, M. Mansorhoseini, S. Mohajerzadeh, N. Madani, W. Shams-Kolahi, Structural properties of indium tin oxide thin films prepared for application in solar cells, Mater. Res. Bull. 40 (2005) 1303-1307, https://doi.org/10.1016/j.materresbull.2005.04.007.

[28] J.S. Jang, J. Kim, U. Ghorpade, H.H. Shin, M.G. Gang, S.D. Park, H-J. Kim, D.S. Lee, J.H. Kim, Comparison study of ZnO-based quaternary TCO materials for photovoltaic application, J. Alloys Compd. 793 (2019) 499-504, https://doi.org/10.1016/j.jallcom.2019.04.042.

[29] F.I. Chowdhury, T. Blaine, A.B. Gougam, Optical Transmission Enhancement of Fluorine Doped Tin Oxide (FTO) on Glass for Thin Film Photovoltaic Applications, Energy Procedia 42 (2013) 660-669, https://doi.org/10.1016/j.egypro.2013.11.068.

[30] T. Minami, Transparent and conductive multicomponent oxide films prepared by magnetron sputtering, J. Vac. Sci. Technol. A 17 (1999) 1765-1772, http://dx.doi.org/10.1116/1.581888.

[31] T. Minami, T. Miyata, T. Yamamoto, Work function of transparent conducting multicomponent oxide thin films prepared by magnetron sputtering, Surf. Coat. Tech. 108-109 (1998) 583-587, https://doi.org/10.1016/S0257-8972(98)00592-1.

[32] K.U. Ritzau, M. Bivour, S. Schr€oer, H. Steinkemper, P. Reinecke, F. Wagner, M. Hermle, TCO work function related transport losses at the a-Si:H/TCO-contact in SHJ solar cells, Sol. Energy Mater. Sol. Cells 131 (2014) 9-13, https://doi.org/10.1016/j.solmat.2014.06.026.

[33] A. Belfar, Simulation study of the a-Si:H/nc-Si:H solar cells performance sensitivity to the TCO work function, the band gap and the thickness of i-a-Si:H absorber layer, Sol. Energy 114 (2015) 408-417, https://doi.org/10.1016/j.solener.2015.02.010.

[34] Z. Zang, Efficiency enhancement of ZnO/Cu_2O solar cells with well oriented and micrometer grain sized Cu_2O films, Appl. Phys. Lett. 112 (2018) 042106, https://doi.org/10.1063/1.5017002.

[35] H. Heriche, Z. Rouabah, N. Bouarissa, New ultra thin CIGS structure solar cells using SCAPS simulation program, Int. J. Hydrogen Energy 42 (2017) 9524-9532, https://doi.org/10.1016/j.ijhydene.2017.02.099.

[36] S. Boudour, I. Bouchama, N. Bouarissa, M. Hadjab, A study of CdTe solar cells using Ga-doped $Mg_xZn_{1-x}O$ buffer/TCO layers: Simulation and performance analysis, J. Sci.: Adv. Mater. Devices 4 (2019) 111-115, https://doi.org/10.1016/j.jsamd.2018.12.001.

[37] S.B. Mitta, P. Murahari, K.R. Nandanapalli, D. Mudusu, R. Karuppannan, D. Whang, Si/ZnO heterostructures for efficient diode and water-splitting applications, Int. J. Hydrogen Energy 43 (2018) 16015-16023, https://doi.org/10.1016/j.ijhydene.2018.07.038.

[38] S. Laidoudi, A.Y. Bioud, A. Azizi, G. Schmerber, J. Bartringer, S. Barre, A. Dinia, Growth and characterization of electrodeposited Cu_2O thin films, Semicond. Sci. Technol. 28 (2013) 115005, https://doi.org/10.1088/0268-1242/28/11/115005.

[39] E. Fortunato, V. Figueiredo, P. Barquinha, E. Elamurugu, R. Barros, Thin-film transistors based on p-type Cu_2O thin films produced at room temperature, Appl. Phys. Lett. 96 (2010) 192102, https://doi.org/10.1063/1.3428434.

[40] L. Zhu, G. Shao, J.K. Luo, Numerical study of metal oxide heterojunction solar cells, Semicond. Sci. Technol. 26 (2011) 085026, https://doi.org/10.1088/0268-1242/26/8/085026.

[41] W. Wei, C. Jin, J. Narayan, R.J. Narayan, Optical and electrical properties of bandgap engineered gallium-doped $Mg_xZn_{1-x}O$ films, Solid State Commun. 149 (2009) 1670-1673, https://doi.org/10.1016/j.ssc.2009.06.021.

[42] W. Wei, C. Jin, J. Narayan, R.J. Narayan, Optical and electrical properties of gallium-doped $Mg_xZn_{1-x}O$, J. Appl. Phys. 107 (2010) 013510, https://doi.org/10.1063/1.3271415.

[43] M. Green, E. Dunlop, J. Hohl-Ebinger, M. Yoshita, N. Kopidakis, X. Hao, Solar cell efficiency tables (version 57). Prog Photovolt Res Appl. (2020)1–13, https://doi.org/10.1002/pip.3371.

[44] F.Z. Bedia, A. Bedia, B. Benyoucef, S. Hamzaoui, Electrical characterization of n-ZnO/p-Si heterojunction prepared by spray pyrolysis technique, Physics Procedia 55 (2014) 61-67, https://doi.org/10.1016/j.phpro.2014.07.010.

[45] A.A. El-Amin, High Efficiency Computer Simulation for Au/n-ZnO/p-Si/Al Schottky-Type Thin Film Heterojunctions, Silicon 9 (2017) 385-393, https://doi.org/10.1007/s12633-016-9430-z.

[46] B.M. Basol, Thin film CdTe solar cells -A review, Record of Photovoltaic Specialists Conference, New York, IEEE, US, 1 (1990) 588-594, .

[47] A. Nowshad, S. Kamaruzzaman, K. Makoto, Numerical modeling of CdS/CdTe and CdS/CdTe/ZnTe solar cells as a function of CdTe thickness, Sol. Energy Mater. Sol. Cells 91 (2007) 1202-1208, https://doi.org/10.1016/j.solmat.2007.04.006.

[48] A. Salavei, I. Rimmaudo, F. Piccinelli, A. Romeo, Influence of CdTe thickness on structural and electrical properties of CdTe/CdS solar cells, Thin Solid Films 535 (2013) 257-260, https://doi.org/10.1016/j.tsf.2012.11.121.

[49] J. Lauwaert, L.V. Puyvelde, J. Lauwaert, J.W. Thybaut, S. Khelifi, M. Burgelman, F. Pianezzi, A.N. Tiwari, H. Vrielinck, Assignment of capacitance spectroscopy signals of CIGS solar cells to effects of non-ohmic contacts, Sol. Energy Mater. Sol. Cells 112 (2013) 78-83, https://doi.org/10.1016/j.solmat.2013.01.014.

[50] S.U. Park, R. Sharma, K. Ashok, S. Kang, J.K. Sim, C.R. Lee, A study on composition, structure and optical properties of copper-poor CIGS thin film deposited by sequential sputtering of CuGa/In and In/(CuGaþIn) precursors, J. Cryst. Growth 359 (2012) 1-10, https://doi.org/10.1016/j.jcrysgro.2012.08.013.

[51] T. Eisenbarth, T. Unold, R. Caballero, C.A. Kaufmann, D. Abou-Ras, H.W. Schock, Origin of defects in $CuIn_{1-x}Ga_xSe_2$ solar cells with varied Ga content, Thin Solid Films 517 (2009) 2244-2247, https://doi.org/10.1016/j.tsf.2008.10.142.

[52] R. Baier, C. Leendertz, D. Abou-Ras, M.C. Lux-Steiner, S. Sadewasser, Properties of electronic potential barriers at grain boundaries in $Cu(In,Ga)Se_2$ thin films, Sol. Energy Mater. Sol. Cells 130 (2014) 124-131, https://doi.org/10.1016/j.solmat.2014.07.002.

[53] K. Djessas, A. Abatchou, G. Masse, Diffusions in (In,Se)-$Cu(In,Ga)Se_2/SnO_2$ thin film structures, J. Appl. Phys. 88 (2000) 5710, https://doi.org/10.1063/1.1320005.

[54] I. Bouchama, K. Djessas, F. Djahli, A. Bouloufa, Simulation approach for studying the performances of original superstrate CIGS thin films solar cells, Thin Solid Films 519 (2011) 7280-7283, https://doi.org/10.1016/j.tsf.2011.01.182.

[55] T. Minami, New n-Type Transparent Conducting Oxides, MRS Bulletin 25 (2000) 38-44, https://doi.org/10.1557/mrs2000.149.

[56] H. Hosono, K. Ueda (2017) Transparent Conductive Oxides. In: Kasap S., Capper P. (eds) Springer Handbook of Electronic and Photonic Materials. Springer Handbooks. Springer, Cham.

[57] C.L. Chen, H.b. Pu,M. Wang, X. Wang, Y. Zang, C.Y. Gao, A facile way for fabrication of nano-sized p-NiO/n-SiC heterojunction using sol–gel technique, Superlattices Microstruct. 136 (2019) 106251, https://doi.org/10.1016/j.spmi.2019.106251.

[58] N. Zhang, J. Sun, H. Gong, Transparent p-Type Semiconductors: Copper-Based Oxides and Oxychalcogenides, Coatings 9 (2019) 137, https://doi.org/10.3390/coatings9020137.

[59] V. Kampylafka, A. Kostopoulos, M. Modreanu, M. Schmidt, E. Gagaoudakisc, K. Tsagaraki, V. Kontomitrou, G. Konstantinidis, G. Deligeorgis, G. Kiriakidis, E. Aperathitis, Long-term stability of transparent n/p ZnO homojunctions grown by rf-sputtering at room-temperature, J. Materiomics 5 (2019) 428-435, https://doi.org/10.1016/j.jmat.2019.02.006.

[60] R.P. Wijesundera, L.K.A.D.D.S. Gunawardhana, W.Siripala, Electrodeposited Cu_2O homojunction solar cells: Fabrication of a cell of high short circuit photocurrent, Sol. Energy Mater. Sol. Cells 157 (2016) 881-886, https://doi.org/10.1016/j.solmat.2016.07.005.

[61] L. Liao, H.B. Lu, J.C. Li, C. Liu, D.J. Fu, Y.L. Liu, The sensitivity of gas sensor based on single ZnO nanowire modulated by helium ion radiation, Appl. Phys. Lett. 91 (2007) 173110, https://doi.org/10.1063/1.2800812.

[62] B. Cai, Y. Zhou, M. Zhao, H. Cai, Z. Ye, L. Wang, J. Huang, Synthesis of ZnO-CuO porous core-shell spheres and their application for non-enzymatic glucose sensor, Appl. Phys. A 118 (2015) 989–996, https://doi.org/10.1007/s00339-014-8855-8.

[63] S. Bhatia, N. Verma, Photocatalytic activity of ZnO nanoparticles with optimization of defects, Mater. Res. Bull. 95 (2017) 468-476, https://doi.org/10.1016/j.materresbull.2017.08.019.

[64] C.H. Tang, K.Y. Chen, C.Y. Chen, Solution-processed ZnO/Si based heterostructures with enhanced photocatalytic performance, N. J. Chem. 42 (2018) 13797-13802, https://doi.org/10.1039/C8NJ03015D.

[65] Z. Zang, M. Wen, W. Chen, Y. Zeng, Z. Zu, X. Zeng, X. Tang, Strong yellow emission of ZnO hollow nanospheres fabricated using polystyrene spheres as templates, Mater. Des. 84 (2015) 418–421, https://doi.org/10.1016/j.matdes.2015.06.141.

[66] R. Vyas, S. Sharma, P. Gupta, A.K. Prasad, S.K. Dhara, A.K. Tyagi, K. Sachdev, S.K. Sharma, Nitrogen dioxide induced conductivity switching in ZnO thin film Nanostructures, J. Alloys Compd. 571 (2013) 6-11, https://doi.org/10.1016/j.jallcom.2013.03.217.

[67] L.L. Chen, S.Q. Wang, Chapter 18 - Nanotechnology in Photoprotection, Nanoscience in Dermatology (2016) 229-236.

[68] B.L. Guo, P. Han, L.C. Guo, Y.Q. Cao, A.D. Li, J.Z. Kong, H.F. Zhai, D. Wu, The antibacterial activity of Ta-doped ZnO nanoparticles. Nanoscale Res. Lett. 10 (2015) 1047, https://doi.org/10.1186/s11671-015-1047-4.

[69] H.Y. Huang, H.J. Chiang, C.Z. Wu, Y. Lin, Y.K. Shen, Analysis on characteristics of ZnO surface acoustic wave with and without micro-structures, Micromachines 10 (2019) 434, https://doi.org/10.3390/mi10070434.

[70] A. Aissat, M.A. Ghomrani, W. Bellil, A. Benkouider, J.P. Vilcot, The doping effect on the properties of zinc oxide (ZnO) thin layers for photovoltaic applications, Int. J. Hydrogen Energy 40 (2015) 13685–13689, https://doi.org/10.1016/j.ijhydene.2015.02.075.

[71] H. Morkoc, U. Ozgur (2009) Zinc Oxide: Fundamentals, Materials and Device Technology, WILEY-VCH Verlag GmbH & Co. KGaA.

[72] D. P. Norton, Y. W. Heo, M.P. Ivill, K. Ip, S.J. Pearton, M.F. Chisholm, T. Steiner, ZnO: growth, doping & processing, Mater. Today 7 (2004) 34-40, https://doi.org/10.1016/S1369-7021(04)00287-1.

[73] A. Henni, Elaboration de films minces à base d'oxydes métalliques (ZnO) sur supports transparents et leurs applications en photovoltaïque, Thèses Doctorat, 2015, Faculté des Sciences, Département de Chimie, Université Mohamed Boudiaf de M'Sila.

[74] N. Baydogan, O. Karacasu, and H. Cimenoglu, ZnO:Al thin films used in ZnO: Al/p-Si heterojunctions, J. Sol-Gel Sci. Technol. 61 (2012) 620-627, https://doi.org/10.1007/s10971-011-2668-4.

[75] R.A. Afre, N. Sharma, M. Sharon, M. Sharon, Transparent conducting oxide films for various applications: a review, Rev. Adv. Mater. Sci. 53 (2018) 79-89, https://doi.org/10.1515/rams-2018-0006.

[76] Y.Q. Chen, X.J. Zheng, X. Feng, The fabrication of vanadium-doped ZnO piezoelectric nanofiber by electrospinning, Nanotechnology 21 (2009) 055708-055711, https://doi.org/10.1088/0957-4484/21/5/055708.

[77] E. Oh, S.H. Jung, K.H. Lee, S.H. Jeong, S. Yu, S.J. Rhee, Vertically aligned Fe-doped ZnO nanorod arrays by ultrasonic irradiation and their photoluminescence properties, Mater. Lett. 62 (2008) 3456-3458, https://doi.org/10.1016/j.matlet.2008.02.073.

[78] R. Mohan, K. Krishnamoorthy, S.J. Kim, Enhanced photocatalytic activity of Cudoped ZnO nanorods, Solid State Commun. 152 (2012) 375-380, https://doi.org/10.1016/j.ssc.2011.12.008.

[79] L. Yanmei, W. Tao, S. Xia, F. Qingqing, L. Qingrong, S. Xueping, I.S. Zaoq, Structural and photoluminescent properties of Ni doped ZnO nanorod arrays prepared by hydrothermal method, Appl. Surf. Sci. 257 (2011) 6540-6545, https://doi.org/10.1016/j.apsusc.2011.02.074.

[80] H. Hao, M. Qin, P. Li, Structural, optical, and magnetic properties of Co-doped ZnO nanorods fabricated by a facile solution route, J. Alloy. Comp. 515 (2012) 143-148, https://doi.org/10.1016/j.jallcom.2011.11.112.

[81] F. Ahmed, N. Arshi, M.S. Anwar, R. Danish, B.H. Koo, Mn-doped ZnO nanorod gas sensor for oxygen detection, Curr. Appl Phys. 13 (2013) S64-S68, https://doi.org/10.1016/j.cap.2012.12.029.

[82] S.K. Lim, S.H. Hong, S.H. Hwang, S. Kim, H. Park, Characterization of Ga-doped ZnO nanorods synthesized via microemulsion method, J. Mater. Sci. Technol. 29 (2013) 39-43, https://doi.org/10.1016/j.jmst.2012.11.005.

[83] N. Chahmat, A. Haddad, A. Ain-Souya, R. Ganfoudi, N. Attaf, M. Salah Aida, M. Ghers, Effect of Sn doping on the properties of ZnO thin films prepared by spray pyrolysis, J. Mod. Phys. 3 (2012) 1781-1785, https://doi.org/10.4236/jmp.2012.311222.

[84] X. Chong, L. Li, X. Yan, D. Hu, H. Li, Y. Wang, Synthesis, characterization and room temperature photoluminescence properties of Al doped ZnO nanorods, Physica E 44 (2012) 1399-1405, https://doi.org/10.1016/j.physe.2012.03.001.

[85] H. Çolak, E. Karaköse, Tm-doped ZnO nanorods as a TCO for PV applications, J. Rare Earths 36 (2018) 1067-1073, https://doi.org/10.1016/j.jre.2018.03.020.

[86] P. Bharati, M. Aslam, D.S. Misra, D. Bahadur, Structural, optical and magnetic properties of Gd-doped ZnO nanorods by a novel aqueous solution method, Int. J. Nanosci. 10 (2011) 629-633, https://doi.org/10.1142/S0219581X11009052.

[87] M. Xin, Optical properties of nanostructured ZnO:Eu film by sol–gel method. Surf. Eng. 35 (2019) 974-953, https://doi.org/10.1080/02670844.2019.1573344.

[88] K. Jeyasubramaniana, R.V. William, P. Thiruramanathan, G.S. Hikku, M.V. Kumar, B. Ashima, P. Veluswamy, H. Ikeda, Dielectric and magnetic properties of nanoporous nickel doped zinc oxide for spintronic applications, J. Magn. Magn. Mater. 485 (2019) 27-35, https://doi.org/10.1016/j.jmmm.2019.04.032.

[89] S. Kahraman, H. M. Çakmak, S. Çetinkaya, F. Bayansal, H.A. Çetinkara, H.S. Güder, Characteristics of ZnO thin films doped by various elements, J. Cryst. Growth 363 (2013) 86-92, https://doi.org/10.1016/j.jcrysgro.2012.10.018.

[90] M. Maache, T. Devers, A. Chala, Al-Doped and Pure ZnO Thin Films Elaborated by Sol–Gel Spin Coating Process for Optoelectronic Applications, Semiconductors 51 (2017) 1604-1610, https://doi.org/10.1134/S1063782617120132.

[91] J. Narayan, A.K. Sharma, A. Kvit, C. Jin, J.F. Muth, O.W. Holland, Novel cubic $Zn_xMg_{1-x}O$ epitaxial heterostructures on Si (100) substrates. Solid State Commun. 121 (2002) 9-13, https://doi.org/10.1016/S0038-1098(01)00431-8.

[92] A. Sarkar, S. Maity, P. Chankraborty, S.K. Chakraborty, Effect of annealing temperature on Mg-Al co doped ZnO Nano particles synthesized via sol-gel method for gas sensing application, Mater. Today: Proc. 4 (2017) 10367-10371, https://doi.org/10.1016/j.matpr.2017.06.382.

[93] H. Noorikalkenari, K. bin Deraman, Nanostructure of Al-ZnO Thin Films on ITO/Glass Substrate Prepared via Sol-Gel Spin Coating Process. Solid State Phenomena 268 (2017) 279-283, https://doi.org/10.4028/www.scientific.net/SSP.268.279.

[94] R. Amari, A. Mahroug, A. Boukhari, B. Deghfel, N. Selmi, Structural, Optical and Luminescence Properties of ZnO Thin Films Prepared by Sol-Gel Spin-Coating Method: Effect of Precursor Concentration, Chin. Phys. Lett. 35 (2018) 016801, https://doi.org/10.1088/0256-307X/35/1/016801.

[95] M. Dosmailov, L.N. Leonat, J. Patek, D. Roth, P. Bauer, M.C. Scharber, N.S. Sariciftci, J.D. Pedarnig, Transparent conductive ZnO layers on polymer substrates: Thin film deposition and application in organic solar cells. Thin Solid Films 591 (2015) 97-104, https://doi.org/10.1016/j.tsf.2015.08.015.

[96] Z. Liu, Z. Jin, W. Li, X. Liu, Ordered porous ZnO thin films formed by dip-coating method using PS templates. J. Sol-Gel Sci. Technol. 40 (2006) 25-30, https://doi.org/10.1007/s10971-006-8421-8.

[97] R.M. Alwan, Q.A. Kadhim, K.M. Sahan, R.A. Ali, R.J. Mahdi, N.A. Kassim, A.N. Jassim, Synthesis of Zinc Oxide Nanoparticles via Sol-Gel Route and Their Characterization, Nanoscience and Nanotechnology 5 (2015) 1-6, https://doi.org/10.5923/j.nn.20150501.01.

[98] M.I. Khan, K.A. Bhatti, R. Qindeel, N. Alonizan, H.S. Althobaiti, Characterizations of multilayer ZnO thin films deposited by sol-gel spin coating technique, Results Phys. 7 (2017) 651-655, https://doi.org/10.1016/j.rinp.2016.12.029.

[99] T. Ivanovaa, A. Harizanova, T. Koutzarova, B. Vertruyen, B. Stefanov, Structural and morphological characterization of sol-gel ZnO:Ga films: Effect of annealing

temperatures, Thin Solid Films 646 (2018) 132-142, https://doi.org/10.1016/j.tsf.2017.11.042.

[100] N.H. Hashim, S. Subramani, M. Devarajan, A.R. Ibrahim, Properties of undoped ZnO and Mg doped ZnO thin films by sol-gel method for optoelectronic applications, Journal of the Australian Ceramic Society 53 (2017) 421-431, https://doi.org/10.1007/s41779-017-0051-9.

[101] M. Shkir, M. Arif, V. Ganesh, M.A. Manthrammel, A. Singh, I.S. Yahia, Shivaraj, R. Maidur, P.S. Patil, S. AlFaify, Investigation on structural, linear, nonlinear and optical limiting properties of sol-gel derived nanocrystalline Mg doped ZnO thin films for optoelectronic applications, J. Mol. Struct. 1173 (2018) 375-384, https://doi.org/10.1016/j.molstruc.2018.06.105.

[102] S. Stoleriu, C. Lungu, C.D. Ghitulica, A. Surdu, G. Voicu, A. Cucuruz, C.S. Turculet, L.T. Ciocan, (2020). Influence of Dopant Nature on Biological Properties of ZnO Thin-Film Coatings on Ti Alloy Substrate, Nanomaterials 10 (2020) 129, https://doi.org/10.3390/nano10010129.

[103] N. Siregar, Motlan, D.J. Panggabean, The effect magnesium (Mg) on structural and optical properties of ZnO:Mg thin film by sol-gel spin coating method, J. Phys.: Conf. Ser. 1428 (2020) 012026, https://doi.org/10.1088/1742-6596/1428/1/012026.

[104] K. Huang, Z. Tang, L. Zhang, J. Yu, J. Liu, X. Liu, F. Liu, Preparation and characterization of Mg-doped ZnO thin films by sol-gel method, Appl. Surf. Sci. 258 (2012) 3710-3713, https://doi.org/10.1016/j.apsusc.2011.12.011.

[105] S. Aksoy, Y. Caglar, S. Ilican, M. Caglar, Sol-gel derived Li-Mg co-doped ZnO films: Preparation and characterization via XRD, XPS, FESEM, J. Alloys Compd. 512 (2012) 171-178, https://doi.org/10.1016/j.jallcom.2011.09.058.

[106] B. Khanizadeh, M. Khosravi, M.A. Behnajady, A. Shamel, B. Vahid, Mg and La Co-doped ZnO Nanoparticles Prepared by Sol-gel Method: Synthesis, Characterization and Photocatalytic Activity, Periodica Polytechnica Chemical Engineering 64 (2020) 61-74, https://doi.org/10.3311/PPch.12959.

[107] O.O. Abegunde, E.T. Akinlabi, O.P. Oladijo, S. Akinlabi, A.U. Ude, Overview of thin film deposition techniques, AIMS Materials Science, 6 (2019) 174-199, https://doi.org/10.3934/matersci.2019.2.174.

[108] D.G. Ayana, Synthesis and Characterization of Sol-Gel Derived ZnO Thin Films for Memristive Applications, Ph.D. Thesis, May 2017, Department of Industrial Engineering, University of Trento, Italy.

[109] O. Tari, Sol-Gel Synthesis and Characterisation of pure and doped Transparent and Conductive ZnO Thin Films, Ph.D. Thesis, March 2013, Department of Physics, University of Naples Federico II.

[110] Brinker CJ, Scherer GW. Sol-gel science: the physics and chemistry of sol-gel processing, Boston, MA: Academic Press 839 (1990).

[111] D.P. Birnie, Spin Coating Technique. Sol-Gel Technologies for Glass Producers and Users (2004) 49-55, https://doi.org/10.1007/978-0-387-88953-5_4.

[112] I. Bouchama, S. Boudour, N. Bouarissa, Z. Rouabah, Quantum and conversion efficiencies optimization of superstrate CIGS thin-films solar cells using In2Se3 buffer layer, Opt. Mater. 72 (2017), 177-182, http://dx.doi.org/10.1016/j.optmat.2017.05.056.

[113] A. Aissat, M. El bey, R. Bestam, J.P. Vilcot, Modeling and simulation of $Al_xGa_yIn_{1-x-y}As$/InP quaternary structure for photovoltaic, Int. J. Hydrogen Energy 39 (2014) 15287-15291, https://doi.org/10.1016/j.ijhydene.2014.04.162.

[114] M. Reuter, W. Brendle, O. Tobail, J.H. Werner, 50 μm thin solar cells with 17.0% efficiency, Sol. Energy Mater. Sol. Cells 93 (2009) 704-706, https://doi.org/10.1016/j.solmat.2008.09.035.

[115] J. Yoon, L. Li, A. Semichaevisky, J. Ha Ryu, H.T. Johnson, R.G. Nuzzo, J.A. Rogers, Flexible concentrator photovoltaics based on microscale silicon solar cells embedded in luminescent waive guides, Nat. Commun. 2 (2011) 343, https://doi.org/10.1038/ncomms1318.

[116] J.L. Cruz-Campa, M. Okandan, P.J. Resnick, P. Clews, T. Pluym, R.K. Grubbs, V.P. Gupta, D. Zubia, G.N. Nielson, Microsystems enabled photovoltaics: 14.9% efficient 14 μm thick crystalline silicon solar cell, Sol. Energy Mater. Sol. Cells 95 (2011) 551-558, https://doi.org/10.1016/j.solmat.2010.09.015.

[117] G. Li, He Li, J.Y.L. Ho, M. Wong, H. S.K. Kwok, Nanopyramid Structure for Ultrathin c‑Si Tandem Solar Cells, Nano Lett. 14 (2014) 2563-2568, https://doi.org/10.1021/nl500366c.

[118] M. Pavian, S. Rühle, A. Ginsburg, D.A. Keller, H.N. Barad, P.M. Sberna, D. Nunes, R. Martins, A.Y. Anderson, A. Zaban, E. Fortunato, TiO_2/Cu_2O all-oxide heterojunction solar cells produced by spray pyrolysis, Sol. Energy Mater. Sol. Cells 132 (2015) 549-556, https://doi.org/10.1016/j.solmat.2014.10.005.

[119] M.H. Tran, J.Y. Cho, S. Sinha, M.G. Gang, J. Heo, Cu_2O/ZnO heterojunction thin-film solar cells: the effect of electrodeposition condition and thickness of Cu_2O. Thin Solid Films 661 (2018) 132-136, https://doi.org/10.1016/j.tsf.2018.07.023.

[120] O. Isabella, K. Jäger, A. Smets, R. Vian Swaaij, M. Zeman, Solar energy: The physics and engineering of photovoltaic conversion, technologies and systems, UIT Cambridge (2016).

[121] D. Yan and A. Cuevias, Empirical determination of the energy band gap narrowing in highly doped n+ silicon, J. Appl. Phys. 114 (2013) 044508, https://doi.org/10.1063/1.4816694.

[122] F.E. Rougieux, C. Sun, D. Macdonald, Determining the charge states and capture mechanisms of defects in silicon through accurate recombination analyses: A review, Sol. Energy Mater. Sol. Cells 187 (2018) 263-272, https://doi.org/10.1016/j.solmat.2018.07.029.

[123] B.L. Williams, J.D. Major, L. Bowen, L. Phillips, G. Zoppi, I. Forbes, K. Durose, Challenges and prospects for developing CdS/CdTe substrate solar cells on Mo foils, Sol. Energy Mater. Sol. Cells 124 (2014) 31-38, https://doi.org/10.1016/j.solmat.2014.01.017.

[124] N. Dhar, P. Chelvanathan, K.S. Rahman, M.A. M Bhuiyan, M.M. Alam, K. Sopian, A. Nowshad, Effect of p-type transition metal dichalcogenide molybdenum ditelluride (p-$MoTe_2$) layer formation in cadmium telluride solar cells from numerical analysis, IEEE 39th Photovoltaic Specialists Conference (PVSC) 14116353 (2013) 3487-3492, https://doi.org/10.1109/PVSC.2013.6744244.

[125] K. Djessas, S. Yapi, G. Masse, Diffusion of Cu, In, and Ga in In_2Se_3/$CuGaSe_2$/SnO_2 thin film photovoltaic structures, J. Appl. Phys. 95 (2004) 4111, https://doi.org/10.1063/1.1652252.

[126] G. Masse, K. Djessas, p-n Junctions in (In,Se)/Cu(In,Ga)$(Se,S)_2$ Photovoltaic Systems, J. Appl. Phys. 94 (2003) 6985, https://doi.org/10.1063/1.1621715.

[127] I. Bouchama, K. Djessas, F. Djahli, A. Bouloufa, Simulation approach for studying the performances of original superstrate CIGS thin films solar cells, Thin Solid Films 519 (2011) 7280-7283, https://doi.org/10.1016/j.tsf.2011.01.182.

[128] S.Q. Hussain, W.K. Oh, S. Ahn, A.H.T. Le, S. Kima, Y. Lee, J. Yi, RF magnetron sputtered indium tin oxide films with high transmittance and work function for a-Si:H/c-Si heterojunction solar cells, Vacuum 101 (2014) 18-21, https://doi.org/10.1016/j.vacuum.2013.07.004.

[129] T. Nakada, Y. Hirabayashi, T. Tokado, D. Ohmori, T. Mise, Novel device structure for Cu(In,Ga)Se2 thin film solar cells using transparent conducting oxide back and front contacts, Sol. Energy 77 (2004) 739-747, https://doi.org/10.1016/j.solener.2004.08.010.

[130] S.H. Demtsu, Impact of Back-contact Materials on Performance and Stability of CdS/CdTe Solar Cells, PhD Thesis, 2006, Colorado State University, Fort Collins, Colorado.

[131] W. Monch, Semiconductor Surfaces and Interfaces, Third Revised Edition, Springer, 2001.

[132] L. Zhu, G. Shao, J.K. Luo, Numerical study of metal oxide Schottky type solar cells, Solid State Sci. 14 (2012) 857-863, https://doi.org/10.1016/j.solidstatesciences.2012.04.020.

[133] Baer D.R., and S. Thevuthasan. 2010. "Characterization of Thin Films and Coatings." In Handbook of Deposition Technologies for Films and Coatings, edited by PM Martin. 749-864. Amsterdam:Elsevier. PNNL-SA-65322.

[134] F. K. Shan, B. I. Kim, G. X. Liu, Z. F. Liu, J. Y. Sohn et al., Blueshift of near band edge emission in Mg doped ZnO thin films and aging, J. Appl. Phys. 95 (2004) 4772, https://doi.org/10.1063/1.1690091.

[135] M. Rouchdi, E. Salmani, B. Fares, N. Hassanain and A. Mzerd, Synthesis and characteristics of Mg doped ZnO thin films: Experimental and ab-initio study, Results Phys. 7 (2017) 620-627, https://doi.org/10.1016/j.rinp.2017.01.023.

[136] R.Yousefia, A. Khorsand Zak, F. Jamali-Sheini, Growth, X-ray peak broadening studies and optical properties of Mg-doped ZnO nanoparticles, Mater. Sci. Semicond. Process 16 (2013) 771-777, https://doi.org/10.1016/j.mssp.2012.12.025.

[137] M.N.H. Mia, M.F. Pervez, M.K. Hossain, H.K. Ghosh, M. Hoq, M.R. Rahman, M. Jalal Uddin, M.A. Al Mashud, Influence of Mg content on tailoring optical bandgap of Mg-doped ZnO thin film prepared by sol-gel method, Results Phys. 7 (2007) 2683-2691, https://doi.org/10.1016/j.rinp.2017.07.047.

[138] K. A. Amedome Min-Dianey, H.-C. Zhang, N. L. P. M'Bouana, K. Kougblenou, X. Xia, Limitation of optical properties through porous silicon photonic crystals influenced by porosity and lattice dynamic. Opt. Mater. 75 (2018) 150–165, https://doi.org/10.1016/j.optmat.2017.10.023.

[139] J. Sengupta, A. Ahmed, R. Labar, Structural and optical properties of post annealed Mg doped ZnO thin films deposited by the sol-gel method, Mater. Chem. Phys.109 (2013) 265-268, https://doi.org/10.1016/j.matlet.2013.07.104.

PUBLICATIONS AND CONFERNCES

Publications

[1] I. Bouchama, **S. Boudour**, N. Bouarissa, Z. Rouabah, Quantum and conversion efficiencies optimization of superstrate CIGS thin-films solar cells using In_2Se_3 buffer layer, Opt. Mater. 72 (2017), 177-182, http://dx.doi.org/10.1016/j.optmat.2017.05.056.

[2] **S. Boudour**, I. Bouchama, N. Bouarissa, M. Hadjab, A study of CdTe solar cells using Ga-doped $Mg_xZn_{1-x}O$ buffer/TCO layers: Simulation and performance analysis, J. Sci.: Adv. Mater. Devices 4 (2019) 111-115, https://doi.org/10.1016/j.jsamd.2018.12.001.

[3] **S. Boudour**, I. Bouchama, M. Hadjab, S. Laidoudi, Optimization of defected ZnO/Si/Cu_2O heterostructure solar cell, Opt. Mater. 98 (2019) 109433, https://doi.org/10.1016/j.optmat.2019.109433.

[4] M. Hadjab, J.M. Wagner, F. Bouzid, **S. Boudour**, A. Hadj Larbi, H. Bennacer, M.I. Ziane, M.A. Saeed, H. Abid, S. Berrah, A numerical optimization study of CdS and Mg0.125Zn0.875O buffer layers in CIGS-based solar cells using wxAMPS-1D package, International Journal of Modelling and Simulation (2020), https://doi.org/10.1080/02286203.2020.1857129.

[5] S. Laidoudi, M.R. Khelladi, L. Lamiri, O. Belgherbi, **S. Boudour**, C. Dehchar, R. Boufnik , Non-enzymatic glucose detection based on cuprous oxide thin film synthesized via electrochemical deposition. Appl. Phys. A 127, 160 (2021), https://doi.org/10.1007/s00339-021-04299-x.

International Conferences

[1] **S. Boudour**, I. Bouchama, M. Hadjab, Optimization of CdTe solar cell performances using Ga-doped $Mg_xZn_{1-x}O$ buffer layer, 6th International Symposium on Transparent Conductive Materials (TCM2016), October 2016, Crete, Greece.

[2] S. Ali Saoucha, I. Bouchama Idris, **S. Boudour**, A. Nowshad, Properties of electronic potential barriers of superstrate In_2S_3/ODC/CIGS solar cell using one-dimentional model, 6th International Symposium on Transparent Conductive Materials (TCM2016), October 2016, Crete, Greece.

[3] **S. Boudour**, I. Bouchama, M. Hadjab, S. Laidoudi, Numerical Modeling of Metal Oxide Heterojunction AZO/Cu_2O Solar Cell, The 3rd International Conference on Power Electronics and their Applications (ICPEA2017), September 2017, Djelfa, Algeria.

[4] M. Hadjab, **S. Boudour**, F. Bouzid, A. Hadj Larbi, H. Nezzari, Computational study of the fundamental properties of chalcopyrite semiconductors, for photovoltaic applications: Density Functional Theory, International Congress of Engineering of Advanced Materials (ICEAM2017), October 2017, Erlangen-Nürnberg, Germany.

[5] M. Hadjab, H. Bennacer, M. Ibrir, F. Bouzid, A. Hadj Larbi, **S. Boudour**, H. Nezzari, A. Hadj Larbi, H. Nezzari, First principle prediction of the optical properties of wide band gap of ZnO for photovoltaic applications, International on Electronics and New Technologies (ICENT2017), November 2017, M'sila, Algeria.

[6] **S. Boudour**, I. Bouchama, Optimized study of new ZnO/Si/Cu_2O solar cell structure using one dimensional AMPS modeling simulation, Spring Meeting E-MRS, June 2018, Strasbourg, France.

[7] **S. Boudour**, M. Hadjab, I. Bouchama, S. Laidoudi, Optimization of AZO/ZnO/Cu_2O Thin Film Hetero-junction Solar Cell with Gaussian Defect, International Conference on Communications and Electrical Engineering (ICCEE2018), December 2018, El Oued, Algeria.

[8] M. Hadjab, M. Ibrir, B. Gazi Yalcin, F. Bouzid, A. Hadj Larbi, **S. Boudour**, H. Nezzari, Elastic, mechanical and thermodynamic properties of zincblende III-X (X=As, Sb): ab-initio calculations, International Conference on Mechanics and Energy (ICME2018), December 2018, Hammamet, Tunisia.

[9] M. Hadjab, J-M. Wagner, F. Bouzid, M. Ibrir, A. Hadj Larbi, **S. Boudour**, H. Bennacer, M. I. Ziane, M. Ibrir, First-principles calculations and numerical modeling on the structural and optoelectronic properties of chalcopyrite materials for solar cells application, 2nd Algerian-German International Conference on New Technologies and their applications (AGICNT2019), September 2019, Sétif, Algeria.

[10] M. Hadjab, A. Kassaa, S. Berrah, F. Bouzid, M. Ibrir, A. Hadj Larbi, **S. Boudour**, H. Bennacer, Experimental investigation and first-principles calculations on the physical properties of $CuGaTe_2$ for solar cells application, Congres International De Physique Et Chimie Quantique (CIPCQ2019), November 2019, Béjaia, Algeria.

[11] S. Laidoudi, M. Redha Khelladi, C. Dehchar, **S. Boudour**, L. Lamiri, O. B., R. Boufnik, Optical, structural and morphological characterization of electrodeposited cuprous oxide thin films: effect of deposition time, 5th International conference on advances in mechanical engineering Istanbul, December 2019, Istanbul, Turkey.

[12] L. Lamiri, A. Tounsi, B. Nessark, O. Belgherbi, S. Laidoudi, **S. Boudour**, F. Habelhames, Polypyrrole-coated manganese dioxide as electrode material for hydrogen peroxide reduction, XIII^{èmes} Journées Maghrébines des Sciences des Matériaux- JMSM2020, Université Oran 1 Ahmed Ben Bella, Mars 2020, Oran, Algérie.

National Conferences

[1] **S. Boudour**, M. Hadjab, I. Bouchama, S. Aziez, Numerical Simulation of CdTe thin films solar cells using AMPS, Premier séminaire national sur la simulation numérique dans les sciences appliqués, Décembre 2016, Guelma, Algérie.

[2] **S. Boudour**, M. Hadjab, I. Bouchama, S. Laidoudi, Metal Oxide Heterojunction AZO/Cu_2O Solar Cell: numerical modeling of the temperature effect, 1ere Ecole d'hiver sur l'Analyse de cycle de vie Et L'Eco-conception, Février 2018, Boumerdès, Algérie.

[3] S. Laidoudi, C. Dehchar, L. Lamiri, R. Yekhlef, **S. Boudour**, R Boufnik, Effect of deposition time on the properties of Cu_2O thin film electrodeposited on ITO substrates, 1ere Ecole d'hiver sur l'Analyse de cycle de vie Et L'Eco-conception, Février 2018, Boumerdès, Algérie.

Optical Materials 72 (2017) 177–182

Contents lists available at ScienceDirect

Optical Materials

journal homepage: www.elsevier.com/locate/optmat

Quantum and conversion efficiencies optimization of superstrate CIGS thin-films solar cells using In_2Se_3 buffer layer

Idris Bouchama [a], Samah Boudour [a, b, c], Nadir Bouarissa [d, *], Zahir Rouabah [e]

[a] Electronic Department, Faculty of Technology, University M. Boudiaf, 28000, Msila, Algeria
[b] Research Centre in Industrial Technologies CRTI, P.O. Box 64, Cheraga, 16014, Algiers, Algeria
[c] Thin Films and Applications Unit (UDCMA), Setif, Algeria
[d] Laboratory of Materials Physics and its Applications, University of M'sila, 28000, M'sila, Algeria
[e] Materials and Electronic Systems Laboratory, University of Bordj-Bou-Arreridj, 34000, Bord-Bou-Arreridj, Algeria

ARTICLE INFO

Article history:
Received 27 March 2017
Received in revised form
26 May 2017
Accepted 30 May 2017

Keywords:
$Cu(In,Ga)Se_2$ material
Superstrate solar cells
Transparent conducting oxides
Barrier height
AMPS-1D

ABSTRACT

In this present contribution, AMPS-1D device simulator is employed to study the performances of superstrate SLG/TCO/p-$Cu(In,Ga)Se_2$(CIGS)/n-ODC/n-In_2Se_3/Metal thin film solar cells. The impact of the TCO and Metal work functions on the cell performance has been investigated. The combination of optical transparency and electrical property for TCO front contact layer is found to yield high efficiency. The obtained results show that the TCO work function should be large enough to achieve high conversion efficiency for superstrate CIGS solar cell. Nevertheless, it is desirable for Metal back contact layer to have low work function to prevent the effect of band bending in the n-In_2Se_3/Metal interface. Several TCOs materials and metals have been tested respectively as a front and back contact layers for superstrate CIGS solar cells. An efficiency of 20.18%, with $V_{oc} \approx 0.71$ V, $J_{sc} \approx 35.36$ mA/cm^2 and $FF \approx 80.42\%$, has been achieved with $ZnSn_2O_3$-based as TCO front contact layer. In the case of SnO_2:F front contact and indium back contact layers, an efficiency of 16.31%, with $V_{oc} \approx 0.64$ V, $J_{sc} \approx 31.4$ mA/cm^2 and $FF \approx 79.4\%$, has been obtained. The present results of simulation suggest an improvement of superstrate CIGS solar cells efficiency for feasible fabrication.

1. Introduction

$CuIn_{1-x}Ga_xSe_2$ (CIGS) has a major potential as a semiconductor material for thin film photovoltaic devices. This is due to its high optical absorption coefficient, appropriate band gap and outstanding electro-optical properties [1–3]. CIGS-based solar cells with x = 0.3 corresponds to a bandgap energy range of 1.1–1.2 eV yields the best efficiency both in laboratory and commercial solar cells [4,5]. Recently CIGS thin film solar cells approached efficiencies of 22.8% for substrate configuration [6]. The superstrate configuration is an alternate design, where the deposition sequence is reversed, the absorber is grown on glass coated with the transparent front contact (TFC), followed by an evaporated CdS or In_2Se_3 buffer layers and finished by a sputtered metallic back contact layer [7–9]. Further improvements of the superstrate CIGS solar cells performance require an accurate knowledge of the electronic loss mechanisms.

The properties of Transparent conducting oxide (TCO) films, such as resistivity, band-gap energy and work function, affect obviously the performance of solar device because they affect both the energy barrier height at the heterojunction interfaces and the electron field emission [10]. TCO films are n-type degenerated semiconductors (metallic oxides), they are formed from binary oxides, such as In_2O_3, SnO_2 and ZnO; ternary oxides, such as $Zn_2In_2O_5$, Zn_2SnO_4, $CdSb_2O_6$, $MgIn_2O_4$, $ZnSnO_3$, $GaInO_3$, and $In_4Sn_3O_{12}$ and multi-component oxides composed of combinations of these binary or ternary oxides [11]. The work function of the TCO films (W_{TCO}) has a critical importance in optoelectronic device performance, the change in work function and electron/hole injection barrier is related to the band alignment [12–14]. Ritzau et al. [15] have reported the role of the work function and back contact barrier height on the performance of a-Si:H solar cells. Besides, Belfar et al. [16] investigated the effect of W_{TCO} for the performance of n–i–p+ and n–i–p–p+ solar cells based on hydrogenated amorphous silicon (a-Si:H) and hydrogenated nanocrystalline silicon (nc-Si:H) absorber layers using AMPS-1D simulation tools. Furthermore, Hussain et al. [17] reported

* Corresponding author.
E-mail address: n_bouarissa@yahoo.fr (N. Bouarissa).

http://dx.doi.org/10.1016/j.optmat.2017.05.056
0925-3467/

that the high work function of ITO films can be used for barrier height modification of HIT solar cell and the wide band gap and highly doped ITO films behave electronically similar to metals elements and the electronic behavior of the ITO/*a*-Si:H(p) interface was assumed as similar to a metal/semiconductor junction. Recently, Bouchama et al. [18] have reported that the CIGS solar cell with superstrate configuration has a better photovoltaic performances when lighting through SnO_2:F front contact layer. Moreover, an efficiency higher than 16%, could be obtained for superstrate SLG/SnO_2:F/CIGS/ODC/In_2Se_3/Zn solar cell structure for 300 nm p-CIGS absorber thick.

This paper reports on systematic studies of TCO and Metal work functions including a discussion of their dependence on the superstrate SLG/TCO/p-CIGS/n-ODC/n-In_2Se_3/Metal solar cells photovoltaic properties. Our study is focused on reducing the potential barriers so as to increase carriers collection in the structure.

2. Device simulation and modeling

The model used in the simulation is simple as shown in Fig. 1. Up to five regions of different material parameters can be used to define the cell structure. The structure consists of SLG/TCO/p-$CuIn_{0.7}Ga_{0.3}Se_2$/n-ODC/n-In_2Se_3/Metal in which the light enters through the TCO layer is considered as the solar cell model in the simulation. We insert in the model a significant Ordered Defect Compounds (ODC) n-type layer between the In_2Se_3 and CIGS layers. This layer is usually created experimentally in the CIGS absorber part when the In_2Se_3 buffer layer is deposited onto SLG/TCO/CIGS substrate with high substrate temperature [8,9]. The AMPS-1D software estimates the steady state band diagram, recombination profile, carrier transport in one dimension based on the Poisson equation and the hole and electron continuity equations [19]. The recombination currents are calculated with the Shockley–Read–Hall (SRH) model

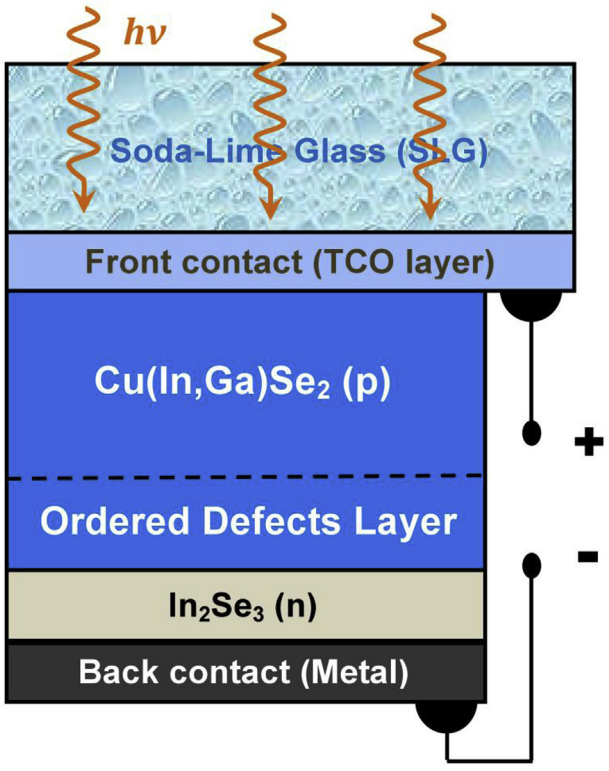

Fig. 1. Schematic cross section of superstrate CIGS solar cell structure.

for bulk defects. The layers parameters used for simulating the device performance are summarized in Table 1. The $CuIn_{0.7}Ga_{0.3}Se_2$ absorber and In_2Se_3 buffer parameters were fixed from our previous research work [18]. The radiation AM1.5G with incident power density of 100 mW/cm^2 is used as an illuminating source. In superstrate CIGS solar cells, a highly doped TCO front contact and Metal back contact layers serve as the front and back electrodes, respectively.

3. Results and discussion

3.1. Effect of TCO work function on cell performance

In the superstrate CIGS structure presented in Fig. 1, an n+-type TCO front contact can be believed to form a barrier with p-CIGS absorber part. The formation of a low resistance, low barrier TCO/p-CIGS front contact is among the most challenging aspects of high performance fabrication of superstrate CIGS solar cells. The wide band gap and highly doped TCO films behave electronically similar to metals elements and the electronic behavior of the TCO/semiconductor interface was assumed as similar to a metal/semiconductor junction [17]. Moreover, the TCO/p-type CIGS contact does not always form a barrier and has the possibility of forming an ohmic contact, which is determined by the difference in work functions between TCO and p-CIGS [20]. For a p-CIGS type semiconductor with band-gap E_g and electron affinity χ(CIGS), and a TCO with work function W_{TCO}, an ohmic TCO/p-CIGS contact is formed when: $W_{TCO} > E_g + \chi$(CIGS) and a rectifying (Schottky) barrier contact is formed when $W_{TCO} < E_g + \chi$(CIGS) [21]. Most TCO materials, however, do not have sufficiently high work-functions and therefore form a Schottky barrier contact to p-CIGS absorber layer.

The understanding of the effects of TCO work function on TCO/p-CIGS/n-ODC/n-In_2Se_3 solar cells in depth requires the calculation of the energy band diagram at thermodynamic equilibrium and the built-in electric field. Fig. 2 depicts the schematic band diagram of the TCO/p-CIGS/ODC part for different TCO work functions. The band bending on the p-CIGS part appeared along with the decrease of TCO work function. Two possible carrier transport mechanisms were expected. In the case of high TCO work function, an ohmic contact was formed in n+-TCO/p-CIGS interface and a direct recombination of holes in the valence band of p-CIGS and electrons in the conduction band of n+-TCO was occurred. The second is a trap-assisted tunneling even if the barrier is formed at the n+-TCO/p-CIGS interface [20]. Photogenerated holes in p-CIGS part can passes across the Schottky barrier and reach TCO contact easily thanks to a trap-assisted tunneling.

Table 1
Physical parameters used in the simulation model for superstrate CIGS solar cell.

Layer parameters	p–CIGS	n–ODC	n–In_2Se_3
W (nm)	500	3500	200
N_D (cm^{-3})	–	1×10^{15}	1×10^{18}
N_A (cm^{-3})	2×10^{16}	–	–
E_G (eV)	1.12	1.3	2.4
χ (eV)	4.1	4.1	3.8
N_c (cm^{-3})	2.2×10^{18}	2.2×10^{18}	2.2×10^{18}
N_v (cm^{-3})	1.8×10^{19}	1.8×10^{19}	1.8×10^{19}
$\varepsilon/\varepsilon_0$ (–)	13.6	13.6	10
μ_e (cm^2 V^{-1} S^{-1})	50	50	50
μ_h (cm^2 V^{-1} S^{-1})	12	12	12
N_{DG}, N_{AG} (cm^{-3})	D: 10^{14}	A: 10^{18}	A: 10^{18}
E_A, E_D (eV)	Mid–gap	Mid–gap	Mid–gap
W_G (eV)	0.1	0.1	0.1
σ_e (cm^2)	10^{-13}	10^{-13}	10^{-15}
σ_h (cm^2)	10^{-15}	10^{-11}	10^{-12}

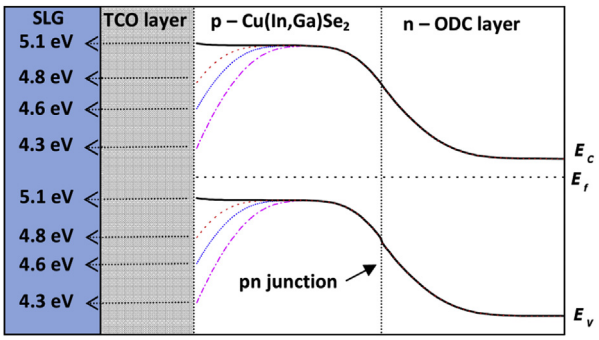

Fig. 2. Band structure in the TCO/p-CIGS interface with different TCO work functions.

The performance of superstrate SLG/TCO/p-CIGS/ODC/n-In_2Se_3/Metal solar cells will be investigated numerically by the variation of TCO work function (W_{TCO}). In the model, P-type CIGS and ODC layer parameters were fixed, and only the work function of TCO films was changed from 4 to 5.5 eV. Zn material was used in this section as a back contact. When TCO work function is below 5 eV, the transport of holes is limited because of the occurrence of the band bending in the p-CIGS part. In the case of the TCO work function is higher than 5 eV, the band bending in the p-CIGS absorber part is reduced to form a flat band. The increase in W_{TCO} leads to the decrease of the Schottky barrier height between TCO and p-CIGS layer; therefore more hole carriers can be collected at the front contact.

Different TCO work functions at the interface between TCO and p-CIGS layer will lead to different built-in electric field. Fig. 3 shows the distribution of built-in electric field in the structure as a function of TCO work function. Note that the electric field decreases gradually in the p-CIGS part near the TCO/p-CIGS interface. Nevertheless, in the region of n-ODC layer the built-in electric field keeps unchanged. In the p-CIGS part with $W_{TCO} \leq 5$ eV, the built-in electric field is positive near the interface, which hinders holes from reaching the front electrodes. When $W_{TCO} > 5.1$ eV, the built-in electric field is negative in the whole of p-CIGS region. This electric field gives the effective force on holes to move to the left region in Fig. 3, which is very beneficial for holes to transport through the p-CIGS region.

One of the aims of this simulation is to determine the proper work function of TCO front contact for designing high conversion efficiency of superstrate CIGS solar cell. So, it is necessary to calculate the photovoltaic parameters of the solar cell on the wide range

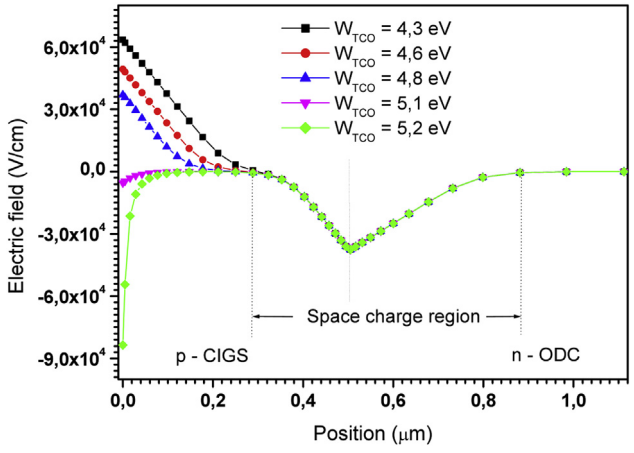

Fig. 3. Distribution of built-in electric field in the structure with various TCO work functions.

of variation of W_{TCO}. Fig. 4 shows the simulated performance of SLG/TCO/p-CIGS/n-ODC/n-In_2Se_3/Metal solar cells as a function of TCO work function. It is easy to note that when W_{TCO} is varied between 4.3 eV and 5.0 eV, the TCO work function has a little impact on J_{SC}. The open-circuit V_{OC} increases rapidly with W_{TCO}, and then become saturated at $W_{TCO} = 4.8$ eV. As the W_{TCO} increases, *FF* also increases due to the migration of holes from p-CIGS part to TCO front contact since the hole injection barrier was reduced. Reduction of the band bending was due to the decrease of the electric field at TCO/p-CIGS interface which can provide low leakage current. At $W_{TCO} = 4.8$ eV, we can achieve an efficiency of about 15.02%, $FF = 80.06\%$, $V_{OC} = 0.63$ V, $J_{SC} = 29.23$ mA/cm^2. It is obvious that at $W_{TCO} = 4.3$ eV, the cell has a poor performance with $\eta = 2.08\%$, $FF = 51.4\%$, $V_{OC} = 0.13$ V and $J_{SC} = 29.21$ mA/cm^2, while at $W_{TCO} = 5.4$ eV, the cell has a good performance with $\eta = 20.71\%$, $FF = 81.80\%$, $V_{OC} = 0.71$ V and $J_{SC} = 35.32$ mA/cm^2. The structure with TCO work function below 4.2 eV does not work at all. This simulation result manifests the critical effect of TCO work function in superstrate CIGS solar cells.

The front contact processes are designed to reduce the downward band-bending in the TCO/p-CIGS interface so that the barrier to holes is reduced and current can be collected. Several TCO layers have been tested in the model as a front contact layers for superstrate CIGS solar cells. Fig. 5 shows the cell-performance results with different TCO front contact layers. $ZnSnO_3$ n-type semiconductor with the wide band gap and high work function of ~5.3 eV, considered as a front contact material, is a potential

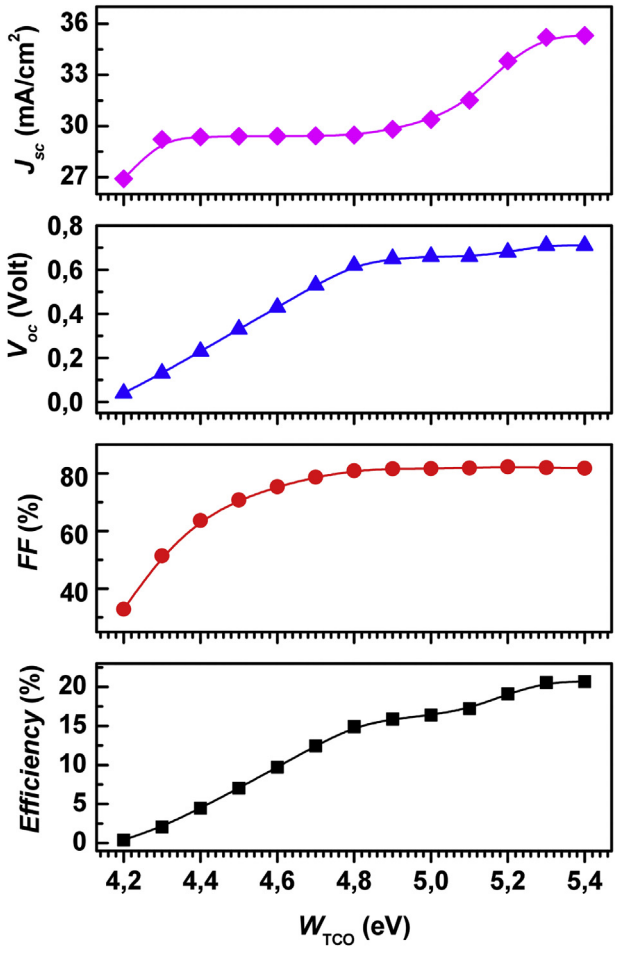

Fig. 4. Performance of superstrate CIGS solar cells as a function of TCO work function.

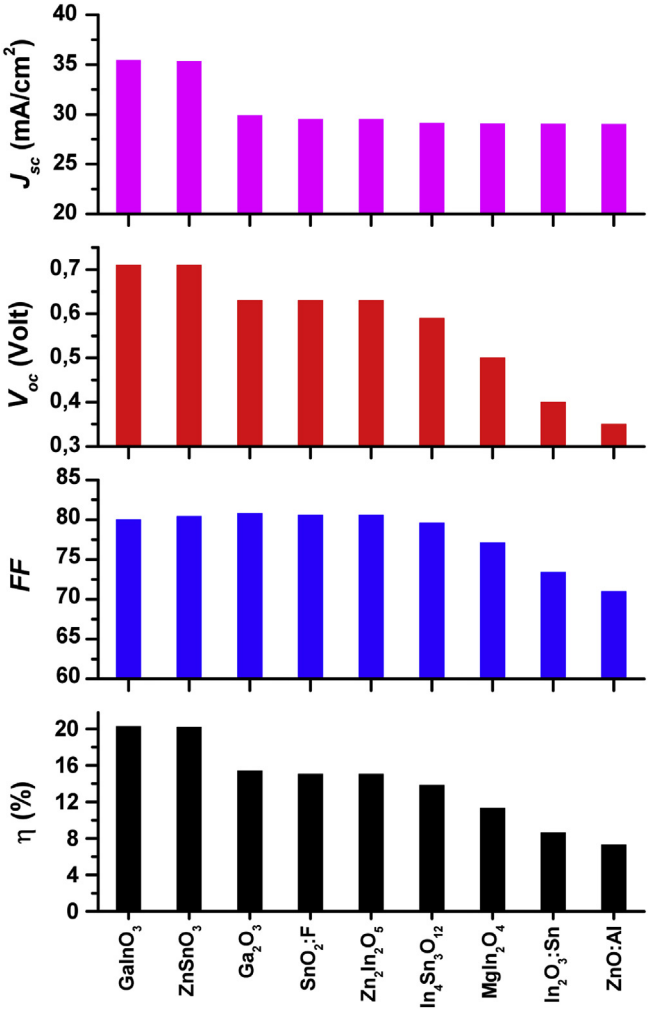

Fig. 5. A summary results of superstrate CIGS solar cells performances with different TCO films.

candidate for a good TCO. With $ZnSnO_3$ front contact we can achieve an efficiency of 20.17%, with $V_{oc} \approx 0.71$ V, $J_{sc} \approx 35.35$ mA/cm^2 and $FF \approx 80.4\%$. ITO films have a low work function which is about 4.6 eV. This degrades the conversion efficiency of solar cells to 8.63%. Solar cell with ZnO:Al front contacts showed also a poor efficiency of 7.31%. The SnO_2:F material with a work function of ~4.9 eV is another candidate similarly to TCO front contact for superstrate CIGS solar cells presenting an efficiency of 15.06%.

Spectral response of various TCO work functions was studied and presented in Fig. 6. With increasing W_{TCO}, the spectral response increases in short wavelength region. The quantum efficiency (QE) has a maximum value close to 80% under 100 mW/cm^2 when the TCO work function reaches 5.2 eV.

3.2. Effect of back metal work function

The metal back contact forms a barrier to n-type In_2Se_3 semiconductor which depends on the work function of both Metal and n-In_2Se_3 material. If the work function of an n-type In_2Se_3 semiconductor ($W_{n\text{-}SC}$) is greater than that of the Metal (W_{Metal}), $W_{n\text{-}SC} > W_{Metal}$, then the n-$In_2Se_3$/Metal heterojunction forms an ohmic contact. If the relative magnitudes are reversed, i.e. $W_{n\text{-}SC} < W_{Metal}$, then the n-$In_2Se_3$/Metal heterojunction forms a blocking or Schottky barrier [22]. The band bending in the n-In_2Se_3 buffer layer

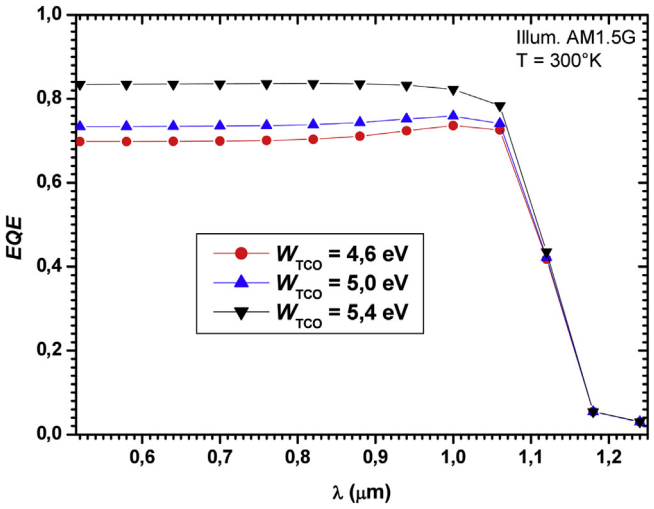

Fig. 6. Effect of TCO work function on the spectral response.

was occurs in the vicinity of the interface. The carrier (electron) transport across n-In_2Se_3/Metal interface is greatly affected by the barrier height resulting in the n-In_2Se_3/Metal interface. At high Metal work function, the tunneling mechanism through the barrier dominates the current transport with high doping n-type In_2Se_3 semiconductor used in the simulation ($N_D(In_2Se_3) = 1 \times 10^{18}$ cm^{-3}), while the thermionic emission acts as a secondary transport mechanism in the n-In_2Se_3/Metal interface. In the case of the thermal emission, the electron has to overcome the whole energy barrier, however, the tunneling takes place through the energy spike resulting in the n-In_2Se_3/Metal interface. The barrier height Φ_b is defined as the potential difference between the Fermi energy of the metal and the band edge where the majority carrier reside. For n-type In_2Se_3 semiconductor the barrier height is obtained as [23]:

$$\Phi_b = W_{Metal} - \chi(In_2Se_3) \quad (1)$$

where W_{Metal} is the work function of the metal and $\chi(In_2Se_3)$ is the electron affinity of the n-In_2Se_3 semiconductor. Fig. 7 shows the work function of selected metals and their calculated barrier height on n-In_2Se_3 part, where the metal work functions varied between 4.1 and 5.2 eV. We can see that the barrier height in the n-In_2Se_3/Metal interface can be varied from 0.2 to 1.3 eV by using various

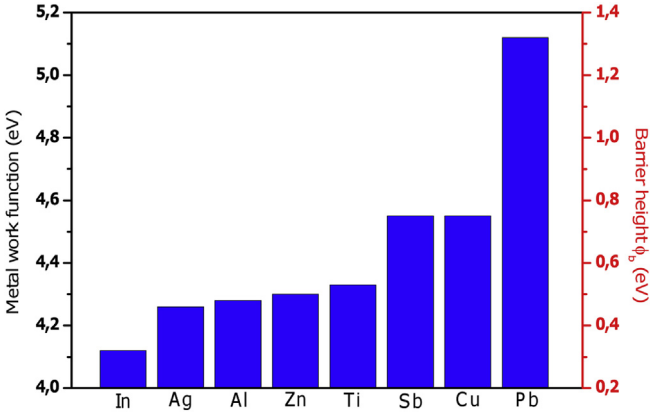

Fig. 7. Work function of selected metals and their calculated barrier height on n-type In_2Se_3 buffer layer.

metals.

To find the influence of the barrier height Φ_b, on cell performance, we have firstly varied the value of Φ_b from 0.46 to 0.6 eV and the simulated current density-voltage (J-V) characteristics are shown in Fig. 8. The results of the calculation were obtained by using SnO_2:F as a TCO front contact layer. It is evident from the behavior of the curves that only the fill factor *FF* was degraded with increasing the barrier height Φ_b. This may be due to the increase in the resistance and the presence of the rectifying n-In_2Se_3/metal junction which forms a Schottky barrier in the structure (Fig. 8). The high potential barrier prevents most charge carriers (electrons) from passing to the metal back contact. Only a small number of carriers have enough energy to overcome the whole energy barrier (thermoionic emission), however, the tunneling effect takes place in some cases. To clarify this dependence in an interval of variation, the barrier height Φ_b was varied from 0 to 0.9 eV.

Fig. 9 summarizes the output performance of J_{SC}, V_{OC}, fill factor (*FF*) and η as a function barrier height Φ_b. All photovoltaic parameters remain almost constant for barrier height below 0.4 eV. By an increase in Φ_b of more than 0.4 eV an incredible decrease in efficiency, V_{OC} and *FF* was found as revealed from Fig. 9. In this case, the majority carriers have insufficient energy to overcome the potential barrier, and are trapped on back side of the interface and cannot contribute to the diffusion current, reducing thus the solar cell performance. It is evident from Fig. 9 that the short-circuit current J_{SC} has a slight decrease as the Φ_b increases from 0.4 to 0.9 eV, which may be due to the tunneling enhancement. The use of SnO_2:F front contact and Zn back contact layers in the structure reported in Ref. [18] led to an efficiency of 15.12%, with $V_{oc} \approx 0.63$ V, $J_{sc} \approx 31.4$ mA/cm^2 and $FF \approx 74.6\%$. Using low metal work function as a metal back contact, such as indium (4.12 eV), a best efficiency of 16.31%, with $V_{oc} \approx 0.64$ V, $J_{sc} \approx 31.4$ mA/cm^2 and $FF \approx 79.4\%$, has been obtained.

4. Conclusion

The presence of the barrier height in the front and back contact layers of the superstrate SLG/TCO/p-CIGS/n-ODC/n-In_2Se_3/Metal solar cells can significantly affect the cell performance by limiting the carriers current flow. The influence of the TCO and Metal work function has been studied using AMPS-1D and the corresponding design optimization has been provided. According to the obtained results, the TCO work function should be large enough of over 4.8 eV to prevent the effect of absorber band bending caused by the difference in the work function between the p-type CIGS absorber and TCO front contact. We notice that all the photovoltaic parameters increase with increasing the TCO work function. This remarkably sharp rise has also been confirmed by the external quantum efficiency. The high W_{TCO} is used to inject holes in the front contact barrier. Thus, the desired values of work functions should be as high as possible. The high work function of $ZnSnO_3$ material is helpful in making low-resistance electrical contact to the *p*-type CIGS layer. Secondly, a significant performance improvement of the cell efficiency can be expected through the minimization of barrier height ($\leq$0.45 eV) in the n-In_2Se_3/Metal interface. When the barrier height of the n-In_2Se_3/Metal interface exceeds 0.5 eV, the degradation came from the reduction of the fill-factor *FF* and open-circuit voltage V_{OC}. The present results may help in the development of superstrate CIGS solar cells with high conversion efficiency and low cost.

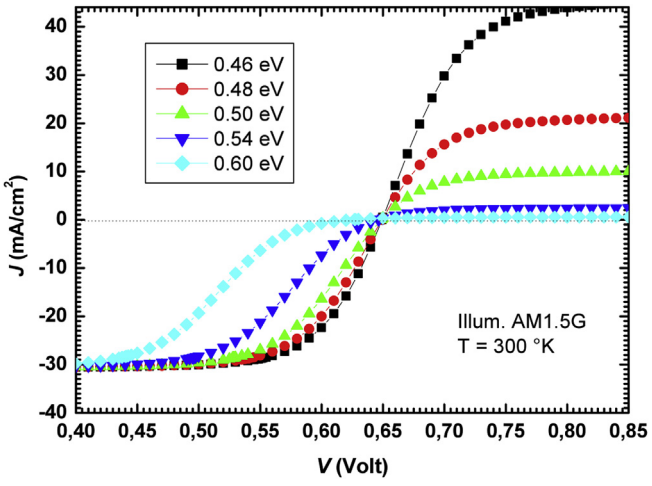

Fig. 8. J-V characteristics of the selected structure with different barrier heights Φ_b.

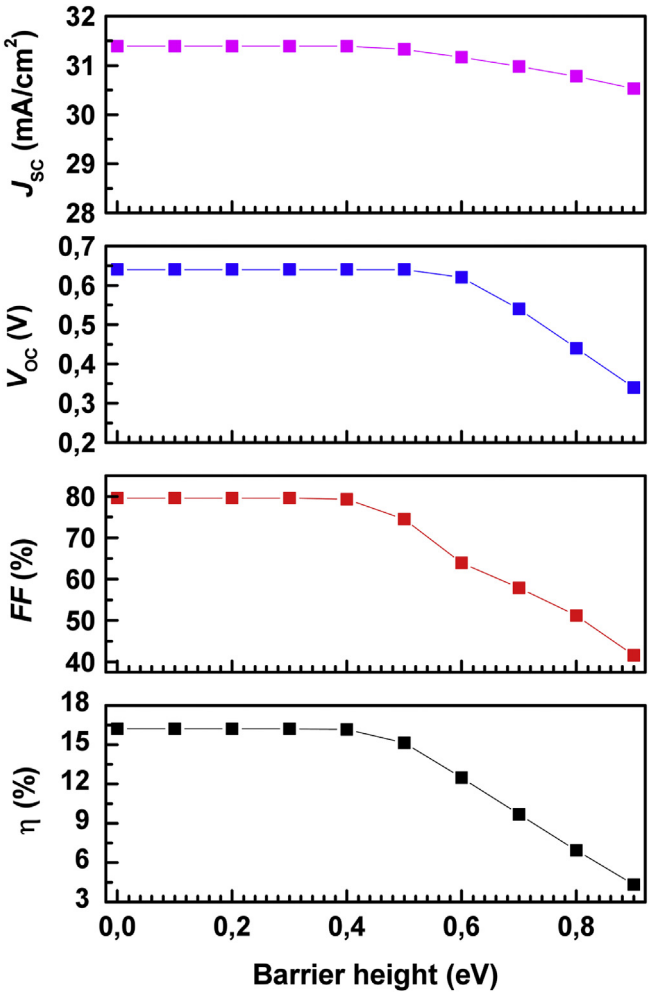

Fig. 9. Solar cell performances as a function of barrier height at the n-In_2Se_3/Metal interface.

Acknowledgements

The modeling calculation of this work used the AMPS-1D software developed by Dr. Fonash's group of Pennsylvania State University.

References

[1] J. Lauwaert, L.V. Puyvelde, J. Lauwaert, J.W. Thybaut, S. Khelifi, M. Burgelman,

F. Pianezzi, A.N. Tiwari, H. Vrielinck, Assignment of capacitance spectroscopy signals of CIGS solar cells to effects of non-ohmic contacts, Sol. Energy Mater. Sol. Cells 112 (2013) 78–83.
[2] S.U. Park, R. Sharma, K. Ashok, S. Kang, J.K. Sim, C.R. Lee, A study on composition, structure and optical properties of copper-poor CIGS thin film deposited by sequential sputtering of CuGa/In and In/(CuGa+In) precursors, J. Cryst. Growth 359 (2012) 1–10.
[3] A. Bouloufa, K. Djessas, D. Todorovic, Mat. Sci. Semicond. Proc. 12 (2009) 82.
[4] T. Eisenbarth, T. Unold, R. Caballero, C.A. Kaufmann, D. Abou-Ras, H.-W. Schock, Origin of defects in $CuIn_{1-x}Ga_xSe_2$ solar cells with varied Ga content, Thin Solid Films 517 (2009) 2244–2247.
[5] R. Baier, C. Leendertz, D. Abou-Ras, M.C. Lux-Steiner, S. Sadewasser, Sol. Energy Mater. Sol. Cells 130 (2014) 124–131.
[6] R. Kamada, T. Yagioka, S. Adachi, A. Handa, K. FaiTai, T. Kato, H. Sugimoto, New world record $Cu(In,Ga)(Se,S)_2$ thin film solar cell efficiency beyond 22%, in: 43rd IEEE Photovoltaic Specialists Conference, #355, 2016 available at: http://www.pvsc-proceedings.org/.
[7] K. Djessas, A. Abatchou, G. Masse, J. Appl. Phys. 88 (2000) 5710.
[8] K. Djessas, S. Yapi, G. Masse, J. Appl. Phys. 95 (2004) 4111.
[9] G. Masse, K. Djessas, J. Appl. Phys. 94 (2003) 6985.
[10] T. Minami, J. Vac. Sci. Technol. A 17 (1999) 1765–1772.
[11] T. Minami, T. Miyata, T. Yamamoto, Work function of transparent conducting multicomponent oxide thin films prepared by magnetron sputtering, Surf. Coat. Tech. 108–109 (1998) 583–587.
[12] L. Zhao, C.L. Zhou, H.L. Li, H.W. Diao, W.J. Wang, Sol. Energy Mater. Sol. Cells 92 (2008) 673–681.
[13] T. Minemoto, J. Julayhi, Curr. Appl. Phys. 13 (2013) 103–106.
[14] A. Chen, K. Zhu, Sol. Energy 107 (2014) 195–201.
[15] K.U. Ritzau, M. Bivour, S. Schröer, H. Steinkemper, P. Reinecke, F. Wagner, M. Hermle, TCO work function related transport losses at the a-Si:H/TCO-contact in SHJ solar cells, Sol. Energy Mater. Sol. Cells 131 (2014) 9–13.
[16] A. Belfar, Simulation study of the a-Si:H/nc-Si:H solar cells performance sensitivity to the TCO work function, the band gap and the thickness of i-a-Si:H absorber layer, Sol. Energy 114 (2015) 408–417.
[17] S.Q. Hussain, W.K. Oh, S. Ahn, A.H.T. Le, S. Kima, Y. Lee, J. Yi, RF magnetron sputtered indium tin oxide films with high transmittance and work function for a-Si:H/c-Si heterojunction solar cells, Vacuum 101 (2014) 18–21.
[18] I. Bouchama, K. Djessas, F. Djahli, A. Bouloufa, Thin Solid Films 519 (2011) 7280–7283.
[19] H. Zhu, A.K. Kalkan, J. Hou, S.J. Fonash, AIP Conf. Proc. 462 (1999) 309.
[20] T. Nakada, Y. Hirabayashi, T. Tokado, D. Ohmori, T. Mise, Sol. Energy 77 (2004) 739–747.
[21] S.H. Demtsu, Impact of Back-contact Materials on Performance and Stability of CdS/CdTe Solar Cells, PhD Thesis, Colorado State University, Fort Collins, Colorado, 2006.
[22] W. Mönch, Semiconductor Surfaces and Interfaces, Third Revised Edition, Springer, 2001.
[23] L. Zhu, G. Shao, J.K. Luo, Numerical study of metal oxide Schottky type solar cells, Solid State Sci. 14 (2012) 857–863.

Journal of Science: Advanced Materials and Devices 4 (2019) 111–115

Contents lists available at ScienceDirect

Journal of Science: Advanced Materials and Devices

journal homepage: www.elsevier.com/locate/jsamd

Original Article

A study of CdTe solar cells using Ga-doped $Mg_xZn_{1-x}O$ buffer/TCO layers: Simulation and performance analysis

Samah Boudour [a, b], Idris Bouchama [b], Nadir Bouarissa [c, *], Moufdi Hadjab [a]

[a] Research Center in Industrial Technologies CRTI, P.O. Box 64, Cheraga 16014, Algiers, Algeria
[b] Electronic Department, Faculty of Technology, University of Mohamed Boudiaf, M'sila, 28000, Algeria
[c] Laboratory of Materials Physics and Its Applications, University of M'sila, 28000 M'sila, Algeria

ARTICLE INFO

Article history:
Received 28 September 2018
Received in revised form
10 December 2018
Accepted 13 December 2018
Available online 18 December 2018

Keywords:
CdTe solar cells
Thin films
Ga-doped $Mg_xZn_{1-x}O$
AMPS-1D

ABSTRACT

The effect of stacked Ga-doped $Mg_xZn_{1-x}O$ (GMZO) thin films being the n-partner buffer layer and of the transparent conducting oxide (TCO) layer on the performance of CdTe thin film solar cells has been investigated. The diversity of the electrical and optical properties of GMZO films versus Ga and Mg doping concentrations suggested the use of low-Ga-doped $Mg_xZn_{1-x}O$ (LGMZO) films as a high resistance transparent buffer layer. Thus, a high-Ga-doped $Mg_xZn_{1-x}O$ (HGMZO) film is nominated as a transparent TCO layer. In this respect, a (n^+)-HGMZO/(n)-LGMZO/(p)-CdTe/$MoTe_2$/Mo suggested structure has been simulated using the Analysis of Microelectronic and Photonic Structures (AMPS-1D) software under the AM1.5G illumination and at a temperature of 300 K. The structure uses the molybdenum ditelluride ($MoTe_2$) layer as a back surface between the CdTe absorber layer and the Mo back contact. The effect of the thickness and the carrier concentration of the LGMZO-buffer, and of the CdTe absorber layers on the CdTe cell performance was investigated.

1. Introduction

During the last decades, transparent conductive thin film technologies have been materialized in fastest ways to achieve better electronic and optoelectronic devices, especially solar cell devices [1–3]. On the other hand, the CdTe material is a II–VI compound semiconductor with a near optimum band gap of 1.45 eV. For this reason, CdTe-based thin film heterojunction solar cells are the most capable applicant for high photovoltaic energy conversion [4–6]. These solar cells draw a theoretical efficiency of 29.7% within 2 μm of thickness [7] and confirmed lab-scale efficiencies of 19.6% and 21% were obtained by GE Global Research [8] and First Solar [9], respectively. However, till date, the absorber layer in the CdTe solar cells requires an alternative window and buffer dual-layers with dissimilar electronic properties (opposite polarities) to provide a thin electronic barrier in-between to separate the carriers.

In recent years, alloy thin film transparent conducting oxides (TCO), such as gallium-doped [10–14], aluminum-doped [15–17], indium-doped [18], nitrogen-doped [19], sodium-doped [20] and fluorine-doped [21] $Mg_xZn_{1-x}O$ have received considered attention. Among these alloys, the Ga-doped $Mg_xZn_{1-x}O$ thin films are n-type degenerated semiconductors, and hence are promising candidates in many technical applications, such as transparent electrodes for sandwich structure of light-emitting diodes (LEDs) [22,23] and transparent window layers for thin film solar cells [24]. Wei *et al.* [12,13] suggested that Ga-doped $Mg_xZn_{1-x}O$ (GMZO) thin films grown using pulsed laser deposition (PLD) have good and distinctive electro-optical properties by controlling the concentration of the Ga and Mg dopants. The authors demonstrated that the band gap of GMZO can be tailored to noticeable decimal places from 3.35 to 3.94 eV by using a few or almost negligible percent of Ga (0.05 at.% to 3 at.%) and Mg (5 at.% to 15 at.%). Furthermore, the absorption edge of these degenerate semiconductors was shifted to shorter wavelengths (200–300 nm) with the increasing charge carrier concentrations in which the overall transmittance was above 85% in the wavelength range from 370 to 800 nm. Also, the conductivity was increased or decreased by varying the concentration of the Ga dopant in the GMZO thin films. The low-Ga-doped $Mg_xZn_{1-x}O$ (LGMZO) films showed increased resistivity which could reach 0.9 Ω.cm. However, the high-Ga-doped $Mg_xZn_{1-x}O$ (HGMZO) films displayed a low resistivity which is in the order of 10^{-3} Ω.cm.

* *Corresponding author.*
E-mail address: n_bouarissa@yahoo.fr (N. Bouarissa).
Peer review under responsibility of Vietnam National University, Hanoi.

https://doi.org/10.1016/j.jsamd.2018.12.001

In the present work, the suitability of the GMZO thin films for the use as distinguished layers in CdTe solar cells is investigated. A computer simulation of a modified CdTe solar cell with two stacked GMZO thin films being the n-partner high-resistivity and transparency buffer layer (HRT-BL) and the TCO window layer is performed using the AMPS-1D software [26] under the AM1.5G illumination spectra and at the temperature of 300 K. The thickness and the carrier concentrations of the LGMZO-buffer and the CdTe absorber layers have been investigated and separately discussed to check their impacts on the four J-V characteristics, and hence on the performance of the CdTe solar cell substrate.

2. Device structure and simulation settings

Fig. 1 shows the schematic view of the modified substrate in the (n^+)-HGMZO window layer/(n)-LGMZO buffer layer/(p)-CdTe absorber layer/$MoTe_2$/Metal structure. The electrical properties of selected TCO and HRT-BL partner layers are given in Table 1. The $Mg_{0.05}Zn_{0.95}O$ film doped with high-Ga-content of 0.5 at.% showed the lowest electrical resistivity of about 19.7×10^{-4} Ω•cm with a carrier concentration of 9.3×10^{19} cm^{-3}, while the $Mg_{0.15}Zn_{0.85}O$ film doped with low-Ga-content of 0.05 at.% showed a high electrical resistivity of about 0.98 Ω•cm with a carrier concentration of 1.59×10^{18} cm^{-3} [13]. These interesting experimental data suggest the high electrical resistivity and high optical transparency LGMZO films for the buffer layer employment, while the HGMZO films are suitable for the TCO layer employment in CdTe solar cells. To improve the performance of our suggested CdTe cells, one needs to use a material with a high work function. As well-known, the CdTe material has a high work function of more than 5.7 eV [25]. Therefore, it is hard to form a good ohmic contact on the Mo back contact. To tackle this problem, we apply an efficient back ohmic surface that consists of a $MoTe_2$ thin layer with a tunable band gap and a high conductivity [26].

The One-dimensional Analysis of Microelectronic and Photonic Structures AMPS-1D code is used to analyze the one-dimensional transport physics in thin film solar cells by solving the two continuity equations and the Poisson's equation with six boundary conditions, and hence the analysis of the capture cross -section of the electrical and optical parameters such as the discrete energy levels, the concentrations of electrons and holes at the position x along the stacked layers of structure [27]. Tables 2 and 3 describe the parameters of layers needed in AMPS-1D simulator. These parameters were thickness w, permittivity constant ε_r, band gap E_g, electron affinity $q\chi$, electron/hole mobility μ_n/μ_p, effective density of states in conduction/valence band N_c/N_v, donor/acceptor concentration N_d/N_a, the barrier height potentials, the reflections and the thermal velocity recombination for holes/electrons S_n/S_p at front and back contact interfaces.

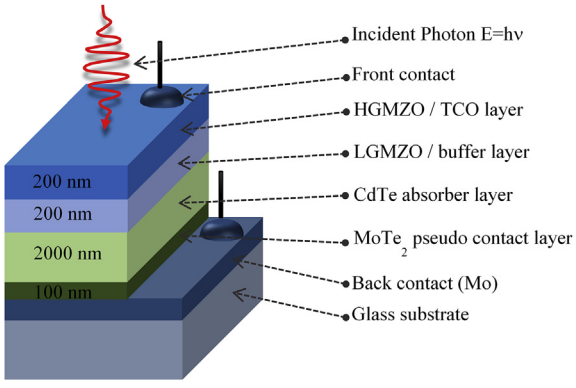

Fig. 1. Schematic view of modified CdTe thin film solar cell.

Table 1
Electrical properties of selected TCO and HRT-BL layers [12,13].

Property	Unit	n^+-HGMZO	n-LGMZO
Ga concentration	%	0.5	0.05
Mg concentration	%	5	15
Doping concentration, N_d	cm^{-3}	9.2×10^{19}	1.59×10^{18}
Mobility	$cm^2\ V^{-1}\ s^{-1}$	34	4.0
Resistivity	Ω.cm	19×10^{-4}	0.98×10^{-2}
Band gap energy, E_g	eV	3.47	3.73

n^+-HGMZO: (0.5 at.%) Ga-doped $Mg_{0.05}Zn_{0.95}O$.
n-LGMZO: (0.05 at.%) Ga-doped $Mg_{0.15}Zn_{0.85}O$.

Table 2
Numerical data of employed material layers needed for AMPS-1D simulation.

Property	n^+-HGMZO	n-LGMZO	p-CdTe	$MoTe_2$
$W\ (nm)$	200	200	2000	100
ε_r	9	9	9.4	13
$\mu_n\ (cm^2V^{-1}s^{-1})$	34	4	320	110
$\mu_p\ (cm^2V^{-1}s^{-1})$	11	1.5	40	426
$N_a(cm^{-3})$	0	0	1×10^{18}	1×10^{15}
$N_d\ (cm^{-3})$	9.3×10^{19}	1.59×10^{18}	0	0
$E_G\ (eV)$	3.47	3.73	1.45	0.97
$N_C\ (cm^{-3})$	2.2×10^{18}	2.2×10^{18}	7.5×10^{17}	3×10^{18}
$N_V\ (cm^{-3})$	1.8×10^{19}	1.8×10^{19}	1.8×10^{19}	4×10^{18}
$q\chi\ (eV)$	4.3	4.3	4.28	4.2

Table 3
Settings tor front and back contact.

Parameter	Front contact	Back contact
$\Phi_{Bo}/\Phi_{Bl}\ (eV)$	0	0.4
$S_n\ (cm/s)$	1.0×10^7	1.0×10^7
$S_p\ (cm/s)$	1.0×10^7	1.0×10^7
Reflectance	0.07	0.4

From Table 2, the electron affinities of LMGZO, CdTe and $MoTe_2$ are 4.3 eV, 4.28 eV and 4.2 eV, respectively, and the band gaps are 3.73 eV, 1.45 eV and 0.97 eV, respectively. These parameters are used to determine the band offsets at layer/layer interfaces. A conduction band offset (ΔE_C) at the n-LGMZO/p-CdTe interface is only 0.02 eV [(E_G of LGMZO)-(E_G of CdTe)] and at CdTe/$MoTe_2$ interface is only 0.08 eV [(E_G of CdTe)-(E_G of $MoTe_2$)], while the valence band offset (ΔE_V) at CdTe/$MoTe_2$ interface is large of about 0.56 eV [($q\chi$+E_G of $MoTe_2$)-($q\chi$+E_G of CdTe)].

3. Results and discussion

Fig. 2 shows the band diagram profiles and the depletion region of the (n^+)-HGMZO/(n)-LGMZO/(p)-CdTe/$MoTe_2$ structure calculated by the AMPS-1D at equilibrium conditions for an acceptor concentration of CdTe, N_a varying from 1×10^{14} to 1×10^{18} cm^{-3}.

From Fig. 2b, when N_a of CdTe is 1×10^{14} cm^{-3}, the depletion region fills the most of CdTe and the electric field is weak and deeply constant. The depletion regions become narrow when N_a has a value beyond 1×10^{16} cm^{-3}. The narrow depletion region influences the buildup of the electric field which reduces the free charge carrier recombination within it.

In Fig. 3, the *J-V* curves are shifted to higher voltages when N_a of CdTe is varied up from 1×10^{14} to 1×10^{18} cm^{-3}. These voltage shifts (from 0.05 V to 0.969 V) suggest that the open-circuit voltage (when the current density is equal to zero) is strongly dependent on N_a of CdTe. For higher N_a of CdTe, the electric field build-up within the depletion region is influenced. The increase of the

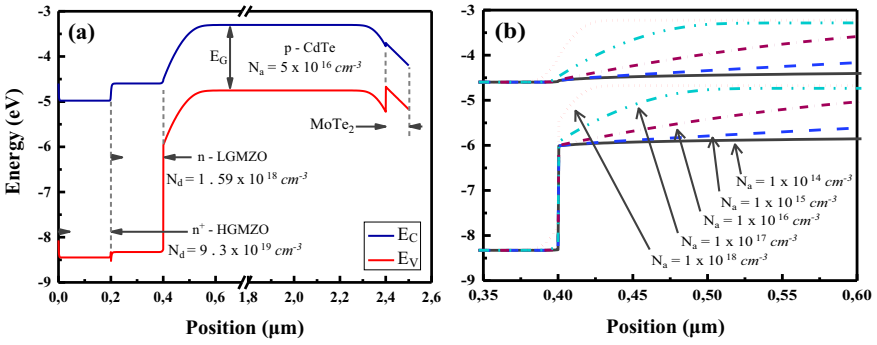

Fig. 2. (a) Band diagram profile at thermodynamic equilibrium conditions and (b) the behavior of the depletion region for various carrier concentrations N_a of CdTe absorber layer.

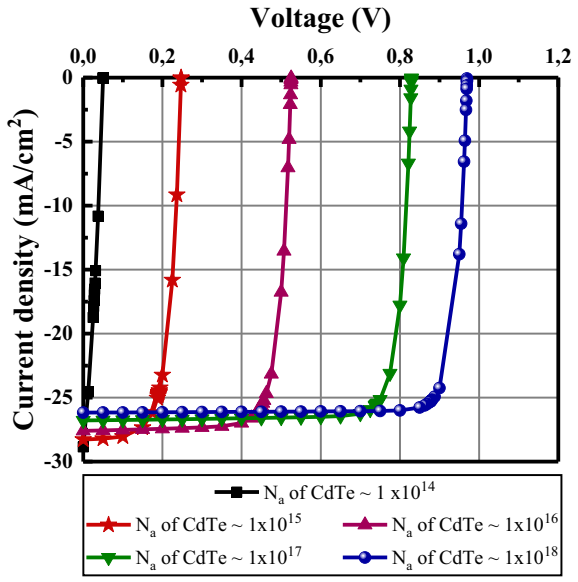

Fig. 3. Simulated *J-V* characteristics for proposed structure with different acceptor concentrations N_a of CdTe absorber layer.

electric field leads to the reduction of the free charge carrier recombination, which increases strongly the open-circuit voltage.

3.1. Effect of the donor concentration N_d in the LGMZO-buffer layer on the cell performance

Fig. 4 summarizes, top to bottom, the behaviors of the short-circuit current (J_{SC}), the efficiency (Efficiency), the open-circuit voltage (V_{OC}) and the fill factor (FF) *J-V* characteristics for a layered structure shown in Fig. 1 with the settings shown in Tables 2 and 3 under the effect of the donor concentration N_d of the LGMZO layer. With varying N_d from 1×10^{17} cm^{-3} to 1×10^{20} cm^{-3}, the cell gives slight improvements of J_{SC}, Efficiency and FF, from 25.68 to 26.32 mA/cm^2, 18.63–20.28% and 82.3–87.4%, respectively. This is due to the low absorption coefficient of the GMZO material. Thus, the cell performance was not affected by the LGMZO doping concentration.

3.2. Effect of the LGMZO-buffer layer thickness on the cell performance

Fig. 5 summarizes the effect of the LGMZO buffer layer thickness (from 10 nm to 700 nm) on the performance of the CdTe solar cell. Because of its wide band gap of 3.73 eV there are no considerable

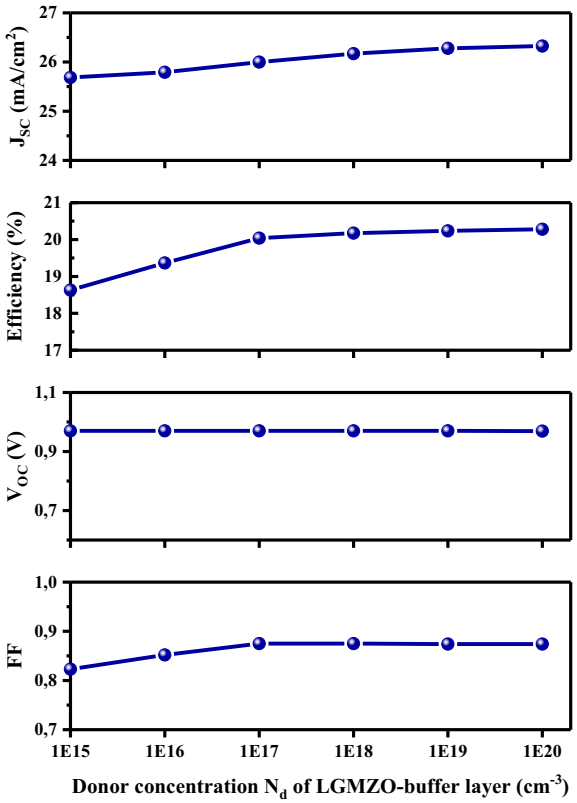

Fig. 4. Effect of the donor concentration N_d of the LGMZO-buffer layer on the CdTe solar cell performance.

carriers generated in the LGMZO buffer bulk. As expected, from top to bottom, the J_{SC}, the Efficiency, the V_{OC} and the FF all showed fixed performance parameters of J_{sc}~26.20 mA/cm^2, Efficiency~20.91%, V_{OC}~0.97 V and FF~87.4%.

3.3. Effect of the acceptor concentration N_a of the CdTe-absorber layer on the CdTe cell performance

As seen in Fig. 6, the Efficiency, the V_{OC} and the FF increased significantly with the increase of the acceptor concentration N_a from 1×10^{14} cm^{-3} to a tolerable limit of 1×10^{18} cm^{-3}. However, J_{SC} decreases from 28.85 to 26.87 mA/cm^2 which is attributed as due to the increase of the free carrier charge recombination that takes place within the bulk. The V_{OC} increases strongly from 0.05 to 0.97 V, and hence the fill factor FF increases sharply from 33% to the maximum value of 87.4%. The efficiency reaches its maximum value

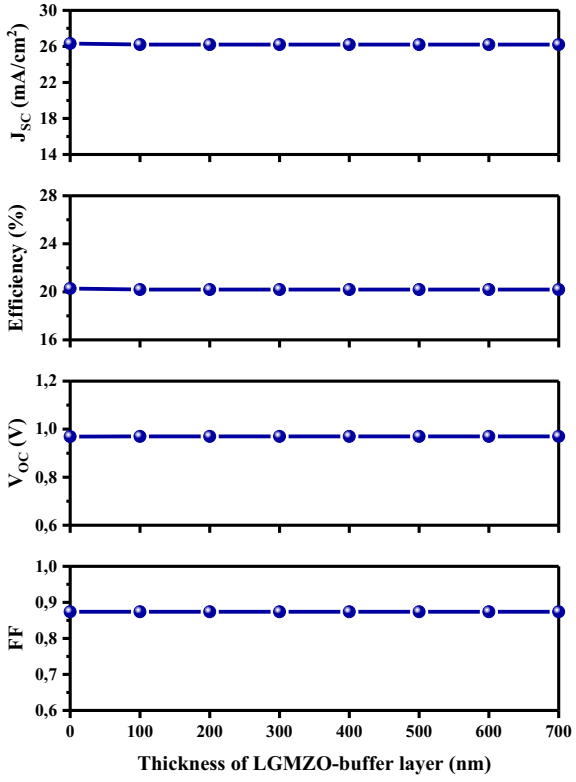

Fig. 5. Effect of the LGMZO-buffer layer thickness on the CdTe solar cell performance.

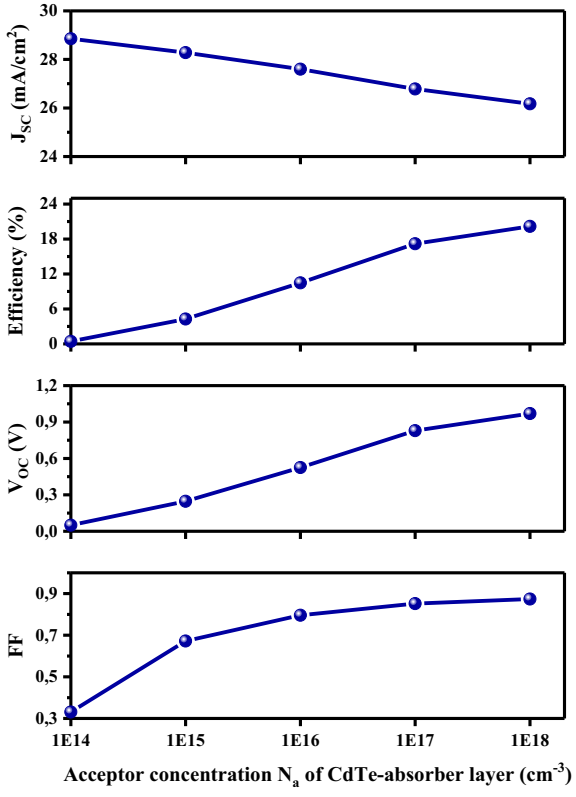

Fig. 6. Effect of the CdTe acceptor concentration N_a on the CdTe solar cell performance.

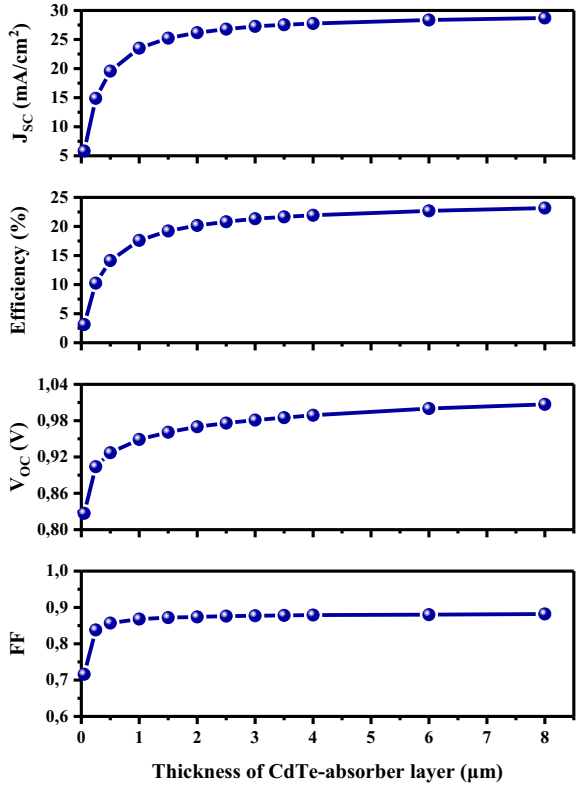

Fig. 7. Effect of the CdTe absorber layer thickness on the CdTe solar cell performance.

of 20.16%. Thus, an optimum performance of the CdTe thin film solar cells can be obtained with an acceptor concentration of about 1×10^{18} cm^{-3}.

3.4. Effect of the CdTe absorber layer thickness on the cell performance

The curves shown in Fig. 7 summarize, from top to bottom, the behaviors of J_{SC}, Efficiency, V_{OC} and FF as a function of the thickness of the CdTe absorber layer, which was varied from 50 nm to 8 µm for the CdTe solar cell. The $MoTe_2$ back surface layer of 100 nm thickness is arranged in order to alienate the back contact from the depletion region and to avoid the feedback of the electrons to the contact. All characteristics are improved significantly with the increasing CdTe absorber layer thickness. At the thickness of 50 nm of the CdTe layer, J_{SC}, Efficiency, V_{OC} and FF are found of 5.18 mA/cm^2, 3.13%, 0.827 V and 71.6%, respectively. When the thickness of the absorber layer is 2 µm, the cell shows the performance parameters of J_{SC}~26.207 mA/cm^2, Efficiency~20.16%, V_{OC}~0.97 V and FF~87.4%, respectively. And at the adsorber layer thickness of 8 µm, the cell exhibits the corresponding performance parameters of J_{SC}~28.70 mA/cm^2, Efficiency~23.17%, V_{OC}~1.00 V and FF~88.2%. The Efficiency improvement is mostly correlated to the increase of J_{SC} which is due to the increase of the collected carriers generated by the absorbed photons in the thicker absorber layer. It is noticed that there is an improvement of about ~85% in the Efficiency between the innitially tested thickness 50 nm and the greatest thickness 2 µm. Increasing the thickness by 6 µm (on going from 2 to 8 µm) causes an improvement of ~16% in the Efficiency. Thus, the optimum thickness of the CdTe absorber layer is chosen of about 2 µm.

4. Conclusion

In summary, a study of the CdTe solar cell using the Ga-doped $Mg_xZn_{1-x}O$ buffer/TCO layers has been performed using the AMPS-1D software under the AM1.5G illumination. Our results showed that the high band gap LGMZO material is found to be important in producing the stable HRT-BL layer for the CdTe solar cell. Thus, the main role of the LGMZO layer with a high resistivity, is to achieve a thinner buffer layer. Besides, our results support the previous findings regarding a CdTe absorber layer with an optimal thickness of 2 μm and a doping density of 1×10^{18} cm^{-3}. The output of the AMPS-1D simulation tool showed that an optimized LGMZO/CdTe hetero-junction gives performance of J_{SC}~26.207 mA/cm^2, Efficiency~20.16%, V_{OC}~0.97 V and FF~87.4%.

Acknowledgements

The authors acknowledge the use of the AMPS program developed by S. Fonash and colleagues at the Pennsylvania State University.

References

[1] K.L. Chopra, S. Major, D.K. Pandya, Transparent conductors-A status review, Thin Solid Films 102 (1983) 1–46.
[2] A.J. Freeman, K.R. Poeppelmeier, T.O. Mason, R.P.H. Chang, T.J. Marks, Chemical and thin film strategies for new transparent conducting oxides, Mater. Res. Soc. Bull. 25 (2000) 45–51.
[3] E. Fortunato, D. Ginley, H. Hosono, D.C. Paine, Transparent conducting oxides for photovoltaics, Mater. Res. Soc. Bull. 32 (2007) 242–247.
[4] B.M. Basol, in: Thin Film CdTe Solar Cells -A Review, Record of Photovoltaic Specialists Conference, vol. 1, IEEE, US, New York, 1990, pp. 588–594.
[5] A. Nowshad, S. Kamaruzzaman, K. Makoto, Numerical modeling of CdS/CdTe and CdS/CdTe/ZnTe solar cells as a function of CdTe thickness, Sol. Energy Mater. Sol. Cells 91 (2007) 1202–1208.
[6] A. Salavei, I. Rimmaudo, F. Piccinelli, A. Romeo, Influence of CdTe thickness on structural and electrical properties of CdTe/CdS solar cells, Thin Solid Films 535 (2013) 257–260.
[7] K. Mertens, Photovoltaics: Fundamentals, Technology and Practice, John Wiley & Sons, Chichester, UK, 2014, p. 115.
[8] M.A. Green, K. Emery, Y. Hishikawa, W. Warta, E.D. Dunlop, M.A. Green, Solar cell efficiency tables (Version 45), Prog. Photovolt. Res. Appl. 22 (2014) 701–710.
[9] M.A. Green, K. Emery, Y. Hishikawa, W. Warta, E.D. Dunlop, M.A. Green, Solar cell efficiency tables (Version 47), Prog. Photovolt. Res. Appl. 24 (2016) 3–11.
[10] C. Harada, H.J. Ko, H. Makino, T. Yao, Phase separation in Ga-doped MgZnO layers grown by plasma-assisted molecular-beam epitaxy, Mater. Sci. Semicond. Process. 6 (2003) 539–541.
[11] Z. Chen, G. Fang, C. Li, S. Sheng, G. Jie, X.Z. Zhao, Fabrication and vacuum annealing of transparent conductive Ga-doped $Zn_{0.9}Mg_{0.1}O$ thin films prepared by pulsed laser deposition technique, Appl. Surf. Sci. 252 (2006) 8657–8661.
[12] W. Wei, C. Jin, J. Narayan, R.J. Narayan, Optical and electrical properties of bandgap engineered gallium-doped $Mg_xZn_{1-x}O$ films, Solid State Commun. 149 (2009) 1670–1673.
[13] W. Wei, C. Jin, J. Narayan, R.J. Narayan, Optical and electrical properties of gallium-doped $Mg_xZn_{1-x}O$, J. Appl. Phys. 107 (2010) 013510.
[14] V. Awasthi, S.K. Pandey, V. Garg, B.S. Sengar, P. Sharma, S. Kumar, C. Mukherjee, S. Mukherjee, Plasmon generation in sputtered Ga-doped MgZnO thin films for solar cell applications, J. Appl. Phys. 119 (2016) 233101.
[15] M. Lorenz, E.M. Kaidashev, H. von Wenckstern, V. Riede, C. Bundesmann, D. Spemann, G. Benndorf, H. Hochmuth, A. Rahm, H.C. Semmelhack, M. Grundmann, Optical and electrical properties of epitaxial $(Mg,Cd)_xZn_{1-x}O$, ZnO, and ZnO:(Ga,Al) thin films on c-plane sapphire grown by pulsed laser deposition, Solid State Electron. 47 (2003) 2205–2209.
[16] K. Ellmer, G. Vollweiler, Electrical transport parameters of heavily-doped zinc oxide and zinc magnesium oxide single and multilayer films heteroepitaxially grown on oxide single crystals, Thin Solid Films 496 (2006) 104–111.
[17] K. Fleischer, E. Arca, C. Smith, I.V. Shvets, Aluminium doped $Zn_{1-x}Mg_xO$-A transparent conducting oxide with tunable optical and electrical properties, Appl. Phys. Lett. 101 (2012) 121918.
[18] C.H. Lau, L. Zhuang, K.H. Wong, In-doped transparent and conducting cubic magnesium zinc oxide thin films grown by pulsed laser deposition, Phys. Status Solidi B 244 (2007) 1533–1537.
[19] M.M. Morshed, Z. Zuo, J. Huang, J.G. Zheng, Q. Lin, X. Yan, J. Liu, Photoluminescence study of nitrogen-doped p-type $Mg_xZn_{1-x}O$ nanocrystalline thin film grown by plasma-assisted molecular beam epitaxy, Appl. Phys. A 117 (2014) 1467–1472.
[20] S.K. Pandey, V. Awasthi, B.S. Sengar, V. Garg, P. Sharma, S. Kumar, C. Mukherjee, S. Mukherjee, Band alignment and photon extraction studies of Na-doped MgZnO/Ga-doped ZnO heterojunction for light-emitter applications, J. Appl. Phys. 118 (2015) 165301.
[21] L. Liu, Z. Mei, Y. Hou, H. Liang, A. Azarov, V. Venkatachalapathy, A. Kuznetsov, X. Du, Fluorine doping: a feasible solution to enhancing the conductivity of high-resistance wide bandgap $Mg_{0.51}Zn_{0.49}O$ active components, Sci. Rep. 5 (2015) 15516.
[22] W.S. Liu, Y.H. Liu, W.K. Chen, K.P. Hsueh, Transparent conductive Ga-doped MgZnO/Ag/Ga-doped MgZnO sandwich structure with improved conductivity and transmittance, J. Alloys Compd. 564 (2013) 105–113.
[23] S.H. Jang, Y.R. Jo, Y.W. Lee, S.M. Kim, B.J. Kim, J.H. Bae, H.C. An, J.S. Jang, Formation mechanism of thermally optimized Ga-doped MgZnO transparent conducting electrodes for GaN-based light-emitting diodes, Electron. Mater. Lett. 11 (2015) 494–499.
[24] B.H. Shim, H.J. Jo, D.J. Kim, J.M. Chae, Enhanced efficiency of transmit and receive module with Ga doped MgZnO semiconductor device by growth thickness, J. Semicond. Technol. Sci. 16 (2016) 39–43.
[25] B.L. Williams, J.D. Major, L. Bowen, L. Phillips, G. Zoppi, I. Forbes, K. Durose, Challenges and prospects for developing CdS/CdTe substrate solar cells on Mo foils, Sol. Energy Mater. Sol. Cells 124 (2014) 31–38.
[26] N. Dhar, P. Chelvanathan, K.S. Rahman, M.A. M Bhuiyan, M.M. Alam, K. Sopian, A. Nowshad, Effect of p-type transition metal dichalcogenide molybdenum ditelluride (p-MoTe2) layer formation in cadmium telluride solar cells from numerical analysis, in: IEEE 39th Photovoltaic Specialists Conference (PVSC) 14116353, 2013, pp. 3487–3492.
[27] S.J. Fonash, A manual for one-dimensional device simulation program (AMPS), Electron. Mater. Process. Res. Lab. (2007). Peensylvania State University.

Optical Materials xxx (xxxx) xxx

Contents lists available at ScienceDirect

Optical Materials

journal homepage: http://www.elsevier.com/locate/optmat

Optimization of defected ZnO/Si/Cu_2O heterostructure solar cell

Samah Boudour [a,b], Idris Bouchama [b,*], Moufdi Hadjab [a], Samiha Laidoudi [a]

[a] Thin Films Development and Applications Unit UDCMA, Setif – Research Center in Industrial Technologies CRTI, B. O. Box 64, Cheraga, 16014, Algiers, Algeria
[b] Electronic Department, Faculty of Technology, University of Msila, Msila, 28000, Algeria

ARTICLE INFO

Keywords:
Heterostructure
Solar cell
Cu_2O
Si
AMPS-1D simulator
J-V characteristics

ABSTRACT

In the present work, we review the optimization of the performance of a newly defected ZnO/Si/Cu_2O heterojunction solar cell using the Analysis of Microelectronic and Photonic Structures (AMPS-1D) computer simulator under the AM1.5G illumination and the operating temperature of 300 K. The light J-V characteristics were investigated by varying the input parameters and the temperature. The use of p-type Cu_2O-back layer in the structure is to enhance the open-circuit voltage (V_{OC}). The performance of ZnO/Si/Cu_2O heterojunction solar cell is studied in order to optimize the layers parameters, such as the thickness of p-Si absorber layer, the doping and the defects concentrations of the p-Si absorber layer and to obtain an efficient proposed structure. The defects concentration of p-Si absorber layer was fixed in the first step at N_{def}(p-Si) = 10^{14}/cm^3. With the optimized p-Si layer parameters, an efficiency of 16.23% was obtained with J_{SC} ~26.25 mA/cm^2, V_{OC} ~0.72 V and *FF*~0.85 for n-ZnO window (0.1 μm)/p-Si Absorber (10 μm)/p-Cu_2O (0.1 μm) heterostructure. For N_{def}(p-Si) lower than 10^{14}/cm^3, the AMPS-1D simulation showed an appreciable performance. For N_{def}(p-Si) = 10^{11}/cm^3 we estimate best characteristics of about: J_{SC} ~27.57 mA/cm^2, V_{OC} ~0.78 V, *FF*~0.90 and Eff ~ 21.78%.

1. Introduction

Intrinsic or doped, either by oxygen vacancies or by substitution of some of the atoms, zinc oxide (ZnO) and cuprous oxide (Cu_2O) based semiconductors have received increasing concern because of their strong points of earth-abundance, non-toxicity, tunable optical band gap, low-cost in resources and ease of processing by versatile technology routes. Such pulse laser deposition [1], sol gel [2], electrodeposition [3], spray [4,5], sputtering [6,7] and other methods [8,9] are potential technologies offers a range of versatile new features and enhancements that meet the needs of ZnO and Cu_2O based applications. So far a large number of studies have been widely conducted to apply ZnO and Cu_2O semiconductors in broad applications such as gas sensors [10,11], glucose sensors [12,13], photocatalyst [14–16], photodegradation sensors [17–20], photoelectrochemical sensors [21], photoluminescence sensors [17,22,23], conductive switching [24] and photovoltaic (PV) devices [25–29].

ZnO thin films are electrically a high n-type conductive and optically an excellent transparent (85%) in the visible range. Furthermore, they have wide energy band gap of around ~3.37 eV at room temperature with high carrier concentration, where they act extensively as most suitable n-type partner with common p-type thin films such as Cu_2O [25, 29], CIGS [30], CdTe [31] and silicon [32]. In addition, Cu_2O thin films are non-stoichiometric, electrically natural p-type conductive and optically absorbing in the short-wavelength considered amount (~10^4/cm) of the luminous spectrum as they have direct energy band gap of 1.9–2.1 eV [18,26,33] with low carrier concentrations of ~10^{-16} cm^{-3} at room temperature [9]. However, the low photovoltaic efficiency of metal oxide-based photovoltaics is still challenging. In other words, ZnO and Cu2O based semiconductors are still under further development in order to become suitable candidates for new photovoltaic heterostructures. Up till now, the achieved practical power conversion efficiencies of the most common ZnO/Cu_2O heterojunction solar cells are remained significantly at lower percentages of ~6% because of some drawbacks, such as the non-ideal band alignment between the two heterojunction-sides and the defects within the layers [34–37]. Nevertheless, the sufficient electrical and optical properties of Cu_2O thin films strongly nominate them to other PV-uses. In particular, to enhance the open-circuit voltage (V_{OC}) by adding Cu_2O back-layer in CuO based solar cells, the one dimensional simulation of Zhu et al. [38] has shown that the conversion efficiency increased from 19% for a non-defected TiO_2/CuO two-layer structure to 28.5% for a non-defected TiO_2/-CuO/Cu_2O three-layers structure. Considering the enormous use of the robust and expensive crystalline silicon materials in advanced photonics

* Corresponding author. Tel.: +213 671 38 16 48.
E-mail address: idris.bouchama@univ-msila.dz (I. Bouchama).

https://doi.org/10.1016/j.optmat.2019.109433
Received 19 August 2019; Received in revised form 23 September 2019; Accepted 30 September 2019

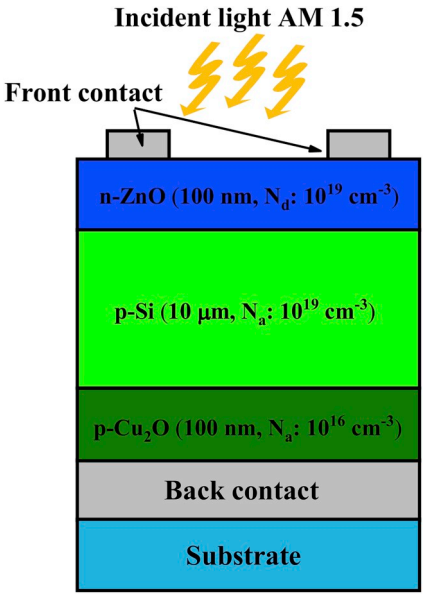

Fig. 1. Schematic of the newly ZnO/Si/Cu_2O heterostructure solar cell.

and electronics, it should be advisable to motivate the present-day extensively studied materials such as the TCOs and chalcopyrite thin films by using them as partners or supporters, side by side with thin films of crystalline silicon. Recently, based on one-dimensional simulator (SCAPS) and using an absorber of 1 µm of CIGS backed by 1 µm of crystalline silicon (c-Si) thin film in order to minimize the indium and gallium constituents, Heriche et al. [30] have reported conversion efficiency of 21.3%. In addition, because of its transparency and excellent electrical properties, ZnO has been integrated as n-type partner with p-type silicon to fabricate low cost thin film solar cells. Currently, the achieved practical power conversion efficiencies of the ZnO/Si heterojunction solar cells are also remained at modest percentages, under 8.5% [39,40]. This modesty is likely due to the strong dependence of the common ZnO/Si heterojunction performance on the properties of deposited ZnO films. Here, ZnO/Si/Cu_2O heterojunction has high harvest of photons because of its double distinct p-type band gaps. The incident photons having energies smaller than the band gap of ZnO and greater than the band gap energy of Si will be absorbed near the depletion region as they competently transmit through the ZnO window. Those photons who have absorption length longer than the absorber

Table 1
Settings for ZnO, Si and Cu_2O layers used in the simulation.

Parameters	n-ZnO	p-Si	p-Cu_2O
w (µm)	0.1	10	0.1
$\varepsilon/\varepsilon_0$	9.0	11.9	9.0
E_g(eV)	3.37	1.12	2.1
$N_{a,d}$(cm^{-3})	N_d: 1×10^{19}	N_a: 1×10^{19}	N_a: 1×10^{16}
χ_e(eV)	4.5	4.05	3.2
μ_n($cm^2V^{-1}s^{-1}$)	100.0	1450	20.0
μ_p($cm^2V^{-1}s^{-1}$)	25.0	500	40.0
N_c(cm^{-3})	2.22×10^{18}	2.80×10^{19}	2.20×10^{18}
N_v(cm^{-3})	1.8×10^{19}	2.65×10^{19}	1.11×10^{19}
N_{def}(cm^{-3})	1×10^{14}	1×10^{14}	1×10^{14}

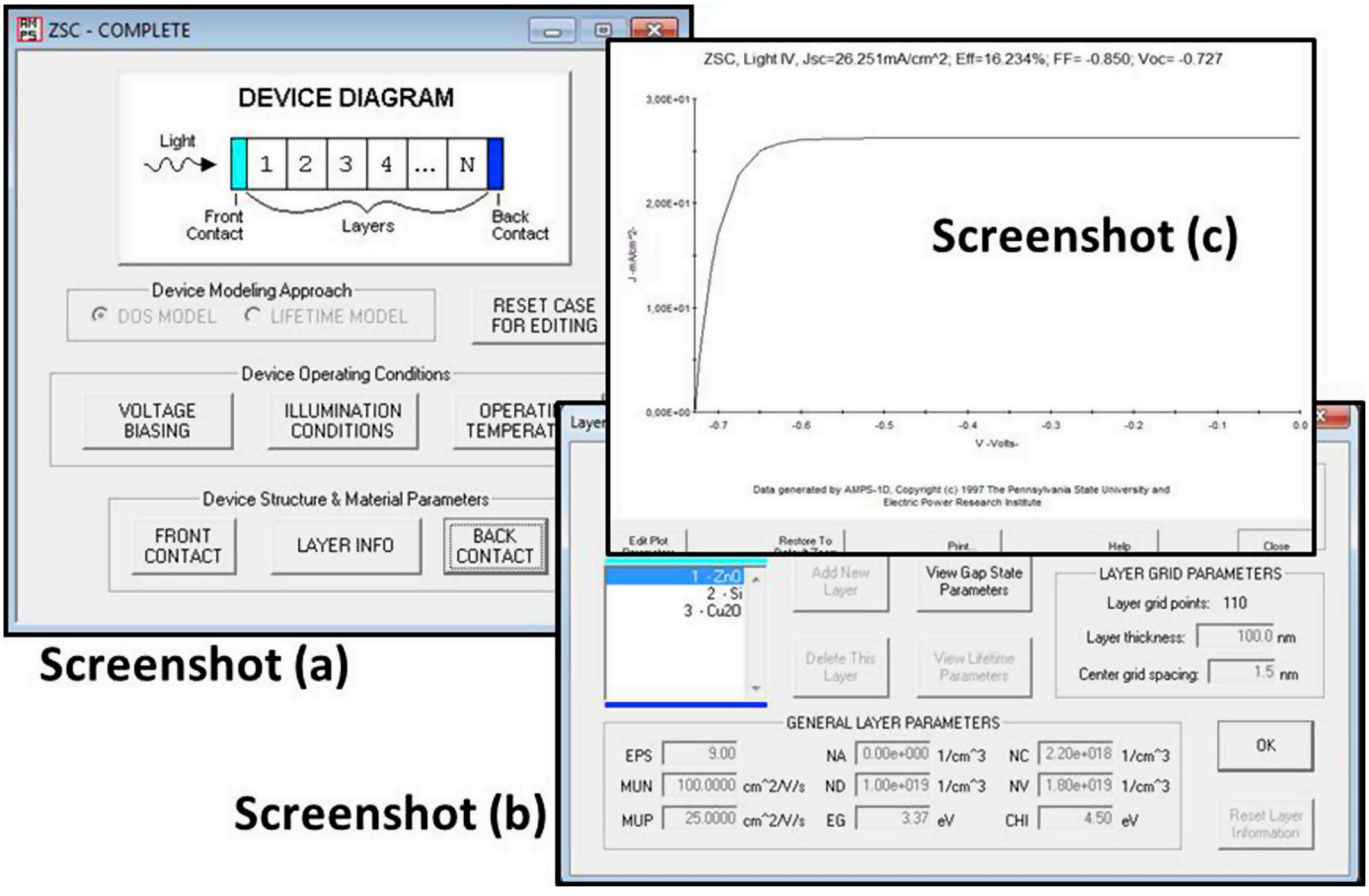

Fig. 2. Typical data input panels of the AMPS-1D graphical user interface, allowing to set the solar cell device and its settings.

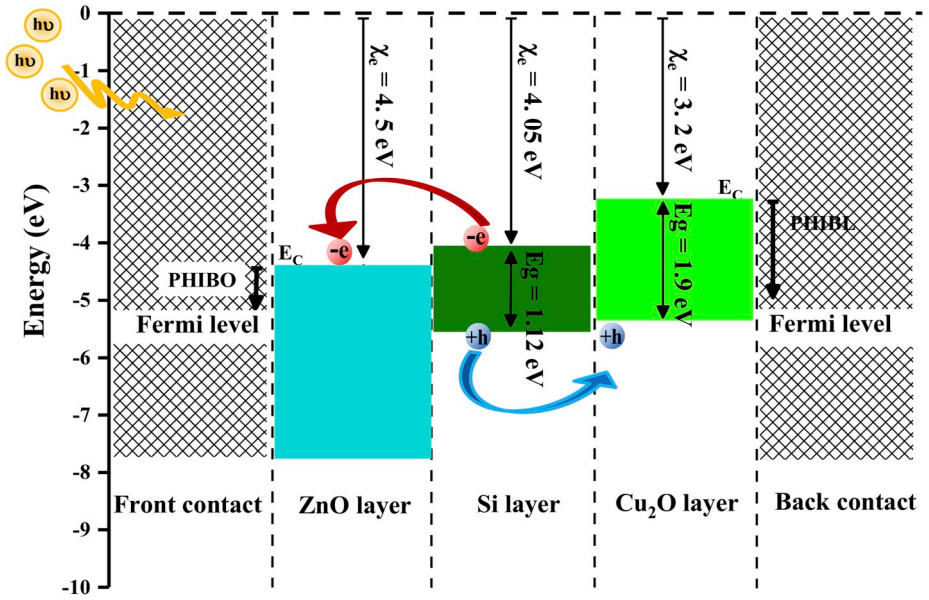

Fig. 3. Separated layers-energy level diagram of ZnO/Si/Cu_2O solar cell heterostructure.

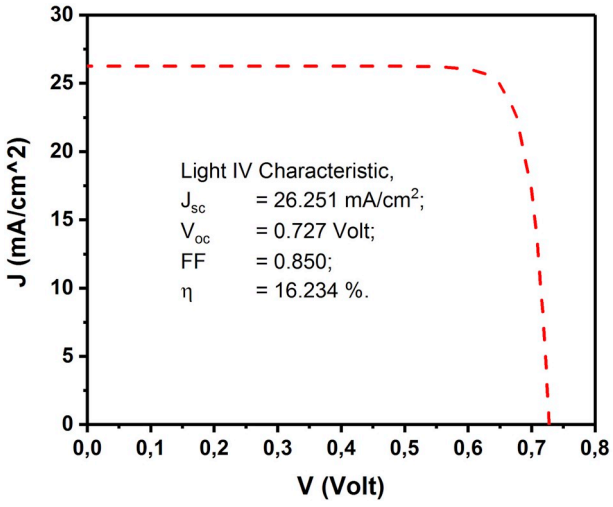

Fig. 4. Light J-V curve of the 0.1 μm-ZnO/10 μm-Si/0.1 μm-Cu_2O solar cell.

interlayer thickness and successfully traveled in the thin film Si interlayer will be absorbed into Cu_2O back layer. The Cu_2O back layer itself will be also acting as barrier layer between p-Si material and the back contact to enhance the open circuit voltage V_{OC} [38] of the ZnO/Si heterojunction.

To avoid wasting resources, effort and time, solar cell community need to understand, explain and solve the physic and technology interferences of solar cell devices by using numerical simulators [30,31,40,41]. These requirements have been reflected on the development of solar cells in which diverse abundant/non-abundant and low/high-cost materials, as well as their large influencing parameters, have been explored to renovate solar cell devices. The freely available Analysis of Microelectronic and Photonic Structures (AMPS-1D) one dimensional program was developed in 1990's by professor Fonash's team at the Pennsylvania State University [42].

In this paper, AMPS-1D simulator was considered to optimize a newly proposed defected ZnO/Si/Cu_2O heterojunction solar cell. The structure is analyzed numerically by changing different input parameters of the device such as thickness, doping and defect densities, and temperature. We examine the structural templates ZnO/Si/Cu_2O by light J-V characteristics and their electrical parameters: the short circuit current (J_{SC}), the open circuit voltage (V_{OC}), the fill factor (*FF*) and the efficiency (η).

2. Device settings and simulation process

Fig. 1 shows schematic of the newly proposed n-ZnO/p-Si/p-Cu_2O heterostructure solar cell. In order to analyze the transport physics in this structure, AMPS-1D solves the dipolar problems of device according to the Poisson equation and the continuity equations for electrons and holes. AMPS-1D simulator is a software environment, which is used to emulate a real solar cell behavior. In general, the simulation process would have to go through the following steps described by the screenshots in Fig. 2. The screenshot (a) shows the typical information input panel of the AMPS-1D graphical user interface for simulation process of solar cell. The input buttons in this panel allow to specify the model of simulation and to access to the device operating conditions and the device structure and material parameters panels. The DOS mode is chosen for the device simulation. The screenshot (b) demonstrates the structure and the set of the material parameters of one particular layer as well as the input buttons of optical properties and defects. The screenshot (c) shows the results of light J-V characteristics visualized in the form of curve and axes. During simulation handling, the AM1.5 illumination spectrum with incident power of 100 mW/cm^2 is considered. The input parameters of each layer of the proposed structure have been summarized in Table 1. These parameters were the thickness, *t*, permittivity constant $\varepsilon/\varepsilon_0$, band gap E_g, electron affinity χ_e, electron/hole mobility μ_n/μ_p, effective density of states in conduction/valence band N_c/N_v, donor/acceptor concentration N_D/N_A, defect concentration N_{def} and the absorption coefficient in the range wavelength of 320–1100 nm. At the front contact, the reflection was neglected. The thermal velocity recombinations for holes/electrons S_n/S_p at front and back contacts were 1.0×10^7 *cm/s*. In Addition, the barrier height potentials *PHIBO* and *PHIBL* were considered Ohmic or slight Schottky barrier. As shown in Fig. 3, *PHIBO* (*PHIBL*) is the difference between the work function of the metal front-contact (back-contact) and the electron affinity of the semiconductor in contact [E_C-E_F] with the unit of eV at front (back) contact.

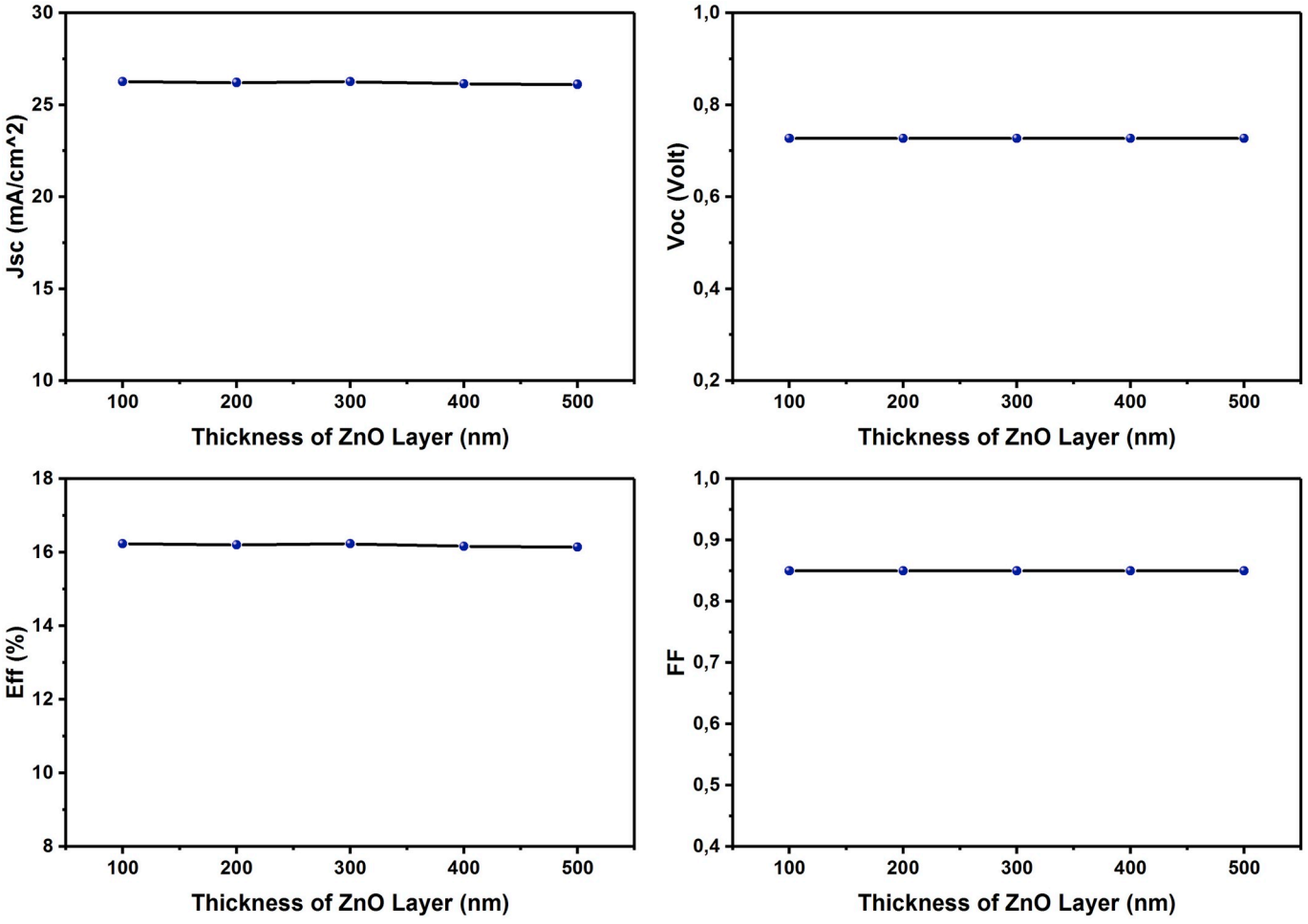

Fig. 5. Photovoltaic parameters of defected ZnO/Si/Cu_2O solar cell as a function of ZnO window layer thickness.

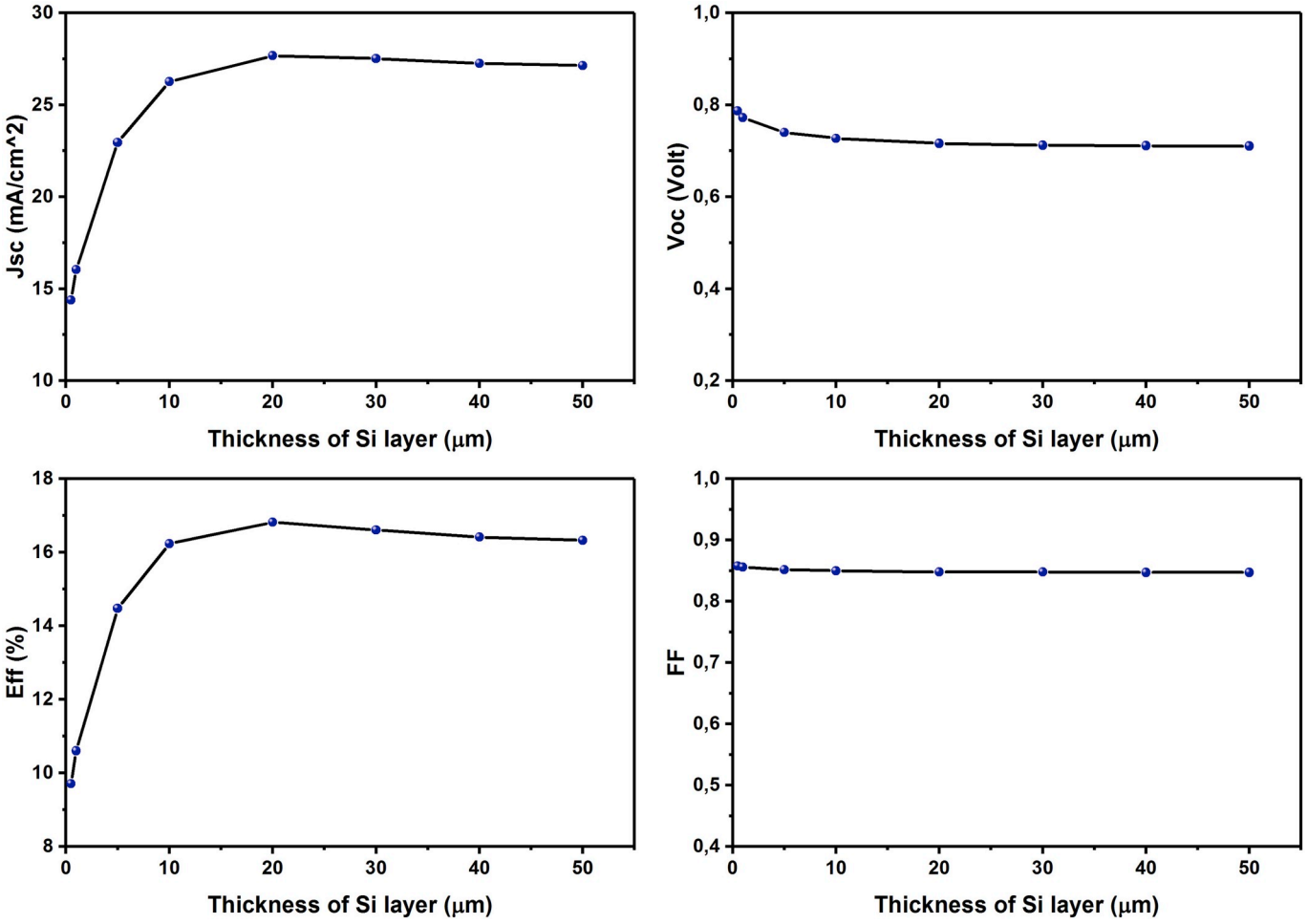

Fig. 6. Photovoltaic parameters of defected ZnO/Si/Cu_2O solar cell as a function of p-Si absorber layer thickness.

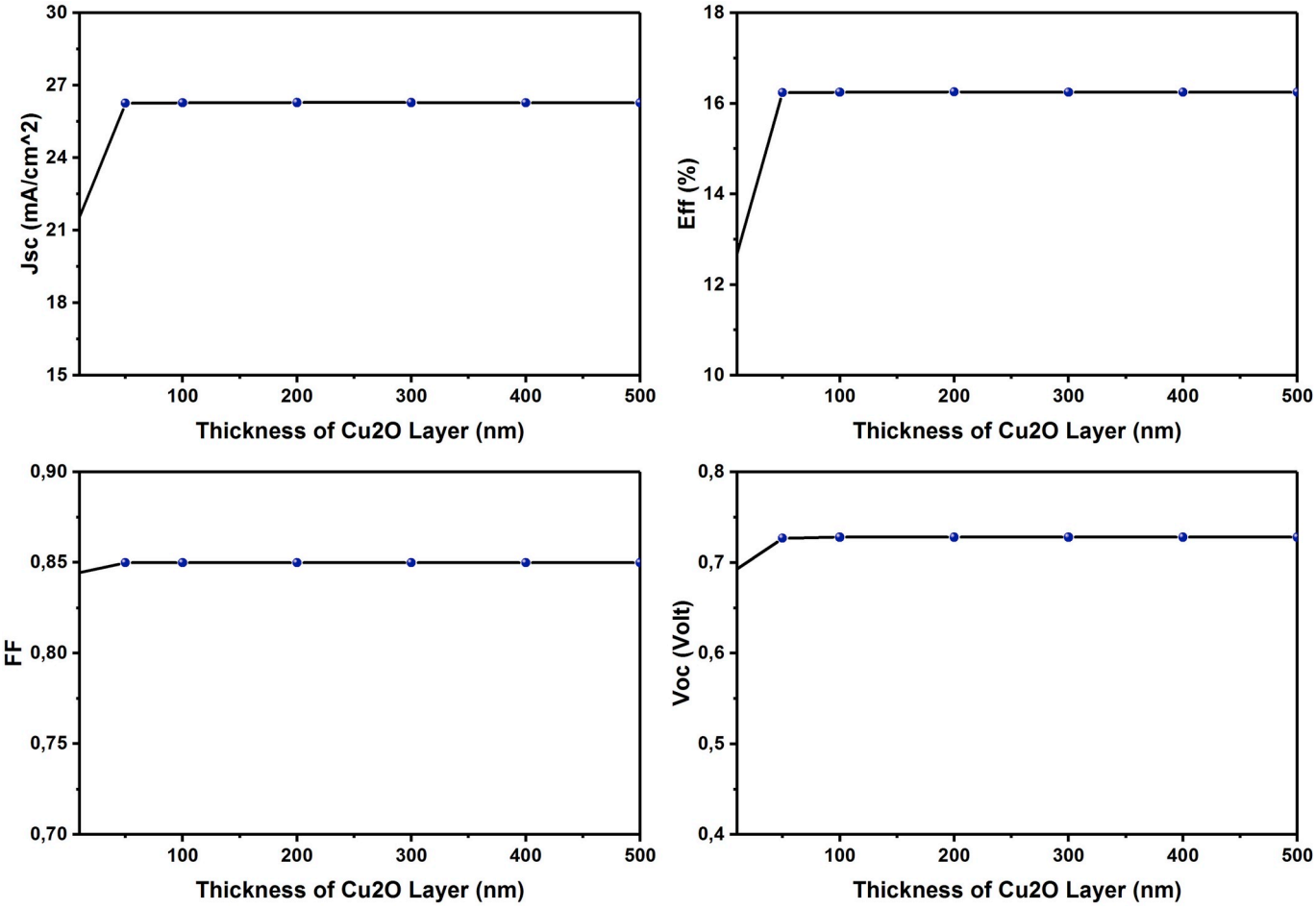

Fig. 7. Photovoltaic parameters of defected ZnO/Si/Cu_2O solar cell as a function of p-Cu_2O back layer thickness.

3. Results and discussion

In this section, we will examine the performance of the ZnO/Si/Cu_2O solar cell based on the settings summarized inTable 1. Fig. 3 shows the separated energy levels diagram for the ZnO, Si, Cu_2O layers. The conduction band offset (ΔE_C) at the ZnO/Si junction is the difference between the electron affinities of the ZnO and Si semiconductors: $\Delta\chi = \chi_{Si} - \chi_{ZnO} = -0.45$ eV. The obtained cliff will allow the transport of photo-generated electrons to get form p-Si absorber layer to ZnO emitter layer before they recombine. On the other hand, the small valence band offset (ΔE_V) for Si/Cu_2O is found to be about −0.07 eV [$(\chi_{Cu2O} + E_{gCu2O}) - (\chi_{Si} + E_{gSi}) = -0.07$eV]. Therefore, this established semi-alignment will allow the holes flowing through the rear contact. Thus, there is a good alignment between ZnO and Si and between Si and Cu_2O.

The light current density-voltage (J-V) characteristics are the fitting of current density versus the voltage. Based on the settings mentioned in Table 1, the light J-V curve and its characteristics, are shown in Fig. 4. The defect concentration of p-Si absorber layer was fixed at N_{def}(p-Si) = 10^{14}/cm^3. It has been demonstrated a good performance: η ~16.234% with J_{SC} ~26.251 mA/cm^2, V_{OC} ~0.727 V and *FF* ~0.85.

3.1. Effect of the ZnO layer thickness on the cell performance

Fig. 5 summarizes the effect of the ZnO window layer thickness on the performance of the ZnO/Si/Cu_2O solar cell from 100 nm to 500 nm. As shown in Fig. 5, all J-V characteristics remain unchanged and a fixed efficiency of about 16.2% was obtained, with J_{SC} ~26.2 mA/cm^2, V_{OC} ~0.72 V and *FF* ~0.85. This behavior is a result of the deficient carrier generation in the ZnO layer due to its wide band-gap energy of 3.37 eV.

3.2. Thickness optimization of p-Si absorber layer

Fig. 6 shows the evolution patterns of V_{OC}, J_{SC}, *FF* and η of ZnO/Si/Cu_2O solar cell as a function of p-Si absorber layer thickness from 0.5 μm to 50 μm. Particularly,J_{SC} and η increase rapidly from 14.37 to about 26.25 mA/cm^2 (by ~ 45.23%) and from 9,71 to about 16.23% (by ~ 40.17%), respectively, when the Si-layer thickness increases from 0.5 to 10 μm. While, V_{OC} (~0.7 V) and *FF* (~0.85) are almost unchanged. For a thick p-Si absorber layer (more than 10 μm), all photovoltaic parameters have almost unchanged values. This overall behavior is resulted from the increase of the photons absorption and even the increase of the electron-hole generation in the p-Si absorber layer. Therefore, the thickness of 10 μm is chosen as an optimum thickness for p-Si absorber layer for efficient ZnO/Si/Cu2O solar cell. This is consistent with what has been found in previous research. It was reported that 10–50 μm thick c-Si based solar cells can have conversion efficiencies up to ~17%. Reuter et al. [43] reported that an efficiency of 17% is achieved on mono-crystalline silicon solar with thickness of approximately 47 μm, which is fabricated by using transfer layer process. Yoon et al. [44] reported an efficiency of about 17.5% within 15 μm thick crystalline Si solar cells. Cruz-Campa et al. [45] obtained an efficiency of 14.9% within 14 μm thick crystalline silicon solar cells. Li et al. [46] attempted to demonstrate that tandem ultra-thin a-Si/c-Si solar cells with a nanopyramid structure could obtain efficiencies as high as 13.3% within

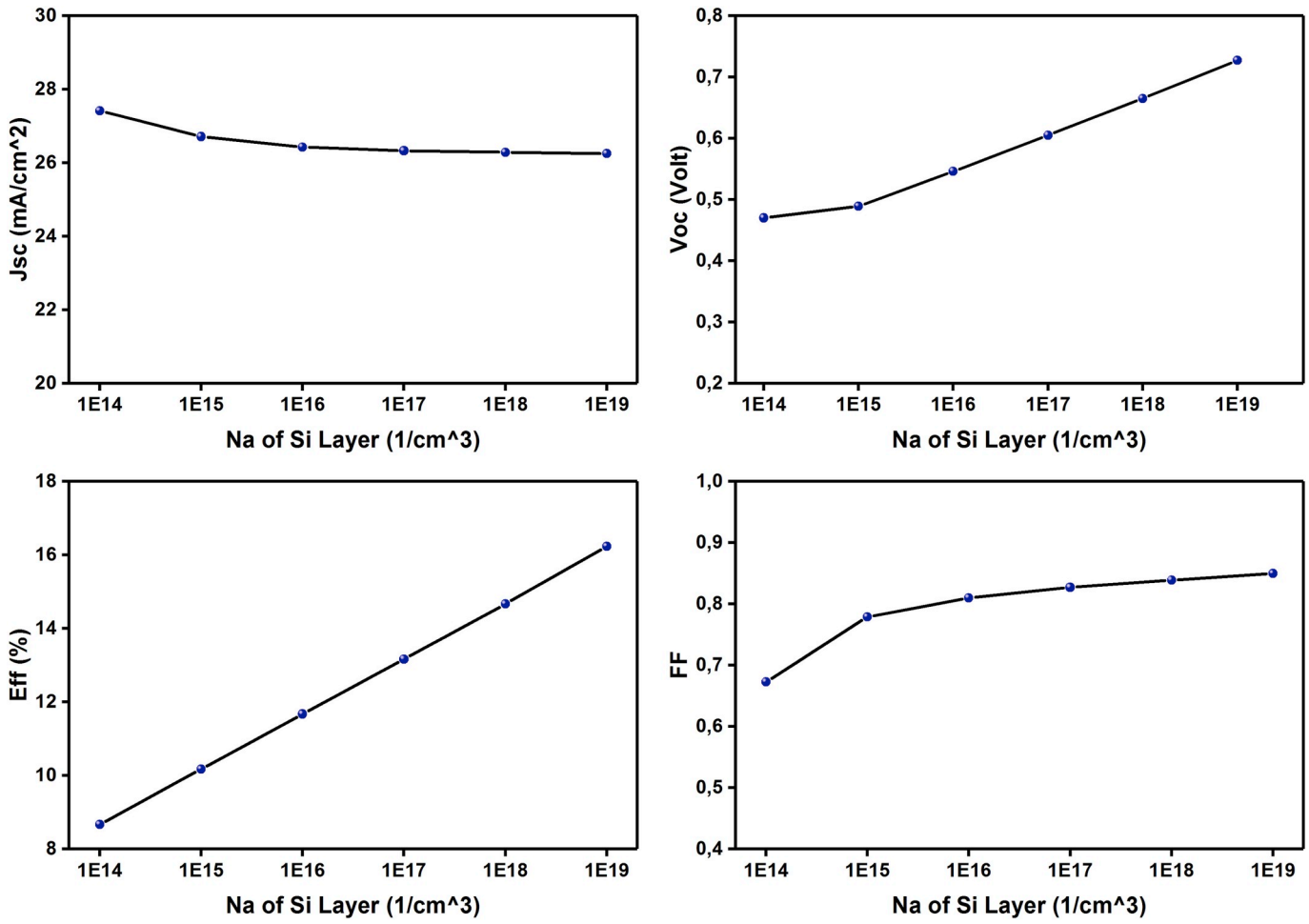

Fig. 8. Photovoltaic parameters of defected ZnO/Si/Cu_2O solar cell as a function of doping concentration N_A(p-Si).

only 8 μm thick silicon solar cells.

3.3. Thickness optimization of Cu_2O back layer

To clarify the effect of the Cu_2O back layer thickness (from 0 nm to 500 nm) on the cell performance, the ZnO/Si/Cu_2O heterostructure was simulated and the results are summarized in Fig. 7. At 0 nm thick (without Cu_2O layer), the photovoltaic parameters are initially low with J_{SC} ~20.42 mA/cm^2, V_{OC} ~0.68 V, *FF* ~0.84 and an efficiency of about 11.77%. In the presence of a Cu_2O layer with an increased thickness, all J-V characteristics remain unchanged at a good efficiency η of about 16.2%, with J_{SC} ~26.2 mA/cm^2, V_{OC} ~0.72 V and *FF* ~0.85. Therefore, a few μm of Si layer give more chances to a few nm of Cu_2O back layer (several hundred nm to few μm for most experimental Cu_2O based solar cells [47,48]) to absorb the photons who have absorption length longer than the p-Si interlayer thickness. Thus, a high efficiency of about 16.2% has been expected.

3.4. Optimization of acceptor density of p-Si absorber layer

Fig. 8 shows the evolution patterns of J_{SC}, V_{OC}, *FF* and η of ZnO/Si/Cu_2O solar cell versus different acceptor concentrations of p-Si absorber layer, N_A(p-Si). For lowest and/or highest doping concentrations (N_A(p-Si) $< 10^{14}$/cm^3 and/or N_A(p-Si) $> 10^{19}$/cm^3), N_A(p-Si) have a large impact on the electronic properties (mobility, conductivity/resistivity and related parameters) of crystalline silicon. Consequently, N_A(p-Si) was varied in a moderate range from 1×10^{14}/cm^3 to 1×10^{19}/cm^3 [49]. When N_A(p-Si) exceed the effective density of states N_v(p-Si) (~10^{19}/cm^3), the crystalline silicon becomes degenerate semiconductor, thus the energy band-gag narrowing will be [50].

At the beginning, for N_A(p-Si) $= 1 \times 10^{14}$/cm^3 the efficiency η and FF were achieved small values of about 8.67% and 0.67, respectively. For N_A(p-Si) $> 1 \times 10^{14}$/cm^3, we observe that J_{SC} shows slight decrease from 27.41 mA/cm^2 at the concentration 1×10^{14}/cm^3 to 26.25 mA/cm^2 at the concentration 1×10^{19}/cm^3. In contrast, the open circuit voltage, V_{OC}, shows a considered increase from 0.47 V at the concentration 1×10^{14}/cm^3 to 0.72 V at the concentration 1×10^{19}/cm^3. For N_A(p-Si) $= 1 \times 10^{19}$/cm^3, the efficiency η and FF were increased to about 16.23% and 0.85, respectively. The recommended acceptor density N_A(p-Si) should be higher than that of its defect density (in this case 1×10^{14}/cm^3).

3.5. Effect of Gaussian defects of ZnO/Si/Cu_2O heterostructure

Simulation results for ZnO/Si/Cu_2O heterostructure with different gaussian (both of acceptor-like and donor-like) defects located in the band gap of p-Si absorber layer are shown in Fig. 9. From this figure, the defect density, N_{def}(p-Si), shows harmful effects on the ovarall performance of the device. The highest possible values of J-V charactristics were obtained when N_{def}(p-Si) $< 1 \times 10^{14}$/cm^3. At lower defects concentration N_{def}(p-Si) $= 1 \times 10^{11}$/cm^3 the corresponding characteristics were: $J_{SC} \sim 27.57$ mA/cm^2, $V_{OC} \sim 0.78$ V, *FF* ~ 0.90 and η~ 21.78%.

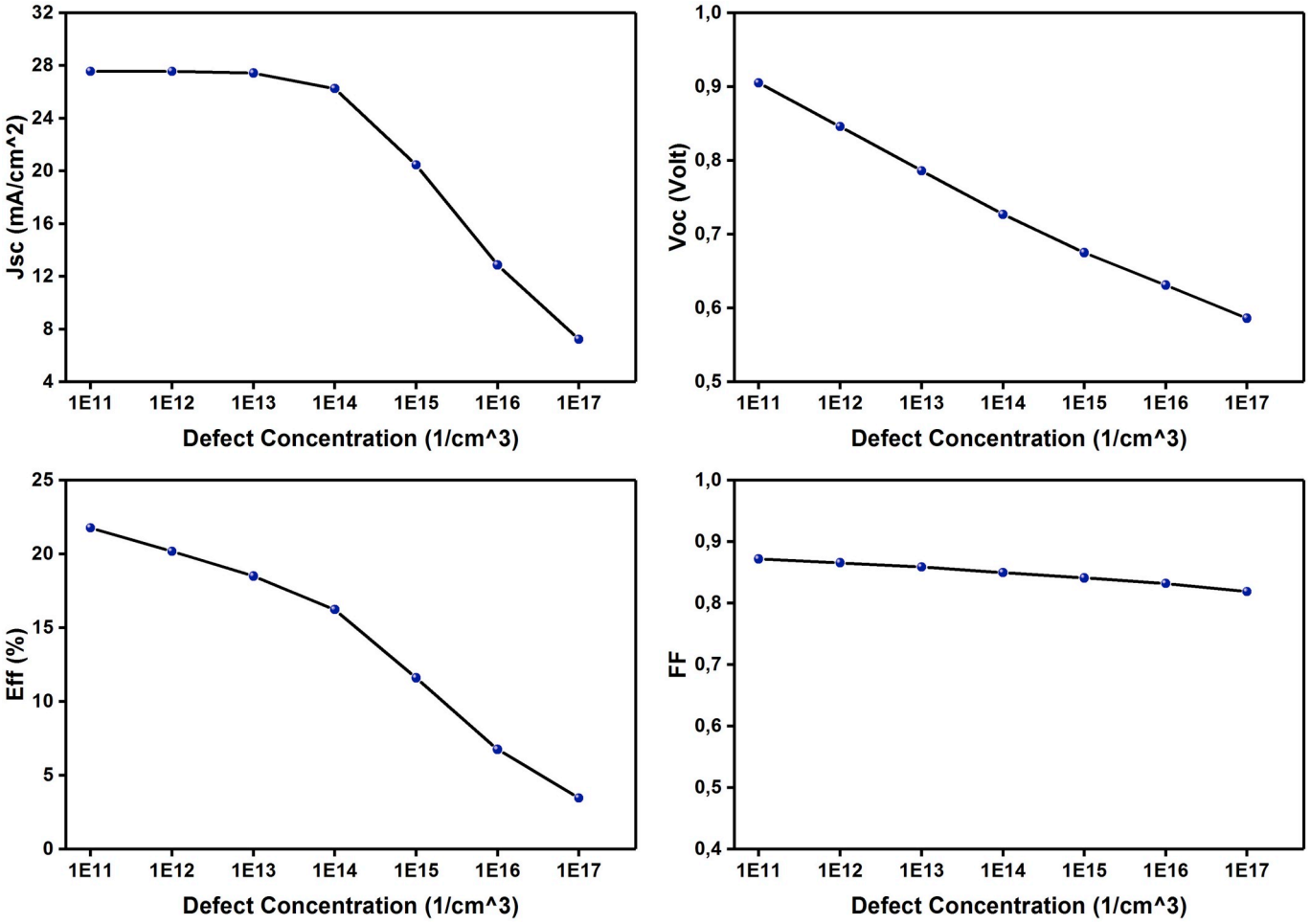

Fig. 9. Photovoltaic parameters of defected ZnO/Si/Cu_2O solar cell as a function of defects concentration N_{def}(p-Si).

Increasing N_{def}(p-Si) more than $1 \times 10^{14}/cm^3$, the J_{SC} and V_{OC} were significantly affected. The defect concentration of $1 \times 10^{17}/cm^3$ caused a sharp fall in the J-V charactristics: J_{SC} ~7.23 mA/cm^2, V_{OC} ~0.58 V, *FF* ~0.82 and η ~3.46%. This poor behavior of the ZnO/Si/Cu_2O device at high bulk defects is resulted from recombination phenomena. Therefore, the current transport may severely affected by the bulk defect density of the layer. This effect is related to created trapping (recombination) in the bulk layer that limits the efficiency [51].

3.6. Operating temperature effect on ZnO/Si/Cu_2O heterostructure performance

In the literature, the dependence of the V_{OC} to the operating temperature is used as an indicator on the stability of solar cells [30]. To testify this vital dependence on the defected ZnO/Si/Cu_2O heterostructure solar cell, the operating temperature is stepped from 300 K to 600 K by 50 K. Fig. 10 shows the evolution pattern of the photovoltaic parameters as a function of the operating temperature. Generally, increasing the operating temperature conduct to a decrease of material band gap and eventually an increase to the leakage current and a decrease to the V_{OC}. The current density J_{SC} has almost unchanged pattern (~26.5 mA/cm^2). From Fig. 10, V_{OC} decreased from ~0.73 V (recorded at 300 K) to ~ 0.32 V (recorded at 600 K). A similar behavior is observed for *FF* and efficiency which decreased from ~0.85 to ~16, 234% (at 300 K) to 0.59 and 4.97% (at 600 K), respectively.

4. Conclusion

In this contribution, a newly proposed ZnO/Si/Cu_2O heterostructure solar cell was studied by computer simulation using AMPS-1D software. We studied firstly the influence of thicknesses of different layers in the proposed structure and the acceptor concentration of p-Si absorber layer on the light J-V characteristics, in order to optimize the input parameters of the ZnO/Si/Cu_2O solar cell. The impact of defects density of p-Si absorber layer and the operating temperature on the proposed ZnO/Si/Cu_2O solar cell performance were also investigated. A 0.1 μm-ZnO/10 μm-Si/0.1 μm-Cu_2O heterostructure with N_A(p-Si) = 10^{19} cm^{-3}, showed a good characteristics: J_{SC} ~ 26.25 mA/cm^2, V_{OC} ~ 0.72 V, *FF* ~ 0.85 and η ~ 16.23%. These considered values were attributed to a low defect density of $1 \times 10^{14}/cm^3$ in p-Si absorber layer. By optimization, we realized a record efficiency for N_{def}(p-Si) lower than $10^{14}/cm^3$. For N_{def}(p-Si) = $10^{11}/cm^3$ best characteristics have been estimated of about: J_{SC} ~ 27.57 mA/cm^2, V_{OC} ~ 0.78 V, *FF* ~ 0.90 and Eff ~ 21.78%. These results are very promising for defected ZnO/Si/Cu_2O solar cells, and leave ample room in the future for further improvement.

Declaration of competing interest

The authors declare that they have no known competing financial interests or personal relationships that could have appeared to influence the work reported in this paper.

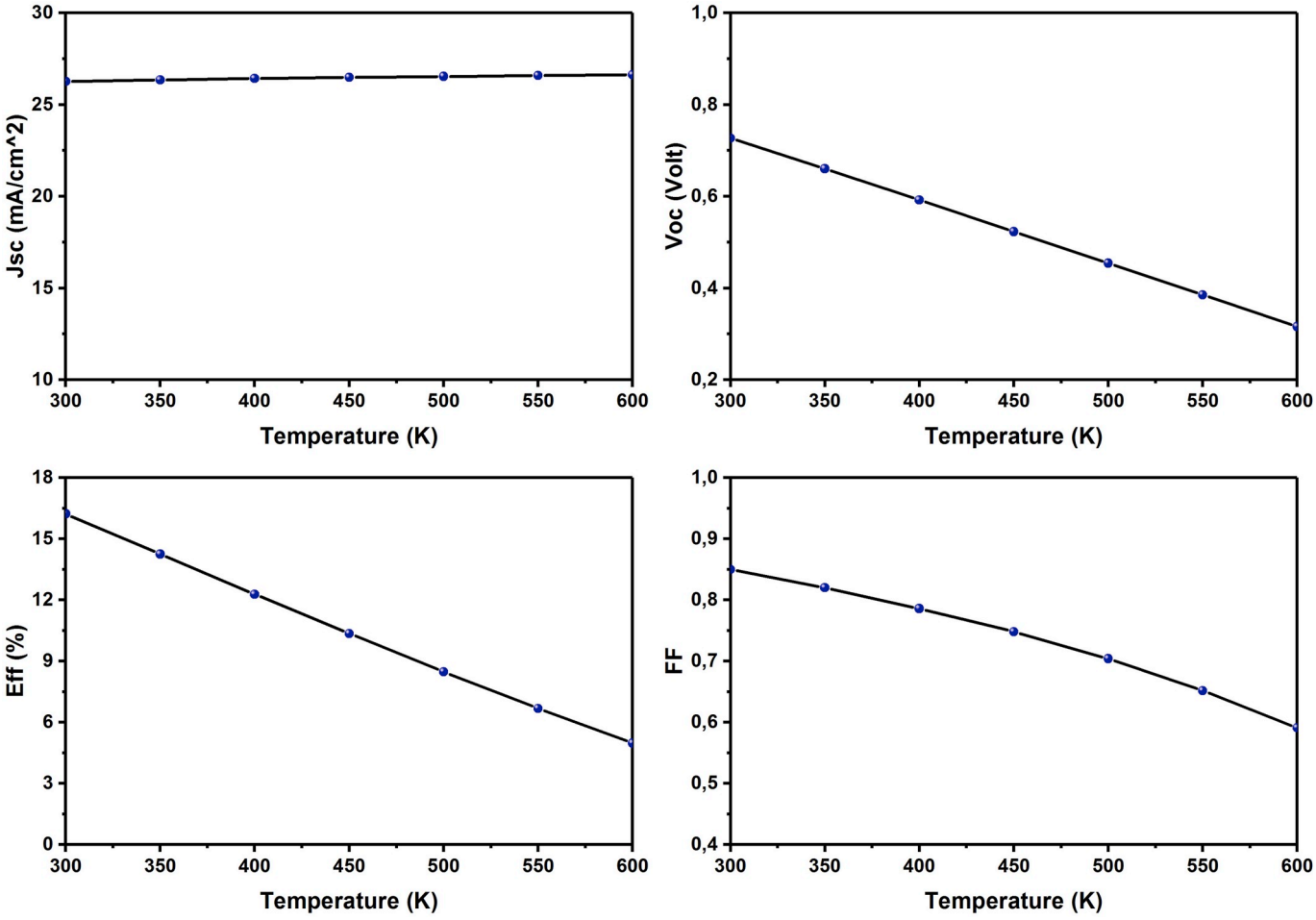

Fig. 10. Photovoltaic parameters of defected ZnO/Si/Cu_2O solar cell as a function of operating temperature.

Acknowledgements

The simulating calculation for this article used the AMPS simulator developed at the Pennsylvania State University by Fonash et al. supported by the Electric Power Research Institute.

References

[1] C.Q. Luo, F.C.C. Ling, M.A. Rahman, M. Phillips, C. Ton-That, C. Liao, K. Shih, J. Lin, H.W. Tam, A.B. Djurišić, S.-P. Wang, Surface polarity control in ZnO films deposited by pulsed laser deposition, Appl. Surf. Sci. 483 (2019) 1129–1135.

[2] A.B. Yadav, S. Jit, Particle size effects on the hydrogen sensing properties of Pd/ZnO Schottky contacts fabricated by sol–gel method, Int. J. Hydrogen Energy 42 (2017) 786–794.

[3] Y. Bicer, G. Chehade, I. Dincer, Experimental investigation of various copper oxide electrodeposition conditions on photoelectrochemical hydrogen production, Int. J. Hydrogen Energy 42 (2017) 6490–6501.

[4] H. Ennaceri, M. Boujnah, D. Erfurt, J. Rappich, X. Lifei, A. Khaldoun, A. Benyoussef, A. Ennaoui, A. Taleb, Influence of stress on the photocatalytic properties of sprayed ZnO thin films, Sol. Energy Mater. Sol. Cells 201 (2019), 110058.

[5] H.K. Juwhari, S.J. Ikhmayies, B. Lahlouh, Room temperature photoluminescence of spray-deposited ZnO thin films on glass substrates, Int. J. Hydrogen Energy 42 (2017) 17741–17747.

[6] M.R. Alfaro-Cruz, O. Ceballos-Sanchez, E. Luévano-Hipólito, L.M. Torres-Martínez, ZnO thin films deposited by RF magnetron sputtering: effects of the annealing and atmosphere conditions on the photocatalytic hydrogen production, Int. J. Hydrogen Energy 43 (2018) 10301–10310.

[7] A.M. Selman, M.A. Mahdi, Z. Hassan, Fabrication of Cu2O nanocrystalline thin films photosensor prepared by RF sputtering technique, Phys. E Low-dimens. Syst. Nanostruct. 94 (2017) 132–138.

[8] F. Baig, Y.H. Khattak, B.M. Soucase, S. Beg, S. Ullah, Effect of anionic bath temperature on morphology and photo electrochemical properties of Cu2O deposited by SILAR, Mater. Sci. Semicond. Process. 88 (2018) 35–39.

[9] E. Fortunato, V. Figueiredo, P. Barquinha, E. Elamurugu, R. Barros, Thin-film transistors based on p-type Cu_2O thin films produced at room temperature, Appl. Phys. Lett. 96 (2010), 192102.

[10] L. Liao, H.B. Lu, J.C. Li, C. Liu, D.J. Fu, Y.L. Liu, The sensitivity of gas sensor based on single ZnO nanowire modulated by helium ion radiation, Appl. Phys. Lett. 91 (2007), 173110.

[11] X. Wan, J. Wang, L. Zhu, J. Tang, Gas sensing properties of Cu_2O and its particle size and morphology-dependent gas-detection sensitivity, J. Mater. Chem. 2 (2014) 13641–13647.

[12] B. Cai, Y. Zhou, M. Zhao, H. Cai, Z. Ye, L. Wang, J. Huang, Synthesis of ZnO–CuO porous core–shell spheres and their application for non-enzymatic glucose sensor, Appl. Phys. A 118 (2015) 989–996.

[13] P.K. Pagare, A.P. Torane, Band gap varied cuprous oxide (Cu_2O) thin films as a tool for glucose sensing, Microchimica Acta 183 (2016) 2983–2989.

[14] E. Luévano-Hipólito, L.M. Torres-Martínez, D. Sanchez-Martinez, M.R. Alfaro-Cruz, Cu_2O precipitation-assisted with ultrasound and microwave radiation for photocatalytic hydrogen production, Int. J. Hydrogen Energy 42 (2017) 12997–13010.

[15] S. Bhatia, N. Verma, Photocatalytic activity of ZnO nanoparticles with optimization of defects, Mater. Res. Bull. 95 (2017) 468–476.

[16] H. Huang, J. Zhang, L. Jiang, Z. Zang, Preparation of cubic Cu_2O nanoparticles wrapped by reduced graphene oxide for the efficient removal of rhodamine B, J. Alloy. Comp. 718 (2017) 112–115.

[17] T. Zhou, Z. Zang, J. Wei, J. Zheng, J. Hao, F. Ling, X. Tang, L. Fang, M. Zhou, Efficient charge carrier separation and excellent visible light photoresponse in Cu_2O nanowires, Nano Energy 50 (2018) 118–125.

[18] P.-H. Hsiao, T.-C. Li, C.-Y. Chen, ZnO/Cu_2O/Si nanowire arrays as ternary heterostructure-based photocatalysts with enhanced photodegradation performances, Nanoscale Res Lett 14 (2019) 244.

[19] C.-H. Tang, K.-Y. Chen, C.-Y. Chen, Solution-processed ZnO/Si based heterostructures with enhanced photocatalytic performance, New J. Chem. 42 (2018) 13797–13802.

[20] C.-H. Tang, P.-H. Hsiao, C.-Y. Chen, Efficient photocatalysts made by uniform decoration of Cu_2O nanoparticles on Si nanowire arrays with low visible reflectivity, Nanoscale Res. Lett. 13 (2018) 312–319.

[21] M. Balık, V. Bulut, I.Y. Erdogan, Optical, structural and phase transition properties of Cu_2O, CuO and Cu_2O/CuO: their photoelectrochemical sensor applications, Int. J. Hydrogen Energy (2018), https://doi.org/10.1016/j.ijhydene.2018.08.159.
[22] Z. Zang, M. Wen, W. Chen, Y. Zeng, Z. Zu, X. Zeng, X. Tang, Strong yellow emission of ZnO hollow nanospheres fabricated using polystyrene spheres as templates, Mater. Des. 84 (2015) 418–421.
[23] Z. Zang, X. Tang, Enhanced fluorescence imaging performance of hydrophobic colloidal ZnO nanoparticles by a facile method, J. Alloy. Comp. 619 (2015) 98–101.
[24] J. Wei, Z. Zang, Y. Zhang, M. Wang, J. Du, X. Tang, Enhanced performance of light-controlled conductive switching in hybrid cuprous oxide/reduced graphene oxide (Cu_2O/rGO) nanocomposites, Opt. Lett. 42 (2017) 911–914.
[25] Z. Zang, Efficiency enhancement of ZnO/Cu_2O solar cells with well oriented and micrometer grain sized Cu2O films, Appl. Phys. Lett. 112 (2018), 042106.
[26] K.H. Han, M. Tao, Electrochemically deposited p-n homojunction cuprous oxide solar cells, Sol. Energy Mater. Sol. Cells 93 (2009) 153–157.
[27] Z. Zang, A. Nakamura, J. Temmyo, Single cuprous oxide films synthesized by radical oxidation at low temperature for PV application, Opt. Express 21 (2013) 11448–11456.
[28] A. Aissat, M.A. Ghomrani, W. Bellil, A. Benkouider, J.P. Vilcot, The doping effect on the properties of zinc oxide (ZnO) thin layers for photovoltaic applications, Int. J. Hydrogen Energy 40 (2015) 13685–13689.
[29] J. Xie, C. Guo, C.M. Li, Interface functionalization with polymer self-assembly to boost photovoltage of Cu_2O/ZnO nanowires solar cells, Int. J. Hydrogen Energy 39 (2014) 16227–16233.
[30] H. Heriche, Z. Rouabah, N. Bouarissa, New ultra thin CIGS structure solar cells using SCAPS simulation program, Int. J. Hydrogen Energy 42 (2017) 9524–9532.
[31] S. Boudour, I. Bouchama, N. Bouarissa, M. Hadjab, A study of CdTe solar cells using Ga-doped MgxZn1-xO buffer/TCO layers: simulation and performance analysis, J. Sci.: Adv. Mater. Devices 4 (2019) 111–115.
[32] S.B. Mitta, P. Murahari, K.R. Nandanapalli, D. Mudusu, R. Karuppannan, D. Whang, Si/ZnO heterostructures for efficient diode and water-splitting applications, Int. J. Hydrogen Energy 43 (2018) 16015–16023.
[33] S. Laidoudi, A.Y. Bioud, A. Azizi, G. Schmerber, J. Bartringer, S. Barre, A. Dinia, Growth and characterization of electrodeposited Cu_2O thin films, Semicond. Sci. Technol. 28 (2013), 115005.
[34] S.S. Jeong, A. Mittiga, E. Salza, A. Masci, S. Passerini, Electrodeposited ZnO/Cu_2O heterojunction solar cells, Electrochim. Acta 53 (2008) 2226–2231.
[35] T. Minami, Y. Nishi, T. Miyata, J. Nomoto, High-efficiency oxide solar cells with ZnO/Cu_2O heterojunction fabricated on thermally oxidized Cu_2O sheets, APEX 4 (2011), 062301.
[36] Y. Nishi, T. Miyata, T. Minami, The impact of heterojunction formation temperature on obtainable conversion efficiency in n-ZnO/p-Cu_2O solar cells, Thin Solid Films 528 (2013) 72–76.
[37] T.K.S. Wong, S. Zhuk, S. Masudy-Panah, G.K. Dalapati, Current status and future prospects of copper oxide heterojunction solar cells, Materials 9 (2016) 271.
[38] L. Zhu, G. Shao, J.K. Luo, Numerical study of metal oxide heterojunction solar cells, Semicond. Sci. Technol. 26 (2011), 085026.
[39] F.Z. Bedia, A. Bedia, B. Benyoucef, S. Hamzaoui, Electrical characterization of n-ZnO/p-Si heterojunction prepared by spray pyrolysis technique, Physics Procedia 55 (2014) 61–67.
[40] A.A. El-Amin, High efficiency computer simulation for Au/n-ZnO/p-Si/Al Schottky-type thin film heterojunctions, Siliconindia 9 (2017) 385–393.
[41] A. Aissat, M. El bey, R. Bestam, J.P. Vilcot, Modeling and simulation of $Al_xGa_yIn_{1-x-y}As$/InP quaternary structure for photovoltaic, Int. J. Hydrogen Energy 39 (2014) 15287–15291.
[42] S.J. Fonash, A manual for one-dimensional device simulation program (AMPS), Electron, in: Mater. Process. Res. Lab, Peensylvania State University, 2007.
[43] M. Reuter, W. Brendle, O. Tobail, J.H. Werner, 50 μm thin solar cells with 17.0% efficiency, Sol. Energy Mater. Sol. Cells 93 (2009) 704–706.
[44] J. Yoon, L. Li, A.V. Semichaevsky, J. Ha Ryu, H.T. Johnson, R.G. Nuzzo, J. A. Rogers, Flexible concentrator photovoltaics based on microscale silicon solar cells embedded in luminescent waveguides, Nat. Commun. 2 (2011) 343.
[45] J.L. Cruz-Campa, M. Okandan, P.J. Resnick, P. Clews, T. Pluym, R.K. Grubbs, V. P. Gupta, D. Zubia, G.N. Nielson, Microsystems enabled photovoltaics: 14.9% efficient 14 μm thick crystalline silicon solar cell, Sol. Energy Mater. Sol. Cells 95 (2011) 551–558.
[46] G. Li, Li He, J.Y.L. Ho, M. Wong, H.S.K. Kwok, Nanopyramid structure for ultrathin c-Si tandem solar cells, Nano Lett. 14 (2014) 2563–2568.
[47] M. Pavan, S. Rühle, A. Ginsburg, D.A. Keller, H.N. Barad, P.M. Sberna, D. Nunes, R. Martins, A.Y. Anderson, A. Zaban, E. Fortunato, TiO2/Cu2O all-oxide heterojunction solar cells produced by spray pyrolysis, Sol. Energy Mater. Sol. Cells 132 (2015) 549–556.
[48] M.H. Tran, J.Y. Cho, S. Sinha, M.G. Gang, J. Heo, Cu2O/ZnO heterojunction thin-film solar cells: the effect of electrodeposition condition and thickness of Cu2O, Thin Solid Films 661 (2018) 132–136.
[49] O. Isabella, K. Jäger, A. Smets, R. van Swaaij, M. Zeman, Solar Energy: the Physics and Engineering of Photovoltaic Conversion, Technologies and Systems, UIT Cambridge, 2016.
[50] D. Yan, A. Cuevas, Empirical determination of the energy band gap narrowing in highly doped n+ silicon, J. Appl. Phys. 114 (2013), 044508.
[51] F.E. Rougieux, C. Sun, D. Macdonald, Determining the charge states and capture mechanisms of defects in silicon through accurate recombination analyses: a review, Sol. Energy Mater. Sol. Cells 187 (2018) 263–272.

Doctoral thesis: Optimization of doped and co-doped Zinc Oxide Quality: Application for Silicon-Based Solar Cells (2021)

By: Samah BOUDOUR **Supervisor:** Prof. Idris BOUCHAMA

الملخص - سلطت هذه الأطروحة الضوء على مسألتين أساسيتين. المسألة الاولى تمثلت في محاكاة و تطوير كفاءة الخلايا الشمسية ذات الطبقات الرقيقة باستعمال طبقات ZnO المطعمة وغير المطعمة من خلال برنامج AMPS-1D. ثلاث تركيبات تم دراستها هي ZnO/Si/Cu_2O, TCO/Ga-doped $Mg_xZn_{1-x}O$/CdTe و TCO/p-CIGS/n-ODC/n-In_2Se_3 . ابتداءًا حقق الهيكل المعيوب n-ZnO/p-Si/p-Cu_2O كفاءة قدرت بـ 16.23%. كما سجل الهيكل المثالي n^+-HGMZO/n-LGMZO/p-CdTe كفاءة قدرت بـ 20.16%، بحيث كل من الغشائين LGMZO وHGMZO ذو فجوات الطاقة المختلفة يمثل غشاء أكسيد الزنك المطعم بـ العنصرين (Ga،Mg). أما دراسة تأثير دالة شغل المعادن لكل من الطبقة الامامية والطبة الخلفية على التركيب ذو الوجهين SLG/TCO/p-CIGS/n-ODC/n-In_2Se_3/Metal حقق كفاءة عالية قدرت بـ 20.18% با لاعتماد على $ZnSn_2O_3$ كنافذة أمامية. اما المسألة الثانية في هذه الأطروحة فقد تناولت صناعة و توصيف الطبقات الرقيقة ZnO غير المطعمة و المطعمة بعنصر المغنيزيوم بنسب مولية مختلفة فوق اسطح زجاجية بتقنية الطرد المركزي للمحلول الهلامي المحضر مخبريا. من ثم تم تشخيص كل الطبقات المحضرة بواسطة أجهزة XRD، SEM، EDX، AFM وUV-Vis. في الأخير قمنا بمناقشة النتائج المحصلة.

الكلمات المفتاحية: أكسيد الزنك، سيليكون، تطعيم بالمغنيسيوم، تقنية الطرد المركزي، تطوير الكفاءة، خلايا شمسية ذات الطبقات الرقيقة، AMPS-1D.

Abstract - This thesis highlighted two main issues. The first was the simulation and optimization of thin film solar cells using doped and/or co-doped ZnO as a window layer through AMPS-1D software. Three solar cells structures were investigated: ZnO/Si/Cu_2O, TCO/Ga-doped $Mg_xZn_{1-x}O$/CdTe and TCO/p-CIGS/n-ODC/n-In_2Se_3. The defected n-ZnO/p-Si/p-Cu_2O structure showed an efficiency of 16.23% using ZnO and Cu_2O as TCO front layer and HT-EBL layer, respectively. The ideal n^+-HGMZO/n-LGMZO/p-CdTe structure showed an optimized efficiency of 20.16%, where both HGMZO and LGMZO are (Mg,Ga) co-doped ZnO films with dissimilar band-gap. The impact of TCOs and metal work functions on superstrate SLG/TCO/p-CIGS/n-ODC/n-In_2Se_3/Metal structure were studied, an efficiency of 20.18% was achieved using transparent and conducting $ZnSn_2O_3$ front layer. The second issue of this thesis was the fabrication and characterization of undoped and Mg-doped ZnO thin films deposited onto glass substrates by the sol-gel spin-coating method. The structural, morphological and optical properties of these films were studied by XRD, SEM, EDX, AFM and UV-Vis analysis. Finally, we discuss the results obtained.

Keywords: Zinc oxide, silicon, Magnesium doping, Spin coating, Thin film solar cell, Optimization, AMPS-1D.

Résumé - Cette thèse a mis le point sur deux sujets. Le premier sujet est la simulation et l'optimisation des cellules solaires en couches minces utilisant des couches fenêtre de ZnO dopées et co-dopées grâce au logiciel AMPS-1D. Trois structures ont été étudies: ZnO/Si/Cu_2O, TCO/Ga-doped $Mg_xZn_{1-x}O$/CdTe et TCO/p-CIGS/n-ODC/n-In_2Se_3. La structure des défauts optimisée n-ZnO/p-Si/p-Cu_2O a montré une efficacité de 16.23% utlisant les couches ZnO et Cu_2O comme couche fenêtre TCO et HT-EBL, respectivement. La structure idéale n^+-HGMZO/n-LGMZO/p-CdTe a montré une efficacité optimisée de 20.16%, où HGMZO et LGMZO sont des couches minces à base de ZnO co-dopées par (Mg,Ga) avec des bandes interdites différentes. L'impact de la fonction de travail des TCO et des métaux dans les structures superstrates SLG/TCO/p-CIGS/n-ODC/n-In_2Se_3/Metal a été étudié, où une efficacité de 20.18% a été obtenue en utilisant $ZnSn_2O_3$ comme couche frontale. Le deuxième sujet étudié dans cette thèse est la fabrication et la caractérisation des couches minces de ZnO non-dopées et Mg-dopées déposées sur des substrats de verre par la technique sol-gel spin-coating. Les propriétés structurales, morphologiques et optiques de ces films ont été étudiées par XRD, SEM, EDX, AFM et UV-Vis. Finalement, on a discuté les résultats obtenus.

Mots clés: Oxyde de zinc, Silicium, Dopage par Magnésium, spin coating, cellule solaire en couches minces, Optimisation, AMPS-1D.